Numerical Schemes for 1-D Two-Phase Flows

by

Qiulan Zeng

A thesis
presented to the University of Waterloo
in fulfillment of the
thesis requirement for the degree of
Doctor of Philosophy
in
Mechanical and Mechatronics Engineering

Waterloo, Ontario, Canada, 2017

Examining Committee Membership

The following served on the Examining Committee for this thesis. The decision of the Examining Committee is by majority vote.

External Examiner	Nikola Popov Adjunct Professor
Supervisor(s)	Fue-Sang Lien Professor
Supervisor(s)	Nusret Aydemir Associate Adjunct Professor
Internal Member	Cecile Devaud Professor
Internal Member	Roydon Fraser Professor
Internal-external Member	Francis Poulin Associate Professor

I hereby declare that I am the sole author of this thesis. This is a true copy of the thesis, including any required final revisions, as accepted by my examiners.

I understand that my thesis may be made electronically available to the public.

Abstract

Modeling of two-phase flows with strong thermal and mechanical non-equilibrium effects is important in engineering applications, such as the nuclear industry. The Advection Upstream Splitting Methods (AUSM-family schemes) are very popular due to their attractive features for multiphase flow modeling. However, the computational efficiency of collocated-grid-based AUSM-family schemes with explicit time integration are inferior due to a number of issues. These include the odd-even decoupling of the collocated-grid-based AUSM-family schemes for low-Mach-number flows, the non-conservative characteristic of the two-phase governing equations, and the Courant-Friedrichs-Levy (CFL) number limitation for the explicit time integration.

This thesis focuses on improving the accuracy and efficiency of calculation for all-Mach-number two-phase flows. In order to achieve this objective, this thesis makes the first attempt at using implicit staggered-grid-based AUSM-family (SG-AUSM-family) schemes. This is a novel approach since most work in the publicly available literature solves multiphase compressible flow problems explicitly over collocated grids. In this thesis, a four-equation generic two-fluid model is mainly considered. In addition, Newton's method with a numerical Jacobian matrix is employed to solve the implicitly discretized equations. The benchmark test cases include Ransom's water faucet, the oscillating manometer, the phase separation, and the air-water shock tube problems.

In the first stage, after thorough mathematical analysis and numerical tests of various explicit AUSM-family schemes on collocated grids, insight into the numerical dissipation mechanism of the AUSM-family schemes was gained. This motivates the author to propose a new scheme, namely, the staggered-grid-based AUSMFVS (SG-AUSMFVS) scheme, to solve the stiff phase separation problem.

The second stage of the work is to examine the numerical accuracy and computational efficiency of collocated-grid-based implicit AUSM-family schemes. Results demonstrate that with certain time step size selections, the implicit AUSM-family schemes are superior to their explicit counterparts, in terms of numerical accuracy and computational efficiency.

The third phase of the work is the application of the first-order SG-AUSM-family schemes on the benchmark test cases. Results demonstrate the advantages of staggered-grid-based AUSM$^+$ (SG-AUSM$^+$) and staggered-grid-based AUSMDV (SG-AUSMDV) over their collocated-grid-based counterparts. With a staggered-grid arrangement, odd-even decoupling issues can be avoided. As a result, no additional diffusion terms are needed when using SG-AUSM$^+$ and SG-AUSMDV schemes for low-Mach-number two-phase flows. Furthermore, since the pressure and void fraction are already stored at the interface of the velocity control volume, no interpolation of interfacial pressure is needed for the momentum equations, thereby saving computational time. Finally, the SG-AUSM$^+$ scheme is capable of producing accurate solutions comparable with or even better than the corresponding collocated-grid-based AUSM$^+$ scheme. In particular, the new SG-AUSMFVS scheme demonstrates superb stability and accuracy for all the test cases considered in this thesis.

Finally, the SG-AUSM-family schemes have been extended to second-order spatial accuracy using the classical Monotonic Upstream-Centered Scheme for Conservation Laws (MUSCL) approach with TVD limiters. The MUSCL technique with the van Albada limiter has also been implemented into the mass equation in CATHENA4. This resulted in improved accuracy of the CATHENA44 code, especially for the oscillating manometer problem.

In summary, this thesis not only improves the accuracy and efficiency of calculation for all-Mach-number two-phase flows, but also helps integrate high-resolution schemes and SG-AUSM-family schemes into staggered-grid-based thermal hydraulic codes in the nuclear industry, such as CATHENA4.

Acknowledgements

I am extremely grateful to Prof. Fue-Sang Lien and Prof. Nusret Aydemir for giving me the opportunity to perform the research into the interesting subject of numerical schemes for 1-D two-phase flows. I would also like to thank their valuable advices, encouragement, and support.

I would also like to thank Prof. Nikola Popov, Prof. Cecile Devaud, Prof. Roydon Fraser, and Prof. Francis Poulin for being my Ph.D committee members and gave me valuable suggestions.

I would also like specially thank Tao Xu for the fruitful discussions, advices, and support throughout these years.

In addition, I would like to express my gratitude to Meishen Li, Chenguang Li, Ping Ma, Yao Deng, Hang Meng, huang-Rui Mo, Tian Yi, Jianyu Chen for their advice, support, and companionship in my Ph.D study.

In particular, I would like to convey my appreciation to the anonymous reviewers for providing very helpful comments on the journal papers. These comments greatly help improving the quality of this thesis and are extremely useful for my research.

I would like to acknowledge the financial support from Canadian Nuclear Laboratories (CNL).

Finally, I dedicate this thesis to my family for their love, support and encouragement during my Ph.D study.

Dedication

To my beloved husband, son and mom.

Table of Contents

List of Tables

List of Figures

List of Acronyms

AUSM Advection Upstream Splitting Method

AUSMD a variation of AUSM similar in form to FDS

AUSMV a variation of AUSM similar in form to FVS

AUSMDV a mixture of AUSMD and AUSMV

AUSM$^+$ an improved version of AUSM

AUSM$^+$-up a variation of AUSM$^+$ that adds velocity and pressure diffusion terms

CANDU CANada Deuterium Uranium

CATHENA4 the fourth version of Canadian Algorithm for THErmalhydraulic Network Analysis

CATHARE the Code for Analysis of THermalhydraulics during an Accident of Reactor and safety Evaluation

CFD Computational Fluid Dynamics

CFL Courant-Friedrichs-Levy number

CNL Canadian Nuclear Laboratories

FDS Flux Difference Splitting

FVS Flux Vector Splitting

HLL Harten, Lax, and van Leer scheme

MUSCL Monotonic Upstream-Centered Scheme for Conservation Laws

PISO Pressure Implicit with Splitting of Operator

PD-AUSM$^+$ a variation of AUSM$^+$ scheme that adds pressure diffusion terms in the liquid mass flux

RELAP5 Reactor Excursion and Leak Analysis Program

SIMPLE Semi-Implicit Method for Pressure Linked Equations

SG-AUSM$^+$ Staggered-Grid-based AUSM$^+$

SG-AUSMD Staggered-Grid-based AUSMD

SG-AUSMV Staggered-Grid-based AUSMV

SG-AUSMDV a mixture of SG-AUSMD and SG-AUSMV

SG-AUSMFVS a mixture of SG-AUSM and SG-FVS

SG-FVS Staggered-Grid-based FVS

T-H Thermal Hydraulic

TVD Total Variation Diminishing

Nomenclature

0.1 Symbols

Symbol	Units	Description
$\boldsymbol{n}$	1	outwards normal vector to the surface
$\boldsymbol{v}$	m/s	velocity
v_z	m/s	velocity in z direction
e	J	specific internal energy
$\boldsymbol{e}_i$	1	a unit vector where only the i^{th} component equals one, and all other components are zero
E	J	specific total energy
h	J	specific enthalpy
H	J	specific total enthalpy
N	1	total number of nodes in a grid
$\boldsymbol{J}$	–	numerical Jacobian matrix
$\boldsymbol{w}$	–	a vector consists of primitive variables
$\boldsymbol{w}^*$	–	initial guess of $\boldsymbol{w}$
$\Delta\boldsymbol{w}$	–	increment of $\boldsymbol{w}$
ψ	–	intensive property
$\boldsymbol{\psi}$	–	conserved quantity
$\boldsymbol{f}$	–	surface flux
ρ	m/s	density

k	1	$k = g$ for the gas phase and l for the liquid phase
t	s	time
Δx	s	mesh size
Δt	s	time step size
Δp	Pa	pressure correction term
z	m	axial coordinate
π	1	3.1415926...
$\boldsymbol{f}$	$-$	flux vector based on primitive variables
$\boldsymbol{F}$	$-$	flux vector based on conserved variables
$\boldsymbol{F}$	$\mathrm{kg}/(\mathrm{m} \cdot \mathrm{s}^2)$	body force in subsections 2.2.1 and 2.2.2
$\boldsymbol{Q}$	$-$	source terms
$\boldsymbol{T}$	$\mathrm{kg}/(\mathrm{m} \cdot \mathrm{s}^2)$	stress tensor
$\boldsymbol{R}$	$-$	residual vector
p	Pa	pressure
$\dot{m}_{ki}$	Pa	mass transfer from phase k to the interface of two phases
ϕ	1	flux limiter in subsection 3.5 and subsection 5.7
ϕ	$-$	volume source in subsection 2.2.1
ϕ	$-$	a parameter in s
ϵ	$-$	perturbation value in the e_i direction for Newton's iteration method
ε	$-$	a convergence tolerance for Newton's iteration method
g	m^2	gravitational acceleration
S_0	m^2	outside surface
S_i	m^2	common interface
τ	$\mathrm{kg}/(\mathrm{m} \cdot \mathrm{s}^2)$	visous stress tensor
α	1	volume fraction
σ	1	coefficient in the pressure correction term
δ	1	Kroeneker's delta
χ	1	weighting factor in $\hat{U}^{\pm}$

0.2 Superscripts

Symbol	Description
i	variables at the interface
m	"m$^{\text{th}}$" Newton-Raphson iteration
n	"n$^{\text{th}}$" time step level
nv	non-viscous source terms

0.3 Subscripts

Symbol	Description
d	disappearing phase
g	gas phase
i	centroid index of mass control volume
I	centroid index of momentum control volume
$i \pm 1/2$	cell border index of mass control volume
$I \pm 1/2$	cell border index of momentum control volume
l	liquid phase
L	left state
r	remaining phase
R	right state
w	Wall

Chapter 1

Introduction

1.1 Background

Modeling of two-phase flow is of high importance in engineering applications. Examples of the applications include the power cooling and heat transfer in nuclear industry, oil industry and chemical industry. In nuclear power plants, it is of great importance to accurately model two phase flow with sharp spatial gradients such as water hammer, to prevent the loss of coolant accidents. During the last decades, one-dimensional thermal hydraulic codes (T-H codes) in the nuclear industry, such as the Canadian Algorithm for THErmalhydraulic Network Analysis (CATHENA4) [2], RELAP5 [3] and CATHARE [4], have been developed. These codes employ a staggered-grid approach along with an implicit time integration scheme to ensure numerical stability. In this thesis, CATHENA4 is mainly concerned. It uses a first-order advective upwind differencing scheme, which generates diffusive results [5]. In the meanwhile, various upwind schemes developed in the last decades makes it possible to increase the predictive accuracy for the above phenomena. In general, these schemes can be classified into the flux difference splitting (FDS) type and the flux vector splitting (FVS) type. The former, including Godunov [6][7], Roe [8][9], and HLL [10][11] schemes, uses either an exact or approximate solution of the local Riemann problem, while the latter such as the van Leer scheme [12], splits the numerical flux into

upstream and downstream traveling parts.

Some T-H codes have already incorporated some of the above schemes. For example, RELAP5/MOD3 uses the Godunov method [13], CATHARE-2 applies the van Leer method [14]. Nevertheless, effciency and accuracy are still the two important issues for the development of T-H codes. It is noted that the Godunov scheme [6] requires large computational resources and lacks generality due to the analytical calculations of the Riemann invariants [8], and the van Leer scheme is too diffusive for solving contact discontinuities and shear layers [9].

This chapter begins with a review of two-phase mathematical models. Then a brief introduction to the challenges of solving two-phase problems using the two-fluid model is given. Following that, a review of numerical methods is undertook. Finally, the objectives of this thesis is presented, followed by a brief summary of the subsequent chapters.

1.1.1 Review of Two-Phase Mathematical Models

Generally, there are two ways to derive equations for two-phase flow: the Euler-Lagrange approach, and the Euler-Euler approach. In the Euler-Lagrange approach, the continuous phase is solved by the time-averaged Navier-Stokes equations, whereas the dispersed phase is treated by tracking numbers of particles, droplets, or bubbles through the continuous field. Consequently, this approach is computationally practical only for the cases where the dispersed phase is very dilute, but inappropriate for any applications where the void fraction of the dispersed phase can not be negligible. On the contrary, in the Euler-Euler approach, different phases are regarded as interpenetrating continua. Through the introduction of void fraction, a set of conservation equations for each phase, which has similar structure for all phases, is employed to perform calculations. Although it may not be as accurate as the Euler-Lagrange approach, the Euler-Euler approach is more computationally practical for the cases where the dispersed phase is not quite dilute. Hence, this thesis adopts the Euler-Euler approach.

In the Euler-Euler approach, there are three classical mathematical models, namely, the homogeneous equilibrium model, the drift-flux model, and the two-fluid model. In the

homogeneous equilibrium model, the phases are assumed to be fully mixed such that the mixture can be treated as a pseudo fluid with mixture properties. The basic assumption in the homogeneous equilibrium model is that the mass, momentum, and energy transfer between the phases are rapid enough to achieve equilibrium. In other words, the temperature, pressure, and velocity between phases are equal. Therefore, it is inappropriate to use this model for the cases where phase acceleration or pressure changes are rapid.

On the other hand, through the introduction of drift fluxes, the drift flux model modifies the homogeneous equilibrium model by incorporating the relative motion between the phases. The drift flux model consists of four field equations: the mixture mass, momentum, energy equations, and the gas mass equation. In addition, the relative motion and energy difference of the two phases are expressed by additional constitutive equations. Therefore, the drift flux model is appropriate for cases where the phases are closely coupled [1] or phases that are locally weakly coupled. Thus, it is useful for problems such as void propagation. However, it is not suitable for problems such as the acoustic wave propagations.

In contrast to the homogeneous equilibrium model and the drift flux model, the two-fluid model [16][15] treats each phase separately in terms of two sets of conservation equations, with interaction terms in those equations as transfer terms across the gas-liquid interface. In other words, each phase has its own set of temperature, pressure, and velocity. To close the governing equations, constitutive relations have to be provided, either from empirical information or from the application of kinetic theory. Therefore, the two-fluid model gives more detailed information about transient two-phase flows than the drift flux model or the homogeneous equilibrium model. In particular, the two-fluid model is very useful for the cases where phases are weakly coupled such as the acoustic wave propagations, for which the aforementioned two models are not available. Consequently, many researchers have used this model to study the two phase flow [17] [18] [19] [20], and this thesis will focus on the two-fluid model.

[1] The phases are strongly coupled means that they response simultaneously to approximate mechanical and thermal equilibrium, or the wave propagations are tightly interlocked. [15]

1.1.2 Difficulties in the Two-Fluid Model

Many numerical difficulties which do not exist in single-phase simulation arise for multi-phase flow problems [21]:

1. The equation system is ill-posed because of its non-hyperbolicity due to the complexity of the system eigenvalues [22] [21] [23] and [24]. This non-hyperbolic nature of the equation system could lead to strong oscillations [21]. The common strategy to handle this problem is the adoption of a pressure correction due to interfacial effects. It is expected that the interface propagates with an intermediate velocity and has an intermediate pressure which should be modeled. This implies the presence of non-conservative terms in the two-fluid model which must be carefully modeled to achieve a stable hyperbolic model. [21]. Other methods use surface tension force terms [25] [26], virtual mass [27] [28], and separate pressures [7]. They also include a pressure diffusion term [29] to improve the hyperbolicity of the system. Even so, an implicit operator or additional numerical dissipation is still necessary to make the calculation stable, leading to excessive diffusion which is usually found in the solutions [30]. In addition, according to [22], "even if the multifluid model is rendered hyperbolic, its eigensystem is still too complicated to be put in an analytical form, hence making it difficult to use the characteristic-based approximate Riemann solvers such as the Roe's scheme or the Osher's scheme."

2. Non-conservative terms in momentum equations can lead to oscillations of solution in the vicinity of the interface [23]. Since the two-fluid model treats the interface as a weak solution in the fluid, and the interface is captured by ensuring the conservation law, non-standard discretization methods are needed to capture the interface exactly [23]. For the non-conservative terms, oscillations can occur in the vicinity of the interface if they are not discretized consistently with the conservative terms. To tackle this issue, it is important that the numerical schemes satisfy the "pressure non-disturbing condition" or Abgrall's principle [6][8][31]. Examples of such efforts include the stratified flow model concept [32][22][23], and a special discretization of

the non-conservative terms described in [9][7]. In Section 3.4, to the best knowledge of the author, it is the first time proved that due to the staggered-grid arrangement, the staggered-grid-based AUSM$^+$ (SG-AUSM$^+$) scheme proposed by this work satisfies Abgrall's principle without any complex treatment of the non-conservative terms.

3. A large disparity in material properties will yield a stiff mathematical system. This property generates considerable difficulty in numerical simulation. [32] [23].

4. As stated in [17], "Considerable uncertainties exist in the closure relations for the two-fluid model". To avoid excessive computational complexity, averaging procedures are always used for models describing two-phase flows in pipe networks, thereby leading to a significant loss of accuracy in the averaging process [33]. A common approach to solve this problem is to augment those models by closure laws [33].

1.1.3 Review of Numerical Methods

Computational methods can be categorized into two classes: pressure-based methods and density-based methods. Pressure-based methods were originally developed to solve incompressible flows. Examples include the well-known Semi-Implicit Method for Pressure Linked Equations (SIMPLE) [34] and Pressure Implicit with Splitting of Operator (PISO) [2] algorithms with a staggered-grid arrangement. On a staggered grid, scalar variables, such as pressure and sound speed, are stored at the centroids of the control volumes, whereas the vector components are stored at the control volume interfaces. On the contrary, for a collocated grid arrangement, all variables are stored at the centroids of the control volumes. For incompressible flows, staggered schemes are appealing because they do not need additional artificial dissipation to avoid spurious pressure oscillations due to odd-even decoupling. Nonetheless, a staggered arrangement is difficult to extend for non-orthogonal or unstructured grids.

To avoid this difficulty, in 1983, Rhie and Chow proposed a momentum interpolation in combination with collocated grids to solve turbulent flows over a 2-D airfoil meshed by a

body-fitted non-Cartesian grid [35]. Later, many research efforts have been made to extend the pressure-based methods with a collocated-grid arrangement to three dimensions.

The major disadvantage of the pressure-based methods is that they are not suitable for high-Mach-number flows unless artificial dissipation is introduced through the "retarded density" [36] or "retarded pressure" approaches [37]. This is because for this case, the governing equations become hyperbolic while the pressure-correction equation remains elliptic [38].

On the other hand, the density-based methods were originally developed to solve compressible flow problems. Over the last several decades, researchers have proposed different upwind schemes to deal with the compressible multi-phase flows. These can generally be categorized into flux difference splitting (FDS) schemes and flux vector splitting (FVS) schemes. The basic idea of FDS is to solve the local Riemann problem to achieve accuracy, thereby requiring expensive computational time due to large matrix calculations. A well-known example is the Godunov-type scheme [39, 40]. On the other hand, FVS splits the flux vector into forward and backward components based on the decomposition of eigenvalues into positive and negative values associated with the Jacobian matrices; Therefore, FVS is less time consuming than FDS. However, FVS introduces excessive numerical dissipation, especially for contact discontinuity and shear layer. To retain the accuracy of FDS and efficiency of FVS, Liou and Steffen proposed the AUSM (Advection Upstream Splitting Method) scheme [41] in 1993. The basic idea of AUSM is to split the inviscid flux vector into two parts, namely the convective and pressure fluxes. The former is regarded as quantities convected by an interfacial velocity or Mach number, whereas the latter is associated with the acoustic speed. Until now, to the best of the author's knowledge, the majority of density-based methods have used the collocated-grid arrangement. Nevertheless, when using a density-based algorithm, particularly in conjunction with an explicit time-stepping scheme, efficiency may be dramatically reduced and accuracy may be lost as the Mach number approaches zero, mainly due to the increased stiffness caused by the weakened pressure-density coupling of the system.

So far, most research efforts have been made to develop pressure-based methods for fluid flow problems at high Mach numbers, and density-based algorithms for fluid flow problems

at low Mach numbers. Generally, for density-based algorithms, two strategies, including the time-derivative preconditioning technique [42, 43, 44] and numerical dissipation [45, 46], can be employed to alleviate the above-mentioned issues.

Since the AUSM scheme possesses the excellent feature of the accuracy of FDS and the efficiency of FVS, it has become popular in the Computational Fluid Dynamics (CFD) community, and variants of the AUSM scheme (or the AUSM-family schemes) have been proposed over the recent decades. Here, the AUSM$^+$ [47] and AUSMDV schemes [1] will mainly be focused on. The AUSM$^+$ scheme, proposed in 1996 by Liou [47], is capable of exactly resolving 1D contact discontinuity and shock waves, while preserving density positivity. Wada and Liou proposed the AUSMDV scheme [1]. This scheme also possesses the above-mentioned favorable properties that the AUSM$^+$ scheme has. The major difference between the AUSM$^+$ scheme and the AUSMDV scheme lies in the definition of interfacial mass flux as the latter has an additional pressure-diffusion term. However, since both schemes are considered as density-based algorithms, the AUSM$^+$ and AUSMDV schemes start to lose accuracy when the Mach number becomes very low. For low-Mach-number flows, they behave like a central difference discretization, leading to odd-even decoupling [45]. To enhance the stability when solving low-Mach-number flow problems, Edwards and Liou in 1998 [45] introduced numerical sound speed to rescale the Mach number in low-Mach-number flow regions, using the time-derivative preconditioning technique. They then added a pressure-diffusion term to the interfacial mass flux in the AUSM$^+$ and AUSMDV schemes to overcome the odd-even decoupling issues. Following this idea, Edwards et al. [46] first successfully extended the AUSM$^+$ scheme to solve phase transitions with a homogeneous equilibrium two-phase flow model. Three years later, Paillère [19] employed the PD-AUSM$^+$ scheme to solve the phase-separation and oscillating manometer problems based on the two-fluid model. In addition to the issues encountered for single-phase flow at low Mach numbers, namely, scaling issues by the sound speed and pressure-velocity decoupling at low speeds, two-phase flow models also have the stiffness problem due to the use of equation of state for water. To deal with the stiffness, Chang and Liou in 2003 [48] added another form of pressure-diffusion and velocity-diffusion terms into the interfacial mass flux and pressure flux, respectively, without using the time-derivative

preconditioning. In 2006, Liou proposed the AUSM$^+$-up scheme [49], which added pressure-difference-based term into the interfacial Mach number instead of pre-processing the Mach numbers by rescaling the interfacial sound speed. In addition, Liou also introduced a velocity-difference-based diffusion term into the pressure flux. The AUSM-family schemes are summarized in Table 1.1.

Table 1.1: Summary of AUSM-family schemes

Scheme	Proposed Year	Features
AUSM [41]	1993	Splits the flux into a convective part according to the flow direction determined by the Mach number sign, and a pressure part based on the acoustic properties of the flow.
AUSM$^+$ [47]	1996	Based on AUSM; uses a set of more general Mach number and pressure splitting functions.
AUSMD [1]	1997	Based on AUSM; removes the dissipation by replacing the velocity splitting functions in van Leer FVS to ensure exact resolution of a stationary and moving contact discontinuity.
AUSMV [1]	1997	Based on AUSM; removes the dissipation by replacing the velocity splitting functions in van Leer FV/DS to ensure exact resolution of a stationary and moving contact discontinuity.
AUSMDV [1]	1997	Based on AUSM; a mixture of AUSMD and AUSMV
PD-AUSM$^+$ [19]	2003	Based on AUSM$^+$; modifies the AUSM$^+$ scheme by adding a pressure diffusion term into the liquid mass flux.
AUSM$^+$-up [49]	2006	Based on AUSM$^+$; modifies AUSM$^+$ by adding a pressure diffusion into the interfacial Mach number, and a velocity difference term into the pressure flux.

To summarize, pressure-based methods on a staggered grid are accurate and efficient for low-Mach-number incompressible flows. On the other hand, density-based methods, such as AUSM-family schemes, with a collocated-grid arrangement are promising in solving compressible flow problems. Nevertheless, additional challenges should be tackled when

solving a compressible flow using pressure-based methods or solving an incompressible flow with density-based methods.

In this thesis, extension of AUSM-family schemes to all-Mach-number flows was one of the objectives. Motivated by the fact that staggered schemes do not need additional artificial dissipation to tackle the odd-even decoupling issues, the present work proposed staggered-grid-based AUSM-family (SG-AUSM-family) schemes to two-phase flow benchmark test problems, including the water faucet problem [50], oscillating manometer problem [50], air-water phase separation problem [17], and the air-water shock tube problems [51] [52][53] [9] .

To date, most studies have solved multi-phase compressible flow problems explicitly using a collocated grid. Explicit schemes have the advantages of relatively straightforward implementation and limited requirement for memory storage. However, explicit schemes are also highly time-consuming due to restrictions on the time step. Especially for compressible flow problems at low Mach numbers, the time step is extremely small as required by the Courant-Friedrichs-Lewy (CFL) stability criterion. For a two-phase flow problem, the definition of CFL number is given by [54]

$$\mathrm{CFL} = \Delta t / \min_{j} \left(\frac{\Delta x}{\max\left(a_g, a_l\right) + \max\left(\left|u_g\right|, \left|u_l\right|\right)} \right)_j, \tag{1.1}$$

where j denotes the j^{th} node, a_g and a_l are the sound speed of gas and liquid phases, respectively; u_g and u_l denote the fluid velocity of gas and liquid phases, respectively; Δt and Δx are time step and length interval, respectively.

To alleviate the acoustic time-step restriction, implicit methods can be used. In this thesis, both implicit and explicit AUSM-family schemes were employed for the benchmark test cases. The comparison of CPU time between implicit and explicit schemes was also reported for the above-mentioned test cases.

1.2 Motivations

This thesis aims at improving the accuracy and efficiency of calculation for all-Mach-number two-phase flows. To achieve this object, both the difficulties in the two-fluid model mentioned in subsection 1.1.2 and the difficulties caused by low-Mach-number flows have to be overcome. On one hand, in order to resolve the non-hyperbolic issue of two-fluid model, an interfacial pressure correction term is included. In addition, this thesis adopts a perturbation method to prove that the inclusion of the interfacial pressure correction term renders the four-equation generic two-fluid model hyperbolic. To overcome the non-conservative difficulties in the two-fluid model, the present work proposed staggered-grid-based AUSM-family (SG-AUSM-family) schemes. The author proves that by using the SG-AUSM$^+$ scheme, the discretized equations satisfy Abgrall's principle without complex treatment of the non-conservative terms. In addition to circumventing the non-conservative issue, the SG-AUSM-family schemes have two major advantages over their collocated-grid-based counterparts. First, since a staggered-grid arrangement is adopted, the odd-even decoupling issues are avoided. Therefore, no additional diffusion terms are needed, which are required when using collocated-grid-based AUSM$^+$ and AUSMDV schemes for low-Mach-number two-phase flows. Secondly, since pressure and void fraction are already stored at the interface of the velocity control volume, no interpolation or calculation of interfacial pressure is needed for momentum equations, thereby improving the computational efficiency. In addition, employing the implicit time integration schemes also help to improve the computational efficiency.

An additional objective of this thesis is to improve the accuracy of one-dimensional thermal hydraulic codes used in the nuclear industry, such as CATHENA4 [2], RELAP5 [3] and CATHARE [4]. Since these codes are based on the staggered-grid approach along with an implicit time integration scheme to ensure numerical stability, the present research provides a way to improve the numerical accuracy of 1-D T-H codes through the implementation of the SG-AUSM-family schemes.

1.3 Thesis Overview

This thesis is organized into four main chapters from Chapter 2 to Chapter 5, followed by Chapter 6 summarizing the main findings and contributions, and proposing future work. The following section reviews the content of each chapter.

Chapter 2 provides background information on the two-fluid flow model. It consists of three main parts. The first section presents the process of deriving averaged two-fluid flow equations. The second section describes the constitutive relationships that are required to close the averaged two-fluid flow model. The third section performs the mathematical analysis of the four-equation generic two-fluid model.

Chapter 3 details the numerical methods that are used to solve the four-equation generic two-fluid model introduced in Chapter 2. This chapter starts by a short description of discretization for the governing equations in terms of explicit and implicit forms. Then, it focuses on the treatment of numerical fluxes, including the AUSM-family schemes in Mach-number-splitting form on collocated grids, AUSM-family schemes in velocity-splitting form on collocated grids, novel SG-AUSM-family schemes proposed by the author, and the Roe scheme developed for two-fluid model. Note that the treatment of numerical fluxes is key to solving the two-fluid model. Next, the discretization of source terms is presented. In this section, it is shown that the SG-AUSM$^+$ scheme proposed by the author satisfies Abgrall's principle. After this, the MUSCL strategy is introduced, which is used to obtain higher-order (second-order in this thesis) spatially accurate numerical solutions for the two-fluid system. Finally, the decoding and updating of variables for explicit method are demonstrated.

Chapter 4 outlines the solution methods for implicit schemes. First, Newton's method for implicit equations is introduced. Then, the algorithm for calculating the numerical Jacobian matrix and residual vectors are explained. Next, the chapter deals with the initial and boundary conditions for the implicit schemes. Finally, the code architecture is provided.

Chapter 5 presents the numerical results for the benchmark test cases. It contains four main parts. This chapter starts by comparing explicit AUSM-family schemes on

collocated grids. Through this comparison, insight into the dissipation mechanism of various AUSM-family schemes is gained. This insight encourages the author to propose proper staggered-grid-based SG-AUSM-family schemes, such as the SG-AUSMFVS scheme. Next, the explicit and implicit schemes on collocated grids are compared. By doing this, results show that implicit schemes are capable of improving computational time while ensuring numerical accuracy. After this, the first-order staggered-grid-based schemes are extended onto the benchmark test cases, including Ransom's water faucet, the oscillating manometer, the phase separation, and three different air-water shock tube problems. During the tests, a new scheme, namely, SG-AUSMFVS is proposed to solve the stiff phase separation problem. Furthermore, the implicit SG-AUSM-family schemes proposed by this work are compared with the implicit collocated-grid-based AUSM-family schemes, on which most researchers are focusing. Results demonstrate the advantages of the former over the latter in terms of both the numerical stability and efficiency. Following this, using the MUSCL interpolation, the first-order implicit SG-AUSM-family schemes are extended to second-order spatial accuracy on the test cases. Finally, the MUSCL scheme with a TVD limiter is implemented in CATHENA4.

Chapter 2

Mathematical Formula for Two-Fluid Flows

2.1 Introduction

This chapter starts with a detailed derivation of the two-fluid model in Section 2.2. This section consists of four parts. First, based on the Reynolds Transport Theorem, a local instant formula for the two-phase flow is derived. This formula can be regarded as local instantaneous conservation equations with corresponding jump conditions. Next, due to the prohibitively great mathematical difficulties in solving the local equations and the limited computational capability in practice, the volume-time average technique is employed on the local instantaneous conservation equations to obtain volume-time averaged balance equations [15]. The averaging techniques generally result in a full set of 3-D equations. However, the geometry of many engineering systems, such as long pipelines, render the fluid mainly in 1-D motion. Hence, it is practical to integrate the 3-D equations over a cross section, which leads to a 1-D two-fluid model. Following the one-dimensional conservation equations, the system equations in CATHENA4 code are presented. Afterwards, in Section 2.3, to close the governing equations, the constitutive relationships are described, including the closure relationship for the interfacial pressure, the closure relationship for

friction, and the equations of state (EOS). Finally, in Section 2.4, mathematical analysis of the two-fluid model is performed using the Taylor expansion method. This analysis reveals that adding a specific pressure correction term ensures the hyperbolicity of the four-equation two-fluid model.

2.2 Derivation of the Two-Fluid Model

2.2.1 Local Instantaneous Conservation

The Reynolds transport theorem [55] [15] can be expressed as follows:

$$\underbrace{\frac{D}{Dt}\int_V (\rho\psi)\, dV}_{\text{Change with the moving system}} = \underbrace{\frac{\partial}{\partial t}\int_V \rho\psi dV}_{\text{Change within the control volume}} + \underbrace{\int_S \rho\psi\left[(\boldsymbol{v}-\boldsymbol{v}_O)\cdot\boldsymbol{n}\right] dS}_{\text{Flux across the boundary}}. \tag{2.1}$$

where ρ is the fluid density, ψ is the intensive property, V refers to the control volume, S denotes the control surface, $\boldsymbol{v}_O$ is the velocity of the control surface, and $\boldsymbol{v}$ is the fluid velocity. Note that the Reynolds transport theorem is a special case of Leibnitz's rule [15].

Consider the control volume of Fig. 2.1, which consists of the gas (g) and liquid (l) phases. In this control volume, V_k represents the volume occupied by phase k, where $k = g$ or l; $S_{O,k}$ denotes the outward surface of phase k; whereas, S_i is the interface between phase g and phase l; $\boldsymbol{v}_i$ is the interface velocity, and $\boldsymbol{v}_{O,k}$ stands for the velocity of $S_{O,k}$.

Therefore, the following equations can be obtained by applying Eq. 2.1 to the control volume of Fig. 2.1:

$$\underbrace{\sum_{k=1}^{2}\frac{\partial}{\partial t}\int_{V_k}\rho_k\psi_k dV}_{\text{Rate of change of }\psi_k} = \underbrace{-\sum_{k=1}^{2}\int_{S_{Ok}}\rho_k\psi_k\boldsymbol{v}_k\cdot\boldsymbol{n}_{Ok}dS}_{\text{Transport term}} \underbrace{-\sum_{k=1}^{2}\int_{S_{Ok}}\boldsymbol{f}_k\cdot\boldsymbol{n}_{Ok}dS}_{\text{Surface tractions}} + \underbrace{\sum_{k=1}^{2}\int_{V_k}\rho_k\phi_k dV}_{\text{Source term}}. \tag{2.2}$$

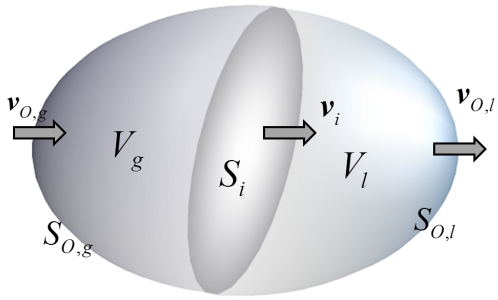

Figure 2.1: Illustration of Reynolds Transport Theorem

Using Leibniz's Rule, the transient term in Eq. 2.2 can be given by Eq. 2.3 as follows:

$$\frac{\partial}{\partial t}\int_{V_k}\rho_k\psi_k dV = \int_{V_k}\frac{\partial}{\partial t}\left(\rho_k\psi_k\right)dV + \int_{S_{Bk}}\rho_k\psi_k\boldsymbol{v}_{Bk}\cdot\boldsymbol{n}_{Bk}dS, \tag{2.3}$$

where $\boldsymbol{v}_{Bk}$ and $\boldsymbol{n}_{Bk}$ are the boundary velocity and the normal vector of phase k, respectively. Note here the surface area of phase k is a union of outward surface S_{Ok} and the interface S_i, that is $S_{Bk} = S_{Ok} \cup S_i$. Since the boundary of the control volume does not move, the normal velocity of the outward surface is zero. Therefore, Eq. 2.3 can be simplified to

$$\frac{\partial}{\partial t}\int_{V_k}\rho_k\psi_k dV = \int_{V_k}\frac{\partial}{\partial t}\left(\rho_k\psi_k\right)dV + \int_{S_i}\rho_k\psi_k\boldsymbol{v}_i\cdot\boldsymbol{n}_{ki}dS. \tag{2.4}$$

Based on the Divergence Theorem of Gauss, the transport and surface tractions terms in Eq. 2.2 can be rewritten by Eqs. 2.5 and 2.6, respectively.

$$\int_{S_{Ok}}\rho_k\psi_k\boldsymbol{v}_k\cdot\boldsymbol{n}_{Ok}dS = \int_{V_k}\nabla\cdot\left(\rho_k\psi_k\boldsymbol{v}_k\right)dV - \int_{S_i}\rho_k\psi_k\boldsymbol{v}_k\cdot\boldsymbol{n}_{ki}dS, \tag{2.5}$$

and

$$\int_{S_{Ok}}\boldsymbol{f}_k\cdot\boldsymbol{n}_{Ok}dS = \int_{V_k}\nabla\cdot\boldsymbol{f}_k dV - \int_{S_i}\boldsymbol{f}_k\cdot\boldsymbol{n}_{ki}dS. \tag{2.6}$$

By substituting Eqs. 2.4, 2.5 and 2.6 into Eq. 2.2, one can obtain the following equation:

$$\begin{aligned}&\sum_{k=1}^{2}\left\{\int_{V_k}\left[\frac{\partial}{\partial t}\left(\rho_k\psi_k\right)+\nabla\cdot\left(\rho_k\psi_k\boldsymbol{v}_k+\boldsymbol{f}_k\right)-\rho_k\phi_k\right]dV\right\}\\&=\sum_{k=1}^{2}\left\{\int_{S_i}\left[\rho_k\psi_k\left(\boldsymbol{v}_k-\boldsymbol{v}_i\right)\cdot\boldsymbol{n}_{ki}+\boldsymbol{f}_k\cdot\boldsymbol{n}_{ki}\right]dS\right\}.\end{aligned}\tag{2.7}$$

Since dV and dS are arbitrary, Eq. 2.7 leads to the local instantaneous conservation equation expressed as

$$\frac{\partial}{\partial t}\left(\rho_k\psi_k\right)+\nabla\cdot\left(\rho_k\psi_k\boldsymbol{v}_k+\boldsymbol{f}_k\right)-\rho_k\phi_k=0,\tag{2.8}$$

with the corresponding jump condition stated as

$$\sum_{k=1,2}\left(\psi_k\dot{m}_{ki}+\boldsymbol{f}_k\cdot\boldsymbol{n}_{ki}\right)=0,\tag{2.9}$$

where $\dot{m}_{ki}$ is mass flux across interface S_i, and $\dot{m}_{ki}$ is defined as follows:

$$\dot{m}_{ki}=\rho_k\left(\boldsymbol{v}_k-\boldsymbol{v}_i\right)\cdot\boldsymbol{n}_{ki}.\tag{2.10}$$

The definition of the variables is given in the Table 2.1.

Table 2.1: Definitions of ψ_k, $\boldsymbol{f}_k$ and ϕ_k

Equations	ψ_k	$\boldsymbol{f}_k$	ϕ_k
Mass	1	0	0
Momentum	$\boldsymbol{v}_k$	$-\boldsymbol{T}_k$	$\boldsymbol{F}_k$
Energy	E_k	$\boldsymbol{q}_k-\boldsymbol{T}_k\cdot\boldsymbol{v}_k$	$\boldsymbol{F}_k\cdot\boldsymbol{v}_k$

In Table 2.1, $\boldsymbol{F}_k$, $\boldsymbol{T}_k$ and E_k are the body force, stress tensor, and the total energy, respectively. $\boldsymbol{T}_k$ and E_k are defined as follows:

$$\boldsymbol{T}_k=-p_k\boldsymbol{\delta}+\boldsymbol{\tau}_k,\tag{2.11}$$

and

$$E_k = e_k + \frac{1}{2}\boldsymbol{v}_k \cdot \boldsymbol{v}_k \tag{2.12}$$

2.2.2 General Form of the Volume-Time Average Equations

Now consider a general control volume of phase k as shown by Fig. 2.2.

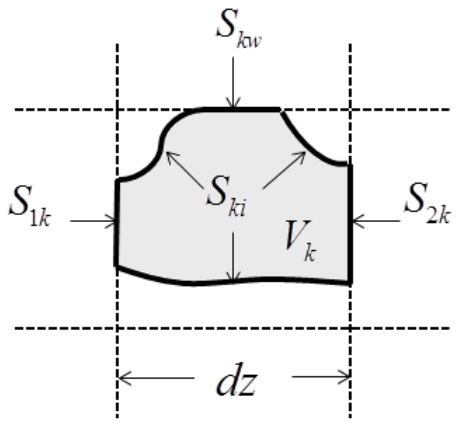

Figure 2.2: Control volume of phase k.

By integrating Eq. 2.8 over the above control volume, one has

$$\int_{V_k} \frac{\partial}{\partial t}(\rho_k \psi_k) dV + \int_{V_k} \nabla \cdot (\rho_k \psi_k \boldsymbol{v}_k + \boldsymbol{f}_k) dV - \int_{V_k} \rho_k \phi_k dV = 0. \tag{2.13}$$

Based on Leibniz's Rule, the first term on the left-hand of the above equation can be expressed as (see Eq. 2.3)

$$\int_{V_k} \frac{\partial}{\partial t}(\rho_k \psi_k) dV = \frac{\partial}{\partial t} \int_{V_k} (\rho_k \psi_k) dV - \int_{S_{ki}} \rho_k \psi_k \boldsymbol{v}_i \cdot \boldsymbol{n}_i dS. \tag{2.14}$$

In addition, the second term on the left-hand of Eq. 2.13 can be written as

$$\int_{V_k} \nabla \cdot (\rho_k \psi_k \boldsymbol{v}_k + \boldsymbol{f}_k)\, dV = \int_{S_{Ok}} (\rho_k \psi_k \boldsymbol{v}_k + \boldsymbol{f}_k) \cdot \boldsymbol{n}_{Ok} dS + \int_{S_{ki}} (\rho_k \psi_k \boldsymbol{v}_k + \boldsymbol{f}_k) \cdot \boldsymbol{n}_{ki} dS. \tag{2.15}$$

The first term on the right-hand side of Eq. 2.15 can be written as

$$\int_{S_{Ok}} (\rho_k \psi_k \boldsymbol{v}_k + \boldsymbol{f}_k) \cdot \boldsymbol{n}_{Ok} dS = \frac{\partial}{\partial z} \int_{V_k} (\rho_k \psi_k \boldsymbol{v}_k + \boldsymbol{f}_k) \cdot \boldsymbol{n}_z dV + \int_{S_{kw}} (\rho_k \psi_k \boldsymbol{v}_k + \boldsymbol{f}_k) \cdot \boldsymbol{n}_{kw} dS. \tag{2.16}$$

Furthermore, assuming that the wall is impermeable leads to the simplification of the second term on the right-hand side of Eq. 2.16 as follows:

$$\int_{S_{kw}} (\rho_k \psi_k \boldsymbol{v}_k + \boldsymbol{f}_k) \cdot \boldsymbol{n}_{kw} dS = \int_{S_{kw}} \boldsymbol{f}_k \cdot \boldsymbol{n}_{kw} dS. \tag{2.17}$$

Substituting Eqs. 2.14 2.16 into Eq. 2.13 gives

$$\begin{aligned} &\tfrac{\partial}{\partial t} \textstyle\int_{V_k} (\rho_k \psi_k) dV + \tfrac{\partial}{\partial z} \textstyle\int_{V_k} (\rho_k \psi_k \boldsymbol{v}_k + \boldsymbol{f}_k) \cdot \boldsymbol{n}_z dV \\ &+ \textstyle\int_{S_{kw}} \boldsymbol{f}_k \cdot \boldsymbol{n}_{kw} dS + \int_{S_{ki}} (\psi_k \dot{m}_{ki} + \boldsymbol{f}_k) \cdot \boldsymbol{n}_{ki} dS - \int_{V_k} \rho_k \phi_k dV = 0. \end{aligned} \tag{2.18}$$

Defining $\langle j \rangle = \frac{1}{V} \int_V j dV$ and $\langle l \rangle = \frac{1}{S} \int_S l dS$, Eq. 2.18 can be written as follows:

$$\begin{aligned} &\tfrac{\partial}{\partial t} V_k \langle \rho_k \psi_k \rangle + \tfrac{\partial}{\partial z} V_k \langle (\rho_k \psi_k \boldsymbol{v}_k + \boldsymbol{f}_k) \cdot \boldsymbol{n}_z \rangle - V_k \langle \rho_k \phi_k \rangle \\ &= - \textstyle\int_{S_{kw}} \boldsymbol{f}_k \cdot \boldsymbol{n}_{kw} dS - \int_{S_{ki}} (\psi_k \dot{m}_{ki} + \boldsymbol{f}_k \cdot \boldsymbol{n}_{ki})\, dS. \end{aligned} \tag{2.19}$$

Based on Table 2.1, the volume-average mass, momentum and energy equation can be expressed as follows:

Volume-average mass equation:

$$\frac{\partial}{\partial t} V_k \langle \rho_k \rangle + \frac{\partial}{\partial z} V_k \langle (\rho_k \boldsymbol{v}_k) \cdot \boldsymbol{n}_z \rangle = - \int_{S_{ki}} \dot{m}_{ki} \cdot \boldsymbol{n}_{ki} dS; \tag{2.20}$$

Volume-average momentum equation:

$$\begin{aligned}&\frac{\partial}{\partial t}V_k\left\langle\rho_k\boldsymbol{v}_k\right\rangle+\frac{\partial}{\partial z}V_k\left\langle\left(\rho_k\boldsymbol{v}_k\boldsymbol{v}_k-\boldsymbol{T}_k\right)\cdot\boldsymbol{n}_z\right\rangle-V_k\left\langle\rho_k\boldsymbol{F}_k\right\rangle\\&=\int_{S_{kw}}\boldsymbol{T}_k\cdot\boldsymbol{n}_{kw}dS-\int_{S_{ki}}\left(\boldsymbol{v}_k\dot{m}_{ki}-\boldsymbol{T}_k\cdot\boldsymbol{n}_{ki}\right)dS;\end{aligned}\tag{2.21}$$

Volume-average energy equation:

$$\begin{aligned}&\frac{\partial}{\partial t}V_k\left\langle\rho_kE_k\right\rangle+\frac{\partial}{\partial z}V_k\left\langle\left(\rho_kE_k\boldsymbol{v}_k+\boldsymbol{q}_k-\boldsymbol{T}_k\cdot\boldsymbol{v}_k\right)\cdot\boldsymbol{n}_z\right\rangle-V_k\left\langle\rho_k\boldsymbol{F}_k\cdot\boldsymbol{v}_k\right\rangle\\&=-\int_{S_w}\left(\boldsymbol{q}_k-\boldsymbol{T}_k\cdot\boldsymbol{v}_k\right)\cdot\boldsymbol{n}_{kw}dS-\int_{S_i}\left(E_k\dot{m}_{ki}+\left(\boldsymbol{q}_k-\boldsymbol{T}_k\cdot\boldsymbol{v}_k\right)\cdot\boldsymbol{n}_{ki}\right)dS.\end{aligned}\tag{2.22}$$

Define volume fraction as

$$\alpha_k=\frac{V_k}{V_T}=\frac{V_k}{A(z,t)\Delta z},\tag{2.23}$$

where V_k is the control volume of phase k and V_T is the total control volume. Rearranging Eq. 2.23, one has

$$V_k=\alpha_kA(z,t)\Delta z.\tag{2.24}$$

Assume Δz is a constant, and $A(z,t)$ is a constant independent of time. Further, substituting Eqs. 2.11 and 2.24 into Eqs. 2.20, 2.21 and 2.22, and projecting the equations on the z-axis for one-dimensional flow, one can obtain the following equations:

1-D Mass

$$\frac{\partial}{\partial t}\alpha_k\left\langle\rho_k\right\rangle+\frac{1}{A}\frac{\partial}{\partial z}\alpha_kA\left\langle\left(\rho_k\boldsymbol{v}_k\right)\cdot\boldsymbol{n}_z\right\rangle=-\left\langle\dot{m}_{ki}\right\rangle,\tag{2.25}$$

where $\langle\dot{m}_{ki}\rangle$ is the averaged interfacial mass flux defined as

$$\left\langle\dot{m}_{ki}\right\rangle=\frac{1}{V_T}\int_{S_{ki}}\dot{m}_{ki}\cdot\boldsymbol{n}_{ki}dS.\tag{2.26}$$

1-D Momentum

$$\begin{aligned}&\frac{\partial}{\partial t}\alpha_k\left\langle\rho_k \boldsymbol{n}_z\cdot\boldsymbol{v}_k\right\rangle+\frac{1}{A}\frac{\partial}{\partial z}\alpha_k A\left\langle\boldsymbol{n}_z\cdot\left(\rho_k\boldsymbol{v}_k\boldsymbol{v}_k+\left(p_k\boldsymbol{\delta}-\boldsymbol{\tau}_k\right)\right)\cdot\boldsymbol{n}_z\right\rangle-\alpha_k\left\langle\rho_k\boldsymbol{n}_z\cdot\boldsymbol{F}_k\right\rangle\\&=\frac{1}{V_T}\int_{S_{kw}}\boldsymbol{n}_z\cdot\left(-p_k\boldsymbol{\delta}+\tau_k\right)\cdot\boldsymbol{n}_{kw}dS-\frac{1}{V_T}\int_{S_{ki}}\boldsymbol{n}_z\cdot\left(\boldsymbol{v}_k\dot{m}_{ki}+\left(p_k\boldsymbol{\delta}-\boldsymbol{\tau}_k\right)\cdot\boldsymbol{n}_{ki}\right)dS\end{aligned},\tag{2.27}$$

where p_{ki} and τ_{ki} are the pressure and shear stress of phase k at the interface, respectively. p_{kw} and τ_{kw} are the pressure and shear stress of phase k at the wall, respectively.

1-D Energy

$$\begin{aligned}&\frac{\partial}{\partial t}\alpha_k\left\langle\rho_k E_k\right\rangle+\frac{1}{A}\frac{\partial}{\partial z}\alpha_k A\left\langle\left[\rho_k H_k\boldsymbol{v}_k+\boldsymbol{q}_k-\boldsymbol{\tau}_k\cdot\boldsymbol{v}_k\right]\cdot\boldsymbol{n}_z\right\rangle-\alpha_k\left\langle\rho_k\boldsymbol{F}_k\cdot\boldsymbol{v}_k\right\rangle\\&\quad=-\frac{1}{V_T}\int_{S_w}\left[\boldsymbol{q}_k+\left(p_k\boldsymbol{\delta}-\boldsymbol{\tau}_k\right)\cdot\boldsymbol{v}_k\right]\cdot\boldsymbol{n}_{kw}dS\\&\quad\quad-\frac{1}{V_T}\int_{S_i}\left[\left(e_k+\frac{1}{2}\boldsymbol{v}_k\cdot\boldsymbol{v}_k\right)\dot{m}_{ki}+\left(\boldsymbol{q}_k+\left(p_k\boldsymbol{\delta}-\boldsymbol{\tau}_k\right)\cdot\boldsymbol{v}_k\right)\cdot\boldsymbol{n}_{ki}\right]dS.\end{aligned}\tag{2.28}$$

Now use v_{kz} and F_{kz} to denote the velocity and body force of phase k in z direction, respectively. That is $v_{kz}=\boldsymbol{n}_z\cdot\boldsymbol{v}_k$ and $F_{kz}=\boldsymbol{n}_z\cdot\boldsymbol{F}_k$.

Assuming z-axis is perpendicular to the normal vector of wall, one has

$$\int_{S_{ki}}\boldsymbol{n}_z\cdot\boldsymbol{n}_{kw}dS=0.\tag{2.29}$$

In addition, based on the Divergence Theorem of Gauss, one can derive the following relationship.

$$\begin{aligned}&\int_{S_{ki}}\boldsymbol{n}_z\cdot\boldsymbol{n}_{ki}dS=\underbrace{\nabla\cdot\boldsymbol{n}_z}_{=0}-\underbrace{\int_{S_{kw}}\boldsymbol{n}_z\cdot\boldsymbol{n}_{kw}dS}_{=0}-\frac{\partial}{\partial z}\int_{V_k}\boldsymbol{n}_z\cdot\boldsymbol{n}_z dV\\&=-\frac{\partial}{\partial z}V_k=-\frac{\partial}{\partial z}\left(\alpha_k A dz\right).\end{aligned}\tag{2.30}$$

Regarding the interfacial pressure terms in Eqs. 2.27 and 2.28, there are several approaches. Here two typical treatments for the interfacial pressure terms in the momentum equation Eq. 2.27 are presented. Similar approaches can be used for the interfacial pressure terms in the energy equations.

Case 1 [56] The interfacial pressure is a constant, that is $p_{ki} = p_i = \text{const.}$. In addition, it is considered to be the summation of the average pressure of phase k, denoted by $\langle p_k \rangle$, and the pressure difference $\Delta p_{ki} = p_{ki} - \langle p_k \rangle$. Thus, the following expressions are obtained.

$$\int_{S_{ki}} n_z \cdot n_{ki} p_k dS = -p_i \frac{\partial \alpha_k A dz}{\partial z} = -\left(\langle p_k \rangle + \Delta p_{ki}\right) \frac{\partial \alpha_k A dz}{\partial z}. \tag{2.31}$$

Case 2 [27] The interfacial pressure varies at the interface, and it is defined as follows:

$$\int_{S_{ki}} n_z \cdot n_{ki} p_k dS = \left(\langle p_k \rangle + \Delta p_{ki}\right) \frac{\partial \alpha_k A dz}{\partial z} + \int_{S_{ki}} n_z \cdot n_{ki} p_k^{'} dS. \tag{2.32}$$

where the last term on the right-hand-side of Eq. 2.32 is called virtual mass.

In order to achieve hyperbolicity of the two-fluid model, either a pressure difference correction or a virtual mass terms can be taken into account. In this thesis, the interfacial pressure correction terms are employed. More detailed discussion of the interfacial pressure correction terms will be presented in Section 2.4.

Define the following relationships shown in Table 2.2.

Table 2.2: Some definitions for the momentum and energy equations

interface-to-fluid momentum transfer	$\dot{m}_{ik} v_{kz} = -\frac{1}{V_T} \int_{S_{ik}} \boldsymbol{n}_z \cdot \boldsymbol{v}_k \dot{m}_{ki} dS$
interfacial shear stress	$\tau_{ki} = \frac{1}{V_T} \int_{S_{ki}} \boldsymbol{n}_z \cdot \boldsymbol{\tau}_k \cdot \boldsymbol{n}_{ki} dS$
wall shear stress	$\tau_{kw} = \frac{1}{V_T} \int_{S_{kw}} \boldsymbol{n}_z \cdot \boldsymbol{\tau}_k \cdot \boldsymbol{n}_{kw} dS$
wall-to-fluid heat transfer	$q_{wk} = -\frac{1}{V_T} \int_{S_w} \left(\boldsymbol{q}_k \cdot \boldsymbol{n}_{wk}\right) dS$
interface-to-fluid heat transfer	$q_{ik} = -\frac{1}{V_T} \int_{S_i} \boldsymbol{q}_k \cdot \boldsymbol{n}_{ki} dS$
work by interfacial shear stress	$\tau_{ki} v_{ki} = \frac{1}{V_T} \int_{S_i} \boldsymbol{\tau}_k \cdot \boldsymbol{v}_k \cdot \boldsymbol{n}_{ki} dS$
interface-to-fluid total enthalpy flux	$H_k \dot{m}_{ik} = -\frac{1}{V_T} \int_{S_i} \left(e_k + \frac{p_k}{\rho_k} + \frac{1}{2} \boldsymbol{v}_k \cdot \boldsymbol{v}_k\right) \dot{m}_{ki} dS$

Therefore, based on Eq. 2.31 and Table 2.2, the following 1D momentum equation can be obtained:

$$\begin{aligned}&\frac{\partial}{\partial t}\alpha_k\left\langle\rho_k v_{kz}\right\rangle+\frac{1}{A}\frac{\partial}{\partial z}\left(\alpha_k A\left\langle\rho_k v_{kz}^2\right\rangle\right)+\frac{1}{A}\frac{\partial}{\partial z}\left(\alpha_k A\left\langle p_k\right\rangle\right)-p_{ki}\frac{1}{A}\frac{\partial}{\partial z}\left(\alpha_k A\right)\\&=\alpha_k\left\langle\rho_k F_{kz}\right\rangle+\tau_{kw}+v_{kz}\dot{m}_{ik}+\tau_{ki}+\frac{1}{A}\frac{\partial}{\partial z}\left(\alpha_k A\left\langle\left(n_z\cdot\tau_k\cdot n_z\right)\right\rangle\right).\end{aligned}\tag{2.33}$$

By rearranging Eq. 2.10, one has

$$\boldsymbol{v}_k\cdot\boldsymbol{n}_{ki}\;=\;\frac{\dot{m}_{ki}}{\rho_k}+\boldsymbol{v}_i\cdot\boldsymbol{n}_{ki}.\tag{2.34}$$

Using Leibniz's Rule, the following relationship can be derived:

$$\frac{\partial}{\partial t}\underbrace{\int_{V_k}1dV}_{V_k}=\underbrace{\int_{V_k}\frac{\partial}{\partial t}1dV}_{0}+\int_{S_i}\boldsymbol{v}_i\cdot\boldsymbol{n}_{ki}dS.\tag{2.35}$$

Therefore,

$$\int_{S_i}\boldsymbol{v}_i\cdot\boldsymbol{n}_{ki}dS=\frac{\partial}{\partial t}V_k.\tag{2.36}$$

Thus, by substituting Eqs. 2.34 and 2.36 into the second term on the right-hand side of Eq. 2.28, one can obtain the following expression:

$$\begin{aligned}&-\tfrac{1}{V_T}\textstyle\int_{S_i}\left(E_k\dot{m}_{ki}+p_k\left(\boldsymbol{\delta}\cdot\boldsymbol{v}_k\cdot\boldsymbol{n}_{ki}\right)\right)dS\\&=-\tfrac{1}{V_T}\textstyle\int_{S_i}\left(E_k\dot{m}_{ki}+p_k\left(\frac{\dot{m}_{ki}}{\rho_k}+\boldsymbol{v}_i\cdot\boldsymbol{n}_{ik}\right)\right)dS\\&=-\tfrac{1}{V_T}\textstyle\int_{S_i}\left(H_k\dot{m}_{ki}\right)dS-\frac{1}{V_T}\int_{S_i}\left(p_k\boldsymbol{v}_i\cdot\boldsymbol{n}_{ki}\right)dS\\&=-\tfrac{1}{V_T}\textstyle\int_{S_i}\left(H_k\dot{m}_{ki}\right)dS-\frac{1}{V_T}\int_{S_i}\left(\left(\left\langle p_k\right\rangle+\Delta p_k\right)\boldsymbol{v}_i\cdot\boldsymbol{n}_{ik}\right)dS\\&=-\tfrac{1}{V_T}\textstyle\int_{S_i}\left(H_k\dot{m}_{ki}\right)dS-\frac{1}{V_T}\left(\left\langle p_k\right\rangle\frac{\partial}{\partial t}V_k\right)-\Delta p_k\frac{1}{V_T}\int_{S_i}\left(\boldsymbol{v}_i\cdot\boldsymbol{n}_{ik}\right)dS.\end{aligned}\tag{2.37}$$

Regarding the last term on the right-hand-side of Eq. 2.37, it is often neglected [19].

Thus, based on Table 2.2 and using Eq. 2.37, Eq. 2.28 becomes

$$
\begin{aligned}
&\tfrac{\partial}{\partial t}\left(\alpha_k \left\langle \rho_k E_k \right\rangle\right) + \underbrace{\frac{1}{A}\frac{\partial}{\partial z}\left(\alpha A \left\langle \rho_k v_{kz} H_k \right\rangle\right)}_{\text{Energy flux}} \\
&\quad + \underbrace{\frac{1}{A}\frac{\partial}{\partial z}\left(\alpha_k A \left\langle q_{kz} \right\rangle\right)}_{\text{Heat conduction}} - \underbrace{\frac{1}{A}\frac{\partial}{\partial z}\left(\alpha_k A \left\langle \boldsymbol{\tau}_k \cdot \boldsymbol{v}_k \cdot \boldsymbol{n}_z \right\rangle\right)}_{\text{Friction dissipation}} - \underbrace{\alpha_k \left\langle \rho_k \boldsymbol{F}_k \cdot \boldsymbol{v}_k \right\rangle}_{\text{Body force dissipation}} \\
&\quad = q_{ik} + q_{wk} + H_k \dot{m}_{ik} - \left\langle p_k \right\rangle \tfrac{\partial}{\partial t}\alpha_k + \tau_{ki} v_{ki}.
\end{aligned}
\tag{2.38}
$$

The following assumptions are made:

(1) The wall is impermeable. Therefore, the first term on the right-hand side of Eq. 2.28 turns to zero.

(2) Friction and body force dissipation terms are negligible compared to the energy transport terms.

(3) Fluid velocity components on x and y direction are negligible compared to the z direction velocity component. In other words, $\boldsymbol{v}_k \cdot \boldsymbol{v}_k \approx v_{kz}^2$.

Under the above-mentioned assumptions, Eq. 2.38 is further simplified into the following equation.

$$
\begin{aligned}
&\tfrac{\partial}{\partial t}\left[\alpha_k \left\langle \rho_k E_k \right\rangle\right] + \tfrac{1}{A}\tfrac{\partial}{\partial z}\left[\alpha_k A \left\langle \rho_k v_{kz} H_k \right\rangle\right] \\
&= q_{ki} + q_{kw} + H_k \dot{m}_{ik} - \left\langle p_k \right\rangle \tfrac{\partial}{\partial t}\alpha_k + \tau_{ki} v_{ki}.
\end{aligned}
\tag{2.39}
$$

In summary, the 1D average volume two phase flow equation system can be written as follows:

Mass equation:

$$
\frac{\partial}{\partial t}\alpha_k \left\langle \rho_k \right\rangle + \frac{1}{A}\frac{\partial}{\partial z}\alpha_k A \left\langle \rho_k u_k \right\rangle = -\left\langle \dot{m}_{ki} \right\rangle . \tag{2.40}
$$

Momentum equation

$$\begin{aligned}&\frac{\partial}{\partial t}\alpha_k\left\langle\rho_k u_k\right\rangle+\frac{1}{A}\frac{\partial}{\partial z}\left(\alpha_k A\left\langle\rho_k u_k^2\right\rangle\right)+\frac{1}{A}\frac{\partial}{\partial z}\left(\alpha_k A\left\langle p_k\right\rangle\right)-\left\langle p_{ki}\right\rangle\frac{1}{A}\frac{\partial}{\partial z}\left(\alpha_k A\right)\\&=\alpha_k\left\langle\rho_k F_{kz}\right\rangle+\tau_{kw}+u_k\dot{m}_{ki}+\tau_{ki}.\end{aligned}\tag{2.41}$$

Energy equation

$$\begin{aligned}&\frac{\partial}{\partial t}\left[\alpha_k\left\langle\rho_k E_k\right\rangle\right]+\frac{1}{A}\frac{\partial}{\partial z}\left[\alpha_k A\left\langle\rho_k u_k H_k\right\rangle\right]\\&=q_{ik}+q_{wk}+H_k\dot{m}_{ik}-\left\langle p_k\right\rangle\frac{\partial}{\partial t}\alpha_k+\tau_{ki}u_k.\end{aligned}\tag{2.42}$$

2.2.3 One-Dimensional Governing Equations

The two-fluid model can be written in the following form [19],

$$\frac{\partial \boldsymbol{U}}{\partial t}+\frac{\partial \boldsymbol{F}}{\partial x}=\boldsymbol{Q}^{nv}+\boldsymbol{Q}^{v}+\boldsymbol{Q},\tag{2.43}$$

where $\mathbf{U}$ is the conservative vector, $\boldsymbol{F}$ is the flux vector, $\boldsymbol{Q}^{nv}$ represents non-viscous differential source terms, $\boldsymbol{Q}^{v}$ contains the viscous differential source terms, and $\boldsymbol{Q}$ is the source terms containing all the non-differential terms such as the gravity force. If viscous terms are not considered, the following reduced form can be obtained:

$$\frac{\partial \boldsymbol{U}}{\partial t}+\frac{\partial \boldsymbol{F}}{\partial x}=\boldsymbol{Q}^{nv}+\boldsymbol{Q}.\tag{2.44}$$

For the six-equation two-phase flow model, the vectors in Eq. 2.44 can be written as

$$
\begin{aligned}
\boldsymbol{U} &= \begin{pmatrix} \alpha_g\rho_g \\ \alpha_l\rho_l \\ \alpha_g\rho_g u_g \\ \alpha_l\rho_l u_l \\ \alpha_g\rho_g E_g \\ \alpha_l\rho_l E_l \end{pmatrix} \quad \boldsymbol{F} = \begin{pmatrix} \alpha_g\rho_g u_g \\ \alpha_l\rho_l u_l \\ \alpha_g\rho_g u_g^2 + \alpha_g p \\ \alpha_l\rho_l {u_l}^2 + \alpha_l p \\ \alpha_g\rho_g u_g H_g \\ \alpha_l\rho_l u_l H_l \end{pmatrix} \\
\boldsymbol{Q}^{nv} &= \begin{pmatrix} 0 \\ 0 \\ p^i \frac{\partial \alpha_g}{\partial x} \\ p^i \frac{\partial \alpha_l}{\partial x} \\ -p\frac{\partial \alpha_g}{\partial t} \\ -p\frac{\partial \alpha_l}{\partial t} \end{pmatrix} \quad \boldsymbol{Q} = \begin{pmatrix} 0 \\ 0 \\ \alpha_g\rho_g g_x + \tau_{gi} \\ \alpha_l\rho_l g_x + \tau_{li} \\ \alpha_g\rho_g u_g g_z \\ \alpha_l\rho_l u_l g_z \end{pmatrix}.
\end{aligned} \tag{2.45}
$$

For isentropic four-equation model, the definitions of $\boldsymbol{U}$, $\boldsymbol{F}$, $\boldsymbol{Q}^{nv}$ and $\boldsymbol{Q}$ can be given by

$$
\begin{aligned}
\boldsymbol{U} &= \begin{pmatrix} \alpha_g\rho_g \\ \alpha_l\rho_l \\ \alpha_g\rho_g u_g \\ \alpha_l\rho_l u_l \end{pmatrix} \quad \boldsymbol{F} = \begin{pmatrix} \alpha_g\rho_g u_g \\ \alpha_l\rho_l u_l \\ \alpha_g\rho_g u_g^2 + \alpha_g p \\ \alpha_l\rho_l {u_l}^2 + \alpha_l p \end{pmatrix} \\
\boldsymbol{Q}^{nv} &= \begin{pmatrix} 0 \\ 0 \\ p_g^i \frac{\partial \alpha_g}{\partial x} \\ p_l^i \frac{\partial \alpha_l}{\partial x} \end{pmatrix} \quad \boldsymbol{Q} = \begin{pmatrix} 0 \\ 0 \\ \alpha_g\rho_g g + \tau_{gi} \\ \alpha_l\rho_l g + \tau_{li} \end{pmatrix},
\end{aligned} \tag{2.46}
$$

where α is volume fraction, ρ is density, u is velocity, p is bulk pressure, and τ_{ki} represents interfacial terms due to drag force. The subscripts g and l stand for gas and liquid phase, respectively.

Note that the pressure is assumed to be equal in the phases. That is $p_g = p_l = p$. The modeling of pressure non-equilibrium or pressure difference between phases is very complex [15]. Generally, three main factors contribute to the pressure difference. These

factors include the surface energy of a curved interface, the mass transfer, and the dynamics effects [57]. In the first case, the pressure difference is proportional to the surface tension of the interface, whereas inversely proportional to the curvature radius. This pressure difference is usually quite small, thereby being neglected in most applications. The second factor is noticeable when the mass flux due to phase change is large at the interface, eg. large evaporation or condensation rates. The third factor plays an important role only when one phase has a larger dynamic pressure relative to the other phase caused by very rapid pressurization effect or energy deposition, eg. a mixture flow of water and air bubbles through a converging-diverging nozzle. Usually, only when the flow velocity approximates or exceeds the sound speed of the multi-phase system will this pressure difference becomes important. Consequently, most applications neglect the pressure difference, and so does this thesis.

2.2.4 System Equations in CATHENA4 Code

CATHENA4 is a thermal-hydraulic code developed by the Canadian Nuclear Laboratories (CNL). It is designed for thermal hydraulic network analysis. This code models 1-D, non-equlibrium two phase flows. The systems of equations adopted by CATHENA4 is given as follows:

Mass equation

$$\frac{\partial}{\partial t}\left(\alpha_k \rho_k\right) + \frac{1}{A}\frac{\partial}{\partial x}\left(A\alpha_k \rho_k u_k\right) = \dot{m}_{ik}. \tag{2.47}$$

Momentum equation

$$\begin{aligned} &\alpha_k \rho_k \tfrac{\partial}{\partial t} u_k + \alpha_k \rho_k u_k \tfrac{\partial}{\partial z} u_k = \\ &-\alpha_k \tfrac{\partial}{\partial z} p - \Delta p_i \tfrac{\partial}{\partial z}\left(\alpha_k\right) + M + \tfrac{\alpha_k \rho_k g}{A} + \tau_{wi} + \tau_{ki}. \end{aligned} \tag{2.48}$$

Energy equation

$$\frac{\partial}{\partial t}\left(\alpha_k \rho_k h_k\right) + \frac{1}{A}\frac{\partial}{\partial z}\left(A\alpha_k \rho_k h_k u_k\right) = \alpha_k \frac{\partial p}{\partial t} + q_{wk} + q_{ik} + \dot{m}_{ik} h_k + \tau_{ki} u_k. \tag{2.49}$$

M is virtual mass term.

2.3 Closure Relationships

2.3.1 Closure Relationships for the Interfacial Pressure

Several important interfacial pressure correction approaches are presented as follows:

(1) Common pressure relations used in RELAP5 [58] [59] are given as follows:

$$\begin{aligned} p - p_g^i &= 0 \\ p - p_l^i &= 0. \end{aligned} \tag{2.50}$$

(2) Pressure corrections are only accounted for liquid phase [60].

$$\begin{aligned} p - p_g^i &= 0 \\ p - p_l^i &= C_p\left(\alpha_g\right)\rho_l(u_g - u_l)^2. \end{aligned} \tag{2.51}$$

(3) Pressure corrections are considered for both gas and liquid phases [32].

$$\begin{aligned} p - p_g^i &= p - p_l^i \\ p - p_l^i &= {C_p}^*\alpha_l\rho_g(u_g - u_l)^2. \end{aligned} \tag{2.52}$$

(4) Bestion [61] proposed another typical pressure corrections accounting for both gas and liquid phase in CATARE .

$$\begin{aligned} p - p_g^i &= p - p_l^i \\ p - p_l^i &= \sigma\frac{\alpha_g\alpha_l\rho_g\rho_l}{\alpha_g\rho_l\alpha_l\rho_g}(u_g - u_l)^2, \end{aligned} \tag{2.53}$$

where σ is a constant. In this thesis, the pressure correction proposed by Bestion shown in Eq. 2.53 will be used.

2.3.2 Closure Relationships for Interfacial Friction

The interfacial friction τ_{ik} is defined as follows [19]:

$$\begin{aligned} \tau_{ig} &= -C_f \alpha_g (1-\alpha_g)\rho_g (u_g - u_l) \\ \tau_{il} &= -\tau_{ig}, \end{aligned} \tag{2.54}$$

where C_f is a positive constant with a unit of (1/s).

2.3.3 Equations of State

The isentropic perfect gas equations of state (EOS) and the so-called Tait's EOS are used as closure equations for the gas and liquid phases, respectively [19]. Tait's equation of state (EOS) models a liquid to be compressible and barotropic, thereby involving only the pressure and density variables. Thus, when a liquid is modeled by this EOS, the energy equation is decoupled from the mass and momentum equations. Tait's EOS can be regarded as a particular case of the stiffened gas EOS under the isentropic assumption [62].

The isentropic perfect gas EOS can be written as:

$$p = p(\rho_g) = p_g^0 \left(\frac{\rho_g}{\rho_g^o} \right)^{\gamma}, \tag{2.55}$$

and

$$a_g = \sqrt{\frac{\gamma p}{\rho_g}}, \tag{2.56}$$

where $p_g^0 = 10^5\ Pa$, $\gamma = 1.4$ and $\rho_g^0 = 1\ kg/m^3$; a_g denotes the gas sound speed.

Tait's EOS is given as follows:

$$p = p(\rho_l) = p_l^0 \left[\left(\frac{\rho_l}{\rho_l^o} \right)^n - 1 \right], \tag{2.57}$$

and

$$a_l = \sqrt{\frac{n}{\rho_l}(p + p_l^0)}, \tag{2.58}$$

where $p_l^0 = 3.3 \times 10^8\ Pa$, $n = 7.15$, $\rho_l^0 = 1000\ kg/m^3$; a_l denotes the liquid sound speed. In addition, the void fraction satisfies the following equation:

$$\alpha_g + \alpha_l = 1. \tag{2.59}$$

2.4 Mathematical Analysis of the Two-Fluid Model

In this section, the mathematical analysis of the two-fluid model will be performed, particularly the eigenstructure and hyperbolic condition, of the isentropic four-equation model. It is necessary to fully understand the mathematical properties of a system before constructing numerical schemes. It is well-known that the original two-fluid model is non-hyperbolic. Non-hyperbolicity will lead to ill-posed issues of the system. In this case, the solutions of the system will not depend continuously upon the initial data. As mentioned in subsection 2.2.2, virtual mass and interfacial pressure correction terms can be used to render the system well-posed. In this thesis, the interfacial pressure corrections will be employed. In particular, the hyperbolicity of the two-fluid system with the interfacial pressure correction term proposed by Bestion will be examined.

There are several methods to study the eigenstructure of a system, including a numerical method, analytical method and perturbation method. Since the numercial method may incur high computational costs, and analytical method needs complex computations, the perturbation method will be used instead. The perturbation method introduces a small perturbation parameter, ϵ. Regarding the perturbation method, one can distinguish:

- Density perturbation method [53]. In this method, a perturbation parameter is introduced such that the Jacobian matrix $\boldsymbol{A}$ in Eq. 2.62 can be split into the following form:

$$\boldsymbol{A}(U) = \frac{1}{\epsilon}\boldsymbol{A}_{-1}(U) + \boldsymbol{A}_0(U) + \epsilon\boldsymbol{A}_1(U). \tag{2.60}$$

Then the eigenstructure of $\boldsymbol{A}$ is obtained through the study of the eigenstructure of $\frac{1}{\epsilon}\boldsymbol{A}_{-1}(U) + \boldsymbol{A}_0(U)$.

- Taylor series expansion of the eigenvalues [63]. In this method, the eigenvalues are Taylor expanded in σ, and then substituted into the characteristic polynomial. After grouping the terms according to power series of σ, and equating the coefficients of the series to be zero, the eigenvalues can be solved.

The Taylor series expansion method can be applied to any system, whereas the density perturbation method has a drawback that for complex EOS or compressible liquid EOS, it is difficult or impossible to transform the Jacobian matrix $\boldsymbol{A}$ into the form shown in Eq. 2.60 [53]. Therefore, in this thesis, Taylor expansion method will be extended to the isentropic four-equation model.

2.4.1 Characteristic Polynomial

Define the Jacobian matrix A such that

$$\frac{\partial \boldsymbol{G}}{\partial x} = \frac{\partial \boldsymbol{F}}{\partial x} - \boldsymbol{Q}^{nv} = \boldsymbol{A}\frac{\partial \boldsymbol{U}}{\partial x}. \tag{2.61}$$

Based on the definition of Eq. 2.61, Eq. 2.44 can be written in the following quasilinear form:

$$\frac{\partial \boldsymbol{U}}{\partial t} + \boldsymbol{A}(\boldsymbol{U})\frac{\partial \boldsymbol{U}}{\partial x} = \boldsymbol{Q}(\boldsymbol{U}), \tag{2.62}$$

where the Jacobian matrix $\boldsymbol{A}$ is given by

$$\boldsymbol{A}(\boldsymbol{U}) = \begin{bmatrix} 0 & 0 & 1 & 0 \\ 0 & 0 & 0 & 1 \\ \omega\left(\alpha_g\rho_l + \Delta p\alpha_l\frac{\partial \rho_l}{\partial p}\right) - u_g^2 & \omega\left(\alpha_g\rho_g - \Delta p\alpha_g\frac{\partial \rho_g}{\partial p}\right) & 2u_g & 0 \\ \omega\left(\alpha_l\rho_l - \Delta p\alpha_l\frac{\partial \rho_l}{\partial p}\right) & \omega\left(\alpha_g\rho_l + \Delta p\alpha_g\frac{\partial \rho_g}{\partial p}\right) - u_l^2 & 0 & 2u_l \end{bmatrix}. \tag{2.63}$$

ω is defined as

$$\omega = \frac{1}{(\partial\rho_l/\partial p)\,\alpha_l\rho_g + (\partial\rho_g/\partial p)\,\alpha_g\rho_l} = \frac{1}{\alpha_l\rho_g/c_l^2 + \alpha_g\rho_l/c_g^2}, \tag{2.64}$$

where $c_k^2 = \partial p/\partial\rho_k$ is the square of the sound speed of phase k. For the derivation of matrix $\boldsymbol{A}$, please refer to Appendix A. Note that $\boldsymbol{A}$ is not the differential of a real-valued flux function $\boldsymbol{G}$. This feature, which is due to the non-conservation of two-fluid flow model system, is a key difference from that of Euler equation. It leads to the difficulty of using FDS to solve two-fluid model. A detailed explanation is given in Subsection 3.3.2.

Therefore, the eigenvalues λ of Eq. 2.62 can be obtained by solving $\det(\mathbf{A} - \lambda\boldsymbol{I}) = 0$, which leads to the following polynomial equation.

$$\begin{aligned} &P_{\mathbf{U}}(\lambda) = \left[\omega\left(\alpha_g\rho_l + \tfrac{\Delta p\alpha_l}{c_l^2}\right) - (\lambda - u_g)^2\right]\left[\omega\left(\alpha_l\rho_g + \tfrac{\Delta p\alpha_g}{c_g^2}\right) - (\lambda - u_l)^2\right] \\ &-\omega^2\left(\alpha_g\rho_g - \tfrac{\Delta p\alpha_g}{c_g^2}\right)\left(\alpha_l\rho_l - \tfrac{\Delta p\alpha_l}{c_l^2}\right) = 0. \end{aligned} \tag{2.65}$$

2.4.2 Extension of the Taylor Expansion to the Isentropic Four-Equation Model

Lemma (Goursat):

By introducing a small perturbation parameter ϵ, the polynomial in Eq. 2.65 can be given by [63]

$$P_U(\lambda, \epsilon) = P_0(\lambda) + P_1(\lambda)\epsilon + P_2(\lambda)\frac{\epsilon^2}{2} + P(\lambda, \epsilon)\epsilon^2 \tag{2.66}$$

with

$$|P(\lambda, \epsilon)| \leq (1 + |\lambda|)^s\varphi(\epsilon) \quad \text{if } s \in N \text{ and } \exists \lim_{\epsilon\to 0}\varphi(\epsilon) = 0, \tag{2.67}$$

where P_0, P_1 and P_2 are polynomials with real coefficients. Then the roots of $P_U(\lambda, \epsilon)$ near a root λ_0 of the polynomial $P_0(\lambda)$ are solved. Two cases are considered according to whether λ_0 is a simple or double root [6].

Case 1: If λ_0 is a simple root of $P_0(\lambda)$, the first-order approximation of $\lambda(\epsilon)$, differentiable in ϵ, can be given by

$$\lambda(\epsilon) = \lambda_0 + \lambda^{'}\epsilon + O(\epsilon^2) \tag{2.68}$$

with

$$\lambda^{'} = -\frac{P_1(\lambda_0)}{P_0^{'}(\lambda_0)}. \tag{2.69}$$

Case 2: If λ_0 is a double root of $P_0(\lambda)$, and $P_1(\lambda_0) = 0$, then the first-order approximation of $\lambda(\epsilon)$ has two simple roots, which can be given by

$$\lambda^{\pm}(\epsilon) = \lambda_0 + \lambda^{'\pm}\epsilon + O\left(\epsilon^2\right) \tag{2.70}$$

with $\lambda^{'\pm}$ being the roots of the following equation:

$$P_0^{''}\left(\lambda_0\right)\left(\lambda^{'}\right)^2 + 2P_1^{'}\left(\lambda_0\right)\lambda^{'} + P_2\left(\lambda_0\right) = 0. \tag{2.71}$$

Accordingly, the roots are real at first order and the system is hyperbolic under the condition

$$\left[P_1^{'}\left(\lambda_0\right)\right]^2 - P_2(\lambda_0)P_0^{''}\left(\lambda_0\right) > 0. \tag{2.72}$$

Interfacial pressure correction

Here, the following variables are defined:

$$k = \frac{\alpha_l\rho_g}{\alpha_g\rho_l}, \quad \hat{\alpha} = \frac{\alpha_l}{\alpha_g}, \quad \mu = \omega\alpha_g\rho_l, \quad \hat{c} = \sqrt{(\alpha_l\rho_g + \alpha_g\rho_l)\omega}, \tag{2.73}$$

where $\tilde{c}$ is approximate mixture sound speed.

In addition, the perturbation parameter ϵ is defined as

$$\epsilon = \frac{u_g - u_l}{\hat{c}(1+k)} \tag{2.74}$$

and

$$\beta\epsilon^2 = \frac{\Delta p}{\rho_l c_g^2}. \tag{2.75}$$

Furthermore, a new variable is introduced as follows:

$$\tilde{\lambda} = \frac{(\lambda - u_g)\sqrt{1+k}}{\hat{c}}. \tag{2.76}$$

By substituting Eqs. 2.73-2.76 into Eq. 2.65, one can obtain the following polynomial equation:

$$\begin{aligned} &\left[(1+\beta\tilde{\alpha}\mu\epsilon^2) - \tilde{\lambda}^2\right] \cdot \left[(k+\beta\epsilon^2) - \left(\tilde{\lambda} + (1+k)^{3/2}\right)\epsilon^2\right] \\ &= (k - \beta\hat{\alpha}\epsilon^2)\left(1 - \beta\mu\epsilon^2\right). \end{aligned} \tag{2.77}$$

Equation 2.77 can be rearranged into the form as Eq. 2.66 with

$$\begin{aligned} P_0(\tilde{\lambda}) &= \tilde{\lambda}^4 - (1+k)\tilde{\lambda}^2 \\ P_1(\tilde{\lambda}) &= -2\tilde{\lambda}\left(1 - \tilde{\lambda}^2\right)(1+k)^{3/2} \\ P_2(\tilde{\lambda}) &= 2\left\{\left(1 - \hat{\lambda}^2\right)\left[\beta - (1+k)^3\right] + \left(k - \tilde{\lambda}^2\right)\beta\hat{\alpha}\mu + \beta\hat{\alpha} + k\beta\mu\right\}. \end{aligned} \tag{2.78}$$

Therefore, P_0 has four real roots

$$\begin{aligned} \tilde{\lambda}^0_{1,2} &= \pm\sqrt{1+k} \\ \tilde{\lambda}^0_{3,4} &= 0. \end{aligned} \tag{2.79}$$

(1) $\tilde{\lambda}^0_1$ and $\tilde{\lambda}^0_2$ are single roots of P_0. Thus, Case 1 of the lemma of Goursat will be employed to obtain the first-order approximation of $\tilde{\lambda}$.

$$\begin{aligned} P_0'(\tilde{\lambda}^0_{1,2}) &= 4\left(\tilde{\lambda}^0_{1,2}\right)^3 - (1+k)\left(\tilde{\lambda}^0_{1,2}\right)^2 \\ &= \pm 2(1+k)^{3/2} \end{aligned} \tag{2.80}$$

$$\tilde{\lambda}'_{1,2} = -\frac{P_1(\tilde{\lambda}^0_{1,2})}{P'_0(\tilde{\lambda}^0_{1,2})} = -\frac{\pm 2k(1+k)^2}{\pm 2(1+k)^{3/2}} = -\frac{k}{\sqrt{(1+k)}}. \tag{2.81}$$

Therefore, one can obtain the following equation:

$$\tilde{\lambda}_{1,2} = \tilde{\lambda}^0_{1,2} + \tilde{\lambda}'_{1,2}\epsilon = \pm\sqrt{(1+k)} - \frac{k}{\sqrt{(1+k)}}\epsilon. \tag{2.82}$$

By substituting Eqs. 2.74 and 2.76 into Eq. 2.82, the first-order approximation of $\tilde{\lambda}_{1,2}$ can be obtained.

$$\lambda_{1,2} = u^p \pm \hat{c}, \tag{2.83}$$

where

$$u^p = \frac{\alpha_g \rho_l u_g + \alpha_l \rho_g u_l}{\alpha_g \rho_l + \alpha_l \rho_g}. \tag{2.84}$$

(2) $\tilde{\lambda}^0_3$ and $\tilde{\lambda}^0_4$ are double roots of P_0. Thus, Case 2 of the lemma of Goursat will be employed to obtain the first-order approximation of $\tilde{\lambda}$.

$$\begin{aligned} P''_0(\tilde{\lambda}^0_{3,4}) &= 12\left(\tilde{\lambda}^0_{3,4}\right)^2 - 2(1+k) = -2(1+k) \\ P'_1(\tilde{\lambda}^0_{3,4}) &= 2\left[3\left(\tilde{\lambda}^0_{3,4}\right)^2 - 1\right](1+k)^{3/2} = -2(1+k)^{3/2} \\ P_2(\tilde{\lambda}^0_{3,4}) &= 2\left\{\beta(1+\hat{\alpha})(1+k\mu) - (1+k)^3\right\}. \end{aligned} \tag{2.85}$$

Hence, based on Eq. 2.71, $\tilde{\lambda}'_{3,4}$ can be obtained as

$$\begin{aligned} \tilde{\lambda}'_{3,4} &= \frac{-P'_1(\tilde{\lambda}^0_{3,4}) \pm \sqrt{\left(P'_1(\tilde{\lambda}^0_{3,4})\right)^2 - P''_0(\tilde{\lambda}^0_{3,4}) P_2(\tilde{\lambda}^0_{3,4})}}{P''_0(\tilde{\lambda}^0_{3,4})} \\ &= -\sqrt{1+k} \pm \frac{\sqrt{\sqrt{4}(1+k)^3 + 4(1+k)[\beta(1+\hat{\alpha})(1+k\mu) - (1+k)^3]}}{-2(1+k)}. \end{aligned} \tag{2.86}$$

Therefore, the following equation can be obtained:

$$\tilde{\lambda}_{3,4} = \tilde{\lambda}^{0}_{3,4} + \tilde{\lambda}^{'}_{3,4}\epsilon = \tilde{\lambda}^{'}_{3,4}\epsilon \tag{2.87}$$

with $\tilde{\lambda}^{'}_{3,4}$ being Eq. 2.86. By substituting Eqs. 2.73, 2.74 and 2.86 into Eq. 2.87, one can obtain the first-order approximation of $\lambda_{3,4}$:

$$\lambda_{3,4} = u^{v} \mp \zeta, \tag{2.88}$$

where

$$u^{v} = \frac{\alpha_l \rho_g u_g + \alpha_g \rho_l u_l}{\alpha_l \rho_g + \alpha_g \rho_l} \tag{2.89}$$

and

$$\zeta = \sqrt{\frac{\Delta p \left(\alpha_l \rho_g + \alpha_g \rho_l\right) - \alpha_g \rho_g \alpha_l \rho_l \left(u_g - u_l\right)^2}{\alpha_g^2 \rho_l^2 \left(u_g - u_l\right)^2}} \tag{2.90}$$

Hyperbolic condition

From Eq. 2.89, it can seen that when the gas velocity and the liquid velocity are not equal, $u_g \neq u_f$, the pressure correction term Δp has to satisfy the following condition to render the system hyperbolic with real eigenvalues.

$$\Delta p \geq \frac{\alpha_g \rho_g \alpha_l \rho_l \left(u_g - u_l\right)^2}{\alpha_l \rho_g + \alpha_g \rho_l}. \tag{2.91}$$

Therefore, when pressure corrections Eq. 2.53 be adopted, the constant σ has to be larger than one to guarantee hyperbolicity of the system. That is

$$\sigma > 1. \tag{2.92}$$

Note that when $\sigma = 1$ or the gas and liquid velocities are equal, $\zeta = 0$ (see Eq. 2.90), which in turn indicates that $\lambda_3 = \lambda_4$ (see Eq. 2.88). In other words, the eigenvalues corresponding to void fraction waves will be degenerate. Hence, in this circumstance, the eigenstructure of the system is similar to that of the Euler equations [64].

Chapter 3

Numerical Methods

3.1 Introduction

This chapter describes the numerical methods to solve the two-fluid model introduced in Chapter 2. The implementation code is developed from scratch by the author and its flow chart can be referred to Fig. 4.2. To begin, in Section 3.2, the discretized governing equations in both explicit and implicit forms are demonstrated. Then, in Section 3.3, the numerical fluxes are illustrated. This section consists of four parts. First, the collocated-grid-based AUSM-family schemes with explicit time integration are reviewed. Then, the Roe scheme for the four-equation two-fluid model is derived. After that, the proposed staggered-grid-based AUSM-family (SG-AUSM-family) schemes are exhibited, followed by a subsection describing a new staggered-grid-based AUSMFVS (SG-AUSMFVS) scheme. Afterwards, in Section 3.4, the discretization of source terms is shown. Following this, in Section 3.5, the high-spatial-order extension of the numerical fluxes are illustrated, including the MUSCL approach and the TVD limiters. Finally, in Section 3.6, the decoding and updating of variables for explicit schemes are addressed. Since the methods for solving implicit schemes are much more complicated than for explicit schemes, they will be illustrated independently in Chapter 4.

3.2 Discretizations of the Governing Equations

Based on the theta method [65], a numerical difference scheme for Eq. 2.44 can be given as follows [66]:

$$\begin{aligned} &\boldsymbol{U}_i^{n+1} + \theta \left\{ \lambda \left(\boldsymbol{F}_{i+1/2}^{n+1} - \boldsymbol{F}_{i-1/2}^{n+1} \right) - \Delta t \left((\boldsymbol{Q}^{nv})_i^{n+1} + \boldsymbol{Q}_i^{n+1} \right) \right\} \\ &= \boldsymbol{U}_i^n - (1-\theta) \left\{ \lambda \left(\boldsymbol{F}_{i+1/2}^{n} - \boldsymbol{F}_{i-1/2}^{n} \right) - \Delta t \left((\boldsymbol{Q}^{nv})_i^{n} + \boldsymbol{Q}_i^{n} \right) \right\}, \end{aligned} \tag{3.1}$$

where $\lambda = \Delta t / \Delta x$; $\boldsymbol{F}_{i\pm1/2}$ are numerical fluxes at the interface; n and $n+1$ represent previous and current time levels, respectively; θ denotes the degree of implicitness, $0 \leq \theta \leq 1$. In particular, when $\theta = 0$, an explicit scheme is obtained, while $\theta = 1$, a fully implicit scheme is gained. Therefore, the fully implicit and explicit discretized form of Eq. 2.44 given as follows:

Implicit:

$$\boldsymbol{U}_i^{n+1} - \boldsymbol{U}_i^n + \frac{\Delta t}{\Delta x} [\boldsymbol{F}_{i+1/2}^{n+1} - \boldsymbol{F}_{i-1/2}^{n+1}] - \Delta t [(\boldsymbol{Q}^{nv})_i^{n+1} + \boldsymbol{Q}_i^{n+1}] = 0, \tag{3.2}$$

Explicit:

$$\boldsymbol{U}_i^{n+1} = \boldsymbol{U}_i^n - \frac{\Delta t}{\Delta x} [\boldsymbol{F}_{i+1/2}^{n} - \boldsymbol{F}_{i-1/2}^{n}] + \Delta t [(\boldsymbol{Q}^{nv})_i^{n} + \boldsymbol{Q}_i^{n}]. \tag{3.3}$$

3.3 Numerical Fluxes

The numerical inviscid flux is crucial in influencing numerical solutions, especially in terms of stability and accuracy [67]. First, this section introduces the collocated-grid-based AUSM-family schemes in both Mach-number-splitting and velocity-splitting forms. Consistent with Wada and Liou [1], the Mach-number-splitting and the velocity-splitting are referred to as "M-splitting" and "U-splitting", respectively. Then, the Roe-type scheme for the two-fluid model is also derived. Next, the proposed SG-AUSM-family schemes are demonstrated, followed by the description of a new SG-AUSMFVS scheme.

3.3.1 Review of the AUSM-Family Schemes

M-splitting AUSM-family schemes

The AUSM-family schemes treat the convective and pressure terms separately [41]. In AUSM-family schemes, the interfacial fluxes are written as follows:

For the generic flow model,

$$\boldsymbol{F}_{k,1/2}(\boldsymbol{U}_L, \boldsymbol{U}_R) = (\dot{m}_k)_{\frac{1}{2}}(\boldsymbol{\psi}_k)_{\frac{1}{2}} + (\boldsymbol{F}_p)_{1/2}, \tag{3.4}$$

where the subscript $\frac{1}{2}$ represents the gas-liquid interface, $(\dot{m}_k)_{\frac{1}{2}}$ is the mass flow rate, $(\dot{m}_k)_{\frac{1}{2}} = (\rho_k u_k)_{1/2}$; the subscript k=g or l, denoting a gas or liquid phase, respectively; $(\boldsymbol{\psi}_k)_{\frac{1}{2}}$ is the convected variables written as follows:

$$(\boldsymbol{\psi}_k)_{\frac{1}{2}} = \begin{cases} \begin{bmatrix} (\alpha_k)_L \\ (\alpha_k u_k)_L \end{bmatrix} & \text{if } (\dot{m}_k)_{\frac{1}{2}} > 0 \\ \\ \begin{bmatrix} (\alpha_k)_R \\ (\alpha_k u_k)_R \end{bmatrix} & \text{otherwise.} \end{cases} \tag{3.5}$$

and the pressure flux vector is given by

$$(\boldsymbol{F}_p)_{1/2} = \begin{bmatrix} 0 & 0 & (\alpha p)_{g,1/2} & (\alpha p)_{l,1/2} \end{bmatrix}^T \tag{3.6}$$

where $(\alpha p)_{k,\frac{1}{2}}$ is the interfacical pressure flux.

(i) AUSM$^+$ [47][54]

The AUSM$^+$ scheme has an excellent capability for resolving contact discontinuities. However, it has difficulty in dealing with strong colliding shocks. For example, when used to calculate the head-on moving shock, the AUSM$^+$ scheme generates large overshoots.

- Convective terms:

  In the AUSM$^+$ scheme, the mass flow rate $(\dot{m}_k)_{\frac{1}{2}}$ is written as

$$(\dot{m}_k)_{\frac{1}{2}}^{\text{AUSM}^+} = (M_k)_{\frac{1}{2}} a_{\frac{1}{2}} \begin{cases} \rho_{k,L}, & \text{if } (M_k)_{\frac{1}{2}} > 0 \\ \rho_{k,R}, & \text{otherwise,} \end{cases} \tag{3.7}$$

  where $a_{\frac{1}{2}}$ is the numerical sound speed at the interface. $a_{1/2}$ can be defined by a simple arithmetic average of the sound speeds for gas and liquid, or by the mixture sound speed as in the AUSMDV scheme. Since both definitions can be used with success, and the mean speed of sound is much easier for a calculation, the AUSM$^+$ scheme utilizes the following definition:

$$\begin{aligned} (a_k)_{\frac{1}{2}} &= \tfrac{1}{2}[(a_k)_L + (a_k)_R] \\ a_{\frac{1}{2}} &= \tfrac{1}{2}[(a_g)_{\frac{1}{2}} + (a_l)_{\frac{1}{2}}]. \end{aligned} \tag{3.8}$$

  $(M_k)_{\frac{1}{2}}$ is the interfacial Mach number, given by

$$(M_k)_{\frac{1}{2}} = M_4^+ \left((M_k)_L\right) + M_4^- \left((M_k)_R\right), \tag{3.9}$$

  where $M_4^{\pm}$ are the splitting Mach number functions, written as

$$\begin{aligned} M_4^{\pm} &= \begin{cases} M_1^{\pm} & \text{if } |M| \geq 1 \\ M_2^{\pm}(1 \mp 16 B M_2^{\mp}) & \text{otherwise} \end{cases} \\ M_1^{\pm} &= \tfrac{1}{2}(M \pm |M|) \\ M_2^{\pm} &= \begin{cases} M_1^{\pm} & \text{if } |M| \geq 1 \\ \pm\frac{1}{4}(M \pm 1)^2 & \text{otherwise.} \end{cases} \end{aligned} \tag{3.10}$$

  M is the Mach number; B is a constant, equal to 1/8; the subscripts '1', '2' and '4' indicate the polynomial orders of those splitting functions. M_L and M_R are Mach numbers at the left and right states, respectively, defined as

$$(M_k)_L = \frac{(u_k)_L}{a_{1/2}}, \quad (M_k)_R = \frac{(u_k)_R}{a_{1/2}}. \tag{3.11}$$

- Pressure terms:

  For the generic flow model, the pressure flux $(\alpha p)_{k,\frac{1}{2}}$ in Eq. 3.4 is given by

$$(\alpha p)_{k,1/2} = \alpha_{k,L} P_5^+ \left((M_k)_L\right) p_L + \alpha_{k,R} P_5^- \left((M_k)_R\right) p_R, \tag{3.12}$$

  where $P_5^\pm$ are the pressure splitting functions, given by

$$P_5^\pm = \begin{cases} M_1^\pm / M & \text{if } |M| \geq 1 \\ \pm M_2^\pm (2 \mp M - 16 A M M_2^\mp) & \text{otherwise,} \end{cases} \tag{3.13}$$

  where $A = 3/16$; the subscript '5' means a fifth-order polynomial.

(ii) PD-AUSM$^+$ [19]

The PD-AUSM$^+$ scheme is the same as the AUSM$^+$ scheme except that the liquid mass flux is modified by adding a pressure diffusion term $\dot{m}_p$. Therefore, the liquid mass flux in the PD-AUSM$^+$ scheme is given as

$$(\alpha_l \rho_l u_l)_{1/2}^{\text{PD-AUSM}^+} = (\alpha_l \rho_l u_l)_{1/2}^{\text{AUSM}^+} + \dot{m}_p. \tag{3.14}$$

$\dot{m}_p$ is defined as

$$\dot{m}_p = \frac{1}{2}\left(\frac{1}{M_0^2} - 1\right)(\tilde{a}_l)_{\frac{1}{2}} \left(\tilde{M}_l\right)_{\frac{1}{2}} \frac{(a_l)_L p_L + (a_l)_R p_R}{(a_l)_{\frac{1}{2}}^{\,2}}, \tag{3.15}$$

where M_0 is a "cut-off" Mach number; $(\tilde{a}_l)_{\frac{1}{2}}$ is the rescaled interfacial numerical sound speed and $\left(\tilde{M}_l\right)_{\frac{1}{2}}$ is the rescaled interfacial liquid Mach number. They are obtained as follows:

$$(\tilde{a}_l)_{\frac{1}{2}} = f\left((M_l)_{\frac{1}{2}}\right)(a_l)_{\frac{1}{2}}, \tag{3.16}$$

and

$$\left(\tilde{M}_l\right)_{\frac{1}{2}} = M_4^+\left(\left(\tilde{M}_l\right)_L\right) - M_1^+\left(\left(\tilde{M}_l\right)_L\right) - M_4^-\left(\left(\tilde{M}_l\right)_R\right) + M_1^-\left(\left(\tilde{M}_l\right)_R\right). \quad (3.17)$$

$(M_l)_{\frac{1}{2}}$ is defined by Eqs. 3.9 and 3.10. f is a scaling factor given by

$$f(M) = \frac{\sqrt{((1-M_0^2)^2 M^2 + 4M_0^2)}}{1+M_0^2} \quad (3.18)$$

and

$$\left(\tilde{M}_l\right)_L = \frac{(u_l)_L}{(\tilde{a}_l)_{\frac{1}{2}}}, \quad \left(\tilde{M}_l\right)_R = \frac{(u_l)_R}{(\tilde{a}_l)_{\frac{1}{2}}}. \quad (3.19)$$

To increase the dissipation in the PD-AUSM$^+$ scheme, a modified PD-AUSM$^+$ scheme is proposed by adding the pressure diffusion term $\dot{m}_p$ into the liquid mass flow rate $\dot{m}_l$ in Eq. 3.7, instead of into only the liquid mass flux $(\alpha_l \rho_l u_l)_{1/2}$. Thus, through the modification of the liquid mass flow rate, diffusion terms are introduced into both the numerical liquid mass and momentum fluxes of the AUSM$^+$ scheme (see Eq. 3.4). Hence, the numerical liquid mass flow rate in the PD-AUSM$^+$ scheme modified by the present work is defined as

$$(\dot{m}_k)_{\frac{1}{2}}^{\text{PD-AUSM}^+} = (\dot{m}_k)_{\frac{1}{2}}^{\text{AUSM}^+} + \dot{m}_p, \quad (3.20)$$

where $\dot{m}_l$ and $\dot{m}_p$ are given by Eqs. 3.7 and 3.15, respectively.

(iii) AUSM$^+$-up [49][22]

- Convective terms:

  Based on the AUSM$^+$ scheme, the AUSM$^+$-up scheme was developed by adding a dissipation term M_{pk} into the interfacial Mach number $(M_k)_{\frac{1}{2}}$, and by adding

another dissipation term p_{uk} into the interfacial pressure $p_{k,1/2}$. Therefore, $(M_k)_{\frac{1}{2}}$ in AUSM$^+$-up scheme is

$$(M_k)_{\frac{1}{2}} = M_4^+ \left((M_k)_L\right) + M_4^- \left((M_k)_R\right) + M_{pk}, \tag{3.21}$$

where M_{pk} is defined as

$$M_{pk} = -K_p \max\left(1 - \bar{M}_k^2, 0\right) \frac{p_R - p_L}{\bar{\rho}_k a_{1/2}^2}. \tag{3.22}$$

K_p is a constant coefficient, and

$$\begin{aligned} \bar{\rho}_k &= \tfrac{\rho_{k,L}+\rho_{k,R}}{2} \\ \bar{M}_k^2 &= \tfrac{1}{2}[(M_k)_L{}^2 + (M_k)_R{}^2]. \end{aligned} \tag{3.23}$$

- Pressure terms:

  Note that in Chang and Liou's work [22], the AUSM$^+$-up scheme for two-phase flows is applied with a stratified flow model. Thus, for the generic flow model [19], the pressure flux is given by

$$(\alpha p)_{k,1/2} = \alpha_{k,L} P_5^+ \left((M_k)_L\right) p_L + \alpha_{k,R} P_5^- \left((M_k)_R\right) p_R + p_{uk} \tag{3.24}$$

  and

$$p_{uk} = -K_u P_5^+ \left((M_k)_L\right) P_5^- \left((M_k)_R\right) \bar{\rho}_k a_{1/2} (u_{k,R} - u_{k,L}), \tag{3.25}$$

  where K_u is also a constant coefficient, and the definition of $P_5^\pm$ and $a_{1/2}$ are the same as those in the AUSM$^+$ scheme.

U-splitting AUSM-family schemes

The AUSM-family schemes can also be written in velocity-splitting form instead of Mach-number-splitting form.

(i) AUSM$^+$ and AUSMD

When given in the velocity-splitting form, the interfacial fluxes $\boldsymbol{F}_{k,1/2}$ of AUSM$^+$ and AUSMD are defined as follows:

$$\begin{aligned}\boldsymbol{F}_{1/2} = &\tfrac{1}{2}\left[(\alpha_g\rho_g u_g)_{1/2}\left(\boldsymbol{\Phi}_{g,L}+\boldsymbol{\Phi}_{g,R}\right) - \left|(\alpha_g\rho_g u_g)_{1/2}\right|\left(\boldsymbol{\Phi}_{g,R}-\boldsymbol{\Phi}_{g,L}\right)\right] \\ &+\tfrac{1}{2}\left[(\alpha_l\rho_l u_l)_{1/2}\left(\boldsymbol{\Phi}_{l,L}+\boldsymbol{\Phi}_{l,R}\right) - \left|(\alpha_l\rho_l u_l)_{1/2}\right|\left(\boldsymbol{\Phi}_{l,R}-\boldsymbol{\Phi}_{l,L}\right)\right] + (\boldsymbol{F}_p)_{1/2},\end{aligned} \tag{3.26}$$

where

$$\begin{aligned}\boldsymbol{\Phi}_g &= [1 \quad 0 \quad u_g \quad 0]^T \\ \boldsymbol{\Phi}_l &= [0 \quad 1 \quad 0 \quad u_l]^T\end{aligned} \tag{3.27}$$

The pressure flux vector $(\boldsymbol{F}_p)_{1/2}$ is given by Eq. 3.6 with

$$(\alpha p)_{k,i+1/2} = \alpha_{k,L}p_L P^+\left(u_{k,L}, a_{1/2}\right) + \alpha_{k,R}p_R P^-\left(u_{k,R}, a_{1/2}\right). \tag{3.28}$$

where $a_{1/2}$ is given by Eq. 3.39. The pressure splitting function $P^\pm$ is defined as

$$P^\pm = U^\pm(u,a)\cdot\begin{cases}\frac{1}{a}\left(\pm 2 - \frac{u}{a}\right), & \text{if } |u|<a \\ \frac{1}{u}, & \text{otherwise}\end{cases} \tag{3.29}$$

with the velocity splitting function $U^\pm$ given by

$$U^\pm(u,\ a) = \begin{cases}\pm\frac{1}{4a}(u\pm a)^2, & \text{if } |u|\le a \\ \frac{1}{2}\left(u\pm|u|\right), & \text{otherwise.}\end{cases} \tag{3.30}$$

Note that $U^\pm(u,a)$ satisfies the following relationship:

$$U^+(u,a) + U^-(u,a) = u. \tag{3.31}$$

The AUSM$^+$ and AUSMD schemes differ at the convective mass flux.

- AUSM$^+$

$$\left(\alpha_k\rho_k u_k\right)_{1/2} = \begin{cases} \left(\alpha_k\rho_k\right)_L, & \text{if } \left(u_k\right)_{1/2} \geq 0 \\ \left(\alpha_k\rho_k\right)_R, & \text{otherwise,} \end{cases} \tag{3.32}$$

where

$$\left(u_k\right)_{1/2} = U^+\left(u_{k,L},\ a_{k,1/2}\right) + U^-\left(u_{k,R},\ a_{k,1/2}\right) \tag{3.33}$$

with $U^\pm$ defined by Eq. 3.30.

- AUSMD

In AUSMD, however, the convective mass flux is defined as

$$\left(\alpha_k\rho_k u_k\right)_{1/2} = \hat{U}^+\left(u_{k,L},\ a_{1/2}, \chi_{k,L}\right)\alpha_{k,L}\rho_{k,L} + \hat{U}^-\left(u_{k,R},\ a_{1/2}, \chi_{k,R}\right)\alpha_{k,R}\rho_{k,R} \tag{3.34}$$

with $\hat{U}^\pm$ given by Eq. 3.30.

$$\hat{U}^\pm\left(u, a, \chi\right) = \begin{cases} \chi U^\pm\left(u, a\right) + \left(1-\chi\right)\frac{u\pm|u|}{2}, & \text{if } |u| \leq a \\ \frac{u\pm|u|}{2}, & \text{otherwise.} \end{cases} \tag{3.35}$$

The parameters $\chi_{L/R}$ are chosen to be [9]

$$\chi_{L/R} = \frac{2\left(\rho/\alpha\right)_{L/R}}{\left(\rho/\alpha\right)_L + \left(\rho/\alpha\right)_R} \tag{3.36}$$

Similar to $U^\pm(u,c)$, $\hat{U}^\pm\left(u, a, \chi\right)$ satisfies the following relationship:

$$\hat{U}^+(u,a) + \hat{U}^-(u,a) = u, \forall(a,\chi). \tag{3.37}$$

The interfacial sound speed $a_{1/2}$ is given by

$$a_{1/2} = \max\left(a_L, a_R\right), \tag{3.38}$$

where

$$a = \sqrt{\frac{\alpha_g\rho_l + \alpha_l\rho_g}{(\partial\rho_g/\partial p)\,\alpha_g\rho_l + (\partial\rho_l/\partial p)\,\alpha_l\rho_g}}. \tag{3.39}$$

$\hat{U}^{\pm}$ is defined to ensure exact resolution of stationary and moving contact discontinuities. Its derivation is given in Appendix B. Moreover, the interfacial sound speed $a_{1/2}$ is common to the left and the right states, which is key to the derivation of $\hat{U}^{\pm}$. As mentioned above, a common sound speed unifies the U-splitting and M-splitting of the AUSM-family schemes.

(ii) AUSMV and FVS

- FVS

  The FVS scheme is capable of solving acoustic waves in a monotone and accurate way. However, it turns out to be too dissipative to solve contact discontinuities. The interfacial fluxes $\boldsymbol{F}_{k,1/2}$ of FVS scheme are defined as follows:

$$\begin{aligned}\boldsymbol{F}_{1/2} = {} & U^{+}\left(u_{g,L},\ a_{1/2}\right)\boldsymbol{\psi}_{g,L} + U^{-}\left(u_{g,R},\ a_{1/2}\right)\boldsymbol{\psi}_{g,R} \\ & + U^{+}\left(u_{l,L},\ a_{1/2}\right)\boldsymbol{\psi}_{l,L} + U^{-}\left(u_{l,R},\ a_{1/2}\right)\boldsymbol{\psi}_{l,R} + \left(\boldsymbol{F}_p\right)_{1/2},\end{aligned} \tag{3.40}$$

  where

$$\begin{aligned}\boldsymbol{\psi}_g &= \left[\alpha_g\rho_g \quad 0 \quad \alpha_g\rho_g u_g \quad 0\right]^T \\ \boldsymbol{\psi}_l &= \left[0 \quad \alpha_l\rho_l \quad 0 \quad \alpha_l\rho_l u_l\right]^T.\end{aligned} \tag{3.41}$$

- AUSMV

  The AUSMV scheme is similar to the FVS scheme except that the velocity splitting function $U^{\pm}(u,a)$ in Eq. 3.40 is replaced by $\hat{U}^{\pm}(u,a,\chi)$. In other words, The interfacial fluxes $\boldsymbol{F}_{k,1/2}$ of the AUSMV scheme are defined as follows:

$$\begin{aligned}\boldsymbol{F}_{1/2} = {} & \hat{U}^{+}\left(u_{g,L},\ a_{1/2}\right)\boldsymbol{\psi}_{g,L} + \hat{U}^{-}\left(u_{g,R},\ a_{1/2}\right)\boldsymbol{\psi}_{g,R} \\ & + \hat{U}^{+}\left(u_{l,L},\ a_{1/2}\right)\boldsymbol{\psi}_{l,L} + \hat{U}^{-}\left(u_{l,R},\ a_{1/2}\right)\boldsymbol{\psi}_{l,R} + \left(\boldsymbol{F}_p\right)_{1/2}.\end{aligned} \tag{3.42}$$

(iii) AUSMDV [1]

The AUSMDV scheme is a combination of AUSMD and AUSMV schemes. Its momentum flux is a weighted average of those in AUSMD and AUSMV schemes, respectively. By combining AUSMD and AUSMV schemes, the AUSMDV scheme possesses accurate and robust property in handling contact and shock discontinuities [47][68]. AUSMD, AUSMV eliminate the numerical dissipation at the contact discontinuity in van Leer/FVS, thereby recovering the AUSM mass flux for contact discontinuity, while keeping the good stability properties of van Leer/FVS for collision of strong shocks [29].

From Eqs. 3.34 and 3.42, it can be seen that in both AUSMD and AUSMV schemes, the numerical mass flux $(\alpha_k\rho_k u_k)_{1/2}$ is defined by

$$(\alpha_k\rho_k u_k)_{1/2} = (\alpha_k\rho_k)_L \hat{U}^+\left((u_k)_L, a_{1/2}, \chi_L\right) + (\alpha_k\rho_k)_R \hat{U}^-\left((u_k)_R, a_{1/2}, \chi_R\right). \quad (3.43)$$

In contrast to the mass fluxes, the momentum fluxes in AUSMD and AUSMV schemes are different. The numerical flux of the AUSMD scheme is similar in form to the FDS scheme as follows:

$$\left(\alpha_k\rho_k u_k^2\right)_{1/2}^{\text{AUSMD}} = \begin{cases} (\alpha_k\rho_k u_k)_{1/2}(u_k)_L, & \text{if } (\alpha_k\rho_k u_k)_{1/2} \geq 0 \\ (\alpha_k\rho_k u_k)_{1/2}(u_k)_R, & \text{otherwise;} \end{cases} \quad (3.44)$$

whereas, the momentum flux of the AUSMV scheme, similar to the the FVS scheme, is given by

$$\begin{aligned}\left(\alpha_k\rho_k u_k^2\right)_{1/2}^{\text{AUSMV}} = {} & (\alpha_k\rho_k u_k)_L \hat{U}^+\left((u_k)_L, a_{1/2}, \chi_L\right) \\ & + (\alpha_k\rho_k u_k)_R \hat{U}^-\left((u_k)_R, a_{1/2}, \chi_R\right).\end{aligned} \quad (3.45)$$

Combining the AUSMD and AUSMV schemes, the AUSMDV scheme can be given

as follows:

$$(\alpha_k\rho_k u_k^2)_{1/2}^{\text{AUSMDV}} = s\,(\alpha_k\rho_k u_k^2)_{1/2}^{\text{AUSMV}} + (1-s)\,(\alpha_k\rho_k u_k^2)_{1/2}^{\text{AUSMD}}, \tag{3.46}$$

where s is a parameter. Referring to [29], $s = \max(\phi_L, \phi_R)$ and $\phi = 1/e^{\kappa\alpha_g} + 1/e^{\kappa(1-\alpha_g)}$ with κ being a constant. The pressure flux term is the same as that in the AUSM$^+$ scheme (see Eq. 3.28).

It should be noted that the AUSM Mach-number splitting form coincide with the velocity-splitting form if a common sound velocity is used. Moreover, the common sound velocity plays an important role in the derivation of the velocity-splitting flux, namely, $\hat{U}^{\pm}$ in the AUSMD, AUSMV schemes. For detailed derivation, please refer to Appendix B.

Dissipative mechanism of mass flux in AUSM-family schemes

Since the mass flux is shared by the convective parts of mass, energy, and momentum equations, it plays a key role in the design of a stable and accurate numerical flux [67]. Therefore, before proceeding to the next section, it is necessary to analyze the dissipative mechanism of mass flux in AUSM$^+$, AUSMD, AUSMV, and FVS schemes. This analysis facilitates the understanding of the excellent capability for resolving contact discontinuities of AUSM$^+$ and AUSMD schemes, and the excessive diffusion for the resolution of contacts of FVS or AUSMV schemes. In addition, this analysis is desirable to design a new SG-AUSMFVS scheme, which combines the AUSM$^+$ and FVS to solve a stiff phase separation problem, as addressed in Section 5.5.

The mass flux of AUSM$^+$, AUSMD, AUSMV and FVS schemes can be written in the following viscous form:

$$(\alpha_k\rho_k u_k)_{1/2} = u_{k,1/2}\frac{(\alpha_k\rho_k)_L + (\alpha_k\rho_k)_R}{2} + \frac{1}{2}d_{k,1/2}, \tag{3.47}$$

where $\frac{1}{2}d_{k,1/2}$ is a dissipation term. The dissipation term for the above-mentioned schemes is given as follows [29].

- AUSM$^+$

$$d_{k,1/2}^{\mathrm{AUSM}^+} = \left|u_{k,1/2}\right| \left(\left(\alpha_k \rho_k\right)_R - \left(\alpha_k \rho_k\right)_L\right) \tag{3.48}$$

with $u_{k,1/2}$ given by Eq. 3.33.

- FVS

$$d_{k,1/2}^{\mathrm{FVS}} = \left[U_{k,1/2}\left(u_{k,R}, a_{1/2}\right)\right]\left(\alpha_k \rho_k\right)_R - \left[U_{k,1/2}\left(u_{k,L}, a_{1/2}\right)\right]\left(\alpha_k \rho_k\right)_L, \tag{3.49}$$

where

$$\left[U\left(u,a\right)\right] = U^+\left(u,a\right) - U^-\left(u,a\right). \tag{3.50}$$

- AUSMD/AUSMV

$$d_{k,1/2}^{\mathrm{AUSMD/V}} = \left[\hat{U}_{k,1/2}\left(u_{k,R}, a_{1/2}\right)\right]\left(\alpha_k \rho_k\right)_R - \left[\hat{U}_{k,1/2}\left(u_{k,L}, a_{1/2}\right)\right]\left(\alpha_k \rho_k\right)_L, \tag{3.51}$$

where

$$\left[\hat{U}\left(u,a\right)\right] = \hat{U}^+\left(u,a\right) - \hat{U}^-\left(u,a\right). \tag{3.52}$$

Therefore, for a moving contact discontinuity where

$$p_L = p_R, \quad u_{g,L} = u_{g,R}, \quad u_{l,L} = u_{l,R}, \quad \alpha_{g,L} = \alpha_{g,R}, \tag{3.53}$$

the dissipation terms in the mass flux of the above-mentioned schemes can be given as follows:

- AUSM$^+$

$$d_{k,1/2}^{\mathrm{AUSM}^+} = \left|u_k\right| \left(\left(\alpha_k \rho_k\right)_R - \left(\alpha_k \rho_k\right)_L\right), \tag{3.54}$$

where the relationship shown in Eq. 3.31 has been used.

- FVS

When $|u_k \leq| a_{1/2}$,

$$d_{k,1/2}^{\mathrm{FVS}} = -\frac{1}{4}\left(\frac{u_k^2}{a_{1/2}} + a_{1/2}\right)\rho_k\left(\alpha_{k,R} - \alpha_{k,L}\right). \tag{3.55}$$

- AUSMD/AUSMV

$$d_{k,1/2}^{\mathrm{AUSMD/V}} = |u_k|\left[\left(\alpha_k\rho_k\right)_R - \left(\alpha_k\rho_k\right)_L\right], \tag{3.56}$$

where Eq. 3.37 is used to perform the derivation.

Therefore, when the phase velocities are zero, $d_{k,1/2}$ becomes zero in AUSM$^+$ and AUSMD, AUSMV from Eqs. 3.54 and 3.56. In other words, at the steady contact discontinuity, there is no numerical dissipation in the mass fluxes of AUSM$^+$ and AUSMD, AUSMV. On the contrary, a numerical dissipation remains in the FVS scheme, which is given by

$$d_{k,1/2}^{\mathrm{FVS}} = -\frac{1}{4}\rho_k a_{1/2}\left(\alpha_{k,R} - \alpha_{k,L}\right) \neq 0. \tag{3.57}$$

To sum up, the FVS scheme has an excellent capability for capturing strong shock waves. However, the FVS scheme generates excessive numerical dissipation at a contact discontinuity. Contrary to the FVS scheme, the AUSM$^+$ scheme is capable of exactly solving a contact discontinuity, but it produces numerical overshoots at shock waves, mainly due to neglecting the density behind a shock in the AUSM$^+$ mass fluxes. The AUSMD scheme modifies the mass flux of the FVS scheme to achieve exact calculation of a contact discontinuity, while at the same time keeps the momentum flux being the same as that of the AUSM$^+$ scheme. Hence, the AUSMD scheme has a desirable property of solving a contact discontinuity; however, it still generates overshoots for the interaction of strong shocks[1]. On the other hand, the AUSMV scheme uses the same mass flux as that of the AUSMD scheme, while employs the momentum flux in a form similar to that of the FVS scheme. The AUSMDV scheme is a mixture of AUSMD and AUSMV scheme.

3.3.2 Roe Scheme

Introduction

The Roe scheme is an approximate Riemann solver based on the Godunov scheme. Its basic idea is to obtain the exact solutions of the linearized Riemann problem [8]. The Roe scheme has a good reputation of accurately capturing single stationary discontinuity without numerical dissipation. However, one of its significant shortcomings is that the Roe scheme generates physically inadmissible solutions such as expansion shock [1]. Although this nonphysical issue can be cured by an entropy fix, the Roe scheme still diverges at strong expansions [1]. Another drawback of the Roe scheme is that it produces significant errors for slow moving shocks [69]. The derivation of the Roe scheme for the four-equation two-fluid model is given as follows:

Neglecting the source term $\boldsymbol{Q}$, Eq. 2.62 can be given as follows:

$$\frac{\partial \boldsymbol{U}}{\partial t} + \boldsymbol{A}(\boldsymbol{U})\frac{\partial \boldsymbol{U}}{\partial x} = 0. \tag{3.58}$$

Using '0' to denote the interface of the control volume, the following nonlinear Riemann problem is solved for the hyperbolic system of the two-fluid model:

$$\begin{aligned} &\partial_t \boldsymbol{U} + \partial_x \boldsymbol{G}(\boldsymbol{U}) = 0 \\ &\boldsymbol{U}(x,0) = \boldsymbol{U}_L(x<0),\ \boldsymbol{U}(x,0) = \boldsymbol{U}_R(x>0), \end{aligned} \tag{3.59}$$

where $\partial_x \boldsymbol{G}(\boldsymbol{U})$ is given by Eq. 2.61.

The general idea of Roe scheme is to introduce a local linearization

$$\partial_t \boldsymbol{U} + \hat{\boldsymbol{A}}\left(\boldsymbol{U}_L,\ \boldsymbol{U}_R\right)\partial_x \boldsymbol{U} = 0, \tag{3.60}$$

where $\hat{\boldsymbol{A}}\left(\boldsymbol{U}_L,\ \boldsymbol{U}_R\right)$ is the Roe-averaged matrix.

For the Euler equations with perfect gases [8] or several real gases [70], $\hat{\boldsymbol{A}}\left(\boldsymbol{U}_L,\ \boldsymbol{U}_R\right)$ is constructed such that it satisfies the following property:

$$\boldsymbol{G}(\boldsymbol{U}_R) - \boldsymbol{G}(\boldsymbol{U}_L) = \hat{\boldsymbol{A}}\,(\boldsymbol{U}_L,\ \boldsymbol{U}_R)\,(\boldsymbol{U}_R - \boldsymbol{U}_L)\,. \tag{3.61}$$

However, as mentioned earlier, for the two-fluid model, the matrix $\boldsymbol{A}(\boldsymbol{U})$ is not the derivative of $\boldsymbol{G}(\boldsymbol{U})$. Therefore, Roe's method can not be applied directly to the two-fluid model, which is non-conservative. To extend the Roe scheme to the two-fluid model, a weak formulation of Roe's approximate Riemann solver has to be introduced [70]. The general idea is to solve the following linear system:

$$\begin{aligned} &\partial_t \boldsymbol{U} + \hat{\boldsymbol{A}}(\boldsymbol{U}_L,\ \boldsymbol{U}_R)_\Phi \partial_x \boldsymbol{U} = 0 \\ &\boldsymbol{U}(x,0) = \boldsymbol{U}_L(x<0),\ \boldsymbol{U}(x,0) = \boldsymbol{U}_R(x>0), \end{aligned} \tag{3.62}$$

where $\hat{\boldsymbol{A}}(\boldsymbol{U}_L,\ \boldsymbol{U}_R)_\Phi$ is a matrix based on $(\boldsymbol{U}_L, \boldsymbol{U}_R)$ and $\Phi\,(s, \boldsymbol{U}_L, \boldsymbol{U}_R)$. $\Phi\,(s, \boldsymbol{U}_L, \boldsymbol{U}_R)$ is a smooth path linking $\boldsymbol{U}_L$ and $\boldsymbol{U}_R$; $s \in [0,1]$. The matrix $\hat{\boldsymbol{A}}(\boldsymbol{U}_L,\ \boldsymbol{U}_R)_\Phi$ satisfies the following property:

$$\int_0^1 \hat{\boldsymbol{A}}\,(\Phi\,(s;\boldsymbol{U}_L,\boldsymbol{U}_R))\,\frac{\partial \Phi}{\partial s}\,(s;\boldsymbol{U}_L,\boldsymbol{U}_R)\,ds = \hat{\boldsymbol{A}}(\boldsymbol{U}_L,\boldsymbol{U}_R)_\Phi\,(\boldsymbol{U}_L - \boldsymbol{U}_R) \tag{3.63}$$

and

$$\int_0^1 \hat{\boldsymbol{A}}\,(\Phi\,(s;\boldsymbol{U}_L,\boldsymbol{U}_R))\,\frac{\partial \Phi}{\partial s}\,(s;\boldsymbol{U}_L,\boldsymbol{U}_R)\,ds = \boldsymbol{G}\,(\boldsymbol{U}_R) - \boldsymbol{G}\,(\boldsymbol{U}_L) \tag{3.64}$$

To sum up, in the weak formulation of Roe's approximate Riemann solver, $\hat{\boldsymbol{A}}(\boldsymbol{U}_L, \boldsymbol{U}_R)_\Phi$ satisfies the following conditions:

C1. $\hat{\boldsymbol{A}}(\boldsymbol{U}_L, \boldsymbol{U}_R)_\Phi\,(\boldsymbol{U}_L - \boldsymbol{U}_R) = \boldsymbol{G}\,(\boldsymbol{U}_R) - \boldsymbol{G}\,(\boldsymbol{U}_L)$.

C2. $\hat{\boldsymbol{A}}(\boldsymbol{U}_L, \boldsymbol{U}_R)_\Phi$ is diagonalizable with real eigenvalues.

C3. $\hat{\boldsymbol{A}}(\boldsymbol{U}_L, \boldsymbol{U}_R)_\Phi \to \boldsymbol{A}(\boldsymbol{U})$ smoothly as $\boldsymbol{U}_L, \boldsymbol{U}_R \to \boldsymbol{U}$.

Using the average $\tilde{\alpha}$ given by [63], that is

$$\tilde{\alpha}_k = \frac{2\alpha_k^L \alpha_k^R}{\alpha_k^L + \alpha_k^R}. \tag{3.65}$$

The Riemann problem is solved for the following conservative system:

$$\partial_t \boldsymbol{U} + \partial_x \tilde{\boldsymbol{G}}(\boldsymbol{U}, \tilde{\alpha}_g, \tilde{\alpha}_l) = 0, \tag{3.66}$$

where $\tilde{\boldsymbol{G}}$ is given by

$$\tilde{\boldsymbol{G}}(\boldsymbol{U}) = \begin{bmatrix} \alpha_g \rho_g u_g \\ \alpha_l \rho_l u_l \\ \alpha_g \rho_g u_g^2 + \alpha_g \Delta p + \tilde{\alpha}_g (p - \Delta p) \\ \alpha_l \rho_l u_l^2 + \alpha_l \Delta p + \tilde{\alpha}_l (p - \Delta p) \end{bmatrix}. \tag{3.67}$$

Therefore, the path Φ will only affect the linearization of the matrix $\hat{\boldsymbol{A}}(\boldsymbol{U}, \tilde{\alpha}_g, \tilde{\alpha}_l)$, which is given as

$$\hat{\boldsymbol{A}}(\boldsymbol{U}, \tilde{\alpha}_g, \tilde{\alpha}_l) = \frac{\partial \tilde{\boldsymbol{G}}(\boldsymbol{U}, \tilde{\alpha}_g, \tilde{\alpha}_l)}{\partial \boldsymbol{U}}. \tag{3.68}$$

Following the method introduced by [70] and [63], the Roe-type matrix $\hat{\boldsymbol{A}}(\boldsymbol{U}_L, \boldsymbol{U}_R)_\Phi$ is constructed as follows:

First, a canonical path is chosen for a parameter vector $\boldsymbol{w}$, that is

$$\Phi(s; \boldsymbol{U}_L, \boldsymbol{U}_R) = \phi_0(\boldsymbol{w}_L + s(\boldsymbol{w}_R - \boldsymbol{w}_L)), \tag{3.69}$$

where ϕ_0 is a smooth function that satisfies $\phi_0(\boldsymbol{w}_L) = \boldsymbol{U}_L$ and $\phi_0(\boldsymbol{w}_L) = \boldsymbol{U}_R$.

Then define a regular matrix $\boldsymbol{A}_0(\boldsymbol{w})$ for every state of $\boldsymbol{w}$ as follows:

$$\boldsymbol{A}_0(\boldsymbol{w}) = \frac{\partial \phi_0}{\partial \boldsymbol{w}}. \tag{3.70}$$

Using Eqs. 3.69 and 3.70, the Roe-type matrix can be given by

$$\boldsymbol{A}\left(\boldsymbol{U}_L, \boldsymbol{U}_R\right)_\Phi = \boldsymbol{C}\left(\boldsymbol{U}_L, \boldsymbol{U}_R\right)_\Phi \boldsymbol{B}\left(\boldsymbol{U}_L, \boldsymbol{U}_R\right)_\Phi^{-1}, \tag{3.71}$$

where

$$\begin{aligned} \boldsymbol{B}(\boldsymbol{U}_L, \boldsymbol{U}_R)_\Phi &= \int_0^1 \boldsymbol{A}_0\left(\boldsymbol{w}_L + s\left(\boldsymbol{w}_R - \boldsymbol{w}_L\right)\right) ds \\ \boldsymbol{C}(\boldsymbol{U}_L, \boldsymbol{U}_R)_\Phi &= \int_0^1 \boldsymbol{A}\left(\phi_0\left(\boldsymbol{w}_L + s\left(\boldsymbol{w}_R - \boldsymbol{w}_L\right)\right)\right) \times \boldsymbol{A}_0\left(\mathbf{w}_L + s\left(\boldsymbol{w}_R - \boldsymbol{w}_L\right)\right) ds. \end{aligned} \tag{3.72}$$

Numerical algorithm

For the four-equation two-fluid model, the following parameter vector is chosen:

$$\boldsymbol{w} = \begin{bmatrix} w_1 \\ w_2 \\ w_3 \\ w_4 \end{bmatrix} = \begin{bmatrix} \sqrt{\alpha_g \rho_g} \\ \sqrt{\alpha_l \rho_l} \\ \sqrt{\alpha_g \rho_g} u_g \\ \sqrt{\alpha_l \rho_l} u_l \end{bmatrix}. \tag{3.73}$$

Thus, based on Eq. 3.73 and the definition of $\boldsymbol{U}$ (see Eq. 2.46), $\phi_0\left(\boldsymbol{w}\right)$ and $\tilde{\boldsymbol{G}}(U)$ can be expressed as follows:

$$\phi_0\left(\boldsymbol{w}\right) = \begin{bmatrix} w_1^2 \\ w_2^2 \\ w_1 w_3 \\ w_2 w_4 \end{bmatrix}, \tag{3.74}$$

and

$$\tilde{\boldsymbol{G}}(\boldsymbol{U}) = \begin{bmatrix} w_1 w_3 \\ w_2 w_4 \\ w_3^2 + \alpha_g \Delta p + \tilde{\alpha}_g\left(p - \Delta p\right) \\ w_4^2 + \alpha_l \Delta p + \tilde{\alpha}_l\left(p - \Delta p\right) \end{bmatrix}. \tag{3.75}$$

Furthermore, according to Eqs. 3.70, 3.72 and 3.74, $\boldsymbol{B}(\boldsymbol{U}_L, \boldsymbol{U}_R)_\Phi$ can be given as

$$\boldsymbol{B}(\boldsymbol{U}_L, \boldsymbol{U}_R)_\Phi = \begin{bmatrix} 2\bar{w}_1 & 0 & 0 & 0 \\ 0 & 2\bar{w}_2 & 0 & 0 \\ \bar{w}_3 & 0 & \bar{w}_1 & 0 \\ 0 & \bar{w}_2 & 0 & \bar{w}_4 \end{bmatrix}, \tag{3.76}$$

where $\bar{w}_j = \frac{1}{2}(w_L + w_R)$; $j = 1, 2,$ or 3.

Based on Eqs. 3.72 and 3.75, $\boldsymbol{C}(\boldsymbol{U}_L, \boldsymbol{U}_R)_\Phi$ can be written as

$$\boldsymbol{C}(\boldsymbol{U}_L, \boldsymbol{U}_R)_\Phi = \begin{bmatrix} \bar{w}_3 & 0 & \bar{w}_1 & 0 \\ 0 & \bar{w}_4 & 0 & \bar{w}_2 \\ \tilde{\alpha}_g\left(\bar{p}_{w_1} - \overline{\Delta p}_{w_1}\right) + \left(\overline{\alpha_g \Delta p}\right)_{w_1} & \tilde{\alpha}_g\left(\bar{p}_{w_2} - \overline{\Delta p}_{w_2}\right) + \left(\overline{\alpha_g \Delta p}\right)_{w_2} & 2\bar{w}_3 & 0 \\ \tilde{\alpha}_l\left(\bar{p}_{w_1} - \overline{\Delta p}_{w_1}\right) + \left(\overline{\alpha_l \Delta p}\right)_{w_1} & \tilde{\alpha}_l\left(\bar{p}_{w_2} - \overline{\Delta p}_{w_2}\right) + \left(\overline{\alpha_l \Delta p}\right)_{w_2} & 0 & 2\bar{w}_4 \end{bmatrix}. \tag{3.77}$$

Therefore, one can obtain the Roe-type matrix using Eqs. 3.71, 3.76 and 3.77:

$$\hat{\boldsymbol{A}}(\boldsymbol{U}_L, \boldsymbol{U}_R)_\Phi = \begin{bmatrix} 0 & 0 & 1 & 0 \\ 0 & 0 & 0 & 1 \\ \frac{\tilde{\alpha}_g\left(\bar{p}_{w_1} - \overline{\Delta p}_{w_1}\right) + \left(\overline{\alpha_g \Delta p}\right)_{w_1}}{2\bar{w}_1} - \left(\frac{\bar{w}_3}{\bar{w}_1}\right)^2 & \frac{\tilde{\alpha}_g\left(\bar{p}_{w_2} - \overline{\Delta p}_{w_2}\right) + \left(\overline{\alpha_g \Delta p}\right)_{w_2}}{2\bar{w}_2} & 2\frac{\bar{w}_3}{\bar{w}_1} & 0 \\ \frac{\tilde{\alpha}_l\left(\bar{p}_{w_1} - \overline{\Delta p}_{w_1}\right) + \left(\overline{\alpha_l \Delta p}\right)_{w_1}}{2\bar{w}_1} & \frac{\tilde{\alpha}_l\left(\bar{p}_{w_2} - \overline{\Delta p}_{w_2}\right) + \left(\overline{\alpha_l \Delta p}\right)_{w_2}}{2\bar{w}_2} - \left(\frac{\bar{w}_4}{\bar{w}_2}\right)^2 & 2\frac{\bar{w}_4}{\bar{w}_2} & 0 \end{bmatrix}. \tag{3.78}$$

$\bar{\mathrm{X}}_{w_j}$ denotes the average of the derivative X_{w_j}, that is

$$\bar{\mathrm{X}}_{w_i} = \int_0^1 \mathrm{X}_{\mathrm{w_i}}\left(\boldsymbol{w}_L + s\left(\boldsymbol{w}_R - \boldsymbol{w}_L\right)\right) ds \tag{3.79}$$

with X being p, Δp or $\alpha_k \Delta p$; $j = 1$ or 2.

By substituting Eqs. 3.73, 3.65, and 3.79 into Eq. 3.78, one can rewrite the Roe-type matrix as follows:

$$\hat{\boldsymbol{A}}(\boldsymbol{U}_L, \boldsymbol{U}_R)_\Phi = \begin{bmatrix} 0 & 0 & 1 & 0 \\ 0 & 0 & 0 & 1 \\ \bar{\omega}\left(\bar{\alpha}_g\bar{\rho}_l + \overline{\Delta p}\bar{\alpha}_l\frac{\partial\bar{\rho}_l}{\partial p}\right) - \bar{u}_g^2 & \bar{\omega}\left(\bar{\alpha}_g\bar{\rho}_g - \Delta p\bar{\alpha}_g\frac{\partial\bar{\rho}_g}{\partial p}\right) & 2\bar{u}_g & 0 \\ \bar{\omega}\left(\bar{\alpha}_l\bar{\rho}_l - \overline{\Delta p}\alpha_l\frac{\partial\rho_l}{\partial p}\right) & \bar{\omega}\left(\bar{\alpha}_g\bar{\rho}_l + \overline{\Delta p}\bar{\alpha}_g\frac{\partial\bar{\rho}_g}{\partial p}\right) - \bar{u}_l^2 & 0 & 2\bar{u}_l \end{bmatrix}, \tag{3.80}$$

where

$$\begin{aligned} \bar{u}_k &= \frac{u_{k,L}\sqrt{(\rho_k\alpha_k)_L} + u_{k,R}\sqrt{(\rho_k\alpha_k)_R}}{\sqrt{(\rho_k\alpha_k)_L} + \sqrt{(\rho_k\alpha_k)_R}} \\ \bar{\alpha}_k &= \tfrac{1}{2}\left(\alpha_{k,L} + \alpha_{k,R}\right) \\ \bar{\rho}_k &= \tfrac{1}{2}\left(\rho_{k,L} + \rho_{k,R}\right) \\ \overline{\Delta p} &= \tfrac{1}{2}\left(\Delta p_L + \Delta p_R\right) \\ \bar{\omega} &= 1/\left(\bar{\alpha}_g\bar{\rho}_g\frac{\partial\rho_g}{\partial p} + \bar{\alpha}_l\bar{\rho}_l\frac{\partial\rho_l}{\partial p}\right). \end{aligned} \tag{3.81}$$

It can be checked that the matrix $\hat{\boldsymbol{A}}(\boldsymbol{U}_L, \boldsymbol{U}_R)_\Phi$ satisfies conditions C1, C2, and C3.

Once the Roe-averaged matrix $\hat{\boldsymbol{A}}(\boldsymbol{U}_L, \boldsymbol{U}_R)_\Phi$ is constructed, $\boldsymbol{U}^{n+1}$ can be calculated using the following expression:

$$\boldsymbol{U}_i^{n+1} = \boldsymbol{U}_i^n - \frac{\Delta t}{\Delta x}\left(\boldsymbol{G}^-\left(\boldsymbol{U}_i^n, \boldsymbol{U}_i^{n+1}\right) + \boldsymbol{G}^+\left(\boldsymbol{U}_i^{n-1}, \boldsymbol{U}_i^n\right)\right), \tag{3.82}$$

where

$$\boldsymbol{G}^\pm\left(\boldsymbol{U}_i^{n-1}, \boldsymbol{U}_i^n\right) = \boldsymbol{A}^\pm\left(\boldsymbol{U}_i^{n-1}, \boldsymbol{U}_i^n\right)_\Phi\left(\boldsymbol{U}_i^n - \boldsymbol{U}_i^{n-1}\right) \tag{3.83}$$

with $\boldsymbol{A}^\pm\left(\boldsymbol{U}_i^{n-1}, \boldsymbol{U}_i^n\right)_\Phi$ being the positive and negative part of the Roe-averaged matrix. They are defined as follows:

$$\hat{\boldsymbol{A}}^\pm\left(\boldsymbol{U}_i^{n-1}, \boldsymbol{U}_i^n\right)_\Phi = \boldsymbol{R}_{i-1/2}\boldsymbol{\Lambda}^\pm_{i-1/2}\boldsymbol{R}^{-1}_{i-1/2}, \tag{3.84}$$

where $\boldsymbol{R}_{i-1/2}$ is the matrix formed by the right eigenvectors of $\hat{\boldsymbol{A}}\left(\boldsymbol{U}_i^{n-1}, \boldsymbol{U}_i^n\right)_\Phi$, and $\boldsymbol{\Lambda}_{i-1/2}^{\pm}$ is the diagonal matrix that consists of the positive and the negative eigenvalues of $\hat{\boldsymbol{A}}\left(\boldsymbol{U}_i^{n-1}, \boldsymbol{U}_i^n\right)_\Phi$. That is

$$\boldsymbol{\Lambda}_{i-1/2}^{\pm} = \operatorname{diag}\left(\lambda_{i-1/2}^{1\pm}, ..., \lambda_{i-1/2}^{m\pm}\right), \tag{3.85}$$

where

$$\begin{aligned} \lambda_{i-1/2}^{m+} &= \max\left(0, \lambda_{i-1/2}^{m}\right) \\ \lambda_{i-1/2}^{m-} &= \min\left(0, \lambda_{i-1/2}^{m}\right). \end{aligned} \tag{3.86}$$

3.3.3 Proposed SG-AUSM-Family Schemes

Illustration of staggered grids

On a staggered grid, only the scalar variables, including the void fraction α, pressure p, and sound speed a, are located at the centroids of the control volumes, whereas the velocity or momentum variables are stored at the control interfaces. This is different from a collocated grid arrangement, where all variables are available at the cell centers of the control volumes. One can also regard the staggered grids as two sets of control volumes, as demonstrated in Fig. 3.1. The scalar variables are stored at the center (dark dots) of the pressure control volume, which is denoted by the lower-case i-index, $1 \leq i \leq N$ (N equals the total number of nodes); while the velocity u is located at the center (black arrows) of the velocity control volume, which is denoted by the upper-case I-index, $0 \leq I \leq (N-1)$. $i \pm 1/2$ and $I \pm 1/2$ represent the boundaries of p-CV and u-CV, respectively.

As can be observed, the p-CV and u-CV are half a control volume away from each other.

Therefore, on a staggered grid, the mass equations can be written in the following implicit form:

$$(\alpha_k \rho_k)_i^{n+1} - (\alpha_k \rho_k)_i^n + \frac{\Delta t}{\Delta x}\left[(f_k)_{i+1/2}^{n+1} - (f_k)_{i-1/2}^{n+1})\right] = 0, \tag{3.87}$$

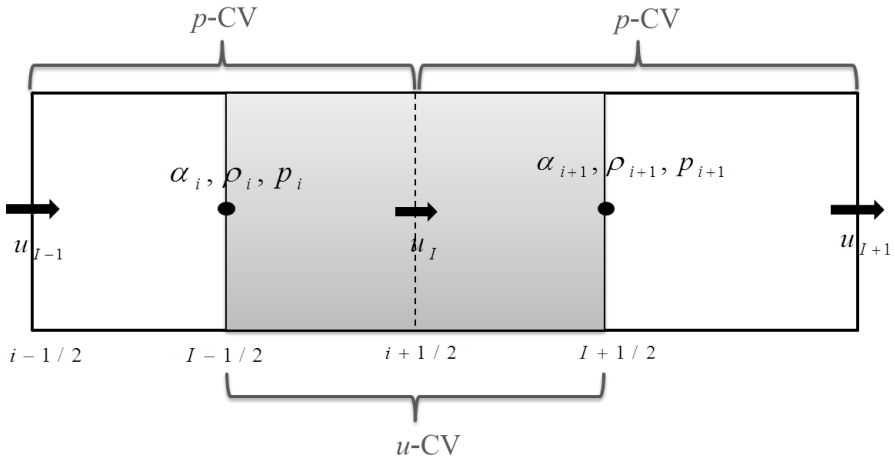

Figure 3.1: Illustration of staggered grids.

where $(f_k)_{i+1/2} = (\alpha_k \rho_k u_k)_{i+1/2}$ is the mass flux of the k^{th} phase at $i + 1/2$ location.

The implicitly discretized momentum equations can be given in the following form:

$$\begin{aligned}
&(\tilde{\alpha}_k \tilde{\rho}_k u_k)_I^{n+1} - (\tilde{\alpha}_k \tilde{\rho}_k u_k)_I^n + \tfrac{\Delta t}{\Delta x}\left[(f_k)_{I+1/2}^{n+1} - (f_k)_{I-1/2}^{n+1}\right] \\
&-\Delta t(\tilde{p}^{int})_I^{n+1} \tfrac{\left[(\alpha_k)_{i+1}^{n+1} - (\alpha_k)_i^{n+1})\right]}{\Delta x} - \Delta t(\tilde{\alpha}_k \tilde{\rho}_k g)_I^{n+1} \\
&-\Delta t C_{k,f} \left(\tilde{\alpha}_g (1 - \tilde{\alpha}_g) \tilde{\rho}_g (u_g - u_l)\right)_I^{n+1} = 0,
\end{aligned} \tag{3.88}$$

where $(f_k)_{I+1/2} = (\alpha_k \rho_k \tilde{u}_k^2 + \alpha_k p)_{I+1/2}$ is the momentum flux of the k^{th} phase at $I + 1/2$ location; $C_{g,f} = C_f$ and $C_{l,f} = -C_f$.

When using staggered grids, scalar variables are not stored at the centroid of the u-control volume. Hence, in Eqs. 3.87 and 3.88, $\tilde{\alpha}_I, \tilde{\rho}_I, \tilde{p}_I$ should be provided. In the present work, a simple two-point arithmetic average is applied as follows:

$$\begin{aligned}
(\tilde{p})_I &= \tfrac{1}{2}[p_i + p_{i+1}] \\
(\tilde{\alpha}_k)_I &= \tfrac{1}{2}[(\alpha_k)_i + (\alpha_k)_{i+1}].
\end{aligned} \tag{3.89}$$

SG-AUSM-family schemes on staggered grids

The SG-AUSM-family schemes proposed by the present work (see also [71]) consider the convective and pressure terms separately [41].

$$\boldsymbol{F}_{k,1/2}(\boldsymbol{U}_L, \boldsymbol{U}_R) = \boldsymbol{F}^c_{k,1/2} + \boldsymbol{P}_{k,1/2}, \tag{3.90}$$

where $\boldsymbol{F}^c_{k,1/2}$ and $\boldsymbol{P}_{k,1/2}$ are the interfacial convective flux and pressure flux, respectively.

$\boldsymbol{P}_{k,1/2}$ has the following form:

$$\boldsymbol{P}_{k,1/2} = \Big(0,\ (\alpha_k p)_{1/2}\Big)^T. \tag{3.91}$$

Since α_k and p are already given at the interface of velocity control volume (u-CV), there is no need to perform the interpolation for $(\alpha p)_{k,1/2}$ as required by the collocated-grid arrangement. Instead, the pressure flux can be directly obtained as $(\alpha p)_{k,I+1/2} = \alpha_{k,i+1} p_{i+1}$. Likewise, based on the pressure control volume (p-CV) (see Figure 3.1), the interfacial mass flux $(f_k)_{i+1/2}$ in Eq. 3.87 can be immediately given by

$$(f_k)_{i+1/2} = (u_k)_{i+\frac{1}{2}}(\rho_k\alpha_k)_{L/R} = (u_k)_I \cdot (\rho_k\alpha_k)_{i/i+1} = \begin{cases} (u_k)_I(\rho_k\alpha_k)_i \ \text{, if } (u_k)_I \geq 0 \\ (u_k)_I(\rho_k\alpha_k)_{i+1} \ \text{, otherwise,} \end{cases} \tag{3.92}$$

where the subscripts L and R denote the left and right states on the interface, respectively. In this work, the first-order version of the scheme is utilized, unless stated otherwise.

For the interfacial momentum flux, the discretization based on the staggered grids arrangement with the SG-AUSM$^+$, SG-AUSMD, SG-AUSMV, and SG-AUSMDV schemes will be introduced in detail as follows:

(1) SG-AUSM$^+$

Based on the u-CV (see Figure 3.1), the momentum flux $(f_k)_{I+1/2}$ in Eq. 3.88 can be written as follows:

$$\left\{(f_k)^c_{I+1/2}\right\}_{\text{SG-AUSM}^+} = \max\left\{(u_k)_{I+1/2}, 0\right\}\cdot(\tilde{\rho}_k\tilde{\alpha}_k u_k)_I + \min\left\{(u_k)_{I+1/2}, 0\right\}\cdot(\tilde{\rho}_k\tilde{\alpha}_k u_k)_{I+1}, \tag{3.93}$$

where $(u_k)_{I+1/2}$ is the interfacial velocity of the k^{th} phases given by

$$(u_k)_{I+1/2} = U^+\left((u_k)_I, a_{I+1/2}\right) + U^-\left((u_k)_{I+1}, a_{I+1/2}\right), \tag{3.94}$$

and $a_{I+\frac{1}{2}}$ is a mathematical mixture sound velocity, defined as [72]

$$a_{I+1/2} = a_{i+1} = \left(\sqrt{\frac{\rho_l\alpha_g + \rho_g\alpha_l}{\frac{\partial\rho_g}{\partial p}\rho_l\alpha_g + \frac{\partial\rho_l}{\partial p}\rho_g\alpha_l}}\right)_{i+1}. \tag{3.95}$$

Again, the staggered-grid arrangement enables SG-AUSM-family schemes to skip the interpolation of the interfacial sound speed as required by the collocated-grid arrangement [9, 22, 19].

$U^\pm$ are the splitting functions, written as

$$U^\pm(u,a) = \begin{cases} \frac{1}{2}(u \pm |u|), & \text{if } |u| \le a \\ \pm\frac{1}{4a}(u \pm a)^2, & \text{otherwise.} \end{cases} \tag{3.96}$$

(2) SG-AUSMDV

$$\left\{(f_k)^c_{I+1/2}\right\}_{\text{SG-AUSMDV}} = s\left\{(f_k)^c_{I+1/2}\right\}_{\text{SG-AUSMV}} + (1-s)\left\{(f_k)^c_{I+1/2}\right\}_{\text{SG-AUSMD}}, \tag{3.97}$$

where

$$\begin{aligned}\left\{(f_k)^c_{I+1/2}\right\}_{\text{SG-AUSMV}} &= \hat{U}^+\left((u_k)_I, a_{I+1/2}, \chi_I\right)(\tilde{\rho}_k\tilde{\alpha}_k u_k)_I \\ &+\hat{U}^-\left((u_k)_{I+1}, a_{I+1/2}, \chi_{I+1}\right)(\tilde{\rho}_k\tilde{\alpha}_k u_k)_{I+1},\end{aligned} \tag{3.98}$$

and

$$\left\{(f_k)^c_{I+1/2}\right\}_{\text{SG-AUSMD}} = \max\left\{(\dot{m}_k)^c_{I+1/2}, 0\right\}(u_k)_I + \min\left\{(\dot{m}_k)^c_{I+1/2}, 0\right\}(u_k)_{I+1}. \tag{3.99}$$

$(\dot{m}_k)^c_{I+1/2}$ is the mass flux at the interface of u-CV, given by

$$(\dot{m}_k)^c_{I+1/2} = \hat{U}^+\left((u_k)_I, a_{I+1/2}, \chi_I\right)(\tilde{\rho}_k\tilde{\alpha}_k)_I + \hat{U}^-\left((u_k)_{I+1}, a_{I+1/2}, \chi_{I+1}\right)(\tilde{\rho}_k\tilde{\alpha}_k)_{I+1}, \tag{3.100}$$

where $\hat{U}^{\pm}$ are splitting functions given by Eq. 3.35 [1] and χ is defined as Eq. 4.15.

In Equation 3.97, s is a switching function. Following [9], it is defined to overcome the stiffness with a smooth transition between single-phase and two-phase flows.

$$s = \max\left(\phi_I, \phi_{I+1}\right). \tag{3.101}$$

ϕ is given by

$$\phi = 1/e^{\kappa\alpha_g} + 1/e^{\kappa\alpha_l}, \tag{3.102}$$

where κ is a parameter which controls the degree of smoothness of ϕ.

(3) SG-FVS

$$\begin{aligned}\left\{(f_k)^c_{I+1/2}\right\}_{\text{SG-FVS}} &= U^+\left((u_k)_I, a_{I+1/2}\right)(\tilde{\rho}_k\tilde{\alpha}_k u_k)_I \\ &+U^-\left((u_k)_{I+1}, a_{I+1/2}\right)(\tilde{\rho}_k\tilde{\alpha}_k u_k)_{I+1}.\end{aligned} \tag{3.103}$$

Comparing Equations 3.98 and 3.103, one can see that the momentum flux of the SG-AUSMV scheme reduces to that of SG-FVS scheme with $\chi = 1$.

3.3.4 New SG-AUSMFVS Scheme

Based on the analysis of SG-AUSM$^+$ and SG-FVS for the phase separation problem (see Subsection 5.5.3), a new scheme here, denoted by SG-AUSMFVS, is proposed. It is a

hybrid approach combining both the staggered SG-AUSM$^+$ and SG-FVS schemes, which is designed to retain the accuracy of SG-AUSM$^+$ and the stability of SG-FVS. The mass fluxes are calculated using Eq. 3.92; whereas, for the momentum flux, the following formula is adopted for the SG-AUSMFVS scheme.

$$\left\{(f_k)^c_{I+1/2}\right\}_{\text{SG-AUSMFVS}} = s\left\{(f_k)^c_{I+1/2}\right\}_{\text{SG-AUSM}^+} + (1-s)\left\{(f_k)^c_{I+1/2}\right\}_{\text{SG-FVS}}, \tag{3.104}$$

where s is a weighting function that determines the choice between SG-AUSM$^+$ and SG-FVS schemes. Following Evje and Flåtten's work for the SG-AUSMDV scheme [9], Eqs. 3.101 and 3.102 are used to calculate s for the proposed SG-AUSMFVS scheme.

3.4 Discretization of Source Terms

3.4.1 Discretization of Source Terms on Collocated Grids

The way of discretization of source terms is given by Eq. 3.105. For the generic flow model, the differential source term is discretized using central difference scheme [19].

$$\boldsymbol{Q}_i^{nv} = \begin{pmatrix} 0 \\ 0 \\ p_i^{\text{int}}(\alpha_{g,i+1} - \alpha_{g,i-1})/(2\Delta x) \\ p_i^{\text{int}}(\alpha_{l,i+1} - \alpha_{l,i-1})/(2\Delta x) \end{pmatrix}. \tag{3.105}$$

3.4.2 Discretization of Source Terms on Staggered Grids

Based on staggered grids, the discretization of the non-conservative interfacial terms can be readily obtained with the following expression:

$$\left(\tilde{p}^{int}\frac{\partial \alpha_k}{\partial x}\right)_I^{n+1} = \left(\tilde{p}^{int}\right)^{n+1} \cdot \left(\frac{\alpha_{i+1} - \alpha_i}{\Delta x}\right)^{n+1}. \tag{3.106}$$

In the following part, this work make the first attempt to prove that with Eq. 3.106, the SG-AUSM$^+$ scheme obeys Abgrall's principle. Abgrall's principle states that *a two-phase flow, uniform in pressure and velocity, must remain uniform in the same variables during its time evolution.* [73]. In other words, if the initial flow condition is

$$u_g = u_l = u^{int} = \text{const}, \quad p = p^{int} = \text{const}, \tag{3.107}$$

the velocity and pressure will remain the same.

According to Eqs. 3.87 and 3.92, the mass equation can be given as

$$(\alpha_k\rho_k)_i^{n+1} - (\alpha_k\rho_k)_i^n - \frac{\Delta t}{\Delta x}\left[(u_k)_I(\rho_k\alpha_k)_{i/i+1} - (u_k)_I(\rho_k\alpha_k)_{i-1/i})\right] = 0. \tag{3.108}$$

For a two-phase flow with uniform velocity, Eq. 3.108 can be rewritten as

$$(\alpha_k\rho_k)_i^{n+1} - (\alpha_k\rho_k)_i^n - u\frac{\Delta t}{\Delta x}\left[(\rho_k\alpha_k)_{i/i+1} - (\rho_k\alpha_k)_{i-1/i})\right] = 0 \tag{3.109}$$

or

$$(\alpha_k\rho_k)_{i+1}^{n+1} - (\alpha_k\rho_k)_{i+1}^n - u\frac{\Delta t}{\Delta x}\left[(\rho_k\alpha_k)_{i+1/i+2} - (\rho_k\alpha_k)_{i/i+1})\right] = 0. \tag{3.110}$$

Adding Eqs. 3.109 and 3.110 gives

$$(\tilde{\alpha}_k\tilde{\rho}_k)_I^{n+1} - (\tilde{\alpha}_k\tilde{\rho}_k)_I^n - u\frac{\Delta t}{\Delta x}\left[(\tilde{\alpha}_k\tilde{\rho}_k)_{I/I+1} - (\tilde{\alpha}_k\tilde{\rho}_k)_{I-1/I})\right] = 0, \tag{3.111}$$

where

$$\begin{aligned} (\tilde{p})_I &= \tfrac{1}{2}[p_i + p_{i+1}] \\ (\tilde{\alpha}_k)_I &= \tfrac{1}{2}[(\alpha_k)_i + (\alpha_k)_{i+1}]. \end{aligned} \tag{3.112}$$

From Eqs. 3.110 and 3.111, the following derivation is performed based on Tait's EOS,

which is barotropic:

$$\begin{aligned}(\tilde{\rho}_k)_I(\tilde{\alpha}_k)_I &= \tfrac{1}{4}\left[(\rho_k)_i + (\rho_k)_{i+1}\right]\left[(\alpha_k)_i + (\alpha_k)_{i+1}\right] \\ &= \tfrac{1}{4}\left[(\alpha_k\rho_k)_i + (\alpha_k\rho_k)_{i+1} + (\rho_k)_i(\alpha_k)_{i+1} + (\rho_k)_{i+1}(\alpha_k)\right] \\ &= \tfrac{1}{4}\left[2(\alpha_k\rho_k)_i + 2(\alpha_k\rho_k)_{i+1}\right] \\ &= \tfrac{1}{2}\left[(\alpha_k\rho_k)_i + (\alpha_k\rho_k)_{i+1}\right].\end{aligned} \tag{3.113}$$

Neglecting the non-differential source terms, Eq. 3.88 can be written as

$$\begin{aligned}&(\tilde{\alpha}_k\tilde{\rho}_k u_k)_I^{n+1} - (\tilde{\alpha}_k\tilde{\rho}_k u_k)_I^n + \tfrac{\Delta t}{\Delta x}\left[(f_k)_{I+1/2}^{n+1} - (f_k)_{I-1/2}^{n+1}\right] \\ &-\Delta t(\tilde{p}^{int})_I^{n+1}\tfrac{\left[(\alpha_k)_{i+1}^{n+1} - (\alpha_k)_i^{n+1})\right]}{\Delta x} = 0.\end{aligned} \tag{3.114}$$

Substituting $(f_k)_{I+1/2} = (f_k^c + \alpha_k p)_{I+1/2}$ into Eq. 3.114 gives

$$\begin{aligned}&(\tilde{\alpha}_k\tilde{\rho}_k u_k)_I^{n+1} - (\tilde{\alpha}_k\tilde{\rho}_k u_k)_I^n + \tfrac{\Delta t}{\Delta x}\left[(f_k^c)_{I+1/2} - (f_k^c)_{I-1/2})\right] \\ &+\tfrac{\Delta t}{\Delta x}\left[(\alpha_k p)_{i+1} - (\alpha_k p)_i\right] - \Delta t(\tilde{p}^{int})_I^{n+1}\tfrac{\left[(\alpha_k)_{i+1}^{n+1} - (\alpha_k)_i^{n+1})\right]}{\Delta x} = 0.\end{aligned} \tag{3.115}$$

For uniform pressure and velocity, the last two terms on the left-hand side of Eq. 3.115 cancel each other out. Therefore, Eq. 3.115 can be simplified into the following equation:

$$\begin{aligned}&(\tilde{\alpha}_k\tilde{\rho}_k u_k)_I^{n+1} - (\tilde{\alpha}_k\tilde{\rho}_k u_k)_I^n + \tfrac{\Delta t}{\Delta x}\left[(f_k^c)_{I+1/2} - (f_k^c)_{I-1/2})\right] \\ &= u(\tilde{\alpha}_k\tilde{\rho}_k)_I^{n+1} - u(\tilde{\alpha}_k\tilde{\rho}_k)_I^n + u\tfrac{\Delta t}{\Delta x}\left[(\tilde{\alpha}_k\tilde{\rho}_k u)_{I/I+1} - (\tilde{\alpha}_k\tilde{\rho}_k u)_{I-1/I}\right].\end{aligned} \tag{3.116}$$

Consequently, it can be concluded that the SG-AUSM$^+$ scheme satisfies Abgralls principle.

3.5 High-Spatial-Order Extension

The MUSCL scheme, which stands for Monotonic Upstream-Centered Scheme for Conservation Laws, was first developed by van Leer [12] [12] [8]. It is a finite volume method that can provide high-order numerical accuracy for a system while preserve the monotonicity. Its basic idea is to obtain high-order accuracy through data reconstruction. Before

introducing the MUSCL approach, it is necessary to illustrate the TVD concept and TVD scheme.

3.5.1 TVD Scheme

The total variation diminishing (TVD) concept was first proposed by Harten [31]. For a discretized function $\{u_j\}$, the total variation is defined as [74]

$$TV = \sum_j |u_{j+1} - u_j|. \tag{3.117}$$

A numerical method is said to be TVD if it does not increase the total variation of solutions, i.e.,

$$TV\left(u^{n+1}\right) \leq TV\left(u^n\right). \tag{3.118}$$

Consider the following linear scalar equation:

$$\frac{\partial u}{\partial t} + \frac{\partial f}{\partial x} = 0. \tag{3.119}$$

Suppose the descritized equation of Eq. 3.119 can be written in the following form:

$$u_i^{n+1} = u_i^n - C_{i-1/2}^- \Delta u_{i-1/2} + C_{i+1/2}^+ \Delta u_{i+1/2}, \tag{3.120}$$

where $\Delta u_{i+1/2} = u_i^{n+1} - u_i^n$; $C_{i+1/2}^{\pm}$ are coefficients in relation to Δx, Δt, u_i^n, and $u_{\pm}^n$.

Harten [31] first proposed the following positivity condition.

$$C_{i+1/2}^- \geq 0, \;\; C_{i+1/2}^+ \geq 0, \;\; 0 \leq C_{i+1/2}^- +; C_{i+1/2}^+ \leq 1. \tag{3.121}$$

Equation 3.121 is often called a TVD condition. According to the positive condition, a TVD scheme can be constructed with high-order accuracy. The construction method is

illustrated as follows:

First, suppose the discretized equation of Eq. 3.119 is written in the following form:

$$u_i^{n+1} = u_i^n + \frac{\Delta t}{\Delta x}\left[f_{i-1/2} - f_{i+1/2}\right]. \tag{3.122}$$

Denote the numerical flux that satisfies the TVD property to be $f_{i+1/2}^{\text{TVD}}$. If the constructed scheme is of high-order accuracy, $f_{i+1/2}^{\text{TVD}}$ can be written in the following form:

$$f_{i+1/2}^{\text{TVD}} = f_{i+1/2}^{\text{LOW}} + \phi_{i+1/2}\left(f_{i+1/2}^{\text{HIGH}} - f_{i+1/2}^{\text{LOW}}\right), \tag{3.123}$$

where $f_{i+1/2}^{\text{LOW}}$ is certain numerical flux with first-order accuracy in smooth regions, whereas $f_{i+1/2}^{\text{HIGH}}$ is the flux with second-order accuracy in smooth regions; $\phi_{i+1/2}$ is called a flux limiter, which is designed to ensure the schemes have second-order accuracy in smooth regions. In other words, the basic idea of constructing a TVD scheme is to modify some higher-accuracy schemes, such as Lax-Wendroff scheme, using the flux limiter.

Here four kinds of limiters are listed: the Superbee limiter, Minmod limiter, van Leers MUSCL limiter, and Symmetric Minmod limiter, whose definitions can be given as:

- Superbee limiter:
$$\phi(r) = \max[0, \min(2r, 1), \min(r, 2)]. \tag{3.124}$$

- Minmod limiter:
$$\phi(r) = \min \ \ \text{mod}(1, r) = \max[0, \min(r, 1)]. \tag{3.125}$$

- van Leers MUSCL limiter:
$$\phi(r) = \max\{0, \min[2, 2r, 0.5(1 + r)]\}. \tag{3.126}$$

- Symmetric Minmod limiter:
$$\phi(r) = \min(1, |r|). \tag{3.127}$$

- Symmetric van Albada limiter:

$$\phi(r) = \left(r^2 + r\right) / \left(r^2 + 1\right). \tag{3.128}$$

r is ratio of solution differences or ratio of flux differences.

Consider the linear conservative law where $f = au$, and a is a constant. When using three stencils, $f_{i+1/2}^{\text{LOW}}$ and $f_{i+1/2}^{\text{HIGH}}$ can be written in the following form:

$$\begin{aligned} f_{i+1/2}^{\text{LOW}} &= \alpha_0 a u_i^n + \alpha_1 a u_{i+1}^n \\ f_{i+1/2}^{\text{HIGH}} &= \beta_0 a u_i^n + \beta_1 a u_{i+1}^n. \end{aligned} \tag{3.129}$$

Note that many choices are available for $f_{i+1/2}^{\text{LOW}}$ and $f_{i+1/2}^{\text{HIGH}}$. For example, if the first-order upwind scheme is chosen to be $f_{i+1/2}^{\text{LOW}}$, and the Lax-Friedrichs scheme to be $f_{i+1/2}^{\text{HIGH}}$, the following relationships can be obtained.

$$\begin{aligned} \alpha_0 &= \tfrac{1}{2}(1+s), \alpha_1 = \tfrac{1}{2}(1-s) \\ \beta_0 &= \tfrac{1}{2}(1+\lambda), \beta_1 = \tfrac{1}{2}(1-\lambda), \end{aligned} \tag{3.130}$$

where $s = \text{sgn}(a)$ and $\lambda = \frac{a\Delta t}{\Delta x}$.

3.5.2 MUSCL Interpolation

Again, consider the scalar linear conservation law, which is given by Eq. 3.119. For convenience, Eq. 3.119 is repeated as follows:

$$\begin{aligned} &\tfrac{\partial u}{\partial t} + \tfrac{\partial f}{\partial x} = 0 \\ &f = au, \end{aligned} \tag{3.131}$$

where a is a constant.

Assuming the initial values of the Riemann problem at the interface $i + 1/2$, namely, u_L and u_R, are prescribed, the solutions of the Riemann problem are given as follows:

$$u(x/t) = \begin{cases} u_L, & \text{if } (x/t) \geq a \\ u_R, & \text{otherwise,} \end{cases} \tag{3.132}$$

where u_L and u_R denote u at the left-hand-side and right-hand-side of the interface of the control volume.

Therefore, if the numerical fluxes $f_{i+1/2}^{\text{TVD}}$ is given by

$$\begin{aligned} f_{i+1/2}^{\text{TVD}} = &\left[\alpha_0 + (\beta_0 - \alpha_0)\,\phi_{i+1/2}\right](au_i^n) \\ &+ \left[\alpha_1 + (\beta_1 - \alpha_1)\,\phi_{i+1/2}\right]\left(au_{i+1}^n\right) \end{aligned}, \tag{3.133}$$

the corresponding initial values of the Riemann problem can be written as follows:

$$\begin{aligned} u_L &= u_i^n + \tfrac{1}{2}\phi_{i+1/2}\left(\tfrac{u_i^n - u_{i-1}^n}{u_{i+1}^n - u_i^n}\right)\left(u_{i+1}^n - u_i^n\right) \\ u_R &= u_{i+1}^n - \tfrac{1}{2}\phi_{i+1/2}\left(\tfrac{u_{i+2}^n - u_{i+1}^n}{u_{i+1}^n - u_i^n}\right)\left(u_{i+1}^n - u_i^n\right). \end{aligned} \tag{3.134}$$

The above-mentioned approach can be directly extended onto non-linear conservative systems.

3.6 Decoding and Updating of Variables for Explicit Schemes

Once the conservative variables $\boldsymbol{U}$ are obtained, the primitive variables have to be decoded for the explicit schemes. Regarding primitive variables, the following vector of physical variables is considered for the four-equation model:

$$\boldsymbol{w} = (\alpha_g, u_g, u_l, p)^T. \tag{3.135}$$

According to the definition of $\boldsymbol{U}$ in Eq. 2.46, u_g and u_l can be obtained as follows:

$$u_g = \frac{U_3}{U_1}, \tag{3.136}$$

and

$$u_l = \frac{U_4}{U_2}. \tag{3.137}$$

Further, the pressure p satisfies the following equation [19].

$$F(p) = \left[1 - \frac{U_1}{\rho_g(p)}\right] \rho_l(p) - U_2 = 0. \tag{3.138}$$

By re-arranging Eqs. 2.55 and 2.57, one has

$$\rho_g = \rho_g^0 (\frac{p}{p_g^0})^{\frac{1}{\gamma}}, \quad \rho_l = \rho_l^0 \left(\frac{p}{p_l^0} + 1\right)^{\frac{1}{n}}. \tag{3.139}$$

Thus, after the substitution of Eq. 3.139 into Eq. 3.138, p can be solved by Newton's method. Accordingly, ρ_g and ρ_l can be obtained by Eq. 3.139; in turn, the air volume fraction can be achieved by

$$\alpha_g = \frac{U_1}{\rho_g(p)}. \tag{3.140}$$

Chapter 4

Methods for Solving Implicitly Discretized Equations

4.1 Introduction

This chapter presents the methods for solving the implicitly discretized equations introduced in Chapter 3. First, Section 4.2 briefly introduces the basic concept of Newton's method for implicit equations, including Newton's iteration method and the procedure for solving implicit equations. Then, the construction of the numerical Jacobian matrix and of the residual vector is elaborated in Section 4.3, followed by a description of initial and boundary conditions in section 4.4. Finally, Section 4.5 demonstrates the architecture of codes.

4.2 Newton's Method for Implicit Equations

Consider the following equation system,

$$\frac{\partial \boldsymbol{w}}{\partial t} + \frac{\partial \boldsymbol{f}}{\partial x} = 0, \tag{4.1}$$

where $\boldsymbol{w}$ is the variable vector and $\boldsymbol{f}$ is the flux vector, which is a function of the variable vector. Then Eq. 4.1 can be discretized as

$$\boldsymbol{w}_i^{n+1} + \lambda[\boldsymbol{f}_{i+\frac{1}{2}}^{n+1}(\boldsymbol{w}_{i-s}^{n+1}, ..., \boldsymbol{w}_i^{n+1}, ..., \boldsymbol{w}_{i+s}^{n+1}) - \boldsymbol{f}_{i-\frac{1}{2}}^{n+1}(\boldsymbol{w}_{i-s}^{n+1}, ..., \boldsymbol{w}_i^{n+1}, ..., \boldsymbol{w}_{i+s}^{n+1})] = \boldsymbol{w}_i^n, \quad (4.2)$$

where s is a positive constant and $\lambda = \Delta t/\Delta x$.

Newton's iteration method is used to solve Eq. 4.2 to obtain $\boldsymbol{w}_i^{n+1}$.

4.2.1 Newton's Iteration Method

Newton's iteration method is illustrated by Fig. 4.1. Consider the following scalar equation:

$$f(x) = 0. \quad (4.3)$$

Assume the current approximation of the solution is x_m, where m denotes the m^{th} iteration. Thus, the derivative of f at x_m can be given by

$$f^{'}(x_m) = \frac{f(x_m) - 0}{x_m - x_{m+1}} \Leftrightarrow f^{'}(x_m) = \frac{-f(x_m)}{\Delta x}, \quad (4.4)$$

where $\Delta x = x_{m+1} - x_m$ and $f^{'}$ denotes the derivative of the function f. Then x_{m+1}, a better approximation of the exact solution, can be calculated as

$$x_{m+1} = x_m - \frac{f(x_m)}{f^{'}(x_m)}. \quad (4.5)$$

Newton's iteration process can be started off with some arbitrary initial value x_0 and repeated until Δx satisfies an imposed criterion.

4.2.2 Process for Implicit Equations

The process for solving implicit equations mainly consists of an outer time loop and an inner Newton's iteration loop. In other words, Newton's iteration loop is contained in the

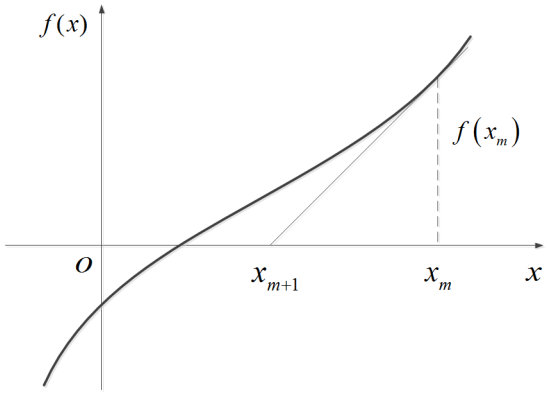

Figure 4.1: Newton iteration

time loop.

According to Eq. 4.2, the implicit discretized governing equations can be expressed in the following form:

$$\boldsymbol{R}(\boldsymbol{w}) = 0, \tag{4.6}$$

where $\boldsymbol{R}$ is the residual vector of the system, which can be rewritten as

$$\boldsymbol{R}(\boldsymbol{w}) = \boldsymbol{w}_i^{n+1} - \lambda\left(\boldsymbol{f}_{i+1/2}^{n+1} - \boldsymbol{f}_{i-1/2}^{n+1}\right) - \boldsymbol{w}_i^{n}. \tag{4.7}$$

Newton's iteration loop: get the solution $\boldsymbol{w}_i^{n+1}$ for Eq. 4.2

To solve $\boldsymbol{w}_i^{n+1}$ in Eq. 4.2, an initial value $(\boldsymbol{w}_i)_0^n$ at the n^{th} time step level is assumed. Similar to the solving procedure for Eq. 4.4, the following equation are solved to get the difference $\Delta\left(\boldsymbol{w}^m\right)$

$$\left(\frac{\partial \boldsymbol{R}_j}{\partial \boldsymbol{w}_i}\right)^m = \frac{-\boldsymbol{R}_j(\boldsymbol{w}^m)}{\Delta \boldsymbol{w}^m}, \tag{4.8}$$

where $\left(\frac{\partial \boldsymbol{R}_j}{\partial \boldsymbol{w}_i}\right)^m$ is the Jacobian matrix. Here the numerical Jacobian calculation will be used for the derivative term [75]:

$$\left(\frac{\partial \boldsymbol{R}_j}{\partial \boldsymbol{w}_i}\right)^m = \frac{\boldsymbol{R}_j(\boldsymbol{w}^m + \epsilon_i \boldsymbol{e}_i) - \boldsymbol{R}_j(\boldsymbol{w}^m)}{\epsilon_i}, \tag{4.9}$$

where $\boldsymbol{e}_i$ is a unit vector consisting of $4 \times N$ components for a four-equation system or of $6 \times N$ components for a six-equation system. N is the total number of nodes. In $\boldsymbol{e}_i$, only the i^{th} component equals one, and all other components are zero. ϵ_i symbolizes the perturbation value in the $\boldsymbol{e}_i$ direction and is specified for each case. $\boldsymbol{R}_j$ symbolizes the j^{th} residual function, and j varies from 1 to $4 \times N$ for four-equation system or to $6 \times N$ for six-equation system.

Once the Jacobian matrix is calculated, the increment $\Delta \boldsymbol{w}$ at the m^{th} iteration can be obtained through Eq. 4.8. In the present work, the UMFPACK (unsymmetric-pattern multifrontal package) sparse matrix solver package [76] is applied to solve the system. This solver is based on the unsymmetric-pattern multifrontal method.

Accordingly, the variable vector $\boldsymbol{w}$ at the $(m+1)^{th}$ iteration is given by

$$(\boldsymbol{w}_i)^{m+1} = (\boldsymbol{w}_i)^m + (\Delta \boldsymbol{w}_i)^m. \tag{4.10}$$

$\boldsymbol{w}^{m+1}$ is the solution of Eq. 4.6 when the l_2-norm of $\Delta \boldsymbol{w}^m$ satisfies the following criteria:

$$\|\Delta \boldsymbol{w}^m\| < \varepsilon, \tag{4.11}$$

where ε is the tolerance.

Time loop: solve values for the next time step

To get the values at the next time step, it is needed to replace $\boldsymbol{w}_i^{n+1}$ for $\boldsymbol{w}_i^n$ in Eq. 4.2, and then give an initial value for $\boldsymbol{w}_i^{n+1}$ to repeat the above-mentioned process.

4.3 Numerical Jacobian Matrix and Residual Vector Calculations

In this section, the four-equation model is considered. The elemental Jacobian matrix is the sub-matrix that corresponds to a node or a link, which can be written in the following form:

$$\begin{bmatrix} \cdots\cdots\cdots\cdots \\ \cdots \quad [\boldsymbol{J}]_i \quad \cdots \\ \cdots\cdots\cdots\cdots \end{bmatrix}, \tag{4.12}$$

where

$$[\boldsymbol{J}]_i = \begin{bmatrix} \frac{\partial R_1}{\partial w_1} & \frac{\partial R_1}{\partial w_2} & \frac{\partial R_1}{\partial w_3} & \frac{\partial R_1}{\partial w_4} \\ \frac{\partial R_2}{\partial w_1} & \frac{\partial R_2}{\partial w_2} & \frac{\partial R_2}{\partial w_3} & \frac{\partial R_2}{\partial w_4} \\ \frac{\partial R_3}{\partial w_1} & \frac{\partial R_3}{\partial w_2} & \frac{\partial R_3}{\partial w_3} & \frac{\partial R_3}{\partial w_4} \\ \frac{\partial R_4}{\partial w_1} & \frac{\partial R_4}{\partial w_2} & \frac{\partial R_4}{\partial w_3} & \frac{\partial R_4}{\partial w_4} \end{bmatrix}_i. \tag{4.13}$$

w_1, w_2, w_3 and w_4 represent α_g, p, u_g and u_l, respectively; R_1 represents the gas phase and R_2 the liquid phase of the mass conservation, R_3 represents the gas phase and R_4 the liquid phase of the energy conservation. $R1 - R4$ for collocated grids and staggered grids are given as follows.

- Collocated Grids:

  Gas mass residual function:

$$R_{1,i} = (\alpha_g \rho_g)_i^{n+1} - (\alpha_g \rho_g)_i^n - \frac{\Delta t}{\Delta x}\left[(\alpha_g \rho_g u_g)_{i+1/2}^{n+1} - (\alpha_g \rho_g u_g)_{i-1/2}^{n+1})\right]. \tag{4.14}$$

  Liquid mass residual function:

$$R_{2,i} = (\alpha_l \rho_l)_i^{n+1} - (\alpha_l \rho_l)_i^n - \frac{\Delta t}{\Delta x}\left[(\alpha_l \rho_l u_l)_{i+1/2}^{n+1} - (\alpha_l \rho_l u_l)_{i-1/2}^{n+1})\right]. \tag{4.15}$$

Gas momentum residual function:

$$R_{3,i} = (\alpha_g \rho_g u_g)_i^{n+1} - (\alpha_g \rho_g u_g)_i^n - \frac{\Delta t}{\Delta x}\left[(\alpha_g \rho_g u_g^2)_{i+1/2}^{n+1} - (\alpha_g \rho_g u_g^2)_{i-1/2}^{n+1})\right] \\ -\Delta t (p^{\text{int}})_i^{n+1} \frac{\left[(\alpha_g)_{i+1}^{n+1} - (\alpha_g)_i^{n+1})\right]}{\Delta x} - \Delta t (\alpha_g \rho_g g)_i^{n+1}. \tag{4.16}$$

Liquid momentum residual function:

$$R_{4,i} = (\alpha_l \rho_l u_l)_i^{n+1} - (\alpha_l \rho_l u_l)_i^n - \frac{\Delta t}{\Delta x}\left[(\alpha_l \rho_l u_l^2)_{i+1/2}^{n+1} - (\alpha_l \rho_l u_l^2)_{i-1/2}^{n+1})\right] \\ -\Delta t (p_{int})_i^{n+1} \frac{\left[(\alpha_l)_{i+1}^{n+1} - (\alpha_l)_i^{n+1})\right]}{\Delta x} - \Delta t (\alpha_l \rho_l g)_i^{n+1}. \tag{4.17}$$

- Staggered Grids

  Gas mass residual function:

$$R_{1,i} = (\alpha_g \rho_g)_i^{n+1} - (\alpha_g \rho_g)_i^n - \frac{\Delta t}{\Delta x}\left[(f_g)_{i+1/2}^{n+1} - (f_g)_{i-1/2}^{n+1})\right]. \tag{4.18}$$

  Liquid mass residual function

$$R_{2,i} = (\alpha_l \rho_l)_i^{n+1} - (\alpha_l \rho_l)_i^n - \frac{\Delta t}{\Delta x}\left[(f_l)_{i+1/2}^{n+1} - (f_l)_{i-1/2}^{n+1})\right]. \tag{4.19}$$

  Gas momentum residual equation:

$$R_{3,I} = (\tilde{\alpha}_g \tilde{\rho}_g u_g)_I^{n+1} - (\tilde{\alpha}_g \tilde{\rho}_g u_g)_I^n - \frac{\Delta t}{\Delta x}\left[(f_g)_{I+1/2}^{n+1} - (f_g)_{I-1/2}^{n+1})\right] \\ -(\tilde{p}_{int})_I^{n+1} \frac{\left[(\alpha_g)_{i+1}^{n+1} - (\alpha_g)_i^{n+1})\right]}{\Delta x} - (\tilde{\alpha}_g \tilde{\rho}_g g)_I^{n+1}. \tag{4.20}$$

  Liquid momentum residual equation:

$$R_{4,I} = (\tilde{\alpha}_l \tilde{\rho}_l u_l)_I^{n+1} - (\tilde{\alpha}_l \tilde{\rho}_l u_l)_I^n - \frac{\Delta t}{\Delta x}\left[(f_l)_{I+1/2}^{n+1} - (f_l)_{I-1/2}^{n+1})\right] \\ -(\tilde{p}_{int})_I^{n+1} \frac{\left[(\alpha_l)_{i+1}^{n+1} - (\alpha_l)_i^{n+1})\right]}{\Delta x} - (\tilde{\alpha}_l \tilde{\rho}_l g)_I^{n+1}. \tag{4.21}$$

4.4 Initial and Boundary Conditions

Before the time loop starts, initial conditions should be provided as follows.

$$\boldsymbol{w}_0 = (\alpha_{g0}, u_{g0}, u_{l0}, p_0). \tag{4.22}$$

In addition, in a time step, an initial guess should be given before each Newton's iteration loop. The following initial guess value is implemented.

$$(\boldsymbol{w})_0^{n+1} = \boldsymbol{w}^n. \tag{4.23}$$

In the code, the boundary conditions are treated as follows: the variables at the boundaries are not solved but updated to the imposed physical values at every iteration [77]; whereas, the variables on the in-between nodes are calculated by constructing a Jacobian matrix and then solved by Newton's iteration method.

4.5 Code Architecture

Figure 4.2 demonstrates the code architecture based on the methods for solving implicitly discretized equations in Sections 4.2 to 4.4.

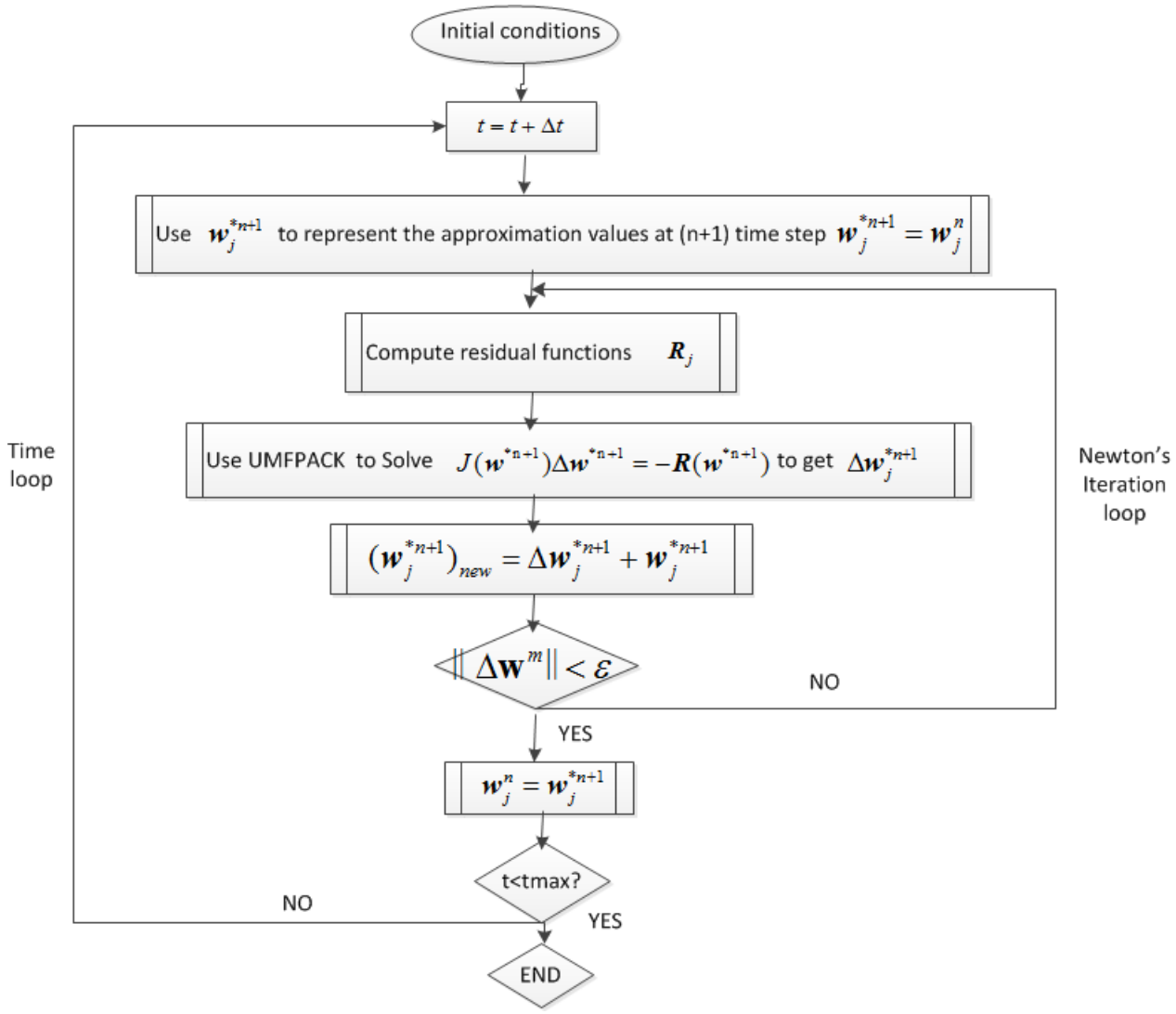

Figure 4.2: Flow chart of in-house code with an implicit time integration method.

Chapter 5

Results and Discussions

5.1 Introduction

This chapter demonstrates the behavior of AUSM-family and SG-AUSM-family schemes with both explicit and implicit time integration on several benchmark test cases. To start, in Section 5.2, a description of the test cases is given, including Ransom's water faucet problem, the oscillating manometer problem, the phase separation problem, and the air-water shock tube problems. Regarding the air-water shock tube problems, three cases, including Toumi's shock tube, Cortes' shock tube, and Ejve's shock tube problems have been studied. Then, in Section 5.3, insight into AUSM-family schemes' dissipation mechanism is gained by comparing various collocated-grid-based AUSM-family schemes with explicit time integration on Ransom's water faucet and Toumi's shock tube problems. After that, in Section 5.4, the accuracy and efficiency between implicit and explicit AUSM-family schemes on collocated grids are compared. Results show that compared to the explicit counterparts, the implicit AUSM-family schemes are capable of increasing computational efficiency with acceptable numerical accuracy. Following this, in Section 5.5, the implicit SG-AUSM-family schemes are proposed, and their advantages are demonstrated in terms of accuracy, stability, and computational efficiency over their collocated-grid-based counterparts. Specifically, the new scheme, the SG-AUSMFVS scheme, originally designed to

solve the phase separation problem, demonstrates distinguished feature in terms of accuracy and stability in solving other aforementioned benchmark test cases. Next, in Section 5.6, the above-mentioned implicit SG-AUSM-family schemes with first-order spatial accuracy are extended to second-order spatial accuracy. Finally, in Section 5.7, the TVD limiter is implemented in CATHENA4 and the numerical accuracy of CATHENA4 is improved.

5.2 Description of Test Cases

One of the objectives of this work is to propose numerical schemes to improve the accuracy and efficiency of modeling all-Mach-number two-phase flows. The typical physical phenomena of two phase flows include interface contact discontinuities, two-phase shocks, phase appearance and disappearance, and phase change.

The water faucet problem [50] is a useful benchmark for testing numerical schemes in tracking void fraction waves. Also, the oscillating manometer problem [50] is a classical case to test the capability of numerical schemes for simulating the oscillating motion of a liquid-gas interface. In addition, the phase separation problem, proposed by Coquel [17], serves as a stiff and yet, useful benchmark for testing numerical schemes for simulating problems with phase appearance and disappearance. This test case demonstrates the transition from two-phase to single-phase flow under the gravitational force. Furthermore, the two-phase shock tube problems are good benchmarks to test a numerical scheme's ability of predicting flows whose initial conditions are far from an equilibrium state.

Therefore, Ransom's water faucet, oscillating manometer, phase separation, and two-phase shock tube problems are selected in this thesis to test the numerical schemes. The Mach number of these benchmark test cases can be as low as on the order of 10^{-3} or even 10^{-4}. The test of the proposed numerical schemes for the phase change problem will be performed as part of the future work since this problem requires solving energy equations or including heat and mass transfer.

5.2.1 Ransom's Water Faucet Problem

Ransom's water faucet problem describes the acceleration of water due to gravity. As shown in Fig. 5.1, initially, the vertical tube at a length of 12 m is uniformly filled with air-water mixture moving at a constant speed of 10 m/s; then, due to the gravity effect, the water jet accelerates and is narrowed with time to satisfy the mass conservation; during this process, the void fraction moves toward the exit; finally, until the void wave is convected out of the system, a steady state is achieved.

The initial states are given by

$$(\alpha_g, u_g, u_l, p) = (0.2, 0 \text{ m/s}, 10 \text{ m/s}, 10^5 \text{ Pa}). \tag{5.1}$$

The inlet boundary condition is set to be the same as Eq. 5.1, except for the pressure, which is extrapolated from its solution at the adjacent interior node. On the contrary, for the outlet boundary condition, the pressure is imposed to be 10^5 Pa and the other variables are extrapolated from their solutions within the computational domain. A grid of 101 nodes is employed unless otherwise stated. Following Paillère et al. [19], the interfacial drag τ_{ki} is not included, and the constant σ in the interfacial pressure term (see Eq 2.45) is set to be 2.0 to ensure hyperbolicity of the two-fluid model.

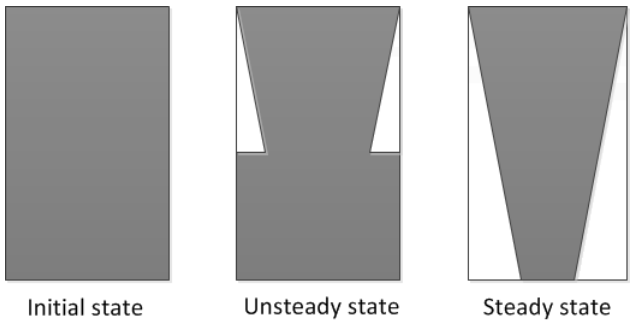

Figure 5.1: Illustrations of the water faucet problem.

The approximate analytical solutions for the void fraction are given in Eq. 5.2 below [50]. They are derived under the assumption that water is incompressible and the pressure

variation is ignored.

$$\alpha(x,t) = \begin{cases} 1 - \frac{(1-\alpha_0)(u_l)_0}{\sqrt{(u_l)_0^2+2gx}} & \text{if } x < 0.5gt^2 + (u_l)_0 t \\ 0.2 & \text{otherwise,} \end{cases} \tag{5.2}$$

where $\alpha_0 = 0.2$, $(u_l)_0 = 10$ m/s, and $g = 9.81$ m/s^2. The CATHENA4 nodalization for this problem consisted of a horizontal branch.

5.2.2 Oscillating Manometer Problem

In this case, a U-shaped tube of an overall length of 20 m is considered. Initially, the "U" tube manometer is filled with gas and water of uniform velocity of 2.1 m/s; the length of the tube filled with water is 10 m, and the water in the two legs is at the same level, as shown in Fig. 5.2. With these initial conditions, one can determine the hydrostatic pressure profile of the system. In addition, the water column will oscillate under the action of gravity. Therefore, the benchmark serves to test the ability of numerical schemes of preserving system mass to simulate the oscillations of the liquid-gas interface.

For simplicity, the origin of the coordinate is set at the top left end, and the body-fitted curvilinear coordinate is employed. Therefore, in terms of the x-coordinate, the gravity acceleration varies by a periodic function which is defined by Eq. 5.3.

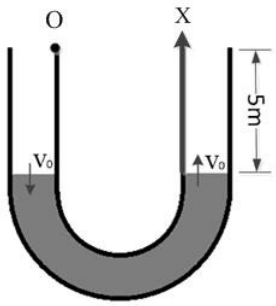

Figure 5.2: Illustration of the oscillating manometer problem.

$$g(x) = \begin{cases} g, & (0 \leq x \leq 5 \text{ m}) \\ g\cos\left(\frac{(x-5)}{10}\pi\right), & (5 \text{ m} < x \leq 15 \text{ m}) \\ -g, & (15 \text{ m} < x < 20 \text{ m}), \end{cases} \tag{5.3}$$

where $g = 9.8$ m/s^2. Accordingly, the hydrostatic head experiences sinusoidal variation in the U-shaped part as described by the following equation:

$$p(x) = \left(10^5 + \rho_l^0 g \frac{10}{\pi} \sin\left(\frac{\pi(x-5)}{10}\right)\right) \text{Pa}, \quad (5 \text{ m} < x \leq 15 \text{ m}), \tag{5.4}$$

where $\rho_l^0 = 10^3$ kg/m^3.

Following the work of Paillère [19], the initial conditions are given by

$$(\alpha_{g0},\ u_{g0},\ u_{l0},\ p_0) = \begin{cases} (0.999,\ 2.1 \text{ m/s},\ 2.1 \text{ m/s},\ 10^5 \text{ Pa}), & (0 \leq x \leq 5 \text{ m}) \\ (0.001,\ 2.1 \text{ m/s},\ 2.1 \text{ m/s},\ p(x) \text{ Pa}), & (5 \text{ m} < x \leq 15 \text{ m}) \\ (0.999,\ 2.1 \text{ m/s},\ 2.1 \text{ m/s},\ 10^5 \text{ Pa}), & (15 \text{ m} < x < 20 \text{ m}). \end{cases} \tag{5.5}$$

For the boundary conditions, both ends of the manometer are open to the atmosphere, leading to $p = 10^5$ Pa at both ends. All variables except for the pressure are extrapolated from their solutions within the solution domain [19]. Assuming that the water column oscillates with a uniform velocity due to the influence of gravity, one can obtain the following approximate analytical solution for the liquid velocity at the bottom of the tube [19, 9].

$$u_l(t) = (u_l)_0 \cos(\omega t), \tag{5.6}$$

where $(u_l)_0 = 2.1$ m/s, $\omega = \sqrt{2g/L}$ and L is the length of the water column, 10 m.

In this test case, a grid of 101 nodes with a time step of $\frac{\Delta x}{2000 \text{ m/s}}$ is employed unless otherwise stated; the friction coefficient C_f in the interfacial drag expression (see Eq. 2.54) is set to be 5×10^4 (s^{-1}). No pressure correction term is included in Eq. 2.45. Note that when using a collocated-grid arrangement for the oscillating manometer problem, addi-

tional models for phase appearance and disappearance are required to enhance numerical stability [19, 22, 54, 5]. Referring to [19] [22] and [54], to enhance stability, the disappearing phase is blended with the remaining phase, thereby giving

$$u_d = G(\alpha_d)u_d + (1 - G(\alpha_d))u_r, \tag{5.7}$$

where the subscripts d and r stand for disappearing and remaining phases, respectively; G is a positive function satisfying $G(0) = G'(0) = 0$ and $G(1) = G'(1) = 0$. Here G is given by

$$G(\alpha_d) = 0.5 + 0.5 \tanh\left(\frac{\alpha_d - a}{b}\right), \tag{5.8}$$

where $a = 0.5$ and $b = 0.0001$.

Nevertheless, when using a staggered-grid arrangement, there is no need to add additional models for the phase appearance and disappearance, but only set the volume fraction in the following range of $[\alpha_{\min}, \alpha_{\max}]$:

$$\alpha_k^{n+1} = \begin{cases} \alpha_{\max} & \text{if } \alpha_k^{n+1} > \alpha_{\max} \\ \alpha_{\min} & \text{if } \alpha_k^{n+1} < \alpha_{\min}, \end{cases} \tag{5.9}$$

where $\alpha_{\min} = 10^{-5}$ and $\alpha_{\max} = 0.9999$ in this test case. For this problem, the CATHENA4 nodalization consisted of two vertical branches, which are connected at the bottom with a link.

5.2.3 Phase Separation Problem

As shown in Fig. 5.3, at the initial state, the vertical tube is uniformly filled with an air-water mixture with void fraction of 0.5 at 1 bar pressure. Due to the gravity effect, the homogeneous mixture of air and water starts to separate, with air rising and water falling down; until the two phases are fully separated, a steady state is reached.

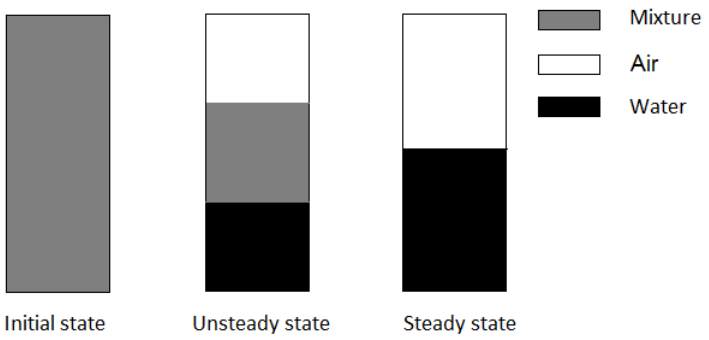

Figure 5.3: Illustrations of the phase separation problem.

In this test case, the length of the tube is set to be 7.5 m. The origin of the Cartesian coordinate is set at the top end of the tube and its direction is straight downward. The initial conditions are given by

$$(\alpha_g, u_g, u_l, p) = (0.5, 0 \text{ m/s}, 0 \text{ m/s}, 10^5 \text{ Pa}). \tag{5.10}$$

At the inlet and outlet boundaries, both the air and water velocities are forced to be 0, and the remaining primitive variables are extrapolated from their solutions at the interior nodes. The simulations were performed on a staggered grid of 101 nodes with a numerical time step set to be $\Delta t = \frac{\Delta x(\text{m})}{3000(\text{m/s})}$, unless otherwise stated. The constant σ in the interfacial pressure term (see Eq. 2.45) is set to be 1.2, unless otherwise mentioned.

The approximate analytical solutions for the void fraction and the liquid velocity are given as follows [9]:

$$\alpha_g(x,t) = \begin{cases} 1.0 & \text{if } x < \frac{1}{2}gt^2 \\ 0.5 & \text{if } \frac{1}{2}gt^2 \le x \le L - \frac{1}{2}gt^2 \\ 0.0 & \text{if } x > L - \frac{1}{2}gt^2 \end{cases} \tag{5.11}$$

and

$$u_l(x,t) = \begin{cases} \sqrt{2gx} & \text{if } x < \frac{1}{2}gt^2 \\ gt & \text{if } \frac{1}{2}gt^2 \leq x \leq L - \frac{1}{2}gt^2 \\ 0 & \text{if } x > L - \frac{1}{2}gt^2, \end{cases} \tag{5.12}$$

where L is the pipe length. It is expected that full separation will be achieved and steady state reached after $t = \sqrt{L/g} = 0.87$ s [9].

5.2.4 Air-water Shock Tube Problem

Three air-water shock tube problems are studied, including Toumi's, Cortes', and Ejve's shock tube problems. Initially, these problems can be regarded as two uniform flows of different properties separated by a diaphragm. As the diaphragm is removed, the mathematical solutions of the flow consist of five constant states that are separated by shocks or expansion waves [78]. In addition, since the sound speed in water than is much higher than that in air, the shock speed or expansion wave speed in water is much higher than those in air [22] [32]. In other words, in the x-t diagram, the slope of shock or expansion wave in water is deeper than that in air.

Since there is no analytical solutions for these test cases, the explicit PD-AUSM$^+$ scheme with $M_0 = 0.2$ on a collocated grid with 10001 nodes with a time step of $\frac{\Delta x}{2400 \text{ m/s}}$ is employed to generate the reference solutions [5]. "P-D" denotes the pressure diffusion (in the mass flux of the liquid phase).

Toumi's shock tube problem

In Toumi's shock tube problem [51], the length of the tube is 100 m, with a diaphragm at $x = 50$ m. The left and right states are defined as follows [51]:

$$\begin{bmatrix} \alpha_g \\ u_g \\ u_l \\ p \end{bmatrix}_L = \begin{bmatrix} 0.25 \\ 0 \text{ m/s} \\ 0 \text{ m/s} \\ 2 \times 10^7 \text{ Pa} \end{bmatrix}, \quad \begin{bmatrix} \alpha_g \\ u_g \\ u_l \\ p \end{bmatrix}_R = \begin{bmatrix} 0.10 \\ 0 \text{ m/s} \\ 0 \text{ m/s} \\ 1 \times 10^7 \text{ Pa} \end{bmatrix}. \tag{5.13}$$

At $t = 0.04$ s, the solution consists of five constant states, separated by a strong shock wave propagating to the liquid phase in the far right region of low pressure, an expansion wave reflected back to the air phase in the far left region of high pressure, and two contact-like discontinuities in the middle. In addition, the pressure keeps nearly constant through the contact-like discontinuities.

Following Flåtten and Evje [79], the constant σ in the interfacial pressure term (see Eq. 2.45) is set to be 1.2. Non-differential source terms are not included. A grid of 101 nodes is used, unless otherwise stated.

Cortes' shock tube problem

In this problem [52][53], the shock tube has a length of 100 m. Initially, the diaphragm is set in the middle. On the left-hand side of the diaphragm, the void fraction and gas velocity are set to be 0.29 m/s and 65 m/s, respectively. On the right-hand side of the diaphragm, the void fraction and gas velocity are imposed to be 0.30 m/s and 50 m/s, respectively. The pressure is 2.65 MPa, and the liquid velocity is 1 m/s. The initial conditions are given as follows:

$$\begin{bmatrix} \alpha_g \\ u_g \\ u_l \\ p \end{bmatrix}_L = \begin{bmatrix} 0.29 \\ 65 \text{ m/s} \\ 1 \text{ m/s} \\ 2.65 \times 10^5 \text{ Pa} \end{bmatrix}, \quad \begin{bmatrix} \alpha_g \\ u_g \\ u_l \\ p \end{bmatrix}_R = \begin{bmatrix} 0.30 \\ 50 \text{ m/s} \\ 1 \text{ m/s} \\ 2.65 \times 10^5 \text{ Pa} \end{bmatrix}. \tag{5.14}$$

This is a larger relative velocity shock. At $t = 0.01$ s, there are two separate void fraction waves in the middle [9]. The computation was performed up to 0.08 s on a grid of 101 nodes.

Ejve's shock tube problem

This problem [9] is the same as Cortes' problem, except that the initial void fraction and liquid velocity are different. The initial conditions are given below:

$$\begin{bmatrix} \alpha_g \\ u_g \\ u_l \\ p \end{bmatrix}_L = \begin{bmatrix} 0.3 \\ 65 \text{ m/s} \\ 10 \text{ m/s} \\ 2.65 \times 10^5 \text{ Pa} \end{bmatrix}, \quad \begin{bmatrix} \alpha_g \\ u_g \\ u_l \\ p \end{bmatrix}_R = \begin{bmatrix} 0.9 \\ 50 \text{ m/s} \\ 15 \text{ m/s} \\ 2.65 \times 10^5 \text{ Pa} \end{bmatrix}. \tag{5.15}$$

5.3 Investigation of the Dissipation Mechanism of AUSM-Family Schemes

In this section, collocated-grid-based AUSM-family schemes with explicit time integration are applied on Ransom's water faucet problem and Toumi's shock tube problem to investigate the dissipation mechanisms of the above-mentioned schemes.

5.3.1 Ransom's Water Faucet Problem

The time step is chosen to satisfy the CFL condition, which is given by Eq. 1.1, and the CFL number is set to be 0.5. Figure 5.4 displays the comparison of void fraction profiles with the following AUSM-family schemes: AUSM$^+$-up with the dissipation coefficients (K_p, K_u)=(0, 0), (1,0), (0.5, 0.5) and (1, 1), AUSMD, AUSMV, AUSMDV. The explicit time integration is used. The results obtained with the FVS scheme and CATHENA4 are also plotted for comparison purpose.

It can be seen that the results obtained with all the above-mentioned schemes are capable of yielding stable results. In addition, the AUSM$^+$, AUSMD, and AUSMDV schemes not only seem to be most accurate but also are basically the same. The agreement between the AUSM$^+$ and AUSMD schemes is expected, since for the moving void contact

discontinuity, the dissipation term in the AUSM$^+$ scheme is the same as that in the AUSMD scheme (see Eqs. 3.48 and 3.56). In addition, the results obtained with the AUSMD scheme agrees with those obtained with the AUSMDV scheme. This agreement is because in the water faucet problem, the tuning parameter s in the AUSMDV scheme (see Eq. 4.16) approximates 0, which renders the AUSMDV scheme completely biased toward the AUSMD scheme. On the contrary, the FVS scheme produces excessively diffusive results, which can also be expected by examining its dissipation term (see Eq. 3.55). The accuracy of the AUSMV scheme lies between the AUSMD and FVS schemes in spite of the fact that the AUSMV and AUSMD schemes share the same mass flux splitting. This indicates that the FVS-type momentum flux splitting possesses much more numerical diffusion than the AUSM$^+$/AUSMD-type momentum flux splitting.

In addition, it can also be seen from Fig. 5.4 that results obtained with the AUSM$^+$-up (0.5, 0.5) and AUSM$^+$-up (1, 1) schemes appear to be much more smeared than those obtained with the AUSM$^+$ and AUSM$^+$-up (1, 0) schemes, because of the pressure-velocity-based dissipation terms in the former schemes (see Eqs. 3.22 and 3.25). Also, results obtained with AUSM$^+$-up (0, 0) and AUSM$^+$-up (1, 0) are in a high degree of conformity. This indicates that the dissipation term M_{pk} in Eq. 3.22, which is based on pressure difference, has less influence on dissipation than p_{uk} in Eq. 3.25, which is based on velocity difference. Furthermore, one can see that only the AUSM$^+$, AUSMD, and AUSMDV schemes are capable of generating more accurate results than the original version of CATHENA4. Therefore, the AUSM$^+$, AUSMD , and AUSMDV schemes are suggested to be implemented into CATHENA4 to increase the numerical accuracy for the water faucet problem.

5.3.2 Toumi's Shock Tube Problem

Figures 5.5 and 5.6 displays the comparison of void fraction, pressure, gas velocity and liquid velocity profiles with the explicit AUSM$^+$, AUSMD, AUSMV, AUSMDV and FVS schemes. It can be seen that the AUSM$^+$ scheme generates oscillations, indicating insufficient numerical diffusion in the AUSM$^+$ scheme for Toumi's shock tube problem. On the contrary, the FVS scheme is capable of yielding stable results, indicating enough numer-

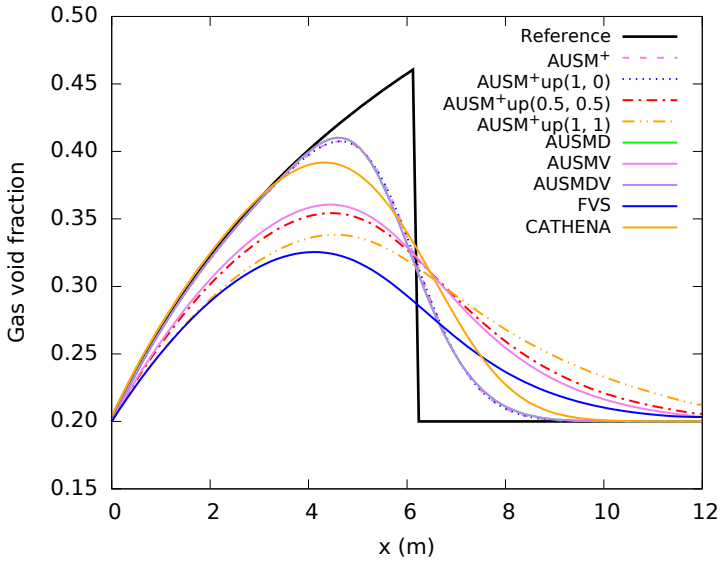

Figure 5.4: Ransom's water faucet problem: comparison of void fraction among explicit AUSM-family schemes at $t = 0.5$ s. $N = 101$; CFL=0.5; $\sigma = 2.0$; $C_f = 0.0$.

ical damping for this test case. The AUSMD, AUSMV, and AUSMDV schemes produce more stable solutions than the AUSM$^+$ scheme, however, these schemes generate overshoots and undershoots at the discontinuity which is located at $x = 50$ m. In other words, the AUSMD, AUSMV, and AUSMDV schemes do not have enough numerical diffusion to suppress spurious oscillations in this test case.

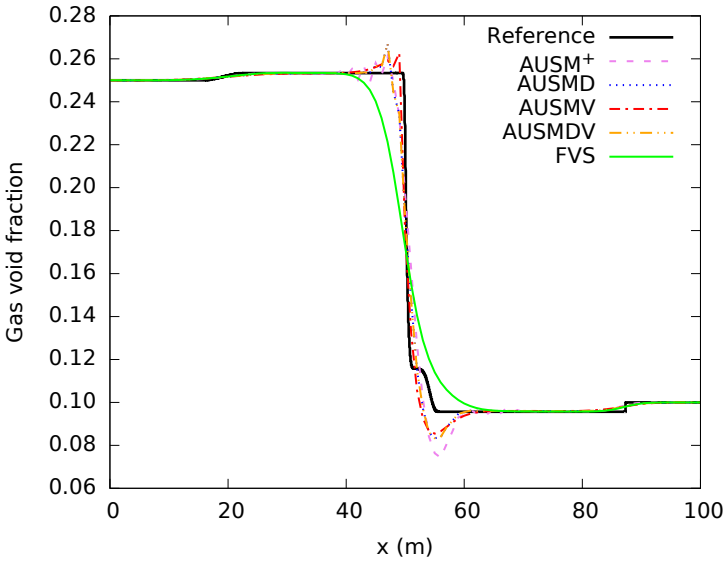

(a)

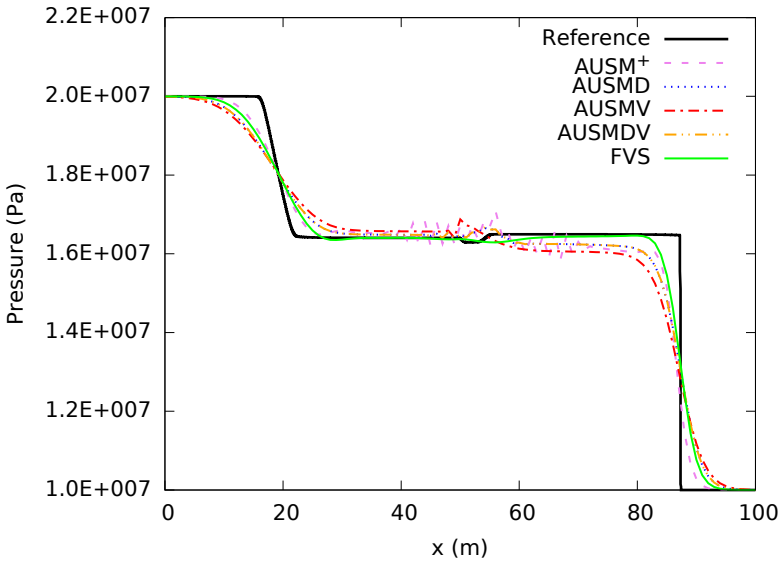

(b)

Figure 5.5: Toumi's shock tube: comparison among the explicit AUSM$^+$, AUSMD, AUSMV, AUSMDV, FVS schemes at $t = 0.04$ s; $N = 101$; CFL=0.5; $\sigma = 1.2$, $C_f = 0.0$. (a) Void fraction; (b) Pressure.

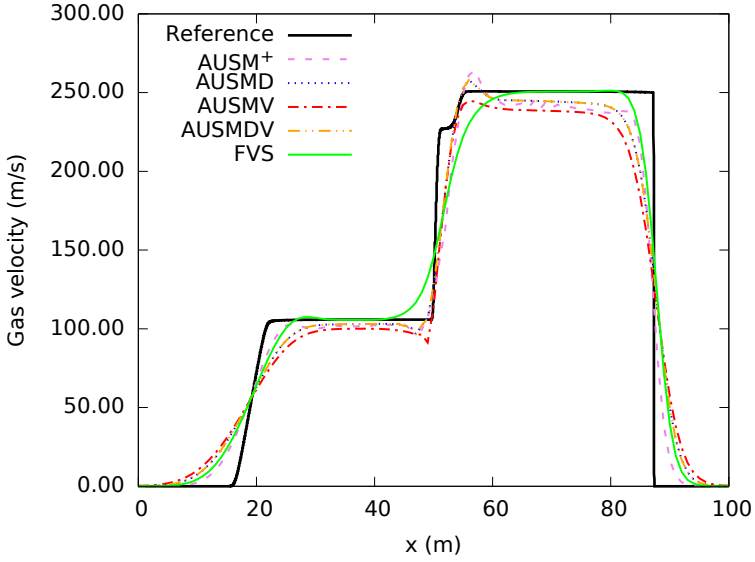

(a)

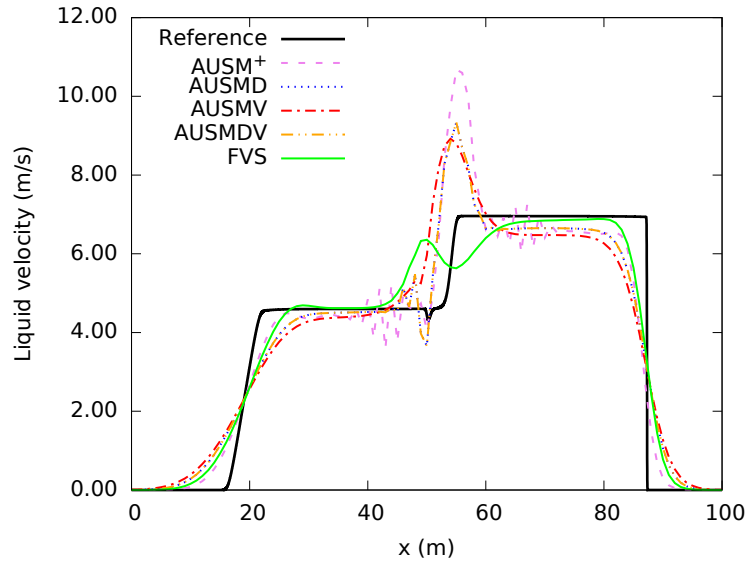

(b)

Figure 5.6: Toumi's shock tube: comparison among the explicit AUSM$^+$, AUSMD, AUSMV, AUSMDV, FVS schemes at $t = 0.04$ s; $N = 101$; CFL=0.5; $\sigma = 1.2$; $C_f = 0.0$. (a) Gas velocity; (b) Liquid velocity.

5.4 Comparison of Accuracy and Efficiency between Implicit and Explicit Methods

5.4.1 Ransom's Water Faucet Problem

Comparison between implicit and explicit methods

In this subsection, the AUSM$^+$-up scheme with various dissipation parameters (K_p, K_u) equal to (0.0, 0.0), (1.0, 0.0), (0.5, 0.5), and (1.0, 1.0), respectively, are applied to solve the water faucet problem on collocated grids. Results are given in Figs. 5.7 and 5.8, using a mesh of 101 nodes. All the computations are performed up to $t = 0.5$ s. The time step Δt is set to be 10^{-5} s to satisfy the CFL condition. For comparison purposes, solutions obtained with CATHENA4 on a grid of 101 nodes are also provided.

As shown in Figs. 5.7 and 5.8, the collocated-grid-based AUSM$^+$-up scheme with both explicit and implicit time integrations are capable of producing stable and non-oscillatory solutions. Furthermore, one can also see that with a collocated grid, results obtained with the explicit AUSM$^+$-up scheme with different dissipation parameters are in good agreement with those obtained with the corresponding implicit AUSM$^+$-up scheme. It should be noted that the truncation error expressions of the explicit and implicit schemes are the same, O(Δt, Δx), for the disrectized equations. Thus, when using an identical time step size Δt and mesh size Δx, the explicit and implicit schemes have the same truncation error and no difference is observed between their results. In addition, one can observe that with an identical time step, the AUSM$^+$ and AUSM$^+$-up(1, 0) schemes are able to generate more accurate results than CATHENA4, whereas the AUSM$^+$-up(0.5, 0.5) and AUSM$^+$-up(1, 1) schemes are not.

Note that for comparison purposes, identical time steps are used in both explicit and implicit schemes for obtaining the above-mentioned results. Yet, results obtained with the implicit scheme indicate that convergence can be achieved with $\Delta t = 0.01$ s, which corresponds to CFL ≈ 1000.

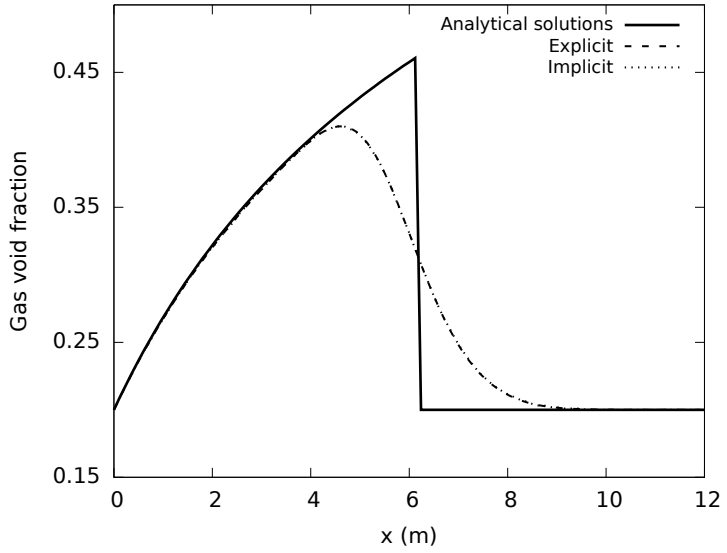

(a)

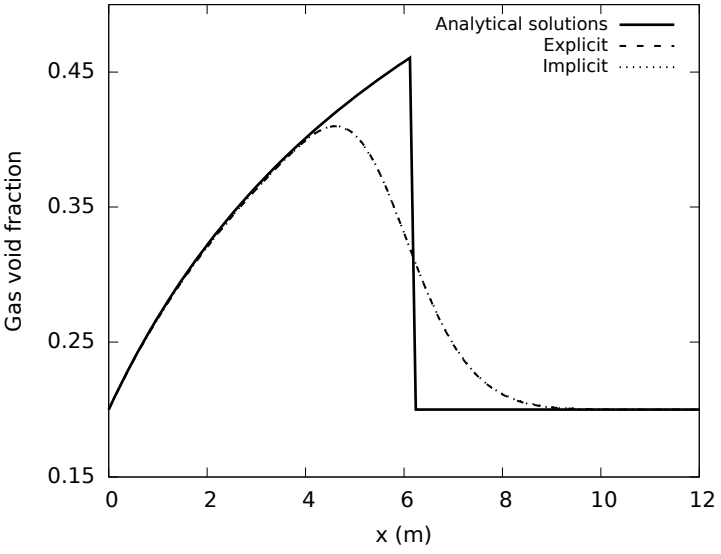

(b)

Figure 5.7: Ransom's water faucet problem: comparison between implicit and explicit AUSM$^+$-up schemes at $t = 0.5$ s; $N = 101$; $\Delta t = 10^{-5}$ s; $\sigma = 2.0$; $C_f = 0.0$. (a) AUSM$^+$; (b) AUSM$^+$-up (1, 0); (c) AUSM$^+$-up (0.5, 0.5); (d) AUSM$^+$-up (1, 1).

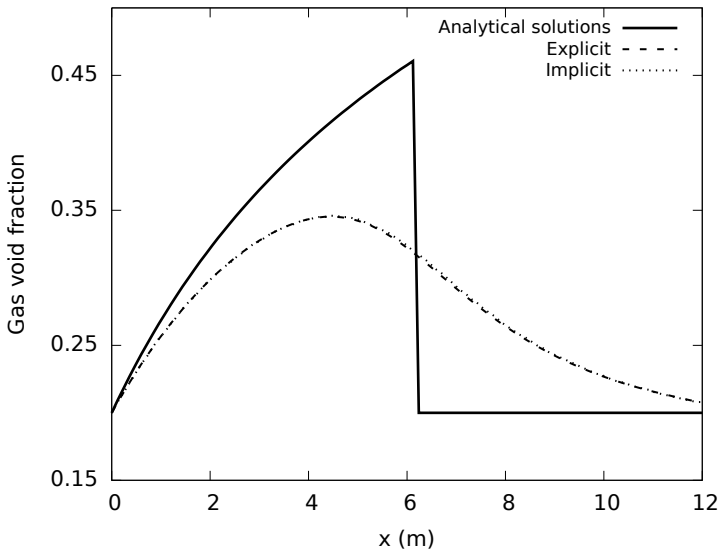

(a)

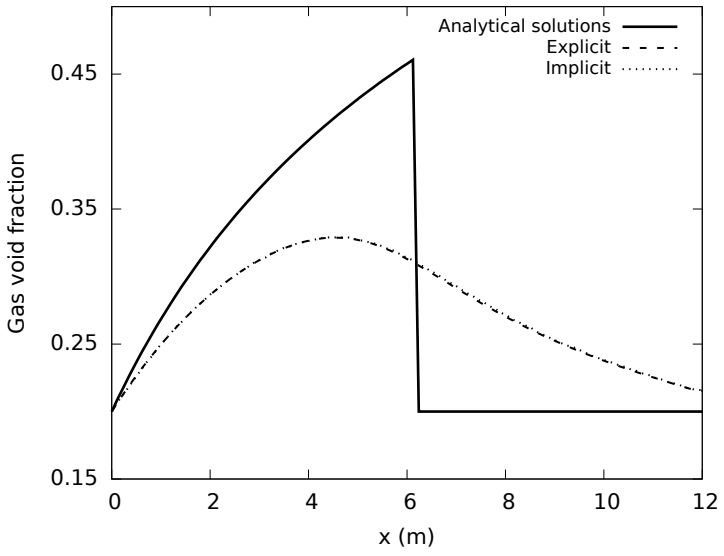

(b)

Figure 5.8: Ransom's water faucet problem: comparison between implicit and explicit AUSM$^+$-up schemes at $t = 0.5$ s; $N = 101$; $\Delta t = 10^{-5}$ s; $\sigma = 2.0$; $C_f = 0.0$. (a) AUSM$^+$-up (0.5, 0.5); (b) AUSM$^+$-up (1, 1).

Figure 5.9 shows the comparison between the implicit AUSM$^+$ scheme with Δt of 10^{-5} s, 10^{-4} s, and 10^{-2} s on a collocated grid of 101 nodes. One can see that the void fraction is more smeared as the time step is increased. However, even the time step differs in three orders, the numerical accuracy of the implicit AUSM$^+$ scheme with $\Delta t = 10^{-2}$ s rivals that of CATHENA4 with $\Delta t = 10^{-5}$ s.

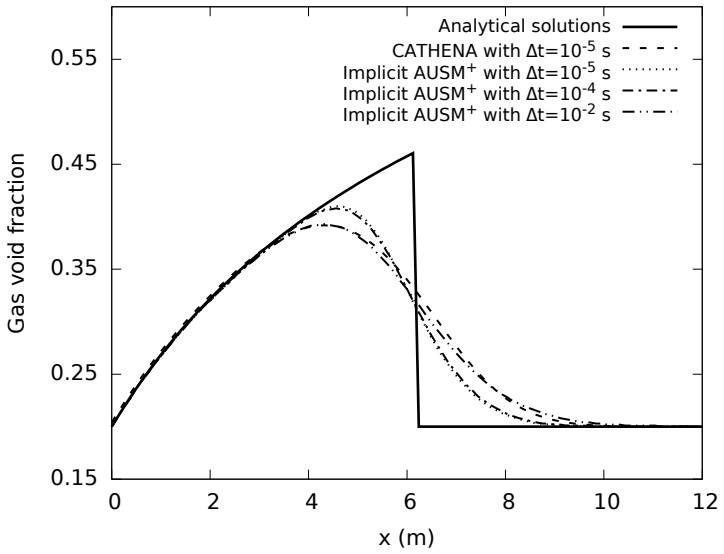

Figure 5.9: Ransom's water faucet problem: comparison among the implicit AUSM$^+$ scheme with Δt of 10^{-5} s, 10^{-4} s and 10^{-2} s at $t = 0.5$ s; $N = 101$; $\sigma = 2.0$; $C_f = 0.0$.

Furthermore, the comparison of CPU time between explicit and implicit AUSM$^+$-up schemes is exhibited in Table 5.1. The total CPU time required by the implicit method is about 7.5 times smaller than that by the explicit method when the time step is set to be 10^{-2} s and 10^{-5} s for the implicit and explicit AUSM$^+$-up schemes, respectively. Consequently, the implicit AUSM-family schemes are quite desirable in terms of computational accuracy and efficiency.

Table 5.1: Comparison of CPU time between explicit and implicit AUSM$^+$-up schemes for Ransom's water faucet problem.

Implicit AUSM$^+$-up Scheme		Explicit AUSM$^+$-up Scheme	
Δt (s)	CPU time (s)	Δt (s)	CPU time (s)
0.00001	25.60	0.00001	1.73
0.01	0.23		

Convergence study

Figures 5.10 and 5.11 show the grid-convergence studies of air volume fraction at $t = 0.5$ s, for the AUSM$^+$-up scheme with different dissipation parameters. Three meshes of 101 nodes, 501 nodes and 1001 nodes are used in this study. All the numerical results are compared with the analytical solution expressed by Eq. 5.2. It is demonstrated that all the cases generate smooth profiles without oscillations. As the mesh gets refined, the solutions approach the analytical one. However, due to the dissipative mechanism, results obtained with AUSM$^+$ and AUSM$^+$-up (1, 0) schemes on a mesh of 101 nodes approach those obtained with AUSM$^+$-up (0.5, 0.5) and AUSM$^+$-up (1, 1) schemes on a mesh of 1001 nodes.

5.4.2 Toumi's Air-water Shock Tube Problem

The computation is performed up to $t = 0.04$ s on a grid of 101 nodes and a time step $\Delta t = \frac{\Delta x}{2400\ (\mathrm{m/s})}$. The explicit and implicit AUSM$^+$ and PD-AUSM$^+$ schemes are employed in this benchmark test. The PD-AUSM$^+$ scheme on a collocated grid with 10001 nodes is applied to generate the reference solutions. Regarding the PD-AUSM$^+$ scheme, M_0 is set to be 0.2 [79].

Figures 5.12 and 5.12 show results obtained with the explicit and implicit AUSM$^+$ and PD-AUSM$^+$ schemes. It is demonstrated that severe oscillations are produced with both explicit and implicit AUSM$^+$ schemes, whereas non-oscillatory results are obtained with explicit and implicit PD-AUSM$^+$ schemes, although slight overshoots still exist. The reduction of oscillations indicates that the pressure diffusion term $\dot{m}_p$ in the PD-AUSM$^+$

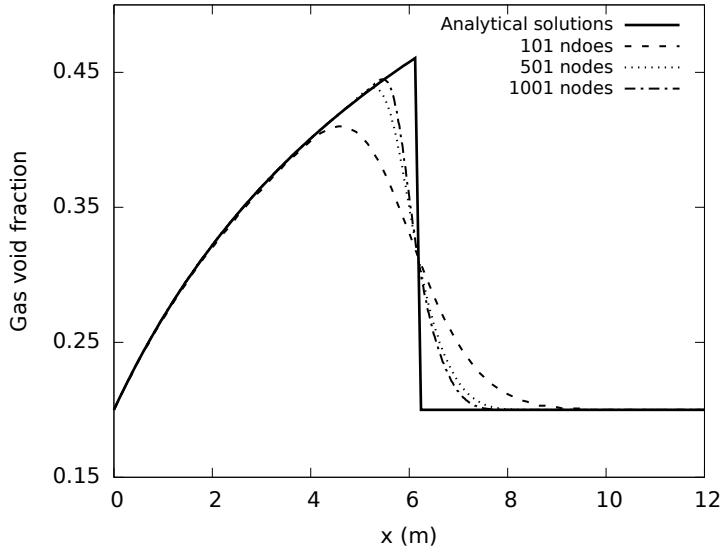

(a)

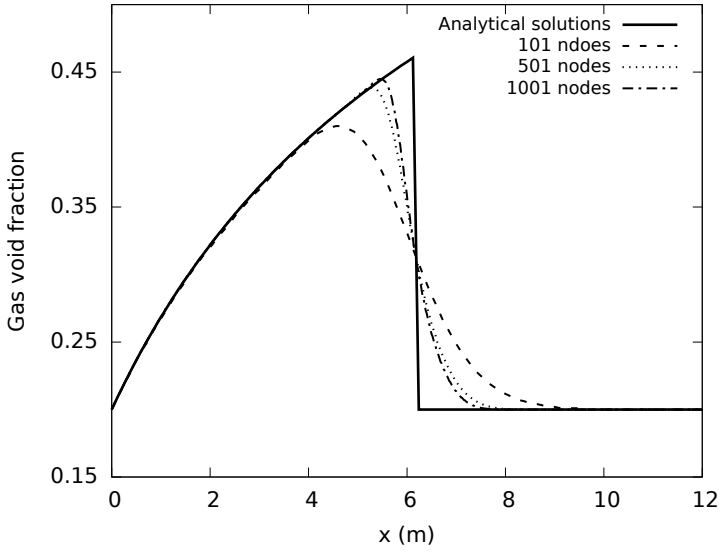

(b)

Figure 5.10: Ransom's water faucet problem: grid convergence study with the implicit AUSM$^+$-up scheme at $t = 0.5$ s; $N = 101$; $\Delta t = 10^{-5}$ s; $\sigma = 2.0$; $C_f = 0.0$. (a) AUSM$^+$; (b) AUSM$^+$-up (1, 0).

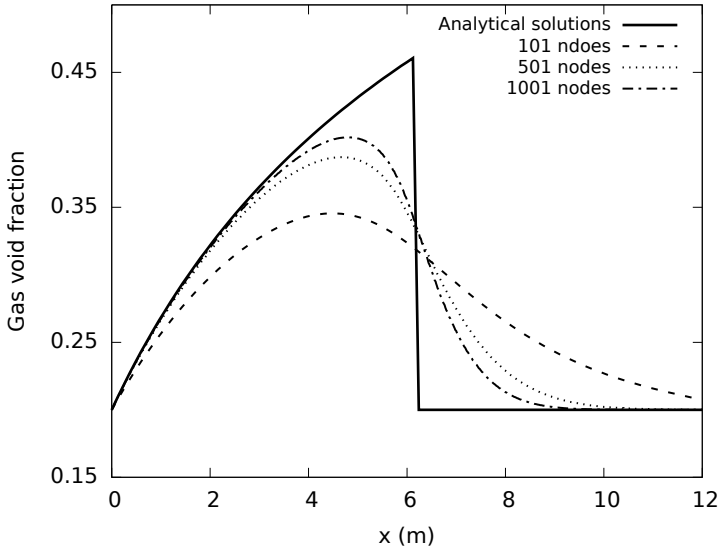

(a)

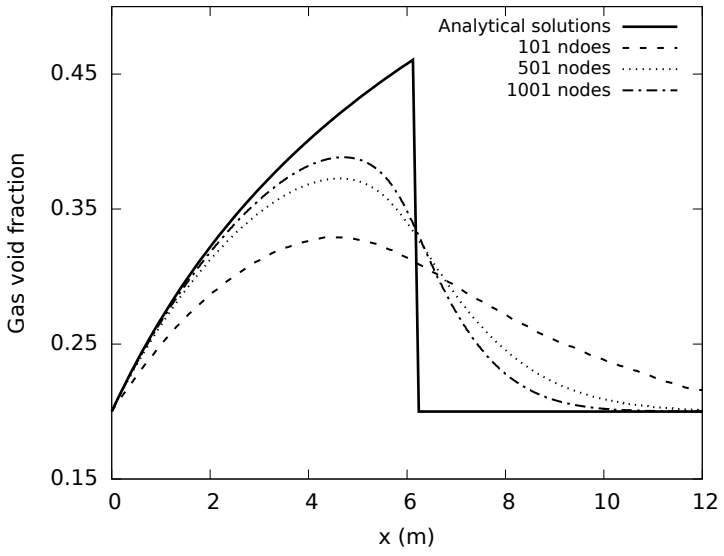

(b)

Figure 5.11: Ransom's water faucet problem: grid convergence study with the implicit AUSM$^+$-up scheme at $t = 0.5$ s on collocated grids; $\Delta t = 10^{-5}$ s; $\sigma = 2.0$; $C_f = 0.0$. (a) AUSM$^+$-up (0.5, 0.5); (b) AUSM$^+$-up (1, 1).

scheme yields proper dissipation for the problem in which the Mach number of the liquid phase approaches zero. These results agree with those reported by Flåtten and Evje [79]. In addition, both implicit and explicit schemes are capable of capturing five separate regions as described in [23] and [19], although according to Toumi [51], the solutions consist of seven constant states. Furthermore, as expected, one can see that the results obtained with implicit schemes are consistent with those obtained with explicit schemes.

Furthermore, with the implicit AUSM$^+$ scheme, the convergence can be obtained with a time step up to 8×10^{-3} s. The comparison of the implicit AUSM$^+$ scheme with $\Delta t = 8 \times 10^{-3}$ s and $\Delta t = 4 \times 10^{-4}$ s is demonstrated in Figs. 5.14 and 5.15. Note that $\Delta t = 4 \times 10^{-4}$ s corresponds to CFL=0.75, whereas $\Delta t = 8 \times 10^{-3}$ s corresponds to CFL=15.0. It can be seen that with $\Delta t = 8 \times 10^{-3}$ s, the gas and velocity profiles are more smeared than those with $\Delta t = 4 \times 10^{-4}$ s.

Table 5.2 displays the comparison of CPU time between the explicit and implicit PD-AUSM$^+$ schemes for this problem. It can be seen that the total CPU time required by the implicit PD-AUSM$^+$ scheme with $\Delta t = 4 \times 10^{-4}$ s is at the same order of magnitude as that required by its explicit counterpart with $\Delta t = 8 \times 10^{-3}$ s. As a result, for Toumi's shock tube problem, the implicit AUSM$^+$ scheme is no better than its explicit counterpart.

Table 5.2: Comparison of CPU time between explicit and implicit PD-AUSM$^+$ schemes for Toumi's air-water shock tube problem.

Implicit PD-AUSM$^+$ Scheme		Explicit PD-AUSM$^+$ Scheme	
Δt (s)	CPU time (s)	Δt (s)	CPU time (s)
0.0004	0.39	0.0004	0.01
0.008	0.01		

5.4.3 Oscillating Manometer Problem

In this test case, explicit and implicit PD-AUSM$^+$ schemes with $M_0 = 0.2$ [19] are applied. Following Paillère [19], a grid of 221 nodes is employed. The time step of 5×10^{-6} s is used for both implicit and explicit schemes.

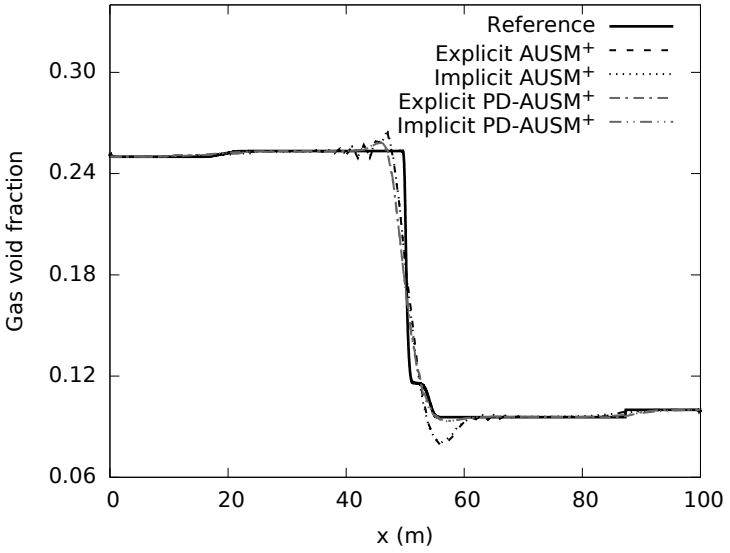

(a)

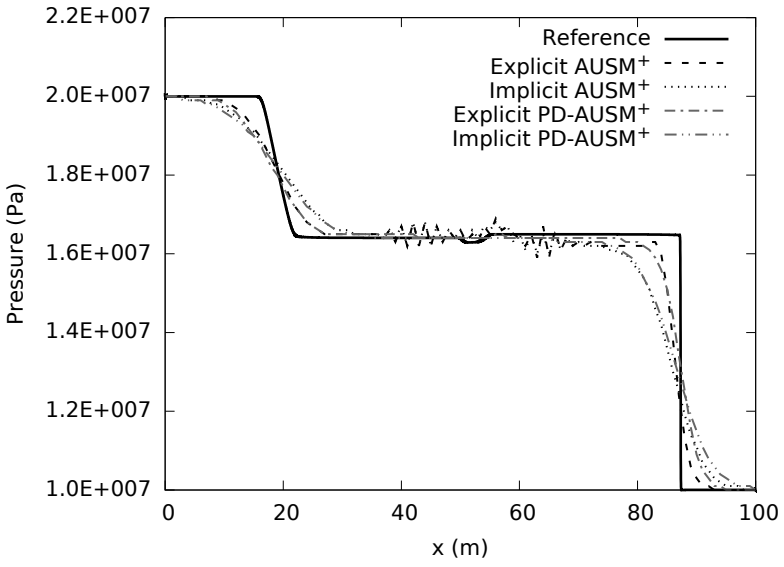

(b)

Figure 5.12: Toumi's air-water shock tube problem: comparison between explicit and implicit AUSM$^+$ and PD-AUSM$^+$ schemes at $t = 0.04$ s; $N = 101$; $\Delta t = \Delta x/(2400(\text{m/s}))$; $\sigma = 1.2$; $C_f = 0.0$. (a) Void fraction; (b) Pressure.

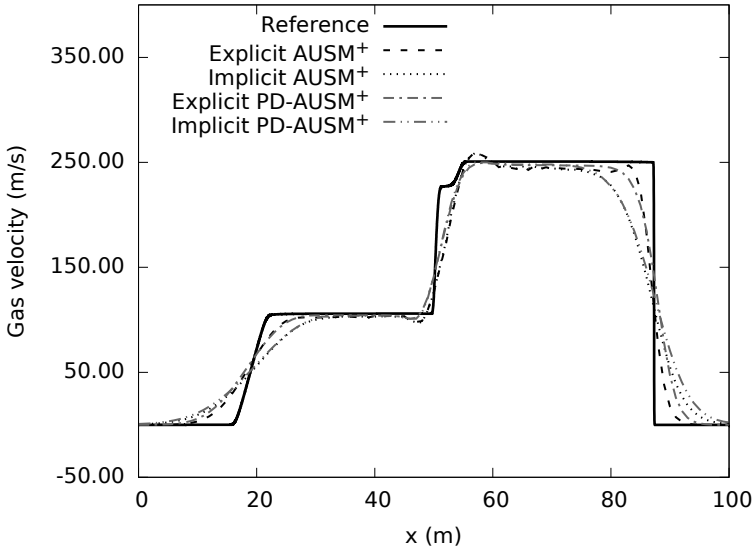

(a)

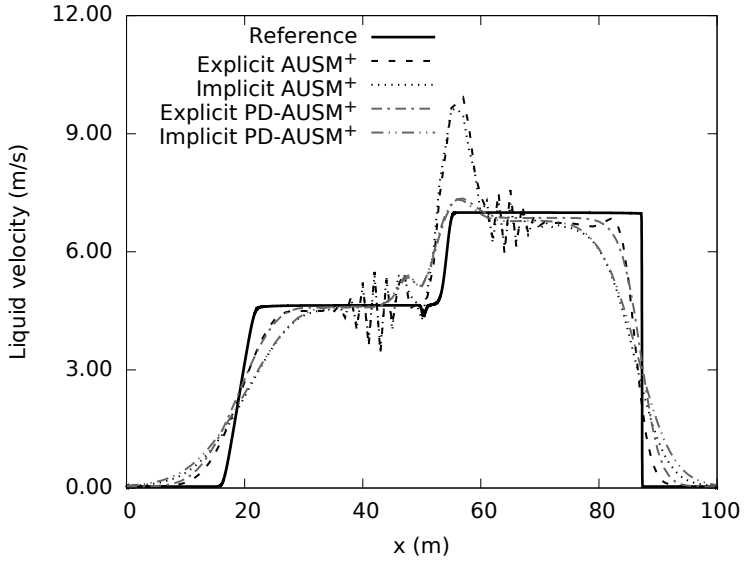

(b)

Figure 5.13: Toumi's air-water shock tube problem: comparison between explicit and implicit AUSM$^+$ and PD-AUSM$^+$ schemes at $t = 0.04$ s; $N = 101$; $\Delta t = \Delta x/(2400(\text{m/s}))$; $\sigma = 1.2$; $C_f = 0.0$. (a) Gas velocity; (b) Liquid velocity.

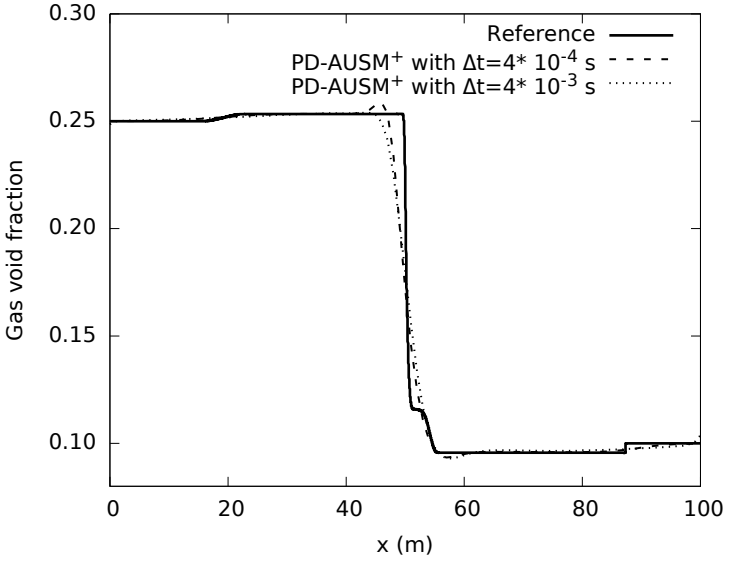

(a)

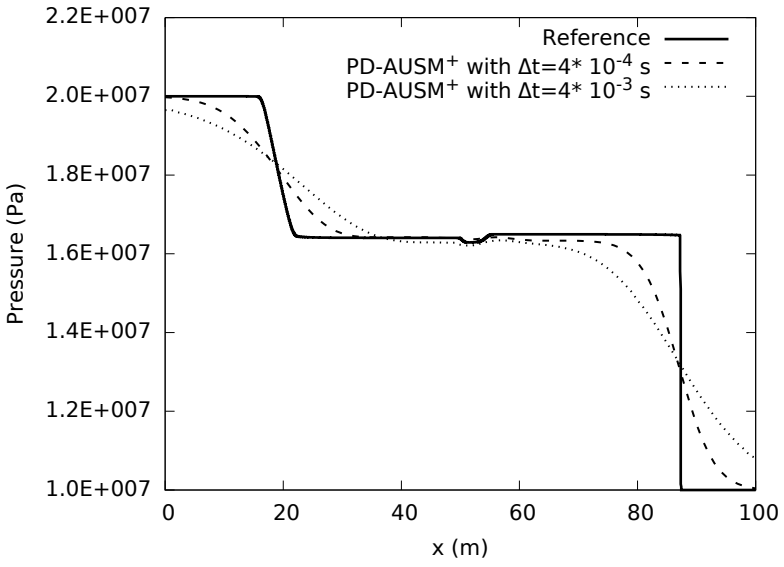

(b)

Figure 5.14: Toumi's shock tube problem: comparison between implicit AUSM$^+$ schemes with $\Delta t = 4 \times 10^{-4}$ s and $\Delta t = 4 \times 10^{-3}$ s at $t = 0.04$ s; $N = 101$; $\sigma = 1.2$; $C_f = 0.0$. (a) Void fraction; (b) Pressure.

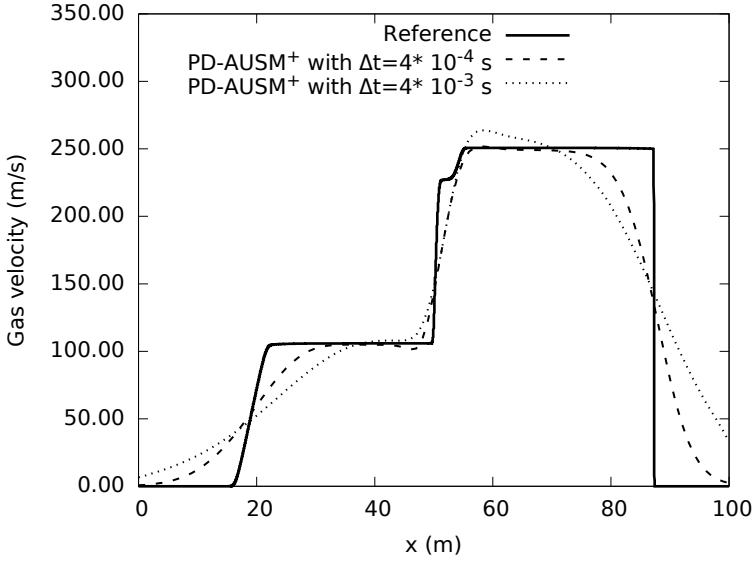

(a)

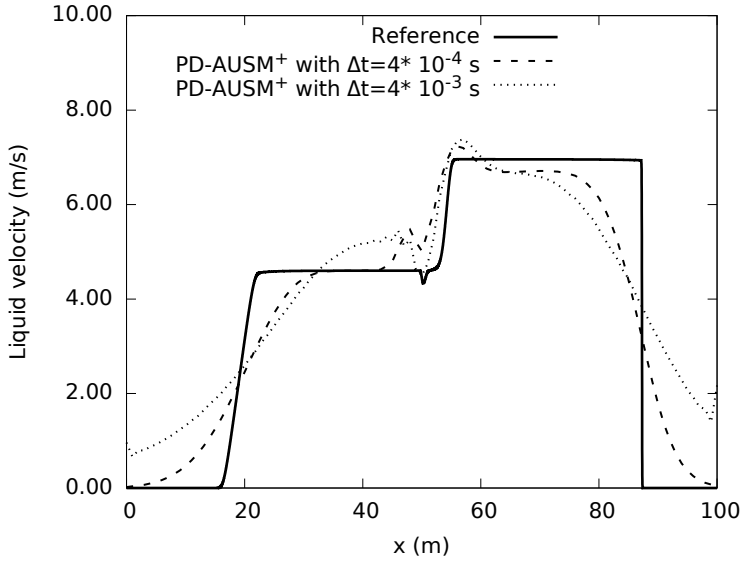

(b)

Figure 5.15: Toumi's shock tube problem: comparison between implicit AUSM$^+$ schemes with $\Delta t = 4 \times 10^{-4}$ s and $\Delta t = 4 \times 10^{-3}$ s at $t = 0.04$ s; $N = 101$; $\sigma = 1.2$; $C_f = 0.0$. (a) Gas velocity; (b) Liquid velocity.

In this problem, for implicit methods, $\varepsilon = 10^{-4}$ (see Eq. 4.11); the perturbation value ϵ_i is set to be 10^{-4} for gas volume fraction, 10^{-1} for pressure and 10^{-3} for both gas and liquid velocities, by referring to the values in the CATHENA4 code.

Figure 5.16 demonstrates the time evolution of liquid velocity at the bottom of the tube. It is shown that results obtained with the explicit and implicit PD-AUSM$^+$ schemes are identical. In addition, similar to the results reported in [19], [9] and [77], the numerical solutions exhibit slight damping compared to the analytical one. Also, a small phase error can be observed. However, these results are much more improved than those in CATHENA4, as discussed in subsection 5.4.3.

For the oscillating manometer problem, the time step can be set to be as large as 5×10^{-3} s to achieve stable solutions. The comparison between CATHENA4 with $\Delta t = 5 \times 10^{-6}$ s (CFL ≈ 0.1) and the implicit PD-AUSM$^+$ with $\Delta t = 5 \times 10^{-6}$ s and $\Delta t = 5 \times 10^{-3}$ s are shown in Fig. 5.19. It is obvious that results generated by the implicit PD-AUSM$^+$ scheme with $\Delta t = 5 \times 10^{-6}$ s and with $\Delta t = 5 \times 10^{-3}$ s are greatly better than those generated by CATHENA4 with $\Delta t = 5 \times 10^{-6}$ s in terms of amplitude damping and phase shifting. In addition, it can be seen that when using the implicit PD-AUSM$^+$ scheme, the profile obtained with $\Delta t = 5 \times 10^{-3}$ is only slightly more smeared than that obtained with $\Delta t = 5 \times 10^{-6}$ s.

Table 5.3 demonstrates the total CPU time for both explicit and implicit PD-AUSM$^+$ schemes. One can see that the implicit scheme with $\Delta t = 5 \times 10^{-3}$ s improves the computational efficiency of simulations by reducing one order of magnitude of CPU time over its explicit counterpart with $\Delta t = 5 \times 10^{-6}$ s. As a consequence, for the oscillating manometer problem, the implicit PD-AUSM$^+$ scheme is superior to its explicit counterpart.

Table 5.3: Comparison of CPU time between the explicit and implicit PD-AUSM$^+$ schemes for the oscillating manometer problem.

Implicit PD-AUSM$^+$ Scheme		Explicit PD-AUSM$^+$ Scheme	
Δt (s)	CPU time (s)	Δt (s)	CPU time (s)
0.000005	25640.97	0.000005	313.41
0.005	32.79		

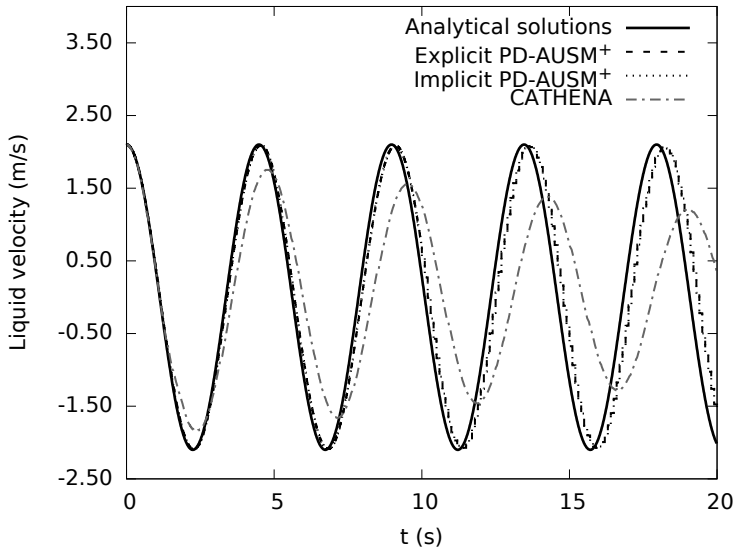

Figure 5.16: Oscillating manometer problem: comparison between explicit PD-AUSM$^+$ and implicit PD-AUSM$^+$; $N = 101$; $\Delta t = 5 \times 10^{-6}$ s; $\sigma = 0.0$; $C_f = 5 \times 10^4$ s^{-1}. Liquid velocity with time at the bottom of the tube.

5.5 Advantages of the Proposed Implicit SG-AUSM-Family Schemes Over Implicit AUSM-Family Schemes

5.5.1 Ransom's Water Faucet Problem

The results of the void fraction at $t = 0.5$ s are given in Fig. 5.20. Four different schemes, including SG-AUSMV, SG-FVS, SG-AUSM$^+$, and SG-AUSMFVS are employed. For SG-AUSMFVS, κ is chosen to be 200 [9]. Analytical solutions and the solutions obtained with CATHENA4 and the Roe scheme are also plotted for comparison purpose.

It is shown in Fig. 5.20 that all the above-mentioned schemes are capable of producing stable and non-oscillatory solutions. Among the above-mentioned schemes, SG-AUSM$^+$ and SG-AUSMFVS are much more accurate than SG-AUSMV, SG-FVS, and CATHENA4. In addition, it is shown that SG-AUSM$^+$ and SG-AUSMFVS are comparable with the Roe scheme in terms of resolving the gas void fraction. This implies that a modest amount of

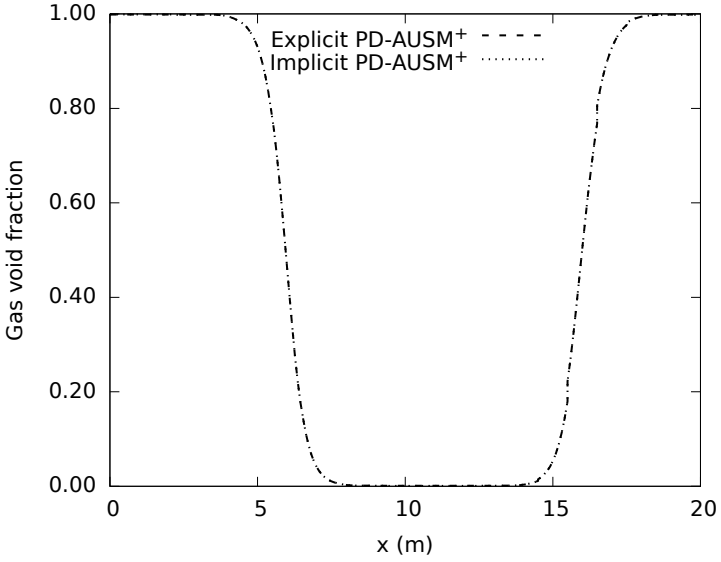

(a)

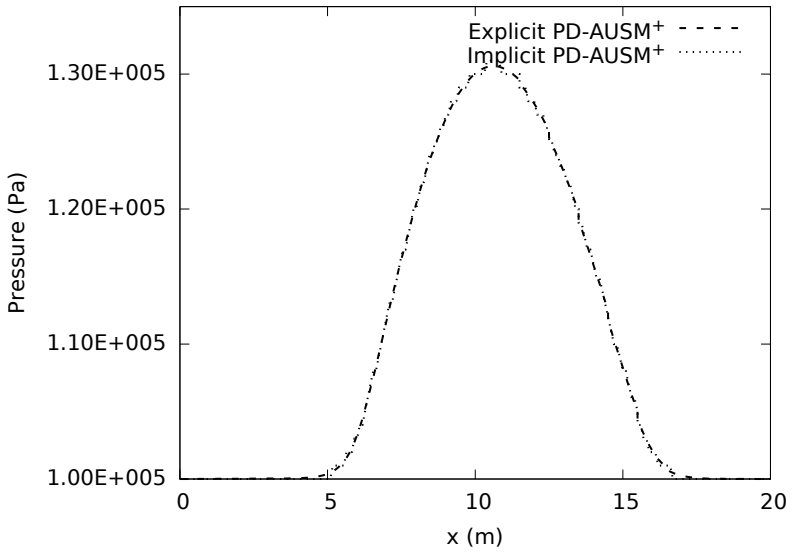

(b)

Figure 5.17: Oscillating manometer problem: comparison between explicit and implicit PD-AUSM$^+$ schemes at $t = 20$ s; $N = 221$; $\Delta t = 5 \times 10^{-6}$ s; $\sigma = 0.0$; $C_f = 5 \times 10^4$ s^{-1}. (a) Void fraction; (b) Pressure.

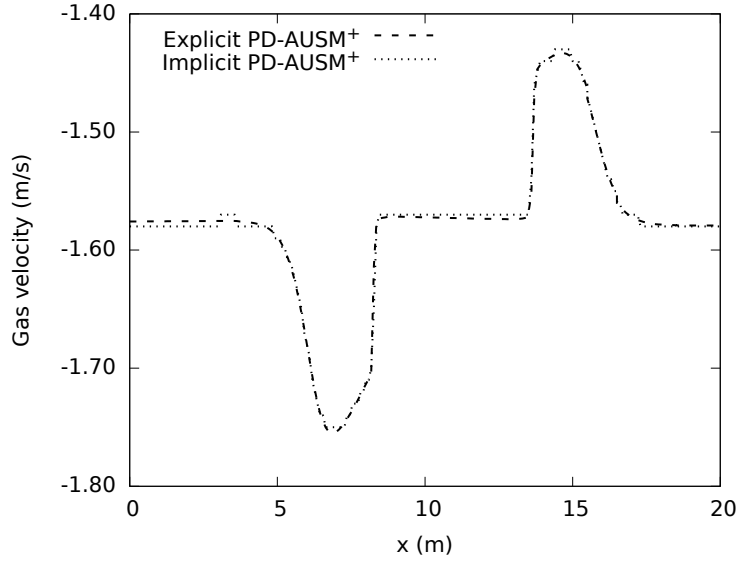

(a)

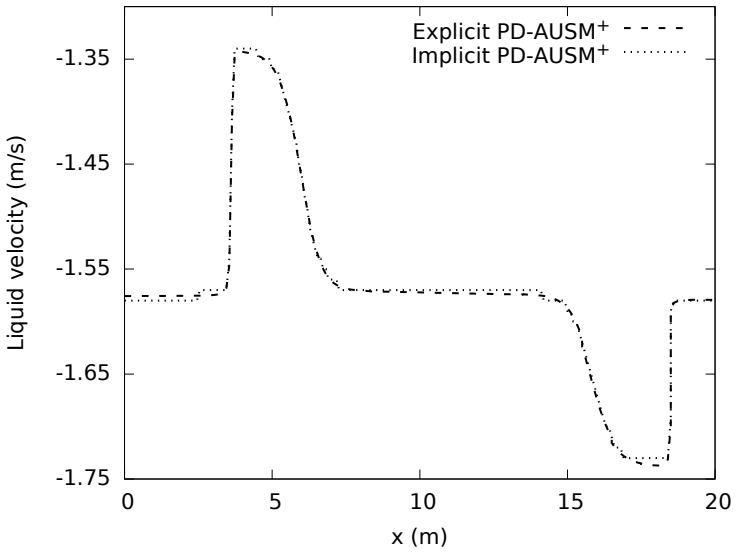

(b)

Figure 5.18: Oscillating manometer problem: comparison between explicit and implicit PD-AUSM$^+$ schemes at $t = 20$ s; $N = 221$; $\Delta t = 5 \times 10^{-6}$ s; $\sigma = 0.0$; $C_f = 5 \times 10^4$ s^{-1}. (a) Gas velocity; (b) Liquid velocity.

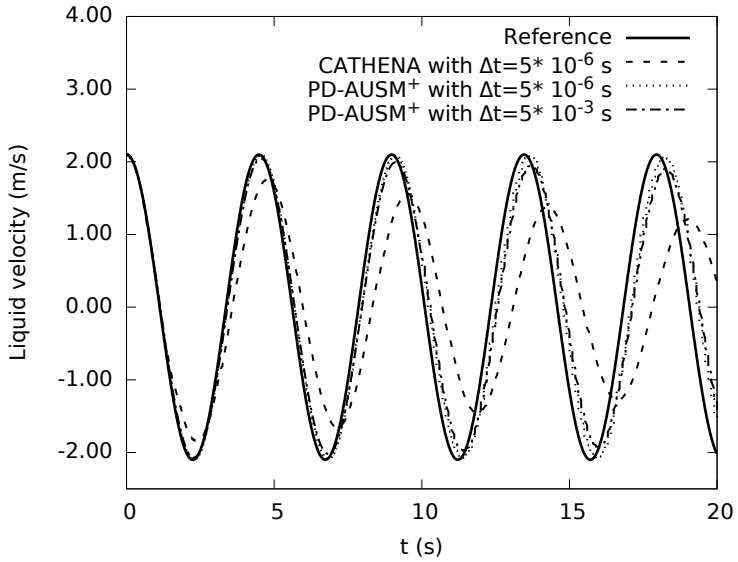

Figure 5.19: Oscillating manometer problem: comparison between the implicit PD-AUSM$^+$ scheme with $\Delta t = 5 \times 10^{-6}$ and $\Delta t = 5 \times 10^{-3}$; $N = 101$; $\sigma = 0.0$; $C_f = 5 \times 10^4$ s^{-1}. Liquid velocity with time at the bottom of the tube.

numerical dissipation is introduced to the SG-AUSM$^+$ and SG-AUSMFVS. It is therefore recommended that SG-AUSM$^+$ and SG-AUSMFVS be implemented into CATHENA4 to enhance its accuracy for the water faucet problem. On the other hand, one can see poor representation of the void wave fronts obtained with SG-AUSMV and SG-FVS. In addition, SG-AUSMV and SG-FVS yield practically the same results since χ is approximately equal to one due to the negligible pressure variations in this test case. Nevertheless, the behavior of SG-AUSMV and SG-FVS is different from that in Evje and Flåtten's work [9], who used AUSMV and FVS. Their results demonstrated that AUSMV exhibits weaker numerical dissipation than that of FVS [9]. The difference between Evje and Flåtten's work and the present work may be explained by the different ways of dealing with interfacial mass fluxes as a result of using different grid arrangements.

Figure 5.21 shows the grid-convergence study in terms of void fraction obtained with SG-AUSMFVS. A series of four grids of 101 nodes, 201 nodes, 501 nodes, and 801 nodes have been employed in this study. One can see from Fig. 5.21 that as grids become finer,

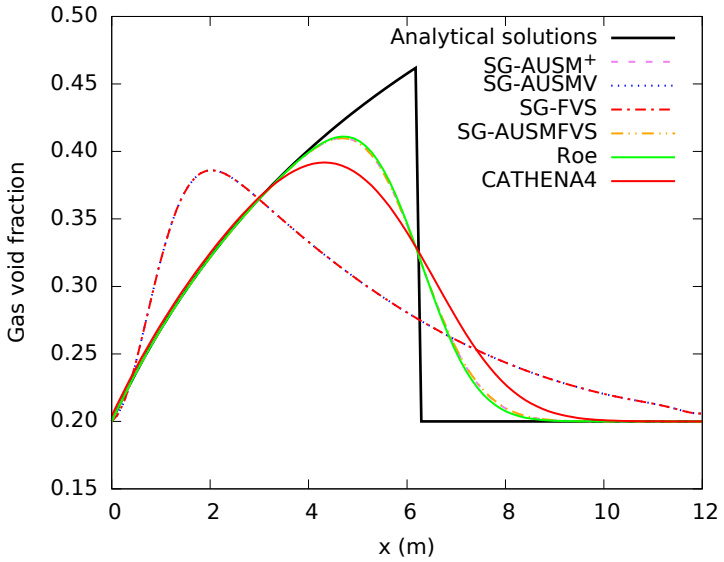

Figure 5.20: Ransom's water faucet problem: comparison of void fraction among the Roe, CATHENA4, SG-AUSMV, SG-FVS, SG-AUSM$^+$, and SG-AUSMFVS ($\kappa = 200$) schemes at $t = 0.5$ s; $N = 101$; $\Delta t = 10^{-4}$ s; $\sigma = 2.0$; $C_f = 0.0$.

convergence is achieved with smooth profiles without any oscillations.

5.5.2 Oscillating Manometer Problem

Figure 5.22 demonstrates the time evolution of the liquid velocity at the bottom of the tube using SG-AUSMV, SG-FVS, SG-AUSM$^+$, SG-AUSMFVS, and CATHENA4. The approximate analytical solutions are also provided for comparison purpose. It is shown that results obtained with all the above-mentioned schemes are capable of producing smooth profiles without any numerical oscillations. Nevertheless, similar to the results reported in [19, 9, 77], the numerical solutions exhibit damping behavior compared to the analytical one. Also, a small phase error can be observed in Figure 5.22. The damping is expected since the interfacial drag force is included in the two-fluid model, which induces the physical damping. In addition, the temporal and spatial discretizations adopt first-order schemes. The dissipative errors associated with the temporal and spatial discretizations can be

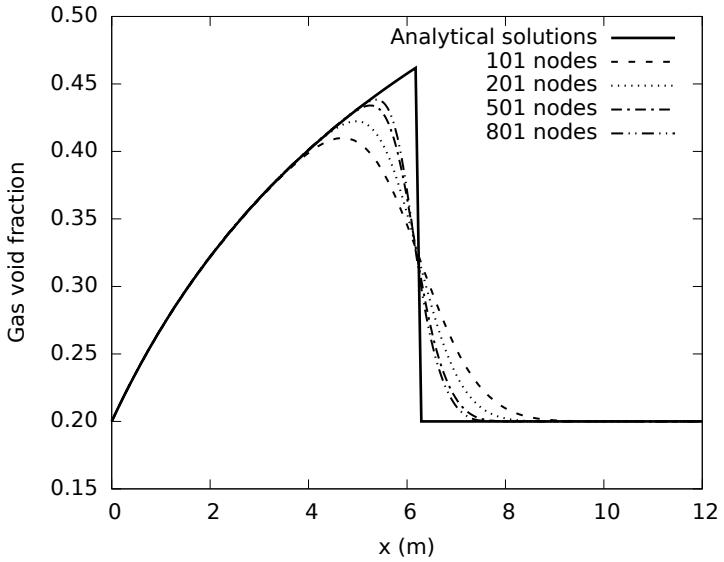

Figure 5.21: Ransom's water faucet problem: grid-convergence study of void fraction with the SG-AUSMFVS ($\kappa = 200$) scheme at $t = 0.5$ s; $N = 101$; $\Delta t = 10^{-4}$ s; $\sigma = 2.0$; $C_f = 0.0$.

alleviated by the Runge-kutta time-stepping scheme and the MUSCL interpolation method, respectively. On the other hand, the phase error indicates the dispersive characteristic of the numerical schemes. From Figure 5.22, one can see that both SG-AUSM$^+$ and SG-AUSMFVS schemes give results with slightest damping. Furthermore, when it comes to dispersive errors, the new SG-AUSMFVS scheme demonstrates much better performance than that of the SG-AUSM$^+$ scheme. On the contrary, CATHENA4 produced severely damped and dispersive solutions. In addition, results obtained with SG-AUSMV and SG-FVS agree well with each other and they are no better than those obtained with the SG-AUSM$^+$ and SG-AUSMFVS, but they are superior to CATHENA4's solutions. This reveals that the new SG-AUSMFVS scheme is the least dissipative and dispersive compared to other schemes examined for the oscillating manometer problem. Therefore, a much better improvement in terms of prediction accuracy for the above phenomenon can be expected, once the implicit staggered SG-AUSMFVS scheme is incorporated into CATHENA4 and/or other first-order accurate thermal-hydraulics codes.

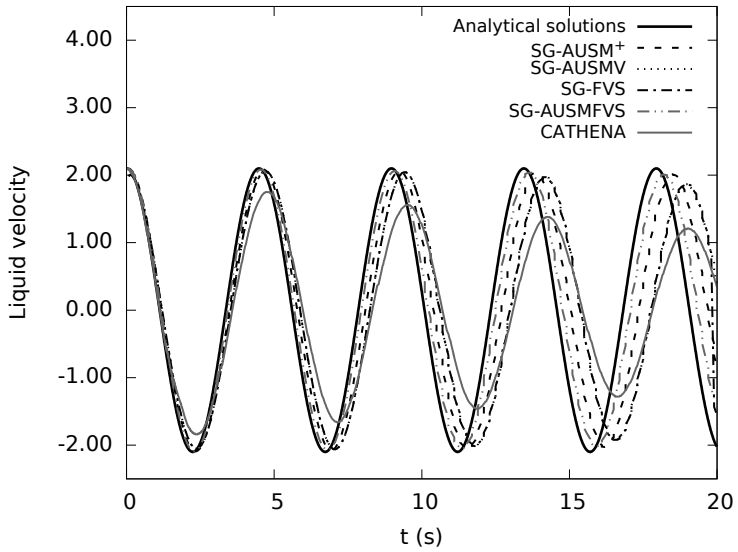

Figure 5.22: Oscillating manometer problem: comparison among CATHENA4, SG-AUSMV, SG-FVS, SG-AUSM$^+$, and SG-AUSMFVS ($\kappa = 200$) schemes; $N = 101$; $\Delta t = \Delta x/(3000\text{m/s})$; $\sigma = 0.0$; $C_f = 5 \times 10^4$ s^{-1}. Liquid velocity with time at the bottom of the tube.

Figure 5.23 shows the profiles of void fraction and pressure at $t = 20$ s. Although the void fraction profile obtained with CATHENA4 appears to be sharper than those obtained with other schemes, as clearly shown in this figure, its pressure profile seems to be unrealistic and has to be corrected. The reason that CATHENA4 gives sharper results may be due to the truncation of the void fraction. However, CATHENA4 is still under development, and the closure law for the interface is still not perfect during transient simulations. The closure law for friction in CATHENA4 is not yet completed. In addition, the dynamic energy $\frac{1}{2}u^2$ is ignored in CATHENA4.

Finally, it is important to accentuate that with the collocated-grid arrangement, a pressure diffusion term has to be added to the liquid mass flux in the basic AUSM$^+$ scheme to make a successful prediction for flows at low Mach numbers [19, 9]. In the oscillating manometer problem, the Mach number of the liquid phase can be as low as 10^{-4}. Therefore, without adding additional numerical dissipation or using the time-derivative precondition-

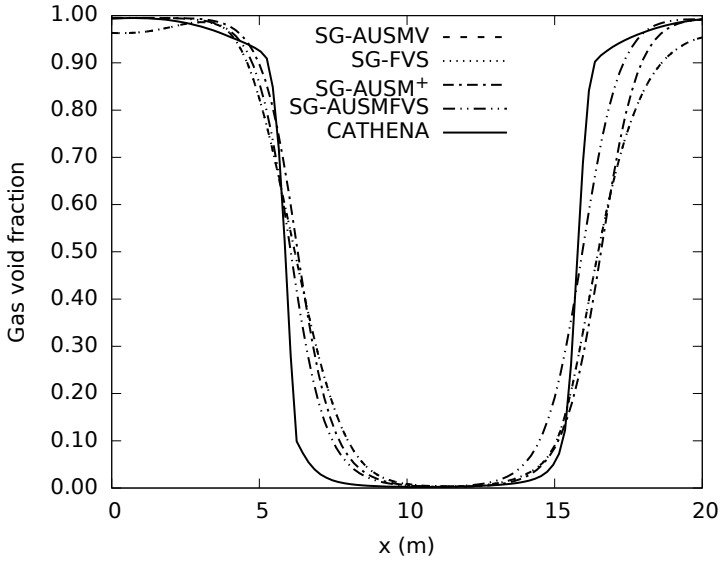

(a)

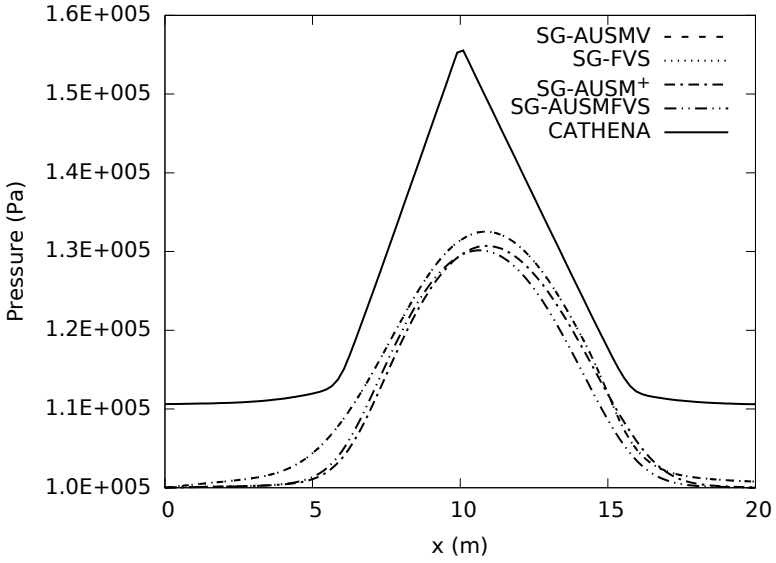

(b)

Figure 5.23: Oscillating manometer problem: comparison among CATHENA4, SG-AUSMV, SG-FVS, SG-AUSM$^+$, and SG-AUSMFVS ($\kappa = 200$) schemes at $t = 20$ s; $N = 101$; $\Delta t = \Delta x/(3000\text{m/s})$; $\sigma = 0.0$; $C_f = 5 \times 10^4$ s^{-1}. (a) Void fraction; (b) Pressure.

ing technique [19], codes will diverge due to the odd-even decoupling in the collocated-grid approach when the AUSM$^+$ scheme is used for the oscillating manometer test case. However, as demonstrated by the present work, using a staggered-grid arrangement combined with SG-AUSMFVS, SG-AUSM$^+$ or other density-based discretization schemes eliminate the odd-even decoupling issues. The elimination of the special treatment required by collocated grids will save computer memory and computational time for two-phase flows at low Mach numbers, which is to be expected.

5.5.3 Phase Separation Problem

The results of the void fraction and water velocity profiles at $t = 0.2$ s obtained with SG-AUSMV, SG-FVS and SG-AUSM$^+$ are shown in Fig. 5.24. The analytical solutions are also provided. Clearly, SG-AUSM$^+$ yields desirable results, which agree well with the analytical solutions. However, at the right corner of the liquid velocity profile, a very slight overshoot is generated (not obvious but can be seen when the figure is enlarged). This overshoot will contaminate the subsequent solutions and divergence occurs after $t = 0.2$ s. On the contrary, SG-FVS and SG-AUSMV produce the same smooth but smearing profiles.

Figure 5.25 displays the transient void fraction profile, using SG-AUSMV and SG-FVS with a damping coefficient $\sigma = 1.2$. These two schemes are capable of achieving convergent results, although the transient void fraction profiles appear rather smeared. In addition, at time $t = 1.0$ s, although pure air ($\alpha_g > 0.9999$) and pure liquid ($\alpha_g < 10^{-5}$) are obtained at the top and bottom regions of the vertical tube, respectively, the air-water mixture is not fully separated yet in the middle part of the tube. The reason why full separation is significantly slowed down with the SG-AUSMV and SG-FVS schemes is because these two schemes possess excessive numerical dissipation at volume-fraction contact discontinuities. The SG-AUSMD and SG-AUSMDV schemes have also been tested for this case. Unfortunately, they are unable to solve this problem.

Figure 5.26 demonstrates the effect of the interfacial pressure correction terms with values σ of 1.2, 6.0 and 10.0 on the void fraction and liquid velocity at $t = 0.6$ s. SG-AUSMFVS with $\kappa = 200$ is used on a grid of 101 nodes. As σ is increased to 10,

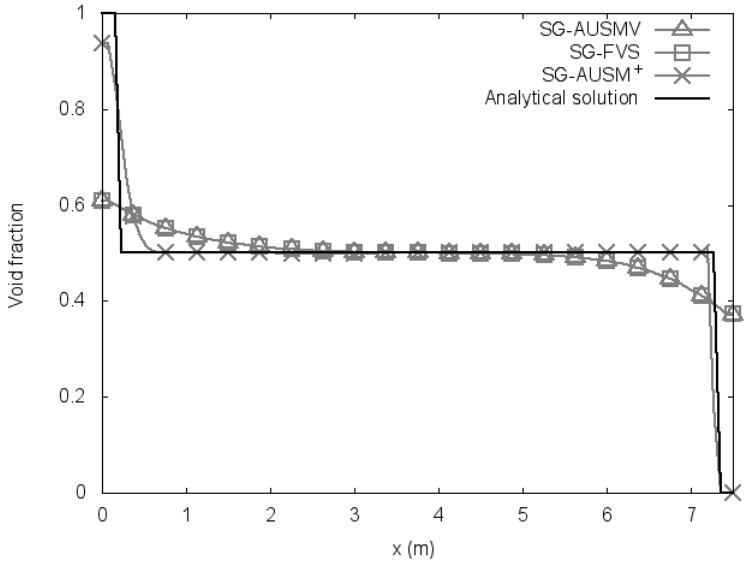

(a)

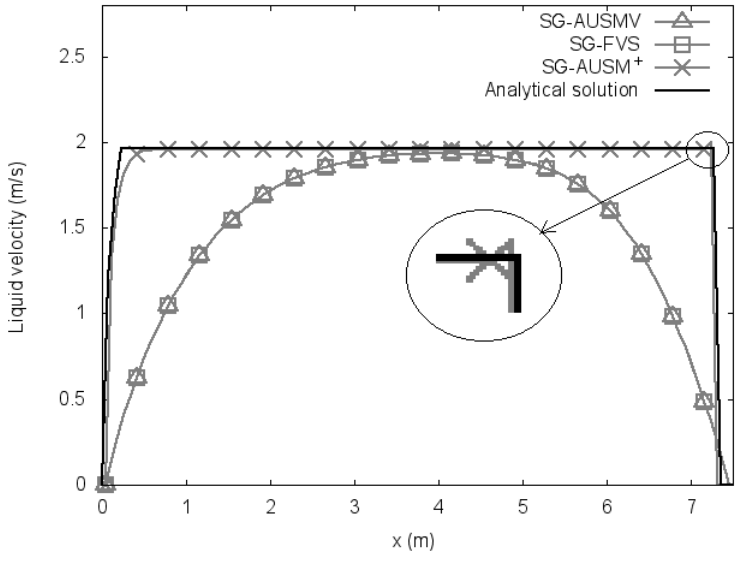

(b)

Figure 5.24: Phase separation problem: comparison among SG-AUSMV, SG-FVS, and SG-AUSM$^+$ at $t = 0.2$ s; $N = 101$; $\Delta t = \Delta x/(2000$ m/s); $\sigma = 1.2$; $C_f = 0.0$. (a) Void fraction; (b) Liquid velocity.

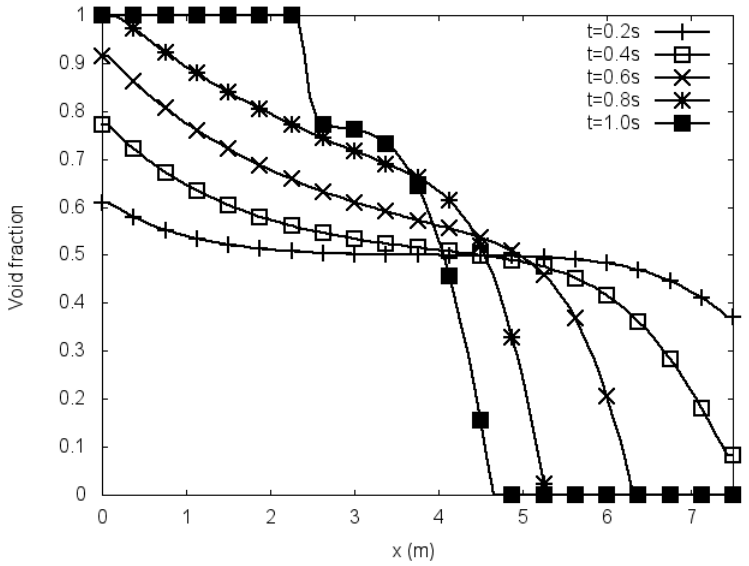

(a)

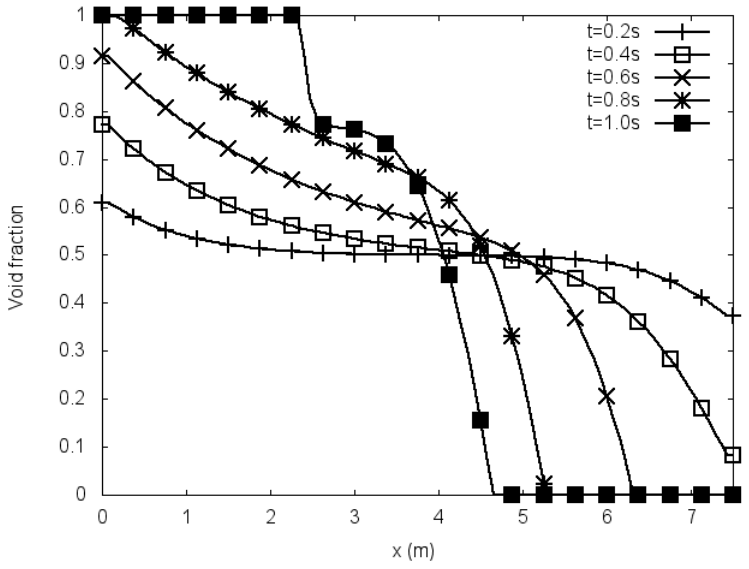

(b)

Figure 5.25: Phase separation problem: time evolution of void fraction profiles; $N = 101$; $\Delta t = \Delta x/(2000 \text{ m/s})$; $\sigma = 1.2$; $C_f = 0.0$. (a) SG-AUSMV; (b) SG-FVS.

the void fraction and liquid velocity profiles appear smeared. On the other hand, the dissipative effect of $\sigma = 1.2$ and $\sigma = 6.0$ on both the void fraction and liquid velocity profiles seem almost the same, and is much smaller than that with $\sigma = 10$. Further, with $\sigma = 6.0$, the overshoot at the right top corner of the liquid velocity profile, which is visible with $\sigma = 1.2$, is suppressed. Therefore, $\sigma = 6.0$ is chosen for the following simulations.

Figure 5.27 shows the void fraction and liquid velocity results at $t = 0.6$ s with different values of the smoothness control parameter κ (κ=20, 100, 200) in the switching function s of SG-AUSMFVS. $\sigma = 6.0$ is taken here. Note that the larger κ, the greater the weight of SG-AUSM$^+$. The results reveal that SG-AUSMFVS with κ=200 is capable of yielding more accurate solutions than that with κ=20 and 100, whose profiles are identical at $t = 0.6$ s. However, with κ=200, serious oscillations will be produced and consequently divergence takes place after $t = 0.6$ s. The oscillations are not shown here. The oscillations appear because κ controls the degree of the smoothness parameter ϕ. This in turn determines s, which is a weighting function that determines whether SG-AUSMFVS is biased towards SG-AUSM$^+$ or SG-FVS (see Eqs. 4.15 3.101 3.102). The larger κ, the more SG-AUSMFVS is biased towards SG-AUSM$^+$, reducing the amount of dissipation for the phase separation problem.

On the contrary, SG-AUSMFVS with κ=100 and 20 is able to give stable transient solutions. Accordingly, κ=100 is a good compromise and recommended here. This indicates that an appropriate choice of κ, and therefore s, will enable SG-AUSMFVS to solve a stiff transition problem from two-phase mixture to two single phases in an accurate and stable way. Since SG-FVS has a robust property for this phase separation problem, the weighting is biased towards SG-FVS to obtain stable solutions.

Figure 5.28 exhibits the time sequence of the void fraction by SG-AUSMFVS with $\sigma = 6.0$ and $\kappa = 100$. Clear upward and downward moving void fronts are observed, and the air-water mixture is completely separated after $t = 1.2$ s. This indicates that with appropriate σ and κ, the proposed SG-AUSMFVS scheme is capable of solving the phase separation problem in a stable and accurate manner.

The role of σ for SG-AUSM$^+$, SG-AUSMD, SG-AUSMV, SG-FVS, and SG-AUSMDV

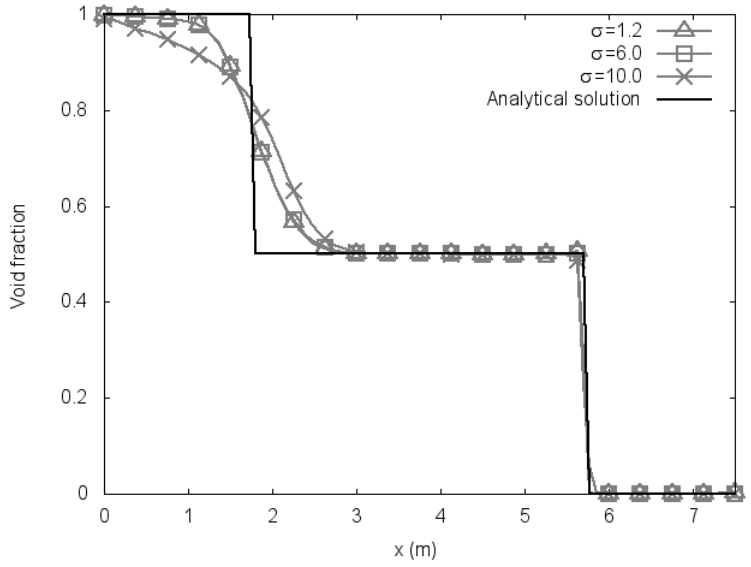

(a)

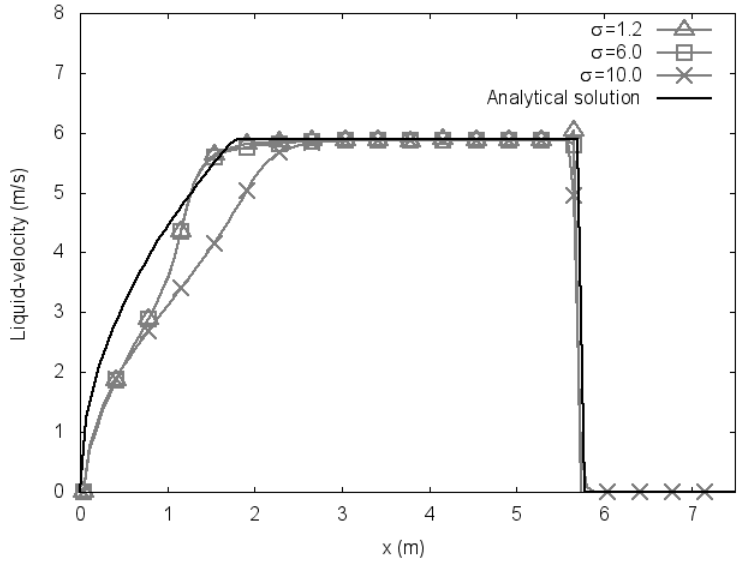

(b)

Figure 5.26: Phase separation problem: comparison among different interfacial pressure correction σ at $t = 0.6$ s by SG-AUSMFVS ($\kappa = 200$); $N = 101$; $\Delta t = \Delta x/(2000$ m/s); $C_f = 0.0$. (a) Void fraction; (b) Liquid velocity.

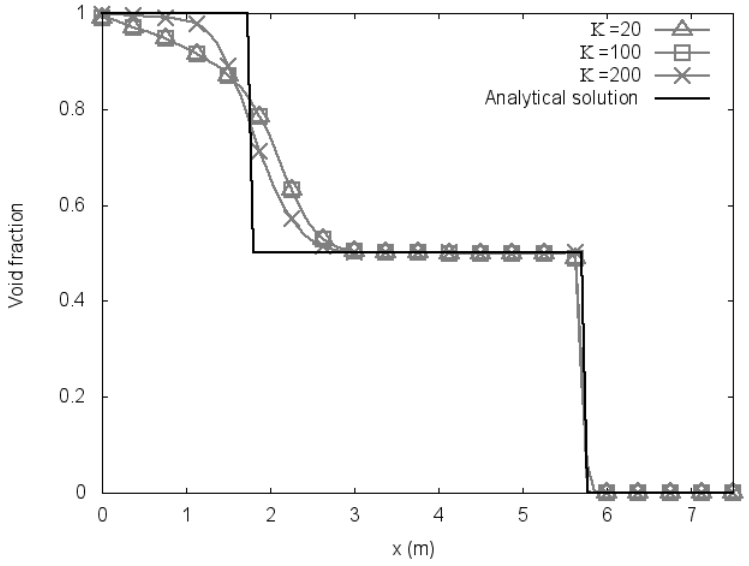

(a)

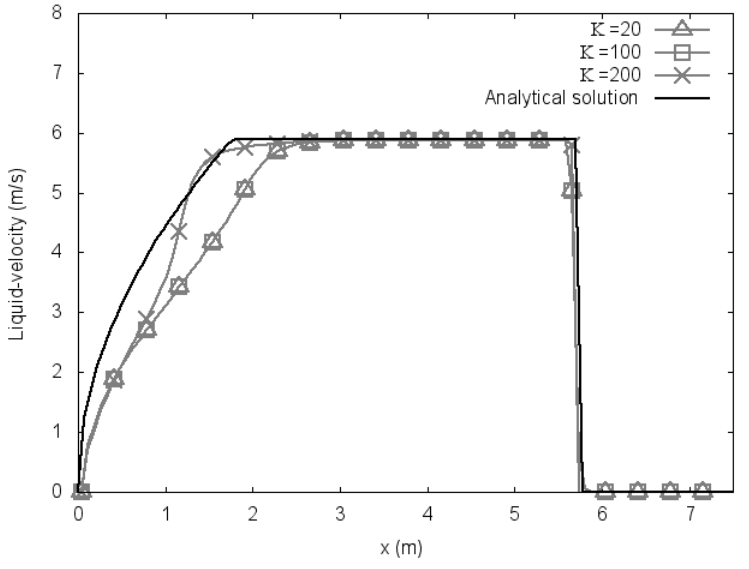

(b)

Figure 5.27: Phase separation problem at $t = 0.6$ s by SG-AUSMFVS with different values of the smoothness control parameter κ; $N = 101$; $\Delta t = \Delta x/(2000\ \mathrm{m/s})$; $\sigma = 6.0$; $C_f = 0.0$. (a) Void fraction; (b) Liquid velocity.

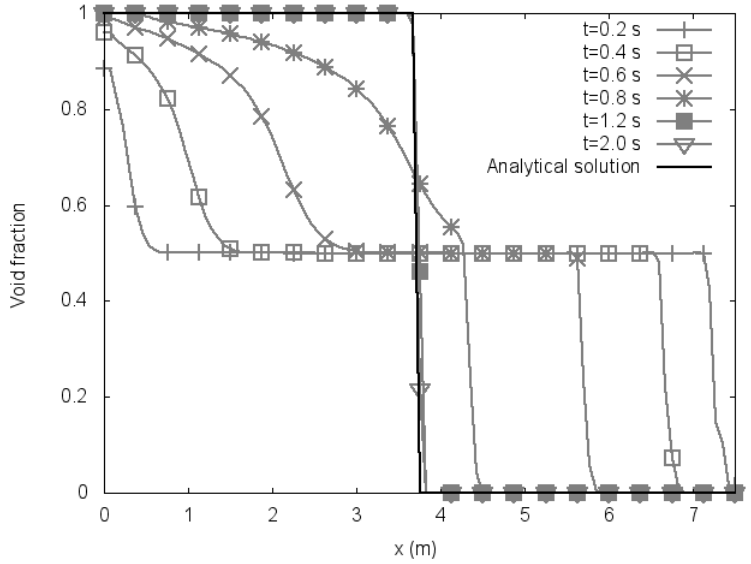

Figure 5.28: Phase separation problem: time evolution of void fraction profiles obtained with SG-AUSMFVS ($\kappa = 100$); $N = 101$; $\Delta t = \Delta x/(2000$ m/s); $\sigma = 6.0$; $C_f = 0.0$.

was also investigated. The SG-AUSM$^+$ scheme diverges when $t > 0.2$ s with $\sigma = 6$ and $\sigma = 10$. Also, the SG-FVS scheme diverges for $t > 1.2$ s with $\sigma = 6$. Both SG-AUSMD and SG-AUSMDV diverge for $t > 0.4$ s with $\sigma = 6$. However, SG-AUSMV is capable of producing stable results with $\sigma = 6$. Comparison of results between SG-AUSMFVS and SG-AUSMV is shown in Figs. 5.29 and 5.30. It is observed that SG-AUSMFVS is more accurate than SG-AUSMV. This is reasonable because SG-AUSMFVS is a combination of AUSM$^+$ and SG-FVS.

5.5.4 Air-Water Shock Tubes

Toumi's two-phase shock tube

The computation is performed up to $t = 0.04$ s on a staggered grid of 101 nodes with a time step $\Delta t = \frac{\Delta x}{2400\text{m/s}}$. The implicit SG-AUSMD/V, SG-FVS, SG-AUSM$^+$ and SG-AUSMFVS schemes are employed in this benchmark test. κ is set to be 5 in the SG-AUSMFVS scheme.

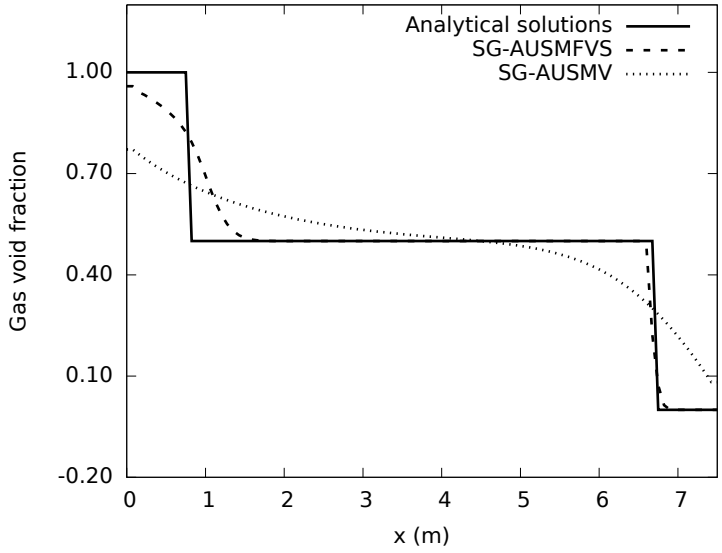

(a)

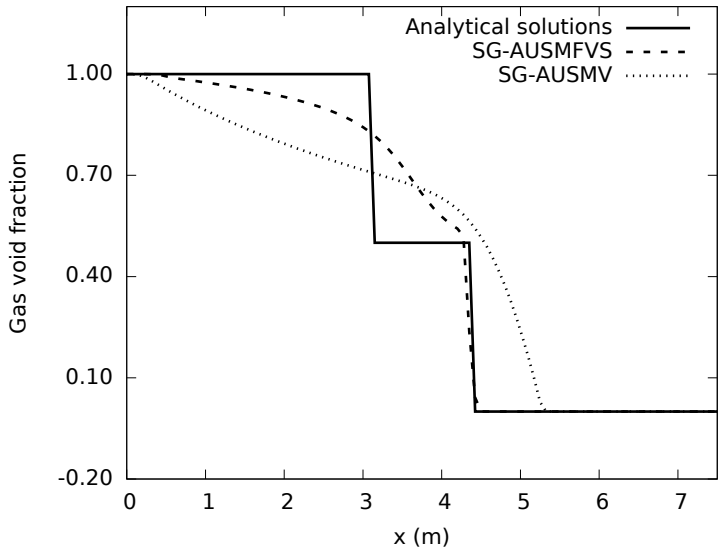

(b)

Figure 5.29: Phase separation problem: Comparison of void fraction between SG-AUSMFVS ($\kappa = 100$) and SG-AUSMV; $N = 101$; $\Delta t = \Delta x/(2000\ \mathrm{m/s})$; $\sigma = 6.0$; $C_f = 0.0$. (a) $t = 0.4$ s; (b) $t = 0.8$ s.

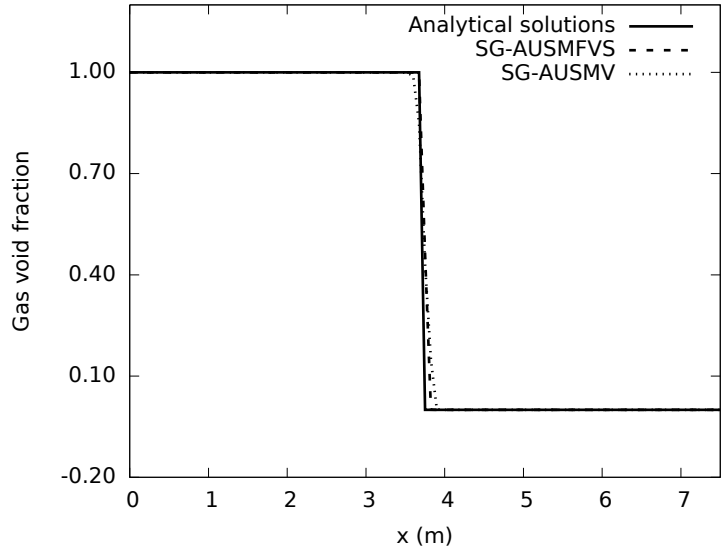

(a)

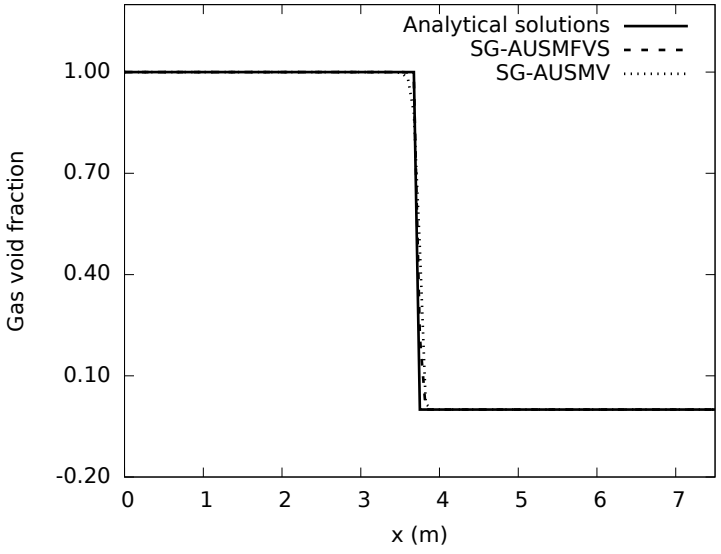

(b)

Figure 5.30: Phase separation problem: Comparison of void fraction between SG-AUSMFVS ($\kappa = 100$) and SG-AUSMV; $N = 101$; $\Delta t = \Delta x/(2000\ \mathrm{m/s})$; $\sigma = 6.0$; $C_f = 0.0$. (a) $t = 1.2$ s; (b) $t = 2.0$ s.

The results obtained with SG-AUSMD, SG-AUSMV, SG-AUSMDV, SG-FVS, SG-AUSM$^+$ and SG-AUSMFVS are given in Figs. 5.31 and 5.32. It is demonstrated that severe oscillations are produced with SG-AUSMD, SG-AUSMDV and SG-AUSM$^+$ in the vicinity of the contact discontinuity. Although SG-FVS, SG-AUSMV, and SG-AUSMFVS still produce overshoots and undershoots in the contact discontinuity, they greatly suppress the oscillations generated by SG-AUSMD, SG-AUSMDV and SG-AUSM$^+$. This indicates that SG-FVS, SG-AUSMV and SG-AUSMFVS are better than SG-AUSMD, SG-AUSMDV and SG-AUSM$^+$ in terms of dissipative mechanism to remove numerical oscillations for the air-water shock tube problem. After comparing the present results with those reported by Flåtten and Evje [79], who applied AUSM$^+$, the SG-AUSM$^+$ scheme significantly reduces the oscillations, especially for the liquid velocity whose Mach number is on the order of 10^{-3}. The alleviation of oscillations confirms the advantages of using the staggered-grid approach for solving the flow field at low Mach numbers.

Figures 5.33 and 5.34 show the grid-convergence study with SG-AUSMFVS for void fraction, pressure, gas velocity, and liquid velocity. A series of three grids, of 101 nodes, 501 nodes, 1001 nodes, have been employed in this study. It can be seen from Fig. 5.21 that as grid becomes finer, the profiles approach the reference one, but with overshoots and undershoots in the middle discontinuity. This indicates a need of adding diffusion terms in the SG-AUSMFVS scheme for Toumi's air-water shock tube problem.

Cortes' two-phase shock tube

The results obtained with SG-AUSMD/V, SG-AUSMDV, SG-FVS, SG-AUSM$^+$, and SG-AUSMFVS for Cortes' two-phase shock tube problem are shown in Figs. 5.35 and 5.36. κ is set to be 5 in SG-AUSMFVS. The reference solution was obtained with the explicit PD-AUSM$^+$ scheme on a grid of 10,001 nodes. In addition, the results obtained with the Roe scheme are also plotted for comparison purposes. It is demonstrated that SG-AUSMV, SG-FVS and SG-AUSMFVS are capable of producing stable solutions; whereas, SG-AUSMD and SG-AUSMDV schemes are not. The SG-AUSM$^+$ scheme generates stable solutions except that a small overshoot is observed at the discontinuity of the void fraction where shock

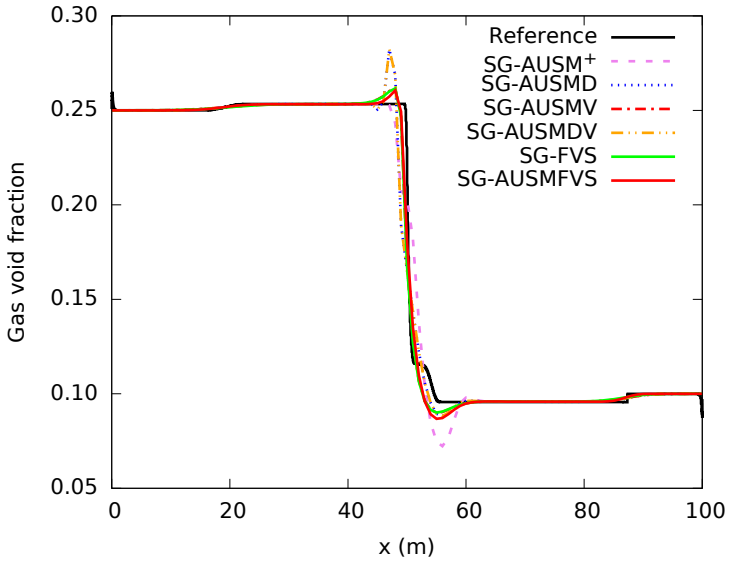

(a)

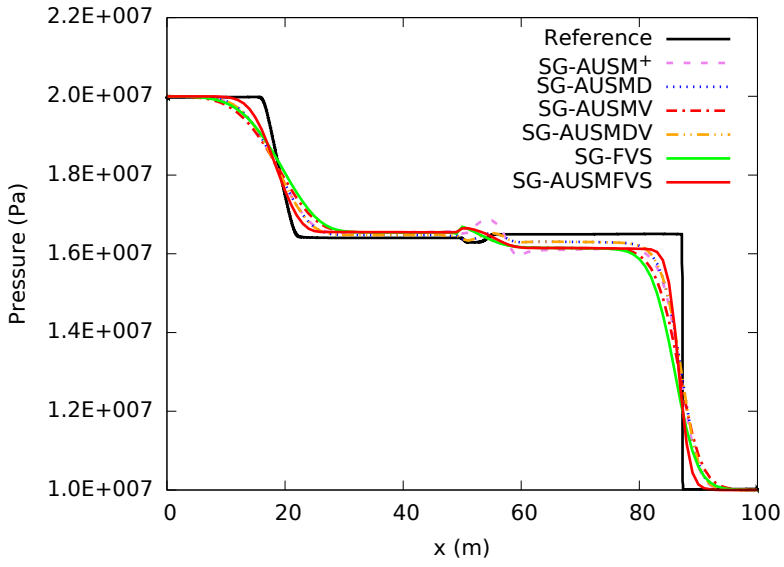

(b)

Figure 5.31: Toumi's air-water shock tube problem: comparison among SG-AUSMD, SG-AUSMV, SG-AUSMDV, SG-FVS, SG-AUSM$^+$ and SG-AUSMFVS ($\kappa = 5$) at $t = 0.04$ s; $N = 101$; $\Delta t = \Delta x/(2400$ m/s); $\sigma = 1.2$; $C_f = 0.0$. (a) Void fraction; (b) Pressure.

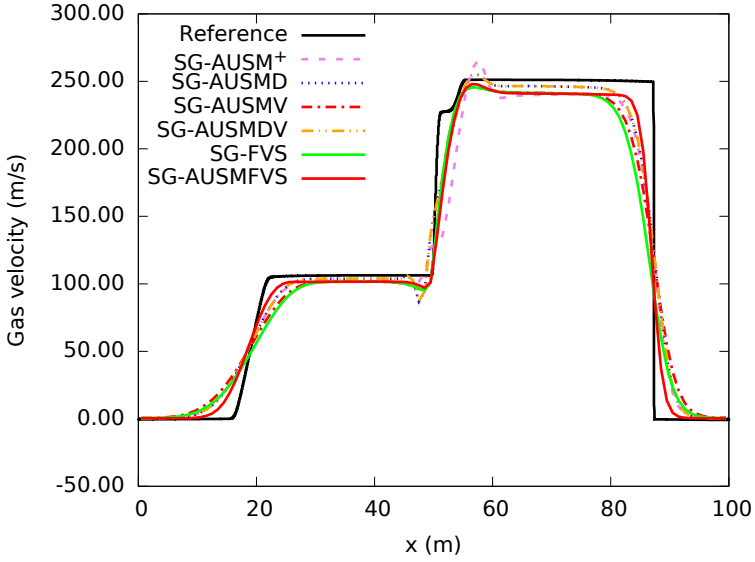

(a)

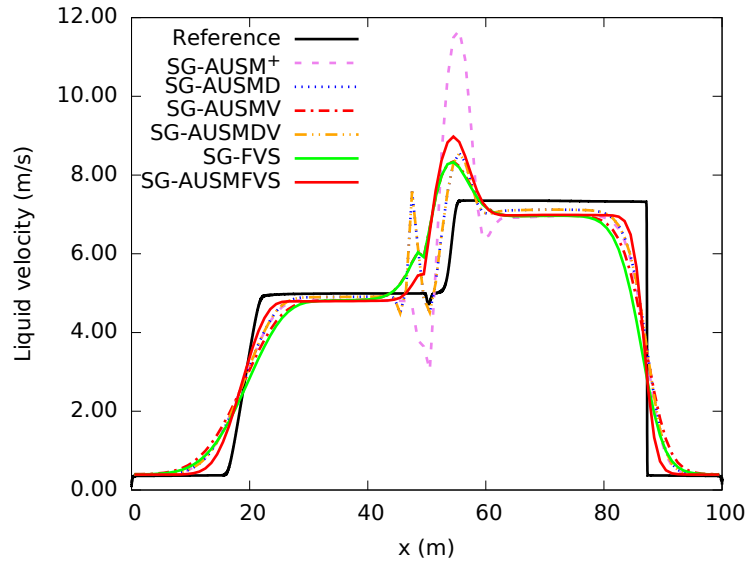

(b)

Figure 5.32: Toumi's air-water shock tube problem: comparison among SG-AUSMD, SG-AUSMV, SG-AUSMDV, SG-FVS, SG-AUSM$^+$ and SG-AUSMFVS ($\kappa = 5$) at $t = 0.04$ s; $N = 101$; $\Delta t = \Delta x/(2400$ m/s); $\sigma = 1.2$; $C_f = 0.0$. (a) Gas velocity; (b) Liquid velocity.

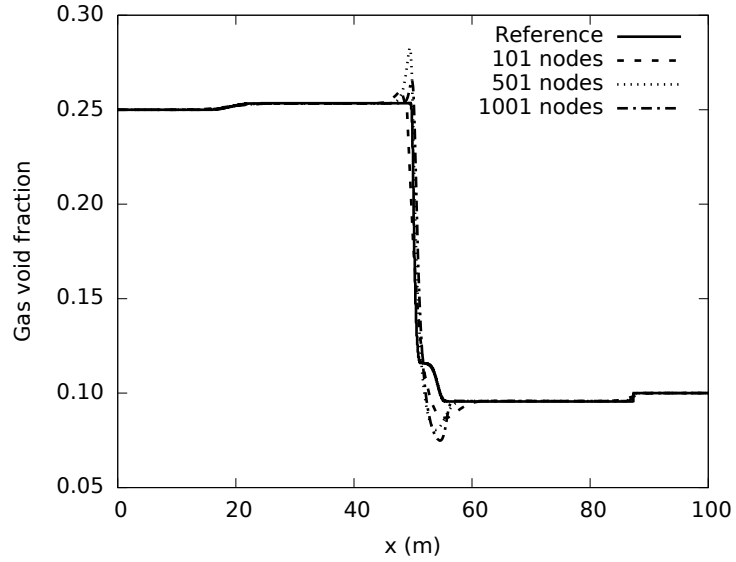

(a)

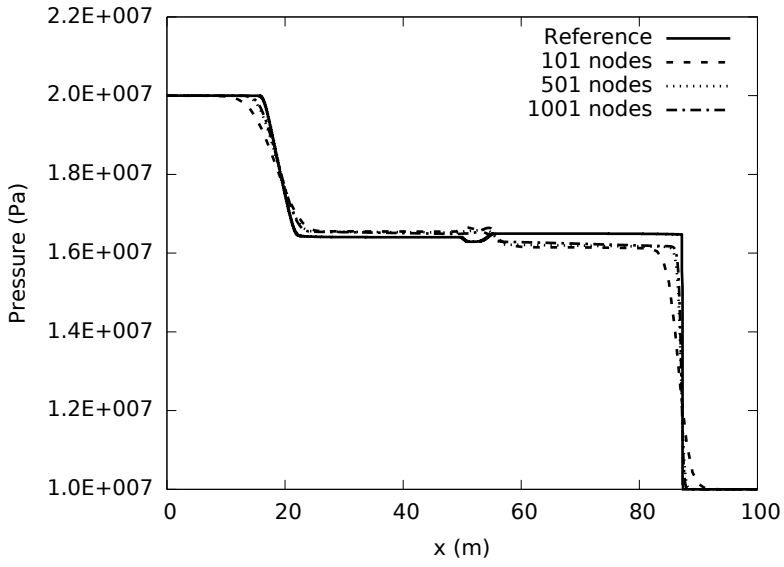

(b)

Figure 5.33: Toumi's air-water shock tube problem: grid convergence study with SG-AUSMFVS ($\kappa = 5$) at $t = 0.04$ s; $\Delta t = \Delta x/(2400$ m/s); $\sigma = 1.2$; $C_f = 0.0$. (a) Void fraction; (b) Pressure.

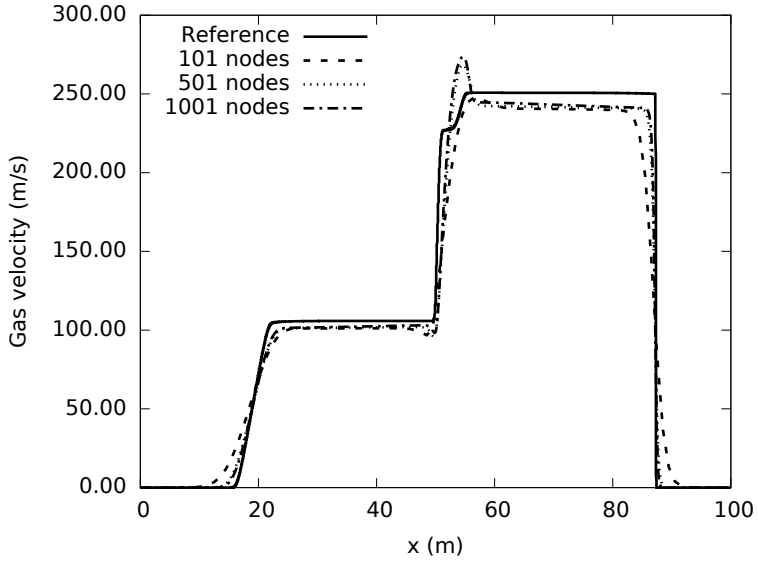

(a)

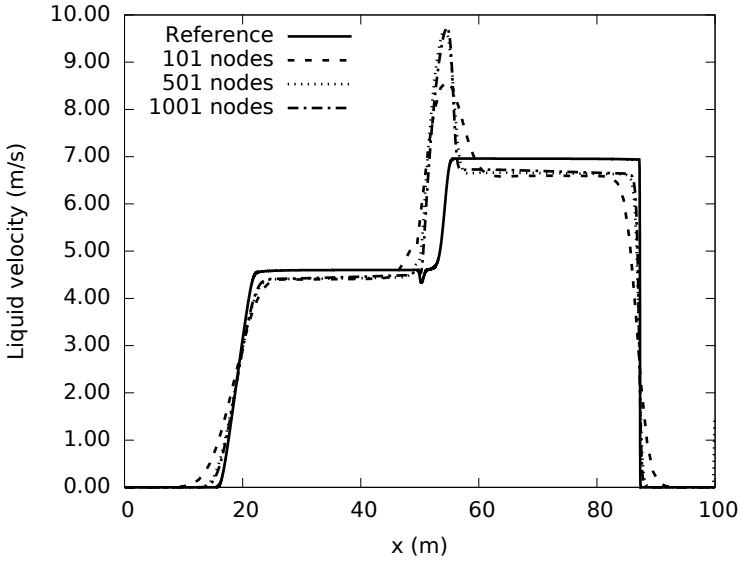

(b)

Figure 5.34: Toumi's air-water shock tube problem: grid convergence study with SG-AUSMFVS ($\kappa = 5$) at $t = 0.04$ s; $\Delta t = \Delta x/(2400$ m/s); $\sigma = 1.2$; $C_f = 0.0$. (a) Gas velocity; (b) Liquid velocity.

occurs. In addition, from Figs. 5.35 and 5.36, it is noticed that the results obtained with SG-FVS are more smeared than those obtained with SG-AUSMFVS. Furthermore, it can be seen that the new SG-AUSMFVS scheme performs slightly better than the Roe scheme in terms of accuracy.

Figures 5.37 and 5.38 show the grid-convergence study with SG-AUSMFVS for the void fraction, pressure, gas velocity, and liquid velocity. A series of three grids of 101 nodes, 501 nodes, and 1001 nodes, have been employed in this study. Figure 5.21 shows that the grid convergence is achieved without any oscillations.

Ejve's two-phase shock tube

The results obtained with SG-AUSMD/V, SG-AUSMDV, SG-FVS, SG-AUSM$^+$, SG-AUSMFVS and Roe schemes for Ejve's two-phase shock tube problem are displayed in Figs. 5.39 and 5.40. κ is set to be 200 in the SG-AUSMFVS scheme. The reference solution was obtained with the explicit PD-AUSM$^+$ scheme on a grid of 10,001 nodes. In this test case, both SG-AUSM$^+$ and SG-AUSMFVS are capable of producing non-oscillating results; whereas, SG-AUSMD and SG-AUSMDV generate severe oscillation at the discontinuity of void fraction where the shock occurs. The Roe scheme is also able to produce smooth solutions without oscillations, but not comparable to SG-AUSM$^+$ and SG-AUSMFVS regarding the accuracy. In addition, although SG-FVS and SG-AUSMV schemes do not generate as severe oscillations as SG-AUSMD and SG-AUSMDV, they produce overshoots and undershoots in the middle discontinuity. This indicates proper numerical dissipation in SG-AUSM$^+$ and SG-AUSMFVS for Ejve's shock tube problem.

Figures 5.41 and 5.42 show the grid-convergence study with SG-AUSMFVS for the void fraction, pressure, gas velocity, and liquid velocity. A series of three grids of 101 nodes, 501 nodes, and 1001 nodes have been employed in this study. Similar to Cortes' shock tube problem, Fig. 5.21 shows that the grid convergence is achieved without any oscillations for Ejve's shock tube problem.

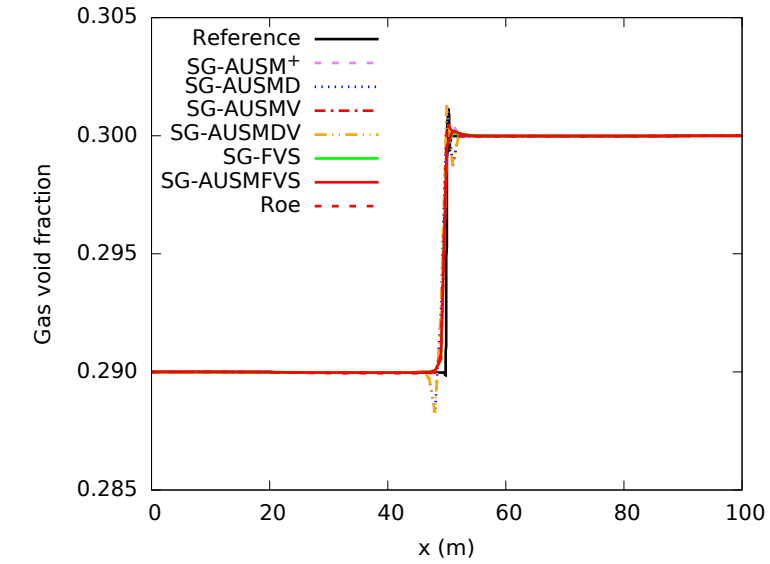

(a)

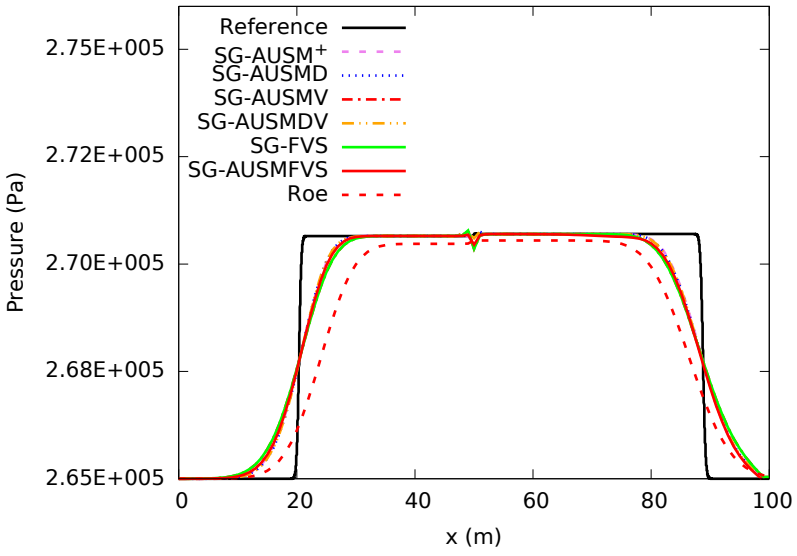

(b)

Figure 5.35: Cortes' air-water shock tube problem: comparison among the Roe, SG-AUSMD, SG-AUSMV, SG-AUSMDV, SG-FVS, SG-AUSM$^+$ and SG-AUSMFVS ($\kappa = 5$) schemes at $t = 0.08$ s; $N = 101$; $\Delta t = \Delta x/(1000$ m/s); $\sigma = 1.2$; $C_f = 0.0$. (a) Void fraction; (b) Pressure.

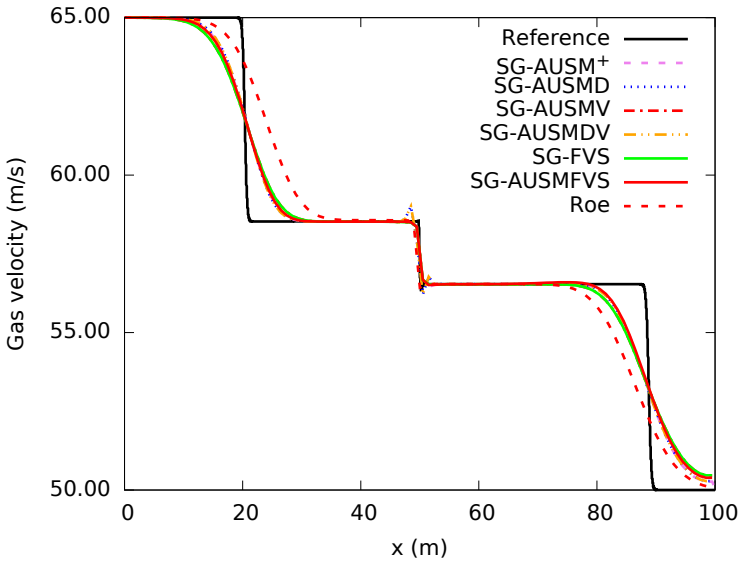

(a)

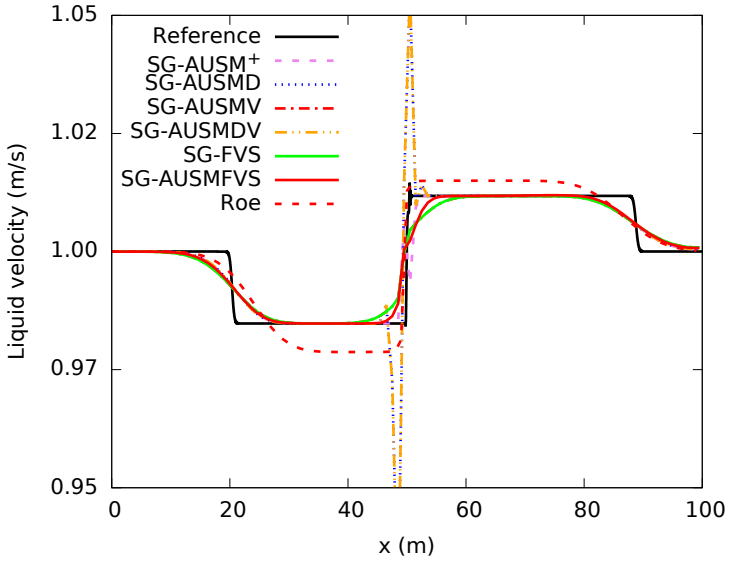

(b)

Figure 5.36: Cortes' air-water shock tube problem: comparison among the Roe, SG-AUSMD, SG-AUSMV, SG-AUSMDV, SG-FVS, SG-AUSM$^+$ and SG-AUSMFVS ($\kappa = 5$) schemes at $t = 0.08$ s; $N = 101$; $\Delta t = \Delta x/(1000$ m/s); $\sigma = 1.2$; $C_f = 0.0$. (a) Gas velocity; (b) Liquid velocity.

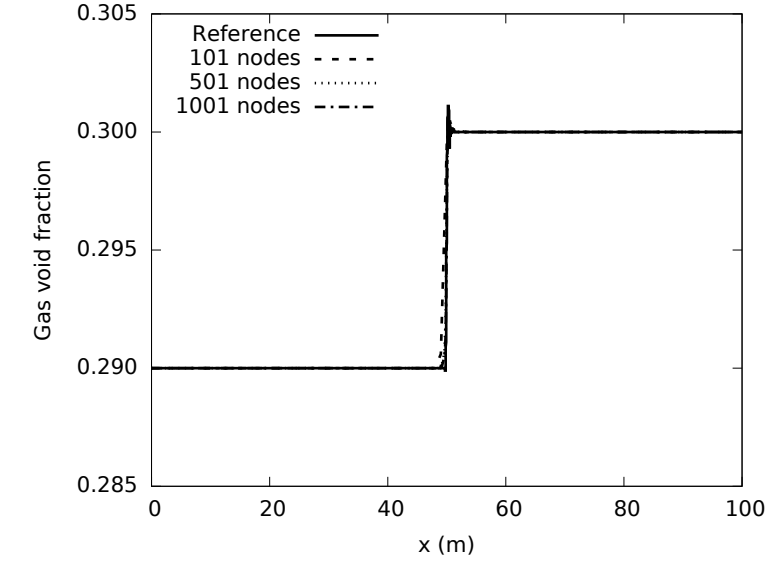

(a)

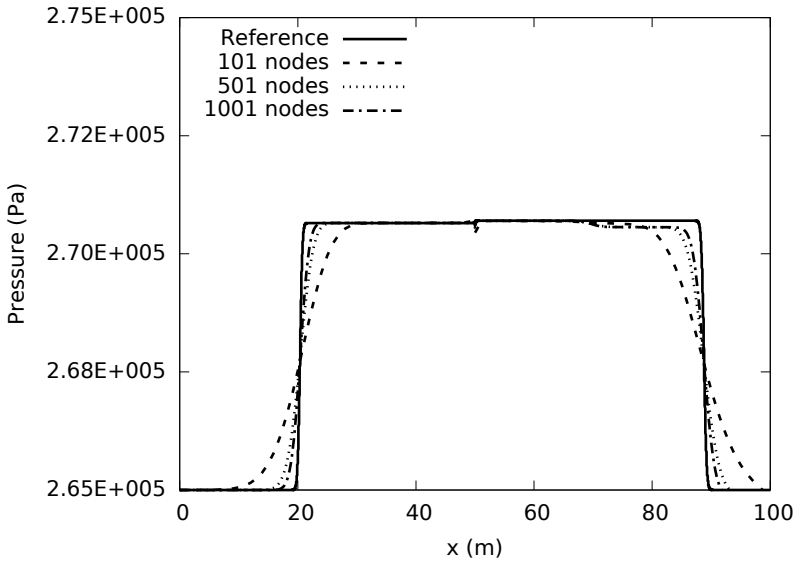

(b)

Figure 5.37: Cortes' air-water shock tube problem: grid-convergence study with SG-AUSMFVS ($\kappa = 5$) at $t = 0.08$ s; $\Delta t = \Delta x/(1000$ m/s); $\sigma = 1.2$; $C_f = 0.0$. (a) Void fraction; (b) Pressure.

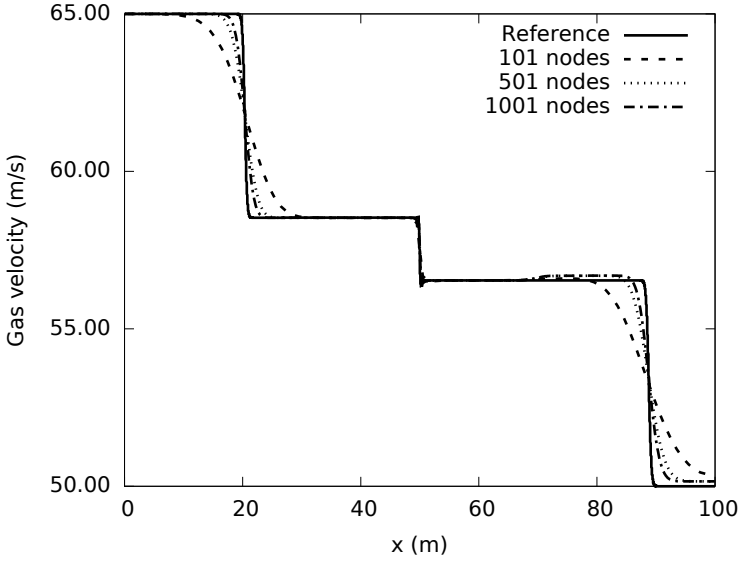

(a)

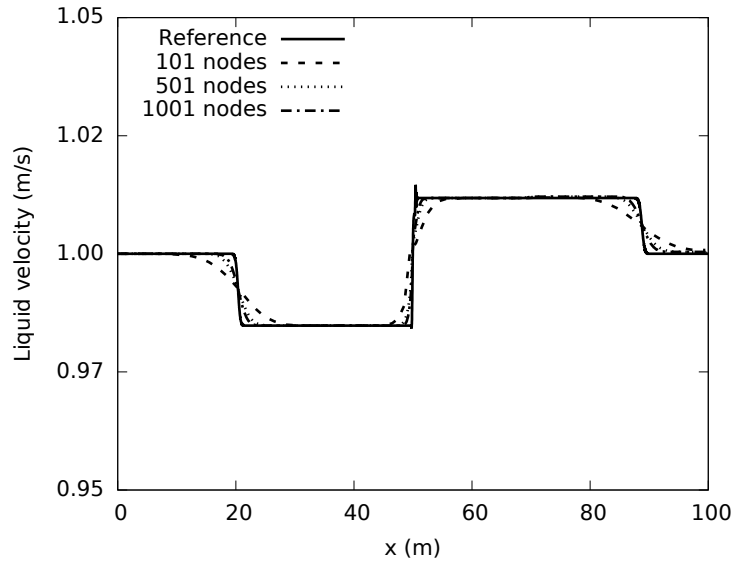

(b)

Figure 5.38: Cortes' air-water shock tube problem: grid-convergence study with SG-AUSMFVS ($\kappa = 5$) at $t = 0.08$ s; $\Delta t = \Delta x/(1000$ m/s); $\sigma = 1.2$; $C_f = 0.0$. (a) Gas velocity; (b) Liquid velocity.

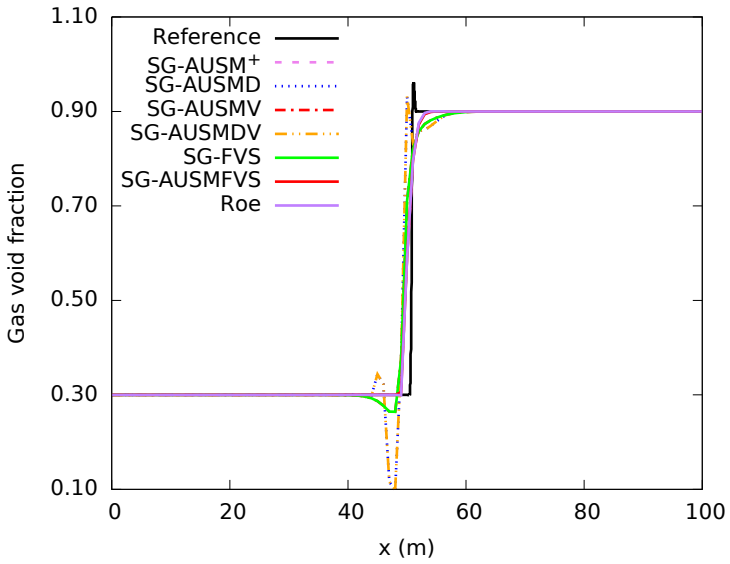

(a)

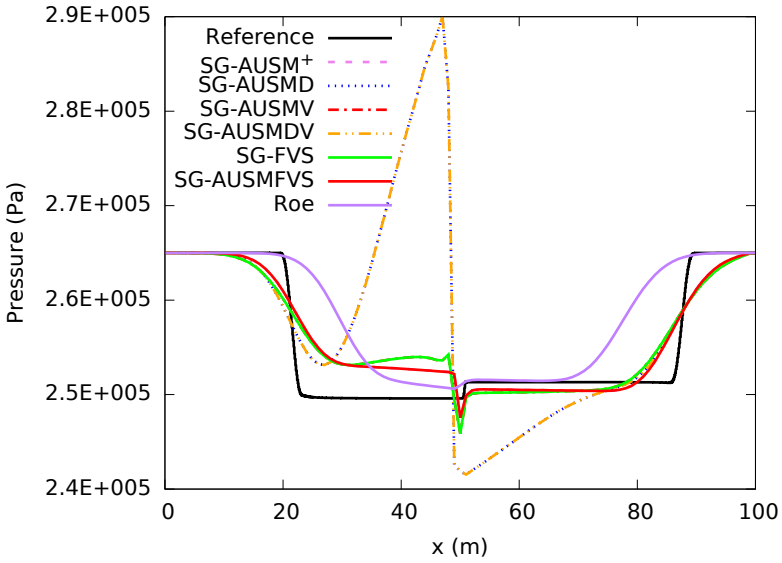

(b)

Figure 5.39: Ejve's air-water shock tube problem: comparison among the Roe, SG-AUSMD, SG-AUSMV, SG-AUSMDV, SG-FVS, SG-AUSM$^+$ and SG-AUSMFVS ($\kappa = 200$) schemes at $t = 0.08$ s; $N = 101$; $\Delta t = \Delta x/(1000\ \mathrm{m/s})$; $\sigma = 1.2$; $C_f = 0.0$. (a) Void fraction; (b) Pressure.

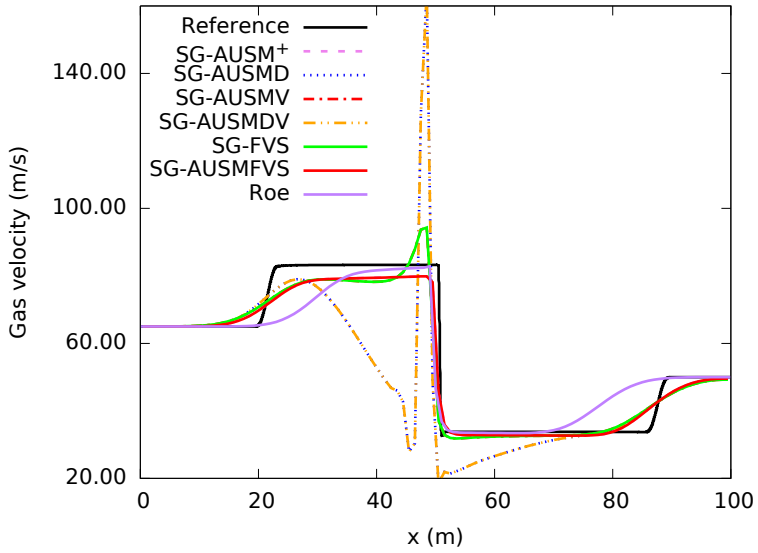

(a)

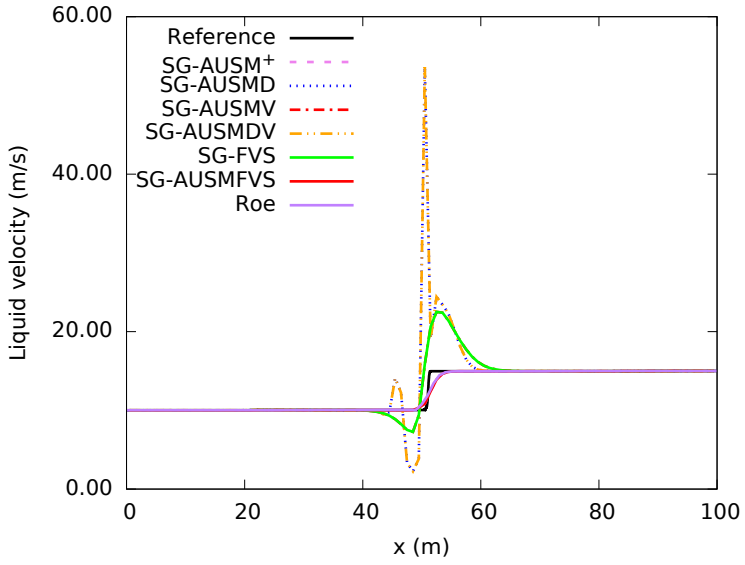

(b)

Figure 5.40: Ejve's air-water shock tube problem: comparison among the Roe, SG-AUSMD, SG-AUSMV, SG-AUSMDV, SG-FVS, SG-AUSM$^+$ and SG-AUSMFVS ($\kappa = 200$) schemes at $t = 0.08$ s; $N = 101$; $\Delta t = \Delta x/(1000$ m/s); $\sigma = 1.2$; $C_f = 0.0$. (a) Gas velocity; (b) Liquid velocity.

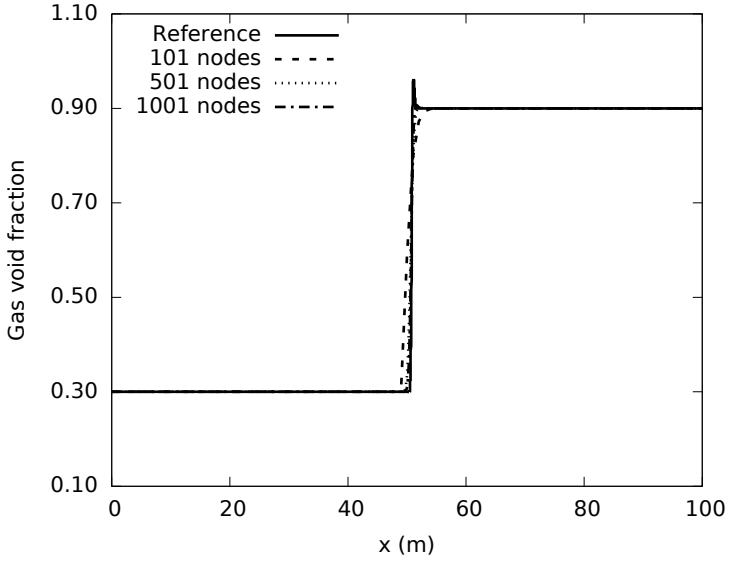

(a)

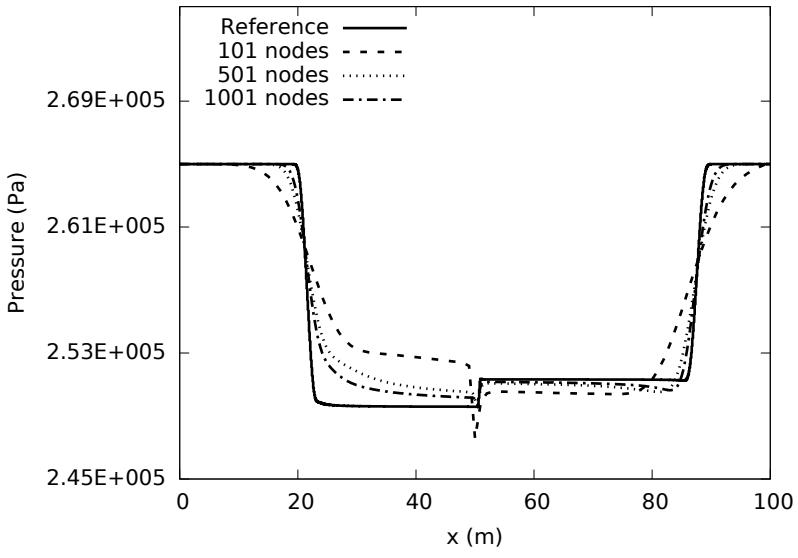

(b)

Figure 5.41: Ejve's air-water shock tube problem: grid-convergence study with SG-AUSMFVS ($\kappa = 200$) at $t = 0.08$ s; $\Delta t = \Delta x/(1000$ m/s); $\sigma = 1.2$; $C_f = 0.0$. (a) Void fraction; (b) Pressure.

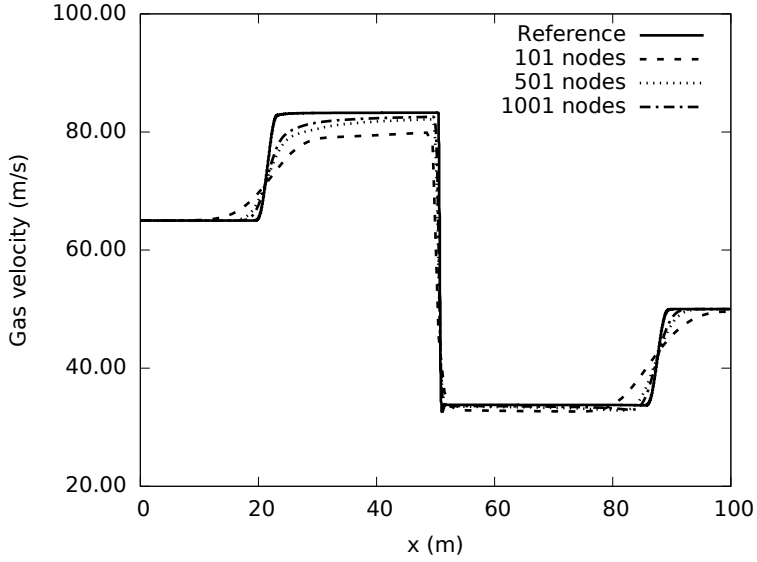

(a)

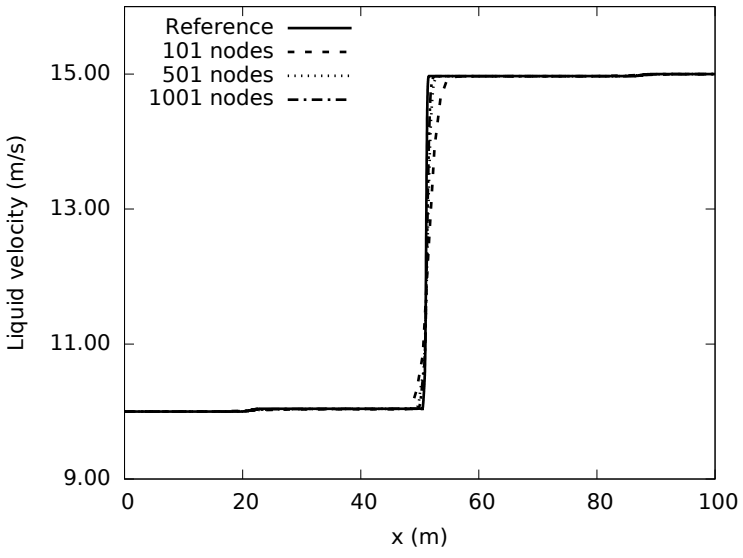

(b)

Figure 5.42: Ejve's air-water shock tube problem: grid-convergence study with SG-AUSMFVS ($\kappa = 200$) at $t = 0.08$ s; $\Delta t = \Delta x/(1000$ m/s); $\sigma = 1.2$; $C_f = 0.0$. (a) Gas velocity; (b) Liquid velocity.

5.5.5 Comparison between Collocated-grid Cases and Staggered-grid Cases

For the water faucet and oscillating manometer problems, the results obtained with both SG-AUSM$^+$ and collocated-grid-based AUSM$^+$ are similar in terms of closeness to the analytical or reference solutions, as shown in Figs. 5.43, 5.44 and 5.45 below. Note that for the oscillating manometer problem, when using a collocated-grid arrangement, additional dissipation in liquid mass flux is required to obtain stable solutions. Therefore, the PD-AUSM$^+$ scheme is adopted on collocated grids for the oscillating manometer problem.

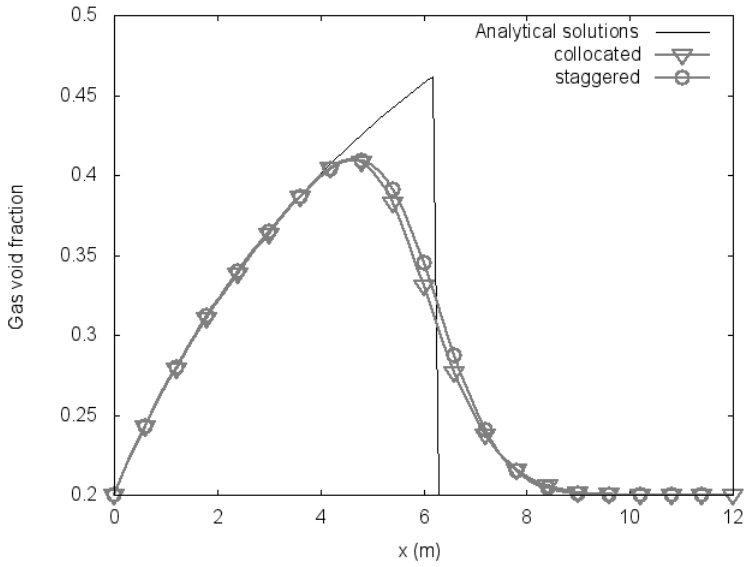

Figure 5.43: Water faucet problem: comparison of the void fraction between AUSM$^+$ and SG-AUSM$^+$ at $t = 0.5$ s; $N = 101$; $\Delta t = 10^{-4}$ s; $\sigma = 2.0$; $C_f = 0.0$.

However, for the shock tube problems, including Toumis, Cortes and Ejves test cases, the staggered-grid approach is more stable than the collocated-grid approach, as shown in Figs. 5.46, 5.47, 5.48, 5.49, 5.50 and 5.51 below.

In addition to the comparison of accuracy between the collocated-gird-based scheme and staggered-grid-based one, a precise quantification of the CPU time is summarized in Table 5.4. The numerical simulations were conducted on SHARCNET (www.sharcnet.ca).

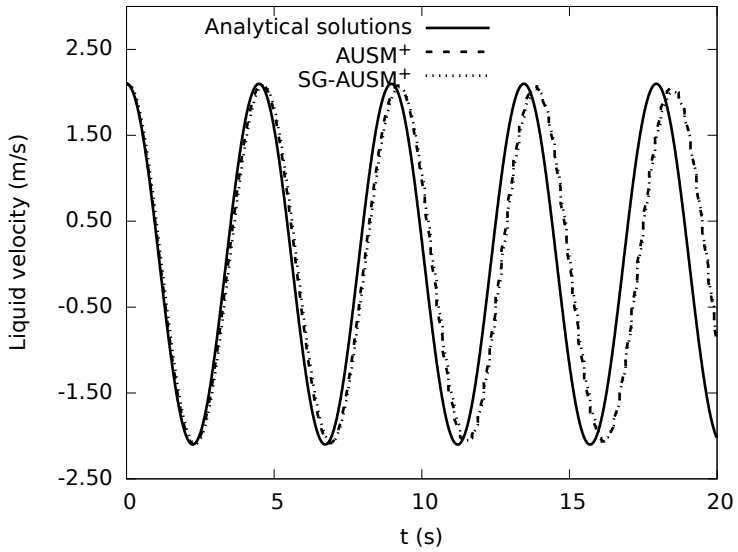

Figure 5.44: Oscillating manometer problem: comparison between AUSM$^+$ and SG-AUSM$^+$; $N = 101$; $\Delta t = \Delta x/3000$ m/s; $\sigma = 0.0$; $C_f = 5 \times 10^4$ s^{-1}. Liquid velocity with time at the bottom of the tube.

Based on the results given in Table 5.4, it can be concluded that SG-AUSM$^+$ saves approximately 60% of the CPU time with respect to AUSM$^+$. The reasons why the staggered-grid-based scheme is more efficient than their collocated-grid-based counterpart are likely due to the following two factors.

First, the time-derivative preconditioning technique or numerical dissipation required for collocated-grid-based schemes for low-Mach-number problems become unnecessary when staggered-grid-based schemes are employed. Second, with the adoption of the staggered-grid arrangement, there is no need for the interpolation of interfacial scalar variables, such as the interfacial pressure for the collocated-grid arrangement. Since these scalar variables are stored at the center of the pressure control volume (p-CV), they are readily available at the interfaces of the velocity control volume (u-CV), which is half a control volume away from p-CV.

Additionally, another advantage of the staggered-based method is that there is no need to make a special treatment for the discretization of the non-conservative term compat-

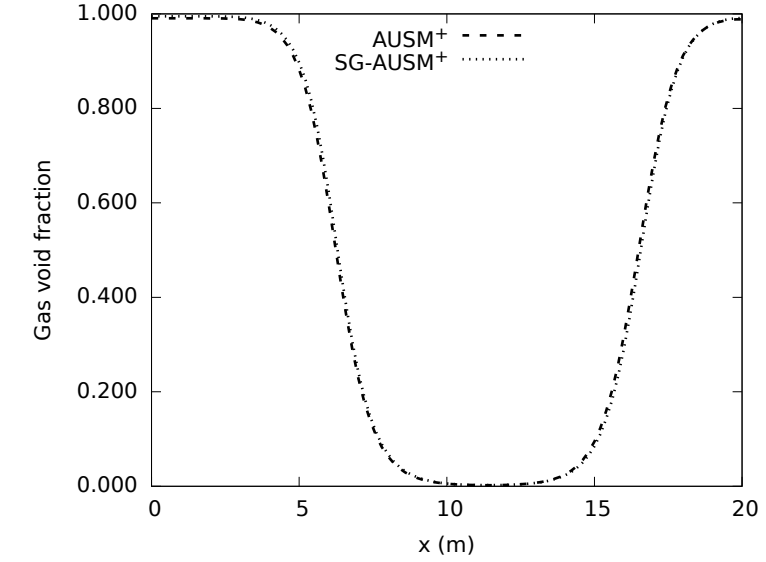

(a)

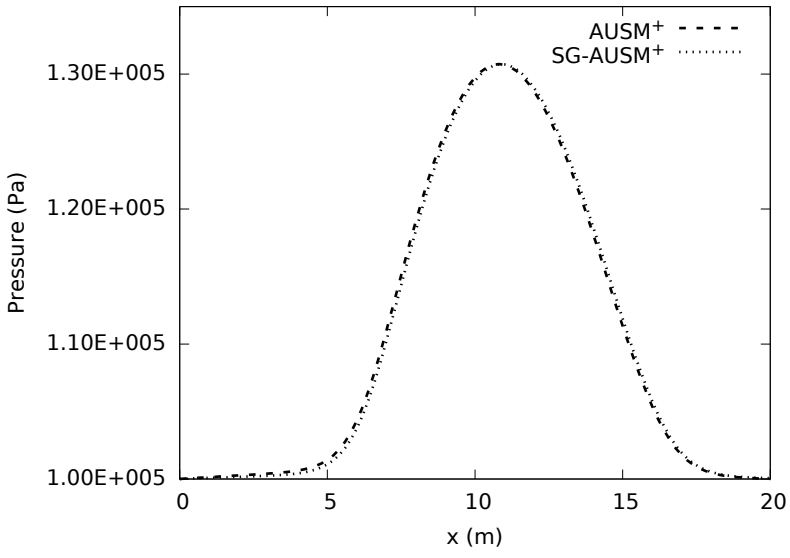

(b)

Figure 5.45: Oscillating manometer problem: comparison between AUSM$^+$ and SG-AUSM$^+$ at $t = 20$ s; $N = 101$; $\Delta t = 6.7 \times 10^{-5}$ s; $\sigma = 0.0$; $C_f = 5 \times 10^4$ s^{-1}. (a) Void fraction and (b) Pressure.

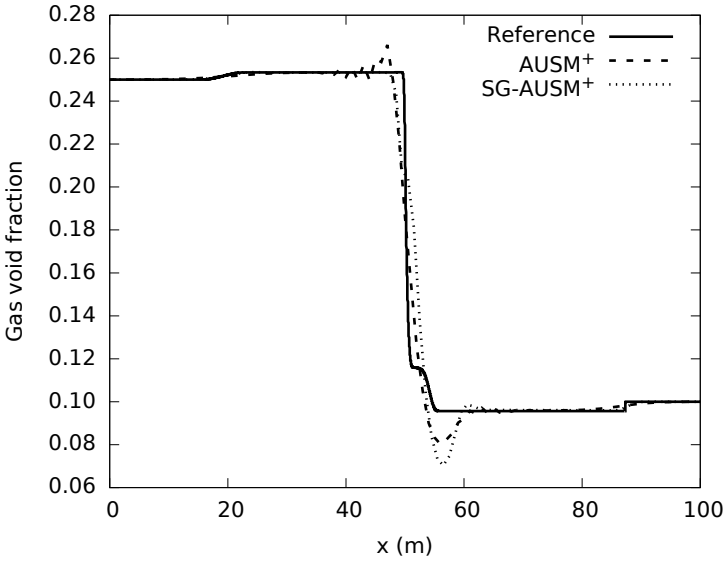

(a)

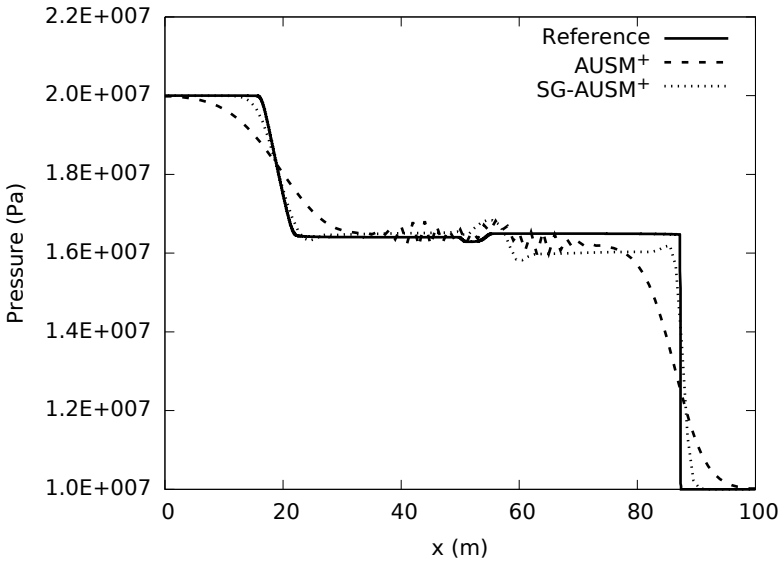

(b)

Figure 5.46: Toumi's air-water shock tube problem: comparison between AUSM$^+$ and SG-AUSM$^+$ at $t = 0.04$ s; $N = 101$; $\Delta t = \Delta x/(2400$ m/s); $\sigma = 1.2$; $C_f = 0.0$. (a) Void fraction; (b) Pressure.

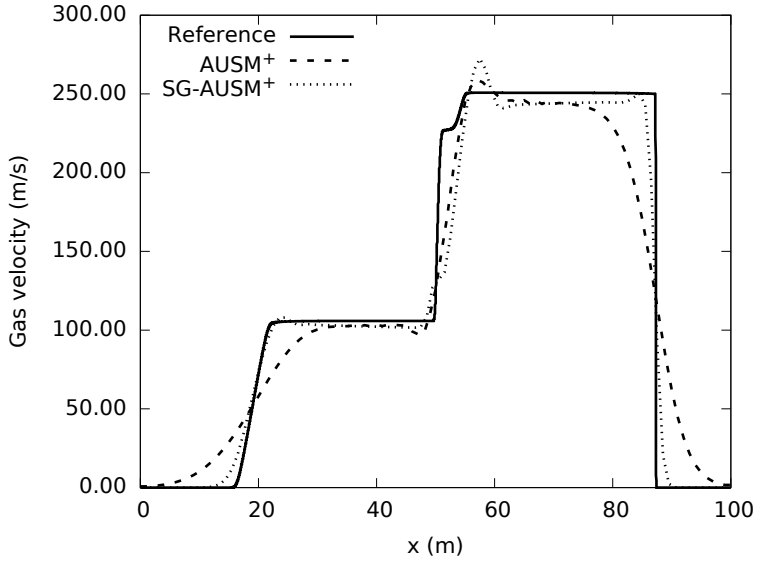

(a)

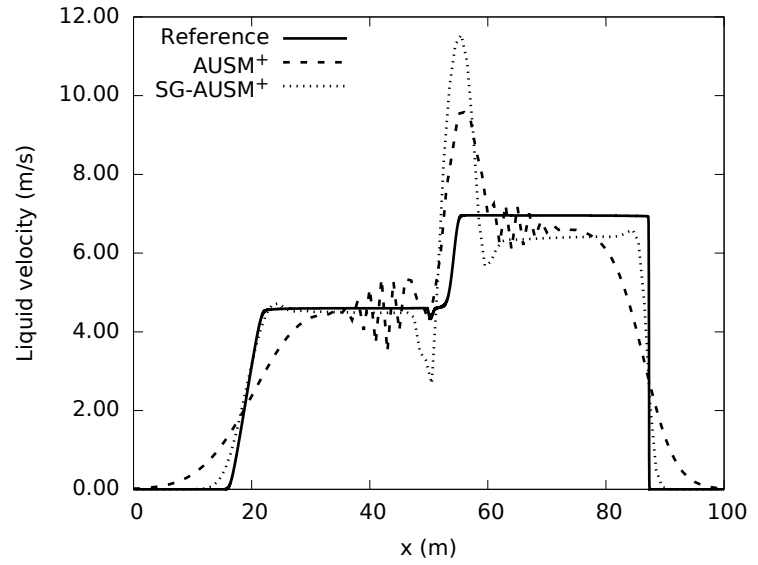

(b)

Figure 5.47: Toumi's air-water shock tube problem: comparison between the AUSM$^+$ and SG-AUSM$^+$ at $t = 0.04$ s; $N = 101$; $\Delta t = \Delta x/(2400 \text{ m/s})$; $\sigma = 1.2$; $C_f = 0.0$. (a) Gas velocity; (b) Liquid velocity.

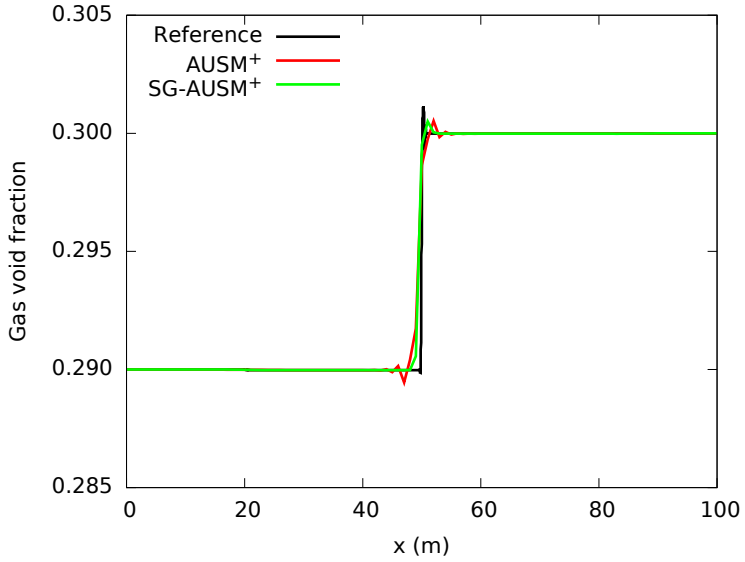

(a)

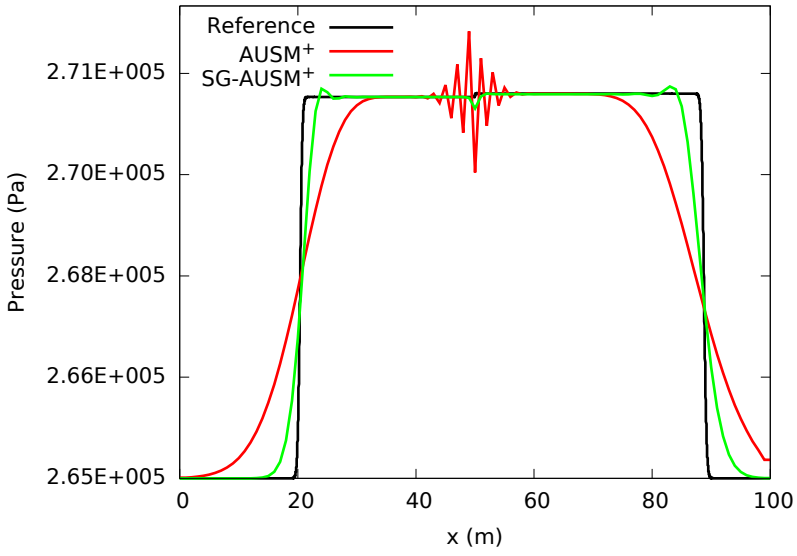

(b)

Figure 5.48: Cortes' air-water shock tube problem: comparison between AUSM$^+$ and SG-AUSM$^+$ at $t = 0.08$ s; $N = 101$;; $\Delta t = \Delta x/(1000$ m/s); $\sigma = 1.2$; $C_f = 0.0$. (a) Void fraction; (b) Pressure.

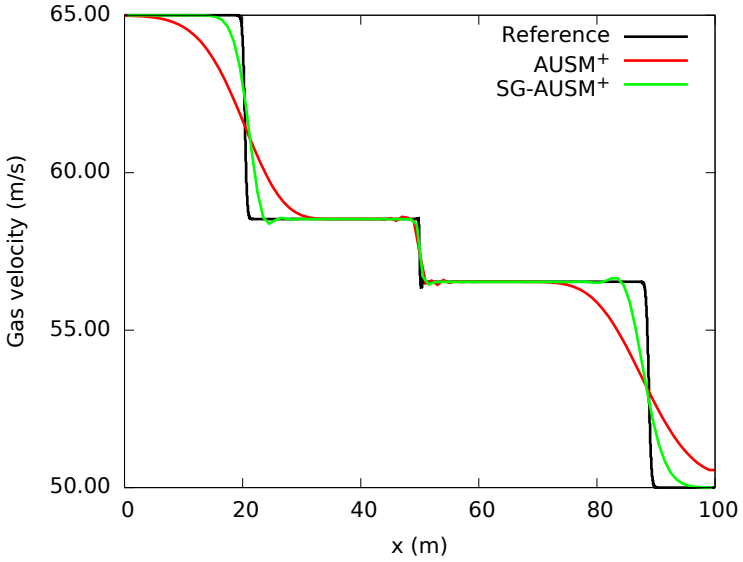

(a)

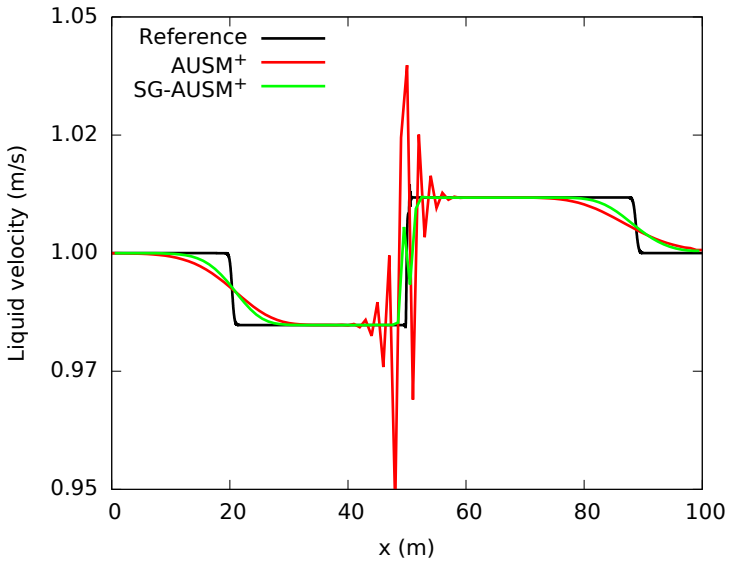

(b)

Figure 5.49: Cortes' air-water shock tube problem: comparison between the AUSM$^+$ and SG-AUSM$^+$ at $t = 0.08$ s; $N = 101$; $\Delta t = \Delta x/(1000$ m/s); $\sigma = 1.2$; $C_f = 0.0$. (a) Gas velocity; (b) Liquid velocity.

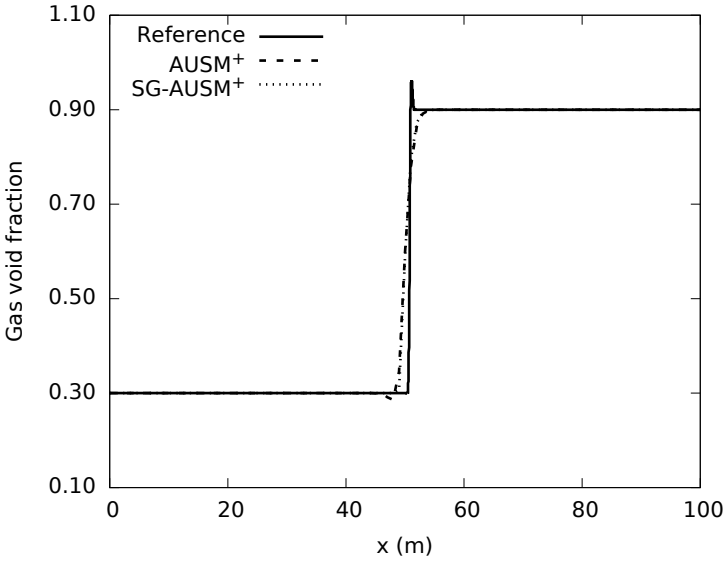

(a)

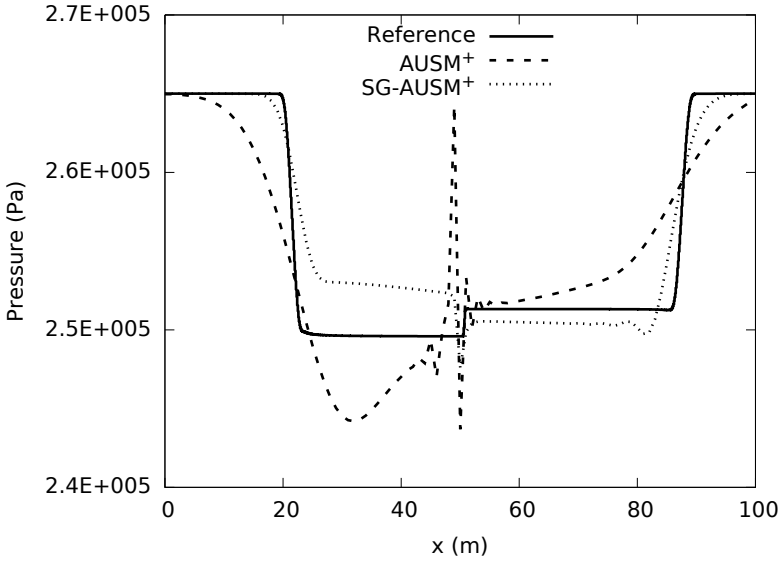

(b)

Figure 5.50: Ejve's air-water shock tube problem: comparison between AUSM$^+$ and SG-AUSM$^+$ at $t = 0.08$ s; $N = 101$; $\Delta t = \Delta x/(1000$ m/s); $\sigma = 1.2$; $C_f = 0.0$. (a) Void fraction; (b) Pressure.

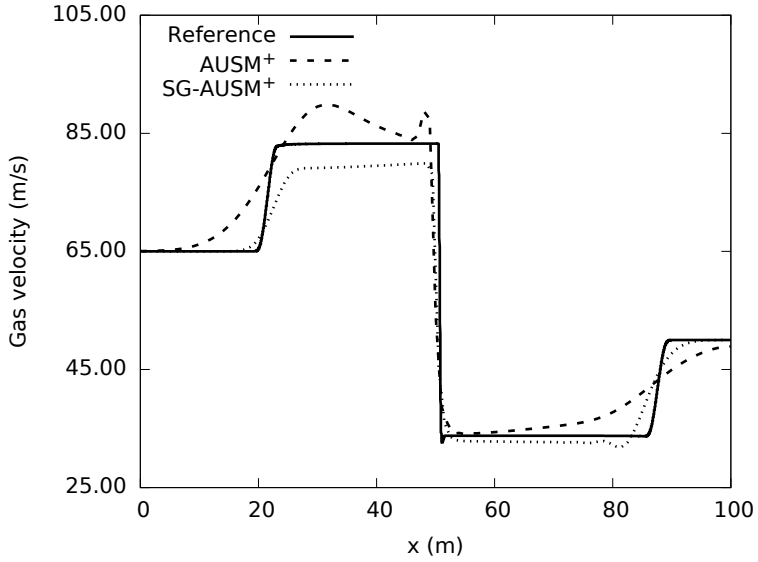

(a)

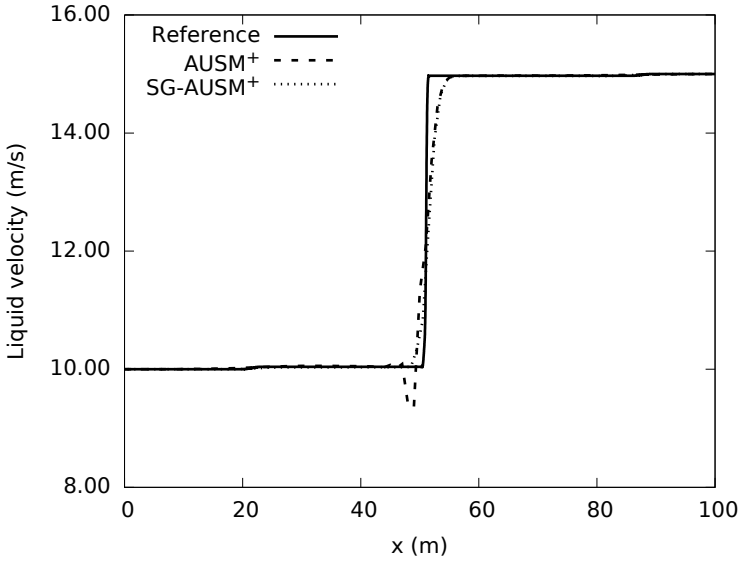

(b)

Figure 5.51: Ejve's air-water shock tube problem: comparison between AUSM$^+$ and SG-AUSM$^+$ at $t = 0.08$ s; $N = 101$; $\Delta t = \Delta x/(1000\ \text{m/s})$; $\sigma = 1.2$; $C_f = 0.0$. (a) Gas velocity; (b) Liquid velocity.

Table 5.4: Comparison of the CPU times between SG-AUSM$^+$ and AUSM$^+$

Test Cases	Δt (s)	t (s)	CPU Time (s) (staggered grids)	CPU Time (s) (collocated grids)	Save
Water faucet	2.0×10^{-3}	0.5	2.90	7.42	60%
Oscillating manometer	6.7×10^{-5}	1	19.55	46.97	58%
Shock tube (Toumi)	4.2×10^{-4}	0.04	0.12	0.26	53%
Shock tube (Cortes)	10^{-3}	0.08	0.10	0.26	61%
Shock tube (Ejve)	10^{-3}	0.08	0.08	0.22	63%

ible with the pressure-flux discretization. This is generally required when a collocated-based method is adopted for the scheme to satisfy Abgralls principle or the pressure non-disturbance condition [73] [7] [22].

Tables 5.5 and 5.6 summarize the results of all the benchmark test cases obtained with AUSM-family and SG-AUSM-family schemes.

5.6 Extension to Second-Order Spatial Accuracy

In this section, second-order extension of SG-AUSM$^+$ and SG-AUSMFVS schemes is studied for the oscillating manometer problem and the air-water shock tube problems. The classical MUSCL technique with several types of TVD limiters such as the van Leer limiter, the van Albada limiter and the Minmond limiter has been applied. Since there is no significant difference of results among the above-mentioned limiters, only results obtained with the van Albada limiter are presented. In addition, primitive variables are chosen to perform the extrapolation in the limiter calculation. Since the second-order extension of the schemes is too oscillatory for the water faucet and phase separation problem, the results of these two problems are not presented here.

Table 5.5: Summary of solutions for the benchmark test cases (S: Successful; A: Acceptable; F: Failure; NA: Not available)

schemes	Water faucet Figs. 5.7-5.8 Fig. 20	Oscillating manometer Fig. 5.16 Fig. 22	Phase separation Figs. 5.29-5.30
AUSM$^+$	S	F (diverge)	F (diverge)
AUSM$^+$-up	A (too diffusive)	NA	NA
PD-AUSM$^+$	NA	S	NA
Roe	S	F (diverge)	F (diverge)
SG-AUSM$^+$	S	S	F (diverge)
SG-AUSMD	F (diverge)	F (diverge)	F (diverge)
SG-AUSMV	A (too diffusive)	S	A (too diffusive)
SG-AUSMDV	F (diverge)	F (diverge)	F (diverge)
SG-FVS	A (too diffusive)	S	F (diverge)
SG-AUSMFVS	S (most accurate)	S (most accurate)	S (most accurate)
CATHENA4	A (too diffusive)	A (too diffusive)	NA

Table 5.6: Summary of solutions for the benchmark test cases (continued) (S: Successful; A: Acceptable; F: Failure; NA: Not available)

schemes	Toumis shock tube Figs. 5.12-5.13 Figs. 5.31-5.32	Cortes shock tube Figs. 5.35-5.36 Figs. 5.48-5.49	Ejves shock tube Figs. 5.39-5.40 Figs. 5.50-5.51
AUSM$^+$	F (oscillatory)	F (oscillatory)	F (oscillatory)
AUSM$^+$-up	NA	NA	NA
PD-AUSM$^+$	A (weakly oscillatory)	NA	NA
Roe	F (diverge)	S (smear)	S (smear)
SG-AUSM$^+$	A (weakly oscillatory)	S	S
SG-AUSMD	A (weakly oscillatory)	F (oscillatory)	F (oscillatory)
SG-AUSMV	A (slight overshoot)	S	S
SG-AUSMDV	A (weakly oscillatory)	F (oscillatory)	F (oscillatory)
SG-FVS	A (slight overshoot)	S	S
SG-AUSMFVS	A (slight overshoot)	S (most accurate)	S (most accurate)
CATHENA4	NA	NA	NA

5.6.1 Oscillating Manometer Problem

For the oscillating manometer problem, Fig. 5.52 shows the liquid velocity evolution at the bottom of the tube. It can be seen that the second-order implicit SG-AUSM$^+$ scheme is capable of generating more accurate results than its first-order counterpart. With the second-order extension, both the dissipative and dispersive errors caused by the first-order implicit SG-AUSM$^+$ scheme are greatly reduced. The number of nodes and the time step of the second-order extension is set to be the same as those of their first-order counterparts.

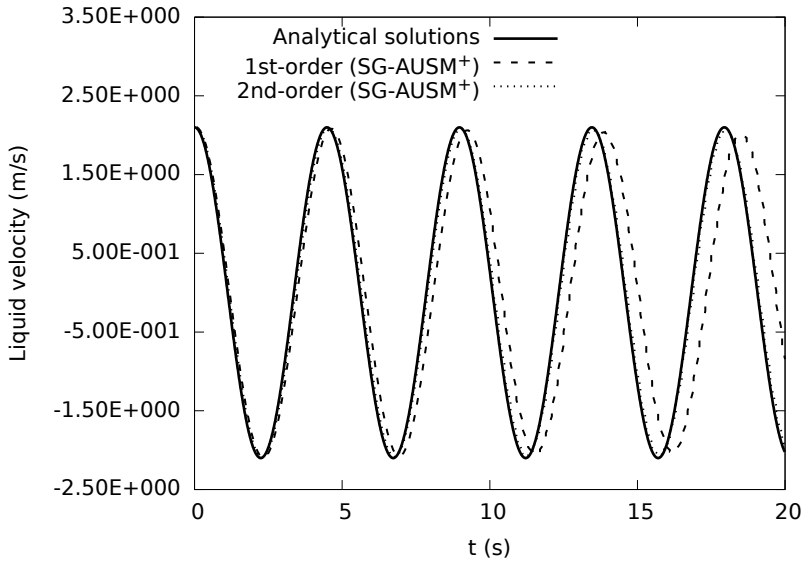

Figure 5.52: Oscillating manometer problem: comparison between the implicit first-order SG-AUSM$^+$ and second-order SG-AUSM$^+$ (with the Albada limiter); $N = 101$; $\Delta t = \Delta x/(3000\ \text{m/s})$; $\sigma = 0.0$; $C_f = 5 \times 10^4\ \text{s}^{-1}$. Liquid velocity with time at the bottom of the tube.

5.6.2 Air-Water Shock Tube Problems

Figures 5.54, 5.54, 5.56, 5.57, 5.58 and 5.59 demonstrate the results for Toumi's, Cortes', and Ejve's shock tube problems, respectively. It can be seen that for Toumi's and Cortes' test cases, the second-order extension of the SG-AUSMFVS scheme yields nearly the same

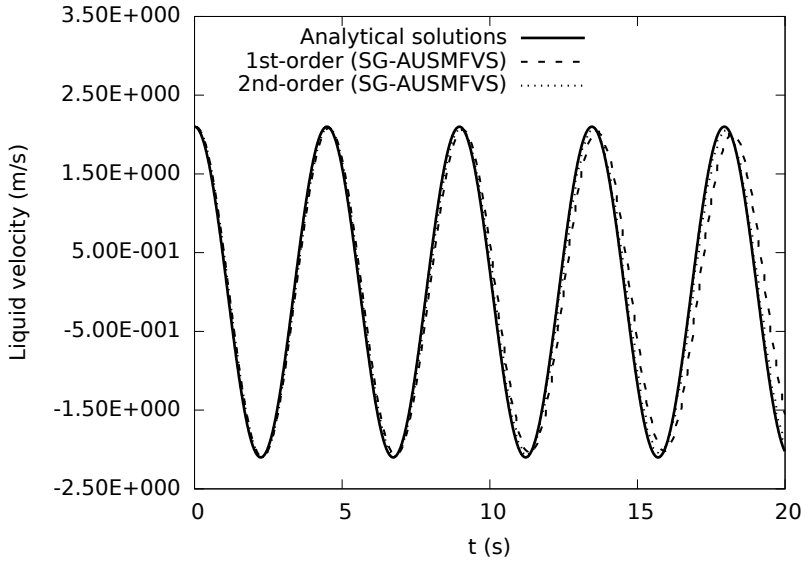

Figure 5.53: Oscillating manometer problem: comparison between implicit first-order SG-AUSMFVS and second-order SG-AUSMFVS (with the Albada limiter); $N = 101$; $\kappa = 200$; $\Delta t = \Delta x/(3000 \text{ m/s})$; $\sigma = 0.0$; $C_f = 5 \times 10^4 \text{ s}^{-1}$. Liquid velocity with time at the bottom of the tube.

results as those obtained with its first-order counterpart. In other words, no improvement of accuracy is achieved using the second-order extension for this shock tube problem. For Ejve's shock tube problem, the second-order extension of the SG-AUSMFVS scheme even generates a small overshoot at the discontinuity of the liquid velocity.

5.7 Implementation of TVD Limiter in CATHENA4

5.7.1 Introduction of CATHENA4

The Canadian algorithm for the thermal hydraulic network analysis (CATHENA4) code was developed by the Canadian Nuclear Laboratories (CNL). It was mainly designed to perform the analysis of postulated accidents in CANDU reactors. Finite-volume numerical methods, along with the first-order advective upwinding scheme, are used to solve the

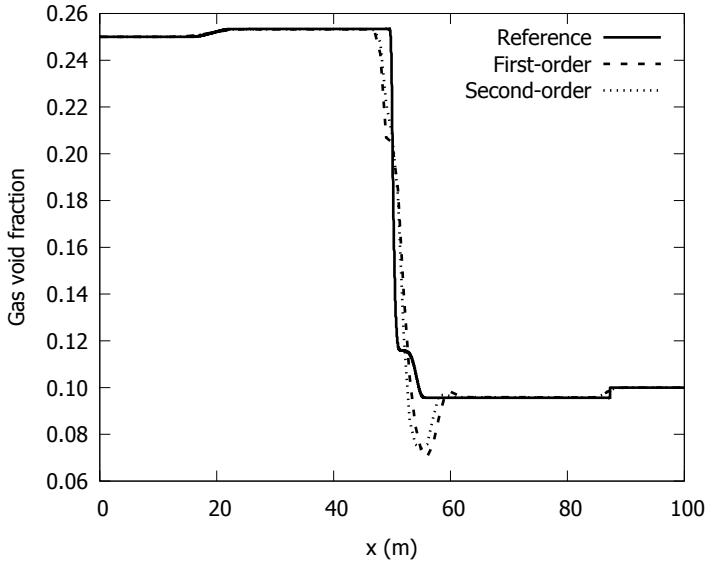

(a)

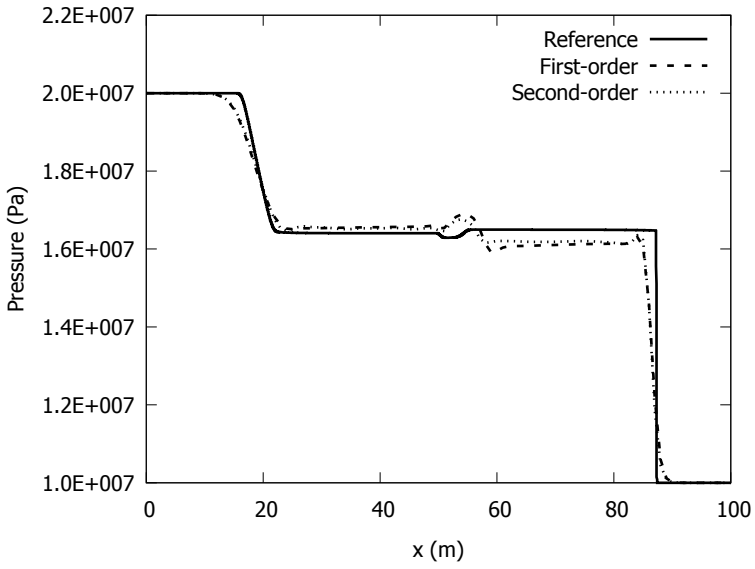

(b)

Figure 5.54: Toumi' shock tube problem: comparison between implicit first-order SG-AUSMFVS and second-order SG-AUSMFVS at $t = 0.04$ s; $N = 101$; $\kappa = 5$; $\Delta t = \Delta x/(2400 \text{ m/s})$; $\sigma = 1.2$; $C_f = 0.0$. (a) Void fraction; (b) Pressure.

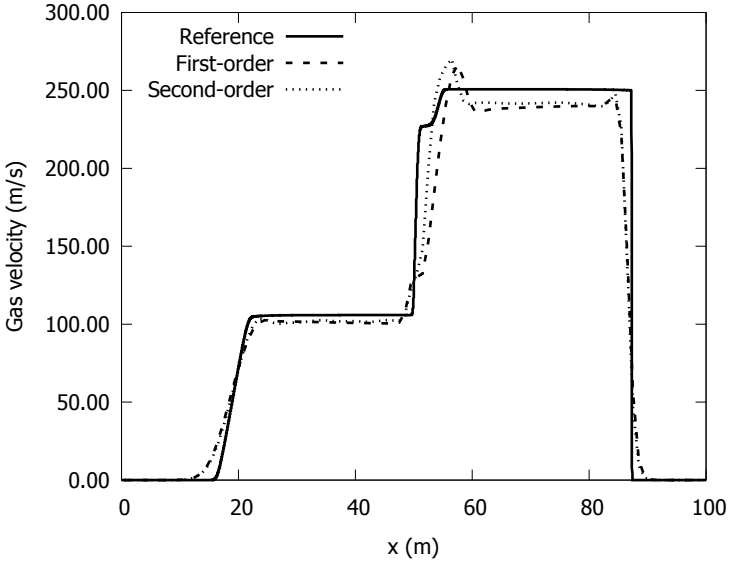

(a)

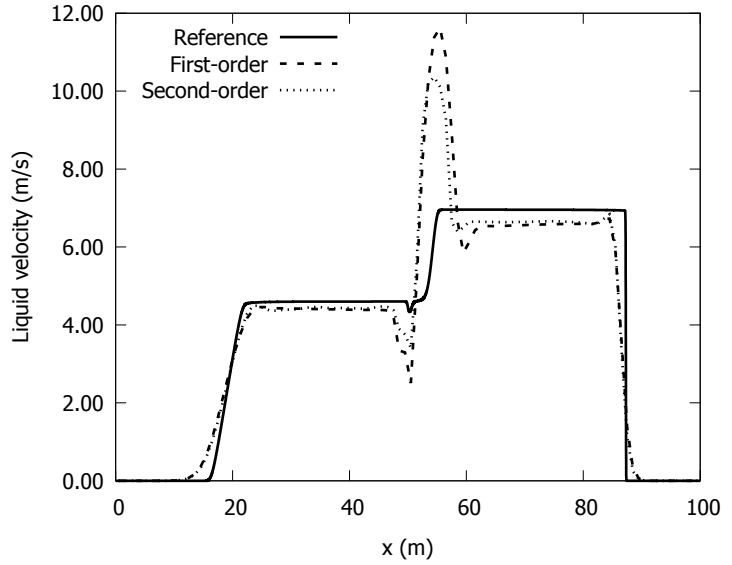

(b)

Figure 5.55: Toumi' shock tube problem: comparison between implicit first-order SG-AUSMFVS and second-order SG-AUSMFVS at $t = 0.04$ s; $N = 101$; $\kappa = 5$; $\Delta t = \Delta x/(2400 \text{ m/s})$; $\sigma = 1.2$; $C_f = 0.0$. (a) Gas velocity; (b) Liquid velocity.

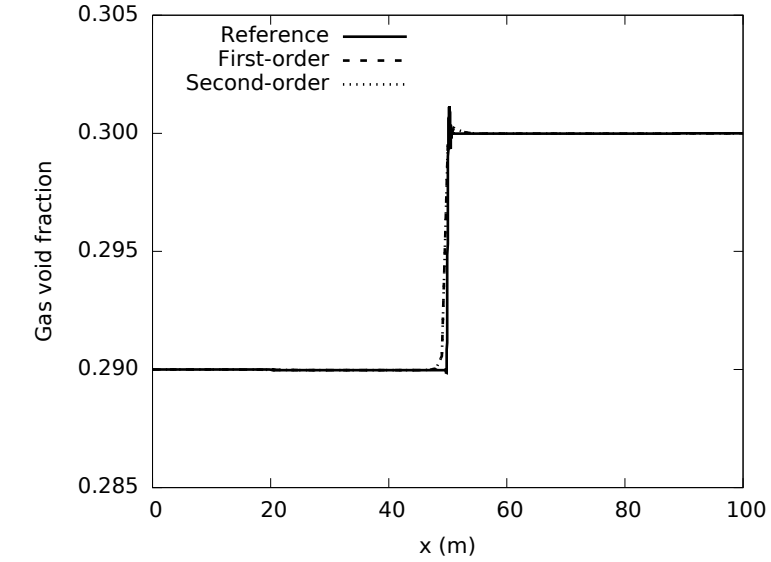

(a)

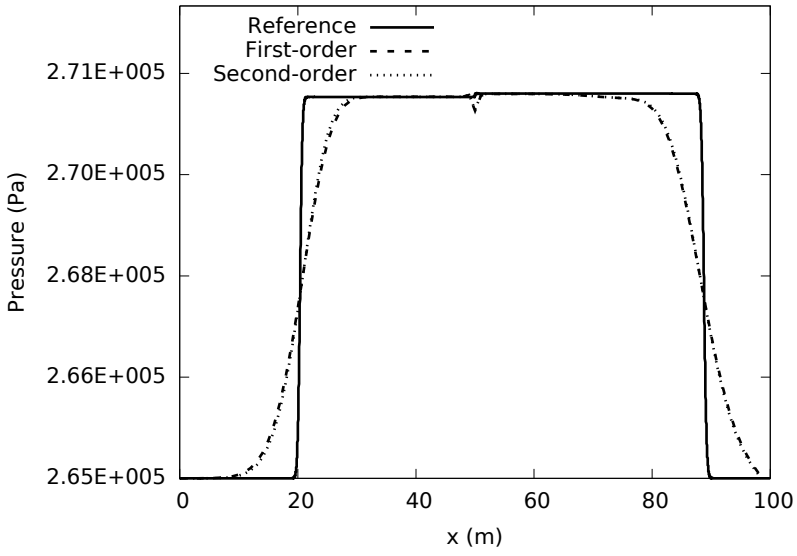

(b)

Figure 5.56: Cortes' shock tube problem: comparison between implicit first-order SG-AUSMFVS and second-order SG-AUSMFVS at $t = 0.08$ s; $N = 101$; $\kappa = 5$; $\Delta t = \Delta x/(1000$ m/s); $\sigma = 1.2$; $C_f = 0.0$. (a) Void fraction; (b) Pressure.

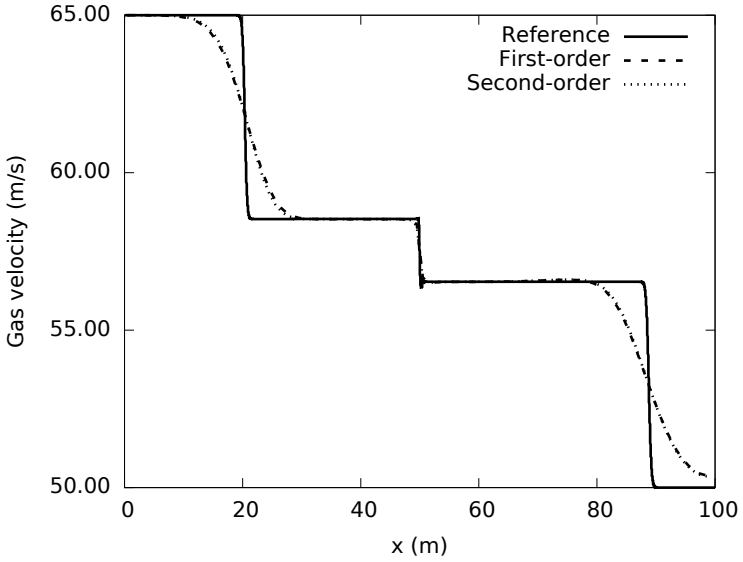

(a)

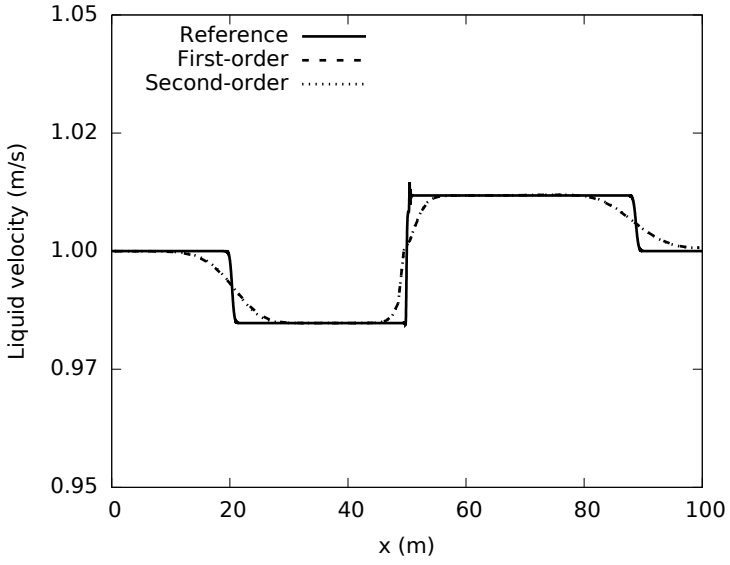

(b)

Figure 5.57: Cortes' shock tube problem: comparison between implicit first-order SG-AUSMFVS and second-order SG-AUSMFVS at $t = 0.08$ s; $N = 101$; $\kappa = 5$; $\Delta t = \Delta x/(1000$ m/s); $\sigma = 1.2$; $C_f = 0.0$. (a) Gas velocity; (b) Liquid velocity.

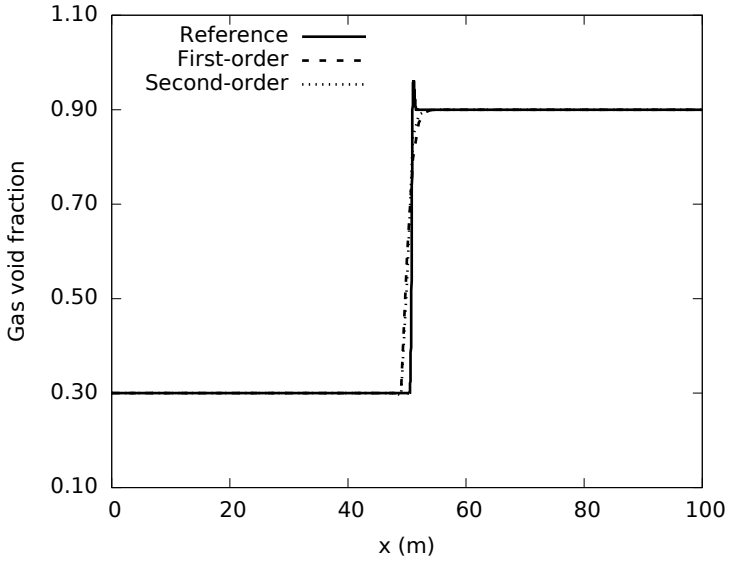

(a)

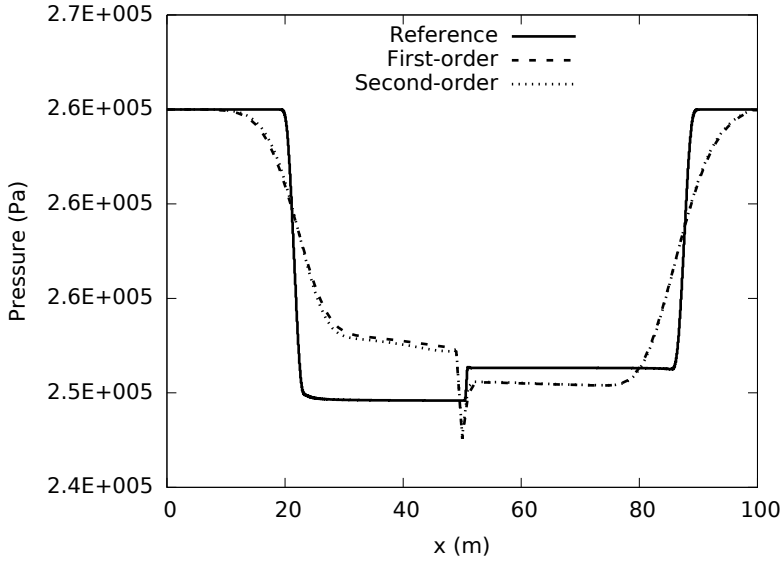

(b)

Figure 5.58: Ejve' shock tube problem: comparison between implicit first-order SG-AUSMFVS and second-order SG-AUSMFVS at $t = 0.08$ s; $N = 101$; $\kappa = 200$; $\Delta t = \Delta x/(1000 \text{ m/s})$; $\sigma = 1.2$; $C_f = 0.0$. (a) Void fraction. (b) Pressure.

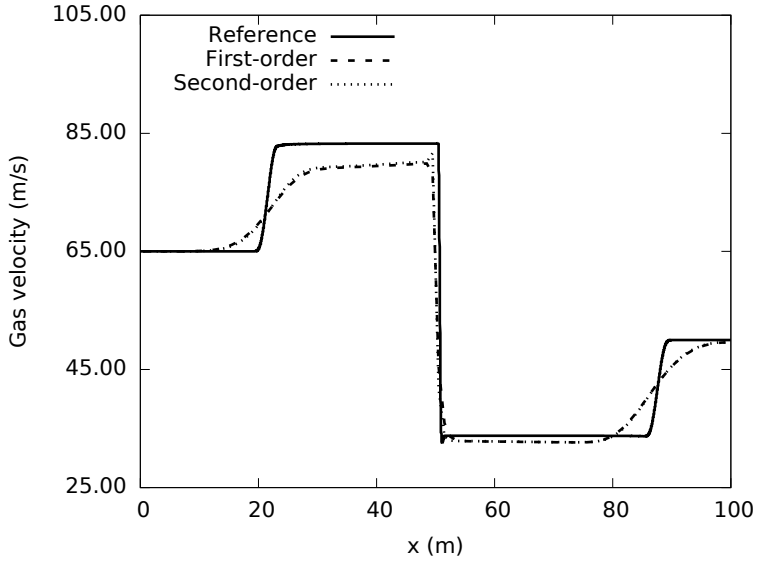

(a)

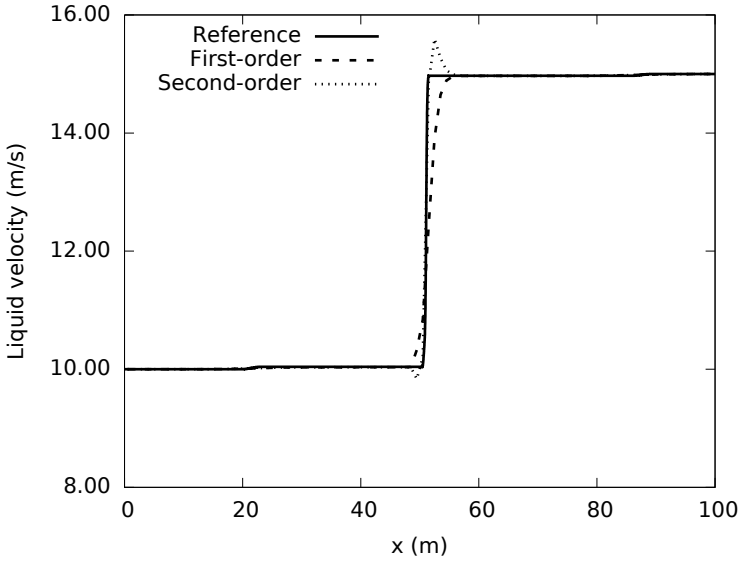

(b)

Figure 5.59: Ejve' shock tube problem: comparison between implicit first-order SG-AUSMFVS and second-order SG-AUSMFVS at $t = 0.08$ s; $N = 101$; $\kappa = 200$; $\Delta t = \Delta x/(1000 \text{ m/s})$; $\sigma = 1.2$; $C_f = 0.0$. (a) Gas velocity; (b) Liquid velocity.

mass, momentum, and energy equations for two-phase flows. The first-order advective upwinding scheme is very robust and efficient, yet excessively diffusive. In CATHENA4, the mass and energy equations of phase k are discretized as follows:

$$\begin{aligned}&(\alpha_k\rho_k\psi_k)_i^{n+1} - (\alpha_k\rho_k\psi_k)_i^n \\ &+\tfrac{\Delta t}{\Delta x}\left\{\left[(\alpha_k\rho_k\psi_k)^{n+1}u_k^{n+1}\right]_{i+1/2} - \left[(\alpha_k\rho_k\psi_k)^{n+1}u_k^{n+1}\right]_{i-1/2}\right\} \\ &-\dot{m}_{ki}^{n+1}\,(\psi_k)_i^{n+1}\,\Delta t = R_i^{n+1},\end{aligned} \tag{5.16}$$

where $\psi_k = 1$ for the mass equation of phase k and $\psi_k = h_k$ for the energy equation of phase k; $\dot{m}_{ki}^{n+1}$ represents the interfacial mass transfer rate for phase k, which is defined as Eq. 2.10. The terms in square brackets in Eq. 5.16 represent the mass or energy fluxes, which are calculated according to the following advective upwind method:

$$\left[(\alpha_k\rho_k\psi_k)^{n+1}u_k^{n+1}\right]_{i+1/2} = u_{k,i+1/2}^{n+1}\begin{cases}(\alpha_k\rho_k\psi_k)_i^{n+1}, & \text{if} \quad u_{k,i+1/2}^{n+1} \geq 0 \\ (\alpha_k\rho_k\psi_k)_{i+1}^{n+1}, & \text{otherwise.}\end{cases} \tag{5.17}$$

The momentum equations in CATHENA4 are also discretized using advective upwind schemes.

$$\begin{aligned}&\underbrace{\overbrace{\frac{1}{2}\left[\alpha_{k,L}^{n+1}\rho_{k,L}^{n+1}\Delta z_L\frac{A_L}{A_{LNK}} + \alpha_{k,R}^{n+1}\rho_{k,R}^{n+1}\Delta z_R\frac{A_R}{A_{LNK}}\right]}^{\Xi_k}(u_k^{n+1}-u_k^n)}_{\text{inertia term}} \\ &+\underbrace{\frac{1}{2}\Xi_k^{n+1}u_k^{n+1}\begin{Bmatrix}(u_{gL}^{n+1} - \text{sgn}\cdot u_{k,L-1}^{n+1}) \\ (\text{sgn}\cdot u_{k,L+1}^{n+1} - u_k^{n+1})\end{Bmatrix}\frac{\Delta t}{\Delta z_{up}}}_{\text{transport term}} + \underbrace{\frac{1}{2}\left[\alpha_{k,L}^{n+1}\Delta z_L\frac{A_L}{A_{LNK}} + \alpha_{k,R}^{n+1}\Delta z_R\frac{A_R}{A_{LNK}}\right]\frac{(P_R^{n+1}-P_L^{n+1})}{\frac{1}{2}(\Delta z_L+\Delta z_R)}\Delta t}_{\text{Pressure gradient term}} \\ &+\underbrace{(\tau_{wL,k}^{n+1}+\tau_{wR,k}^{n+1}+\tau_{\text{int},L,k}^{n+1}+\tau_{\text{int},R,k}^{n+1})\frac{\Delta t}{A_{LNK}}}_{\text{wall friction term}} + \underbrace{\frac{1}{2}\left[\alpha_{k,L}\rho_{k,L}\Delta z_L\frac{A_L}{A_{LNK}}\sin\theta_L + \alpha_{k,R}\rho_{k,R}\Delta z_R\frac{A_R}{A_{LNK}}\sin\theta_R\right]g\Delta t}_{\text{Gravity term}} \\ &+\underbrace{\Delta p^{int}\times 0.5\left[\Delta z_L\frac{A_L}{A_{LNK}} + \Delta z_R\frac{A_R}{A_{LNK}}\right]\times\frac{(\alpha_{k,R}^{n+1}-\alpha_{k,L}^{n+1})}{\frac{1}{2}(\Delta z_L+\Delta z_R)}\Delta t}_{\text{phase-to-interface pressure difference term}} = R_i,\end{aligned} \tag{5.18}$$

where

$$\Delta p^{int} = c_{ki}\rho_m \min\left(0.25, (u_g^{n+1} - u_f^{n+1})^2\right) \tag{5.19}$$

with $c_{ki} = 0.15$.

5.7.2 Extension of Second-order Spatial Accuracy in CATHENA4

The classical MUSCL technique with the van Albada limiter has been employed. In addition, conservative variables are chosen to perform the extrapolation in the limiter calculation [80]. Thus, the mass and energy interfacial fluxes are given as follows:

$$\begin{aligned}
&\left[(\alpha_k\rho_k\psi_k)^{n+1}u_k^{n+1}\right]_{i+1/2} \\
&= u_{k,i+1/2}^{n+1}\begin{cases} (\alpha_k\rho_k\psi_k)_i^{n+1} + \phi_{i+1/2}(r)\frac{(\alpha_k\rho_k\psi_k)_{i+1}^{n+1} - (\alpha_k\rho_k\psi_k)_{i+1}^{n}}{2}, & \text{if } u_{k,i+1/2}^{n+1} \geq 0 \\ (\alpha_k\rho_k\psi_k)_{i+1}^{n+1} - \phi_{i+1/2}(r)\frac{(\alpha_k\rho_k\psi_k)_{i+1}^{n+1} - (\alpha_k\rho_k\psi_k)_{i+1}^{n}}{2}, & \text{otherwise.} \end{cases}
\end{aligned} \tag{5.20}$$

The van Albada limiter is defined by Eq. 3.128, with

$$r = \begin{cases} \frac{(\alpha_k\rho_k\psi_k)_i^{n+1} - (\alpha_k\rho_k\psi_k)_{i-1}^{n+1}}{(\alpha_k\rho_k\psi_k)_{i+1}^{n+1} - (\alpha_k\rho_k\psi_k)_i^{n+1}}, & \text{if } u_{k,i+1/2}^{n+1} \geq 0 \\ \frac{(\alpha_k\rho_k\psi_k)_{i+2}^{n+1} - (\alpha_k\rho_k\psi_k)_{i+1}^{n+1}}{(\alpha_k\rho_k\psi_k)_{i+1}^{n+1} - (\alpha_k\rho_k\psi_k)_i^{n+1}}, & \text{otherwise.} \end{cases} \tag{5.21}$$

Two test cases, including Ransom's water faucet problem and the oscillating manometer problem, have been tested with the above-mentioned second-order flux limiters.

Fig. 5.60 displays the void fraction at $t = 0.5$ s on a grid of 101 nodes for the water faucet problem calculated by the original version of CATHENA4 and the second-order spacial accuracy version of CATHENA4. The former uses the first-order advective upwind method; whereas the latter implements the van Albada limiter. For comparison purposes, the results obtained with the in-house code with the SG-AUSM$^+$ scheme is also plotted. Note that the major difference between the in-house code and CATHENA4 lies in the discretization of momentum fluxes in the momentum equations. In the in-house code,

the momentum fluxes are in a conservative form and discretized using the SG-AUSM$^+$ scheme; whereas, in CATHENA4 the momentum fluxes is in a non-conservative form and discretized using advective upwind scheme, as shown in Eq. 5.18. It can be seen from Fig. 5.60 that the in-house code with the SG-AUSM$^+$ scheme generates the most accurate results compared to those obtained with CATHENA4. Furthermore, with the second-order flux limiter, CATHENA4 is able to yield slightly better results than its first-order counterpart in terms of accuracy.

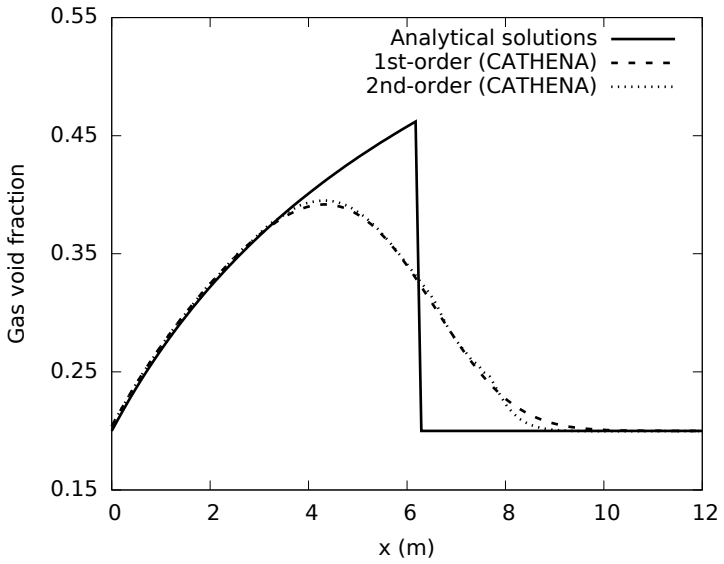

Figure 5.60: Water faucet: comparison of void fraction between the original first-order CATHENA4 and the modified second-order CATHENA4 at $t = 0.5$ s ; $N = 101$; $\Delta t = 10^{-5}$ s.

Figure 5.61 demonstrates the liquid velocity evolution up to $t = 20$ s on a grid of 101 nodes for the water faucet problem calculated by the original version of CATHENA4 and the second-order spacial accuracy version of CATHENA4. For comparison purposes, the results obtained with the in-house code with the PD-AUSM$^+$ scheme is also plotted. Similar to the water faucet case, the in-house code with the PD-AUSM$^+$ scheme generates the most accurate results compared to those obtained with CATHENA4. In addition, with the second-order flux limiter, CATHENA4 is able to mitigate the numerical damping due

to its first-order advective upwind in CATHENA4.

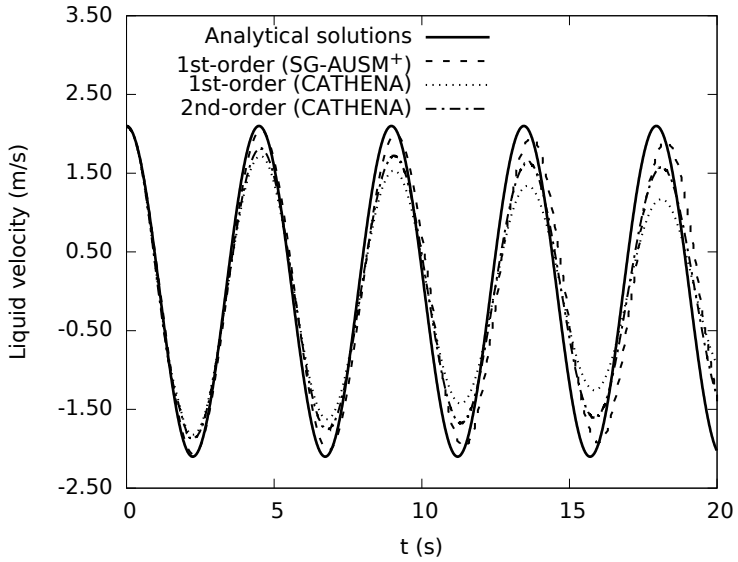

Figure 5.61: Oscillating manometer: comparison between the original first-order CATHENA4 and the modified second-order CATHENA4; $N = 221$; $\Delta t = 5 \times 10^{-6}$ s. Liquid velocity with time at the bottom of the U-tube

Chapter 6

Conclusions and Future Work

6.1 Conclusions

The main objective of this thesis is to improve the accuracy and efficiency of calculation for all-Mach-number two-phase flows. In order to achieve this objective, this thesis makes the first attempt on using both explicit and implicit AUSM-family schemes on collocated and staggered grids, compared to most work in the available literature that solves multi-phase compressible flow problems explicitly with a collocated grid. The four-equation generic two-fluid model is mainly considered. The benchmark test cases include Ransom's water faucet problem, the oscillating manometer problem, the phase separation problem, and the air-water shock tube problems. Regarding the shock tube problems, three cases are solved, including Toumi's case, Cortes'case, and Ejve's case. The main findings and conclusions are summarized as follows.

First, through the theoretical analysis and numerical tests of various explicit AUSM-family schemes on collocated grids, it is concluded that with the explicit time integration, the AUSM$^+$, AUSMD and AUSMDV schemes possess the fewest numerical dissipations among the AUSM-family schemes, thereby being capable of accurately capturing the contact discontinuity or mass fronts. Hence, these schemes are preferred for the solution of the water faucet problem. On the contrary, the FVS scheme, which has more numerical dissi-

pation, is excessively dissipative for the water faucet problem. However, the FVS scheme behaves well for the shock tube problem.

Then, the implicit AUSM-family schemes were studied through the comparison of implicit and explicit AUSM-family schemes on collocated grids. It can be concluded that with certain time steps, the implicit AUSM-family schemes are superior to their explicit counterparts, in terms of numerical accuracy and computational efficiency. Especially for the water faucet and the oscillating manometer problems, the implicit AUSM-family schemes greatly improve computational efficiency and at the same time retain reasonably good accuracy.

Next, the first-order SG-AUSM-family schemes were extended on the benchmark test cases, and they are compared with their collocated-grid-based counterparts. It is found that the SG-AUSM$^+$ scheme possesses the following appealing properties. First, the SG-AUSM$^+$ scheme is capable of producing accurate solutions compatible with or even better than the corresponding collocated-grid-based AUSM$^+$ scheme. Second, the SG-AUSM$^+$ scheme is more efficient than the collocated-grid-based one. Third, the discretization of the non-conservative term is simpler for staggered-grid-based schemes than the collocated-grid-based ones satisfying Abgrall's principle. In addition, based on the findings stated in the preceding two paragraphs, a new staggered-grid-based scheme, namely, SG-AUSMFVS, is proposed. It combines the accuracy of SG-AUSM$^+$ and the stability of van Leer's SG-FVS. The SG-AUSMFVS scheme was originally developed to solve the stiff phase separation problem, where other SG-AUSM-family schemes are not applicable. In addition to the ability of solving the phase separation problem, the SG-AUSMFVS also shows reasonably good accuracy and stability for other test cases in this thesis.

Afterwards, the SG-AUSM-family schemes were extended to second-order spatial accuracy using the classical MUSCL approach with TVD limiters. The oscillating manometer problem and the air-water shock tube problems are selected to study the effect of using a second-order extension of the SG-AUSM$^+$ and SG-AUSMFVS schemes. For the oscillating manometer problem, with the second-order extension, both the dissipative and dispersive errors caused by the first-order implicit SG-AUSM$^+$ scheme are greatly reduced. On the contrary, for the air-water shock tube problems, the second-order extension of the

SG-AUSMFVS scheme yields nearly the same results as those obtained with its first-order counterpart. In other words, no improvement of accuracy is achieved using second-order extension for this shock tube problem.

Finally, the classical MUSCL technique with the van Albada limiter has been implemented into the mass and energy equations in CATHENA4. In addition, conservative variables are chosen to perform the extrapolation in the limiter calculation. It is found that the modified version of CATHENA4 is able to produce more accurate results than the original version, which adopts first-order advective upwind schemes.

In summary, this thesis makes the following salient contributions:

(1) Proposes SG-AUSM-family schemes to solve odd-even decoupling for low-Mach-number flows.

(2) Proves that the novel SG-AUSM$^+$ scheme satisfies Abgrall's principle to solve the non-conservative issue in the two-phase governing equations.

(3) Proposes a new SG-AUSMFVS scheme that is shown to be more accurate and stable than other SG-AUSM-family schemes.

(4) Improves the computational efficiency by using an implicit time integration to alleviate the CFL number limitation, and by using a staggered-grid arrangement.

(5) Improves the numerical accuracy of CATHENA4 by implementing the TVD limiter.

(6) Demonstrates the feasibility of integrating SG-AUSM-family schemes into a thermal hydraulic code, such as CATHENA4.

6.2 Future Work

In this thesis, research is mainly based on the four-equation generic model. In other words, the energy equations are neglected and the isentropic assumption is taken. In addition, the mass and heat transfer are not included. However, in some cases where the energy plays an important role or mass and heat transfer are important such as in the cavitation problem,

the four-equation generic model is no longer applicable. Therefore, further work is required for extending the SG-AUSM-family schemes onto the six-equation two-fluid model. Also, mass and heat transfer should be included in the model as source terms in the future; they are key parameters in thermal-hydraulic systems in practical.

In this project, the accuracy of the original version of CATHENA4 is improved by implementing the MUSCL scheme with a second-order TVD limiter into the mass equations. However, the momentum equations are also important. Therefore, future research should consider discretizing the momentum equations with higher-order schemes, such as second-order SG-AUSM-family schemes. In addition, this work only considered the explicit or fully implicit time integration methods, which have only first-order time and spatial accuracy. Hence, the Crank-Nicolson method, which has second-order time and spacial accuracy, can be studied in the future.

As a final suggestion for future research, it will be useful to study the multi-dimensional all-Mach-number multi-phase flows. Although the new scheme, SG-AUSMFVS, is capable of solving 1-D two-phase flow problems, extensions of SG-AUSMFVS to be applied to multi-dimensional problems still require further investigation. For example, the carbuncle phenomenon could occur in multi-dimensional calculations, even if the scheme works well in 1-D problems.

References

[1] Y. Wada and M.-S. Liou, "An accurate and robust flux splitting scheme for shock and contact discontinuities," *SIAM Journal on Scientific Computing*, vol. 18, no. 3, pp. 633–657, 1997.

[2] B. Hanna, "CATHENA: A thermalhydraulic code for CANDU analysis," *Nuclear Engineering and Design*, vol. 180, no. 2, pp. 113–131, 1998.

[3] K. Carlson, R. Riemke, S. Rouhani, R. Shumway, and W. Weaver, "Relap5/mod3 code manual volume i: Code structure, system models and solution methods," *US NRC NUREG/CR-5535, Washington (DC, USA) June*, 1990.

[4] D. Bestion, F. Barre, and B. Faydide, "Methodology, status and plans for development and assessment of cathare code," Nuclear Regulatory Commission, Washington, DC (United States). Div. of Systems Technology; Nuclear Energy Agency, 75-Paris (France); SCIENTECH, Inc., Boise, ID (United States), Tech. Rep., 1997.

[5] Q. Zeng, N. Aydemir, F. Lien, and T. Xu, "Comparison of implicit and explicit ausm-family schemes for compressible multiphase flows," *International Journal for Numerical Methods in Fluids*, vol. 77, no. 1, pp. 43–61, 2015.

[6] S. K. Godunov, "A difference method for numerical calculation of discontinuous solutions of the equations of hydrodynamics," *Matematicheskii Sbornik*, vol. 89, no. 3, pp. 271–306, 1959.

[7] R. Saurel and R. Abgrall, "A multiphase godunov method for compressible multifluid and multiphase flows," *Journal of Computational Physics*, vol. 150, no. 2, pp. 425–467, 1999.

[8] P. L. Roe, "Approximate Riemann solvers, parameter vectors, and difference schemes," *Journal of computational physics*, vol. 43, no. 2, pp. 357–372, 1981.

[9] S. Evje and T. Flåtten, "Hybrid flux-splitting schemes for a common two-fluid model," *Journal of Computational Physics*, vol. 192, no. 1, pp. 175–210, 2003.

[10] A. Harten, P. D. Lax, and B. Van Leer, "On upstream differencing and godunov-type schemes for hyperbolic conservation laws," in *Upwind and High-Resolution Schemes*. Springer, 1997, pp. 53–79.

[11] G.-S. Yeom and K.-S. Chang, "Numerical simulation of two-fluid two-phase flows by hll scheme using an approximate jacobian matrix," *Numerical Heat Transfer, Part B: Fundamentals*, vol. 49, no. 2, pp. 155–177, 2006.

[12] B. Van Leer, "Towards the ultimate conservative difference scheme iii. upstream-centered finite-difference schemes for ideal compressible flow," *Journal of Computational Physics*, vol. 23, no. 3, pp. 263–275, 1977.

[13] C. Fletcher and R. Schultz, "RELAP5/MOD3 code manual volume : Users guidelines," *Idaho National Engineering Laboratory, Lockheed Idaho Technologies Company, Idaho Falls, Idaho*, vol. 83415, 1995.

[14] F. Barre, C. Sun, and I. Dor, "Overview of the numerical and computational development performed in the frame of the CATHARE-2 code," in *Proceedings of the Conference on Mathematics an Computations, Reactor Physics, and Environmental Analyses, Portland, Oregon*, 1995.

[15] M. Ishii and T. Hibiki, *Thermo-fluid dynamics of two-phase flow*. Springer Science & Business Media, 2010.

[16] M. Ishii and K. Mishima, "Two-fluid model and hydrodynamic constitutive relations," *Nuclear Engineering and design*, vol. 82, no. 2-3, pp. 107–126, 1984.

[17] F. Coquel, K. El Amine, E. Godlewski, B. Perthame, and P. Rascle, "A numerical method using upwind schemes for the resolution of two-phase flows," *Journal of Computational Physics*, vol. 136, no. 2, pp. 272–288, 1997.

[18] S. Evje and K. K. Fjelde, "On a rough AUSM scheme for a one-dimensional two-phase model," *Computers & Fluids*, vol. 32, no. 10, pp. 1497–1530, 2003.

[19] H. Paillère, C. Corre, and J. Garcıa Cascales, "On the extension of the AUSM$^+$ scheme to compressible two-fluid models," *Computers & Fluids*, vol. 32, no. 6, pp. 891–916, 2003.

[20] Y.-Y. Niu, "Advection upwinding splitting method to solve a compressible two-fluid model," *International Journal for Numerical Methods in Fluids*, vol. 36, no. 3, pp. 351–371, 2001.

[21] R. Coelho, P. Lage, and A. Silva Telles, "A comparison of hyperbolic solvers ii: AUSM-type and hybrid lax-wendroff-lax-friedrichs methods for two-phase flows," *Brazilian Journal of Chemical Engineering*, vol. 27, no. 1, pp. 153–171, 2010.

[22] C.-H. Chang and M.-S. Liou, "A robust and accurate approach to computing compressible multiphase flow: Stratified flow model and AUSM$^+$-up scheme," *Journal of Computational Physics*, vol. 225, no. 1, pp. 840–873, 2007.

[23] Y.-Y. Niu, Y.-C. Lin, and C.-H. Chang, "A further work on multi-phase two-fluid approach for compressible multi-phase flows," *International Journal for Numerical Methods in Fluids*, vol. 58, no. 8, pp. 879–896, 2008.

[24] H. Bruce Stewart and B. Wendroff, "Two-phase flow: models and methods," *Journal of Computational Physics*, vol. 56, no. 3, pp. 363–409, 1984.

[25] M.-S. Chung, K.-S. Chang, and S.-J. Lee, "Numerical solution of hyperbolic two-fluid two-phase flow model with non-reflecting boundary conditions," *International journal of engineering science*, vol. 40, no. 7, pp. 789–803, 2002.

[26] S.-J. Lee, K.-S. Chang, and S.-J. Kim, "Surface tension effect in the two-fluids equation system," *International journal of heat and mass transfer*, vol. 41, no. 18, pp. 2821–2826, 1998.

[27] D. Drew, L. Cheng, and R. Lahey Jr, "The analysis of virtual mass effects in two-phase flow," *International Journal of Multiphase Flow*, vol. 5, no. 4, pp. 233–242, 1979.

[28] J. R. Travis, F. H. Harlow, and A. A. Amsden, "Numerical calculation of two-phase flows," *NASA STI/Recon Technical Report N*, vol. 76, p. 18386, 1975.

[29] S. Evje and K. K. Fjelde, "Hybrid flux-splitting schemes for a two-phase flow model," *Journal of Computational Physics*, vol. 175, no. 2, pp. 674–701, 2002.

[30] C.-H. Chang and M.-S. Liou, "Simulation of multifluid multiphase flows with AUSM$^+$-up scheme," in *Computational Fluid Dynamics 2004*. Springer, 2006, pp. 613–618.

[31] A. Harten, "High resolution schemes for hyperbolic conservation laws," *Journal of computational physics*, vol. 49, no. 3, pp. 357–393, 1983.

[32] M.-S. Liou, C.-H. Chang, L. Nguyen, and T. G. Theofanous, "How to solve compressible multifluid equations: a simple, robust, and accurate method," *AIAA Journal*, vol. 46, no. 9, pp. 2345–2356, 2008.

[33] T. Flatten and S. T. Munkejord, "The approximate Riemann solver of Roe applied to a drift-flux two-phase flow model," *ESAIM-Mathematical Modelling and Numerical Analysis*, vol. 40, no. 4, pp. 735–764, 2006.

[34] S. V. Patankar and D. B. Spalding, "A calculation procedure for heat, mass and momentum transfer in three-dimensional parabolic flows," *International Journal of Heat and Mass Transfer*, vol. 15, no. 10, pp. 1787–1806, 1972.

[35] C. Rhie and W. Chow, "Numerical study of the turbulent flow past an airfoil with trailing edge separation," *AIAA Journal*, vol. 21, no. 11, pp. 1525–1532, 1983.

[36] F. Lein, M. Leschziner, U. of Manchester Inst. of Science, and T. U. Kingdom);, *A General Non-orthogonal Collocated FV Algorithm for Turbulent Flow at All Speeds Incorporating Second-moment Closure: Part 1; Computational Implementation*. University of Manchester, Institute of Science and Technology, 1992.

[37] J. J. McGuirk and G. J. Page, "Shock capturing using a pressure-correction method," *AIAA journal*, vol. 28, no. 10, pp. 1751–1757, 1990.

[38] J. Rincon and R. Elder, "A high-resolution pressure-based method for compressible flows," *Computers & Fluids*, vol. 26, no. 3, pp. 217–231, 1997.

[39] A. Harten, P. D. Lax, and B. v. Leer, "On upstream differencing and godunov-type schemes for hyperbolic conservation laws," *SIAM Review*, vol. 25, no. 1, pp. 35–61, 1983.

[40] S. Osher, "Riemann solvers, the entropy condition, and difference," *SIAM Journal on Numerical Analysis*, vol. 21, no. 2, pp. 217–235, 1984.

[41] M.-S. Liou and C. J. Steffen Jr, "A new flux splitting scheme," *Journal of Computational Physics*, vol. 107, no. 1, pp. 23–39, 1993.

[42] Y.-H. Choi and C. L. Merkle, "The application of preconditioning in viscous flows," *Journal of Computational Physics*, vol. 105, no. 2, pp. 207–223, 1993.

[43] J. M. Weiss and W. A. Smith, "Preconditioning applied to variable and constant density flows," *AIAA Journal*, vol. 33, no. 11, pp. 2050–2057, 1995.

[44] B. L. W. Leer and P. Roe, "Characteristic time-stepping or local preconditioning of the euler equations," *Ann Arbor*, vol. 1001, pp. 48 109–2140, 1991.

[45] J. R. Edwards and M.-S. Liou, "Low-diffusion flux-splitting methods for flows at all speeds," *AIAA Journal*, vol. 36, no. 9, pp. 1610–1617, 1998.

[46] J. R. Edwards, R. K. Franklin, and M.-S. Liou, "Low-diffusion flux-splitting methods for real fluid flows with phase transitions," *AIAA journal*, vol. 38, no. 9, pp. 1624–1633, 2000.

[47] M.-S. Liou, "A sequel to AUSM: AUSM$^+$," *Journal of Computational Physics*, vol. 129, no. 2, pp. 364–382, 1996.

[48] C.-H. Chang and M.-S. Liou, "A new approach to the simulation of compressible multifluid flows with AUSM$^+$ scheme," in *16 th AIAA Computational Fluid Dynamics Conference*, 2003.

[49] M.-S. Liou, "A sequel to AUSM, part II: AUSM$^+$-up for all speeds," *Journal of Computational Physics*, vol. 214, no. 1, pp. 137–170, 2006.

[50] V. Ransom, "Numerical benchmark test No. 2.1: Faucet flow," *Multiphase Science and Technology*, vol. 3, no. 1-4, 1987.

[51] I. Toumi, "An upwind numerical method for two-fluid two-phase flow models," *Nuclear Science and Engineering*, vol. 123, no. 2, pp. 147–168, 1996.

[52] G.-S. Yeom and K.-S. Chang, "Flux-based wave decomposition scheme for an isentropic hyperbolic two-fluid model," *Numerical Heat Transfer, Part B: Fundamentals*, vol. 59, no. 4, pp. 288–318, 2011.

[53] J. Cortes, A. Debussche, and I. Toumi, "A density perturbation method to study the eigenstructure of two-phase flow equation systems," *Journal of Computational Physics*, vol. 147, no. 2, pp. 463–484, 1998.

[54] K. Kitamura and M. Liou, "Comparative study of AUSM-family schemes in compressible multiphase flow simulations," *Proceedings of ICCFD7, Big Island, Hawaii*, 2012.

[55] R. Aris, "Vectors, tensors and the basic equations of fluid dynamics," 1962.

[56] J. Stuhmiller, "The influence of interfacial pressure forces on the character of two-phase flow model equations," *International Journal of Multiphase Flow*, vol. 3, no. 6, pp. 551–560, 1977.

[57] R. W. Johnson, *Handbook of fluid dynamics*. Crc Press, 2016.

[58] J. D. Ramshaw and J. A. Trapp, "Characteristics, stability, and short-wavelength phenomena in two-phase flow equation systems," *Nuclear Science and Engineering*, vol. 66, no. 1, pp. 93–102, 1978.

[59] V. H. Ransom, R. Wagner, J. Trapp, K. Carlson, D. Kiser, H. Kuo, H. Chow, R. Nelson, and S. James, "Relap5/mod1 code manual volume 1: System models and numerical methods," *N'REG/CR-1826, EGG-2070, March*, 1982.

[60] R. Lahey Jr, "The prediction of phase distribution and separation phenomena using two-fluid models," *Boiling Heat Transfer*, vol. 85, 1992.

[61] D. Bestion, "The physical closure laws in the cathare code," *Nuclear Engineering and Design*, vol. 124, no. 3, pp. 229–245, 1990.

[62] C. Farhat, A. Rallu, and S. Shankaran, "A higher-order generalized ghost fluid method for the poor for the three-dimensional two-phase flow computation of underwater implosions," *Journal of Computational Physics*, vol. 227, no. 16, pp. 7674–7700, 2008.

[63] I. Toumi and A. Kumbaro, "An approximate linearized Riemann solver for a two-fluid model," *Journal of Computational Physics*, vol. 124, no. 2, pp. 286–300, 1996.

[64] R. J. LeVeque and R. J. Leveque, *Numerical methods for conservation laws*. Springer, 1992, vol. 132.

[65] M. E. Davis, *Numerical methods and modeling for chemical engineers*. Courier Corporation, 2013.

[66] S. Thakur, W. Shyy, and M.-S. Liou, "Investigation of convection and pressure treatment with splitting techniques," *NASA STI/Recon Technical Report N*, vol. 95, p. 24399, 1995.

[67] M.-S. Liou, "Ten years in the making-ausm-family," in *15th AIAA Computational Fluid Dynamics Conference*, 2001, p. 2521.

[68] ——, "Progress towards an improved cfd method-ausm+," in *12th Computational Fluid Dynamics Conference*, 1995, p. 1701.

[69] T. W. Roberts, "The behavior of flux difference splitting schemes near slowly moving shock waves," *Journal of Computational Physics*, vol. 90, no. 1, pp. 141–160, 1990.

[70] I. Toumi, "A weak formulation of roe's approximate riemann solver," *Journal of computational physics*, vol. 102, no. 2, pp. 360–373, 1992.

[71] Q. Zeng, N. U. Aydemir, F.-S. Lien, and T. Xu, "Extension of staggered-grid-based ausm-family schemes for use in nuclear safety analysis codes." *International Journal of Multiphase Flow*, 2017.

[72] G. B. Wallis, *One-dimensional two-phase flow*. McGraw-Hill New York, 1969, vol. 1.

[73] R. Abgrall, "How to prevent pressure oscillations in multicomponent flow calculations: a quasi conservative approach," *Journal of Computational Physics*, vol. 125, no. 1, pp. 150–160, 1996.

[74] C. B. Laney, *Computational gasdynamics*. Cambridge University Press, 1998.

[75] O. Onur and S. Eyi, "Effects of the Jacobian evaluation on Newton's solution of the Euler equations," *International Journal for Numerical Methods in Fluids*, vol. 49, no. 2, pp. 211–231, 2005.

[76] T. A. Davis, "Umfpack version 4.4 user guide," *Department of Computer and Information Science and Engineering, University of Florida, Gainesville, FL*, 2005.

[77] S. Evje and T. Flåtten, "Weakly implicit numerical schemes for a two-fluid model," *SIAM Journal on Scientific Computing*, vol. 26, no. 5, pp. 1449–1484, 2005.

[78] P. D. Lax, *Hyperbolic systems of conservation laws and the mathematical theory of shock waves*. SIAM, 1973.

[79] T. Flåtten and S. Evje, "Comparison of various AUSM type schemes for the two-fluid model," pp. 1–31, 2003.

[80] D. Wang, J. H. Mahaffy, J. Staudenmeier, and C. G. Thurston, "Implementation and assessment of high-resolution numerical methods in trace," *Nuclear Engineering and Design*, vol. 263, pp. 327–341, 2013.

Appendix A

Derivation of Jacobi matrix A

$$\mathbf{U} = \begin{bmatrix} \rho_g\alpha_g \\ \rho_l\alpha_l \\ \rho_g\alpha_g u_g \\ \rho_l\alpha_l u_l \end{bmatrix} = \begin{bmatrix} u_1 \\ u_2 \\ u_3 \\ u_4 \end{bmatrix} \tag{A.1}$$

$$\begin{aligned} \mathbf{A}\frac{\partial \mathbf{U}}{\partial x} &= \frac{\partial}{\partial x}\mathbf{F}^c + \mathbf{F}^{nc} \\ &= \frac{\partial}{\partial x}\begin{bmatrix} \rho_g\alpha_g u_g \\ \rho_l\alpha_l u_l \\ \rho_g\alpha_g u_g^2 \\ \rho_l\alpha_l u_l^2 \end{bmatrix} + \begin{bmatrix} 0 \\ 0 \\ \alpha_g\frac{\partial p}{\partial x} + \Delta p\frac{\partial \alpha_g}{\partial x} \\ \alpha_l\frac{\partial p}{\partial x} + \Delta p\frac{\partial \alpha_l}{\partial x} \end{bmatrix}. \end{aligned} \tag{A.2}$$

$\mathbf{F}^c$ can be easily rewritten as

$$\mathbf{F}^c = \begin{bmatrix} u_3 \\ u_4 \\ \frac{u_3^2}{u_1} \\ \frac{u_4^2}{u_1} \end{bmatrix}. \tag{A.3}$$

Suppose $\mathbf{A}_c = \frac{d\mathbf{F}^c}{d\mathbf{U}}$, one has

$$\mathbf{A}^c = \frac{d\mathbf{F}}{d\mathbf{U}} = \begin{bmatrix} 0 & 0 & 1 & 0 \\ 0 & 0 & 0 & 1 \\ -\frac{u_3^2}{u_1^2} & 0 & 2\frac{u_3}{u_1} & 0 \\ 0 & -\frac{u_4^2}{u_2^2} & 0 & 2\frac{u_4}{u_2} \end{bmatrix} = \begin{bmatrix} 0 & 0 & 1 & 0 \\ 0 & 0 & 0 & 1 \\ -u_g^2 & 0 & 2u_g & 0 \\ 0 & -u_l^2 & 0 & 2u_l \end{bmatrix}. \tag{A.4}$$

Since

$$\frac{u_1}{\rho_g(p)} + \frac{u_2}{\rho_l(p)} = 1, \tag{A.5}$$

a derivative of Eq. A.5 with respect to p leads to

$$-\frac{u_1}{\rho_g^2}\frac{\partial \rho_g}{\partial p}\frac{\partial p}{\partial x} + \frac{1}{\rho_g}\frac{\partial u_1}{\partial x} - \frac{u_2}{\rho_l^2}\frac{\partial \rho_l}{\partial p} + \frac{1}{\rho_l}\frac{\partial u_2}{\partial x} = 0. \tag{A.6}$$

On rearrangement, Eq. A.6 can be simplified to be

$$\left(\alpha_g \rho_l \frac{\partial \rho_g}{\partial p} + \alpha_l \rho_g \frac{\partial \rho_l}{\partial p}\right)\frac{\partial p}{\partial x} = \rho_l \frac{\partial u_1}{\partial x} + \rho_g \frac{\partial u_2}{\partial x}, \tag{A.7}$$

or

$$\alpha_g \frac{\partial p}{\partial x} = \omega \left(\alpha_g \rho_l \frac{\partial u_1}{\partial x} + \alpha_g \rho_g \frac{\partial u_2}{\partial x}\right), \tag{A.8}$$

where

$$\omega = 1/\left(\alpha_g \rho_l \frac{\partial \rho_g}{\partial p} + \alpha_l \rho_g \frac{\partial \rho_l}{\partial p}\right). \tag{A.9}$$

From Eq. A.1, one has

$$u_1 = \alpha_g \rho_g(p). \tag{A.10}$$

Thus, the derivative of Eq. A.10 with respect to x is

$$\frac{\partial u_1}{\partial x} = \rho_g \frac{\partial \alpha_g}{\partial x} + \alpha_g \frac{\partial \rho_g}{\partial p}\frac{\partial p}{\partial x}. \tag{A.11}$$

By substituting Eq. A.8 into Eq. A.11 and on rearrangement, one can obtain the following expression:

$$\frac{\partial \alpha_g}{\partial x} = \omega \left(\alpha_l \frac{\partial \rho_l}{\partial p} \frac{\partial u_1}{\partial x} - \alpha_l \frac{\partial \rho_g}{\partial p} \frac{\partial u_2}{\partial x} \right). \tag{A.12}$$

Therefore, one has

$$\Delta p \frac{\partial \alpha_g}{\partial x} = \omega \Delta p \left(\alpha_l \frac{\partial \rho_l}{\partial p} \frac{\partial u_1}{\partial x} - \alpha_l \frac{\partial \rho_g}{\partial p} \frac{\partial u_2}{\partial x} \right). \tag{A.13}$$

Combining Eqs. A.8 and A.13, one can obtain the following equation for the gas phase:

$$\alpha_g \frac{\partial p}{\partial x} + \Delta p \frac{\partial \alpha_g}{\partial x} = \omega \left(\alpha_g \rho_l + \Delta p \alpha_l \frac{\partial \rho_l}{\partial p} \right) \frac{\partial u_1}{\partial x} + \omega \left(\alpha_g \rho_g - \Delta p \alpha_l \frac{\partial \rho_g}{\partial p} \right) \frac{\partial u_2}{\partial x}. \tag{A.14}$$

In a similar way, one can obtain the following equation for the liquid phase as follows:

$$\alpha_l \frac{\partial p}{\partial x} + \Delta p \frac{\partial \alpha_l}{\partial x} = \omega \left(\alpha_l \rho_l - \Delta p \alpha_l \frac{\partial \rho_l}{\partial p} \right) \frac{\partial u_1}{\partial x} + \omega \left(\alpha_g \rho_g + \Delta p \alpha_g \frac{\partial \rho_g}{\partial p} \right) \frac{\partial u_2}{\partial x}. \tag{A.15}$$

Suppose $\mathbf{F}^{nc} = \mathbf{A}^{nc} \frac{\partial \mathbf{U}}{\partial x}$, based on Eqs. A.14 and A.15, the expression for $\mathbf{A}^{mc}$ can be given by

$$\mathbf{A}^{nc} = \begin{bmatrix} 0 & 0 & 0 & 0 \\ 0 & 0 & 0 & 0 \\ \omega \left(\alpha_g \rho_l + \Delta p \alpha_l \frac{\partial \rho_l}{\partial p} \right) & \omega \left(\alpha_g \rho_g - \Delta p \alpha_g \frac{\partial \rho_g}{\partial p} \right) & 0 & 0 \\ \omega \left(\alpha_l \rho_l - \Delta p \alpha_l \frac{\partial \rho_l}{\partial p} \right) & \omega \left(\alpha_g \rho_l + \Delta p \alpha_g \frac{\partial \rho_g}{\partial p} \right) & 0 & 0 \end{bmatrix}. \tag{A.16}$$

Addition of Eqs. A.4 and A.16 gives

$$\mathbf{A}(\mathbf{U}) = \begin{bmatrix} 0 & 0 & 1 & 0 \\ 0 & 0 & 0 & 1 \\ \omega\left(\alpha_g\rho_l + \Delta p\alpha_l\frac{\partial\rho_l}{\partial p}\right) - u_g^2 & \omega\left(\alpha_g\rho_g - \Delta p\alpha_g\frac{\partial\rho_g}{\partial p}\right) & 2u_g & 0 \\ \omega\left(\alpha_l\rho_l - \Delta p\alpha_l\frac{\partial\rho_l}{\partial p}\right) & \omega\left(\alpha_g\rho_l + \Delta p\alpha_g\frac{\partial\rho_g}{\partial p}\right) - u_l^2 & 0 & 2u_l \end{bmatrix}. \quad \text{(A.17)}$$

Appendix B

Derivation of $\hat{U}^{\pm}$

First, Eq. 3.35 is repeated here.

$$\hat{U}^{\pm}(u,a,\chi) = \begin{cases} \pm\chi\frac{(u\pm a)^2}{4a} + (1-\chi)\frac{u\pm|u|}{2}, & if \ \ |u| \le a \\ \frac{u\pm|u|}{2}, & else. \end{cases} \tag{B.1}$$

For a stationary contact

For a stationary contact discontinuity, where $u_L = u_R = 0, p_{1/2} = p_L = p_R$, the velocity splitting functions $\hat{U}^{\pm}$ can be simplified by using a common sound speed.

$$\begin{aligned} \hat{U}_L^{+} &= \tfrac{1}{4}\chi_L a \\ \hat{U}_R^{-} &= -\tfrac{1}{4}\chi_R a. \end{aligned} \tag{B.2}$$

Therefore, supposing [9]

$$\chi_L\alpha_L = \chi_R\alpha_R, \tag{B.3}$$

the interfacial mass flux in the AUSMD/V schemes (see Eq. 3.34) can be given by

$$\begin{aligned} (\alpha\rho u)_{1/2} &= \hat{U}_L^{+}\alpha_L\rho_L + \hat{U}_R^{-}\alpha_R\rho_R \\ &= \tfrac{1}{4}\chi_L a\alpha_L\rho_L - \tfrac{1}{4}\chi_R a\alpha_R\rho_R = 0, \end{aligned} \tag{B.4}$$

where the relationship, $\rho_L = \rho_R$, has been used.

Hence, for a stationary contact discontinuity, the interface mass flux in the AUSMD/V schemes vanishes. In other words, the AUSMD/V schemes is capable of keeping the contact discontinuity stationary.

For a moving contact

For a moving contact discontinuity, where $u_L = u_R = u \neq 0, p_{1/2} = p_L = p_R$, the velocity splitting functions $\hat{U}^{\pm}$ can be simplified as follows:

$$\begin{aligned} \widehat{U}_L^{+} &= \chi_L \tfrac{(u+a)^2}{4a} + (1-\chi_L)\tfrac{u+|u|}{2} \\ \widehat{U}_R^{-} &= -\chi_R \tfrac{(u-a)^2}{4a} + (1-\chi_R)\tfrac{u-|u|}{2}. \end{aligned} \tag{B.5}$$

Therefore, the interfacial mass flux in the AUSMD/V schemes (see Eq. 3.34) can be given by

$$\begin{aligned} &(\alpha\rho u)_{1/2} = \widehat{U}_L^{+}\alpha_L\rho_L + \widehat{U}_R^{-}\alpha_R\rho_R \\ &= \chi_L\alpha_L\rho_L\tfrac{(u+a)^2}{4a} - \chi_R\alpha_R\rho_R\tfrac{(u-a)^2}{4a} + (1-\chi_L)\alpha_L\rho_L\tfrac{u+|u|}{2} + (1-\chi_R)\alpha_R\rho_R\tfrac{u-|u|}{2}. \end{aligned} \tag{B.6}$$

Using $\chi_L\alpha_L = \chi_R\alpha_R$ [9] and $\rho_L = \rho_R$, one can obtain the following relationship:

$$\begin{aligned} (\alpha\rho u)_{1/2} &= \chi_L\alpha_L\rho_L\left(\tfrac{(u+c)^2}{4c} - \tfrac{(u-c)^2}{4c}\right) \\ &\quad -\chi_L\alpha_L\rho_L u + \alpha_L\rho_L\tfrac{u+|u|}{2} + \alpha_R\rho_R\tfrac{u-|u|}{2} \\ &= \tfrac{1}{2}\left[u\left(\alpha_L\rho_L + \alpha_R\rho_R\right) - |u|\left(\alpha_R\rho_R - \alpha_L\rho_L\right)\right] \\ &= \begin{cases} u\alpha_L\rho_L, & \text{if } u > 0 \\ u\alpha_R\rho_R, & \text{otherwise.} \end{cases} \end{aligned} \tag{B.7}$$

Hence, the mass flux formula of Eq. B.7 exactly equals to that of the Riemann solution for a moving contact discontinuity.

Weighting factor χ

The weighting factor χ is designed to recover the FVS splitting flux ($U^{\pm}$) to achieve maximum stability for continuous flow with $\mathbf{U}_L = \mathbf{U}_R$. In other words, for $\mathbf{U}_L = \mathbf{U}_R$, the

weighting factor should satisfy

$$\chi_L = \chi_R = 1. \tag{B.8}$$

Consequently, based on Eqs. B.3 and B.8, χ is defined as

$$\begin{aligned} \chi_L &= \frac{2\bar{\chi}_L}{\bar{\chi}_L + \bar{\chi}_R} \\ \chi_R &= \frac{2\bar{\chi}_R}{\bar{\chi}_L + \bar{\chi}_R} = 2 - \chi_L, \end{aligned} \tag{B.9}$$

where

$$\begin{aligned} \bar{\chi}_L &= \frac{\rho(p_L)}{\alpha_L} \\ \bar{\chi}_R &= \frac{\rho(p_R)}{\alpha_R} \end{aligned} . \tag{B.10}$$

In other words, the weighting factor χ can be given as the Eq. 3.36. Figure B.1 shows the velocity splitting function $\hat{U}^{\pm}$ in terms of χ $(0 \leq \chi \leq 2)$ [1].

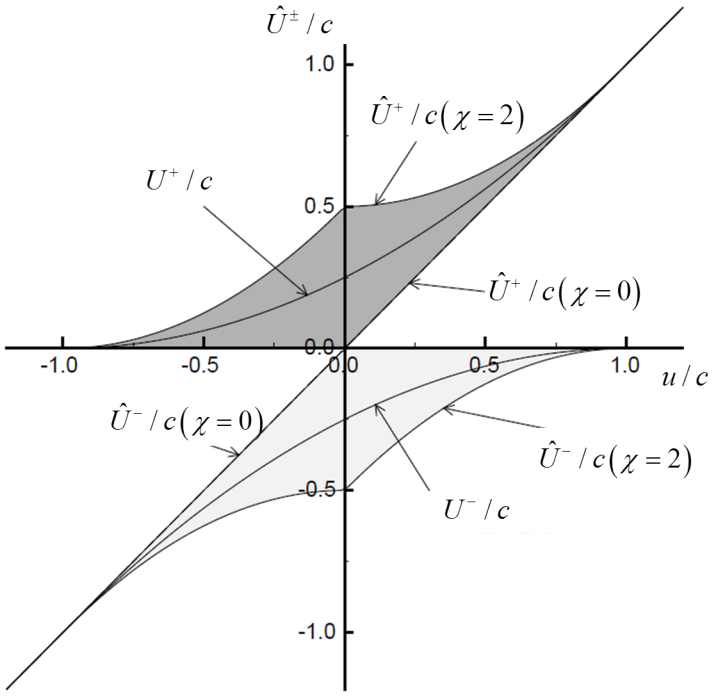

Figure B.1: Velocity splitting function in the AUSMD/V scheme [1].